MODELLING AND ESTIMATION OF LEAKAGE PHENOMENA IN MAGNETIC CIRCUITS

Thesis by

Abraham A. Dauhajre

In Partial Fulfillment of the Requirements

for the Degree of

Doctor of Philosophy

California Institute of Technology

Pasadena, California

1986

(Submitted April 22, 1986)

ACKNOWLEDGMENTS

I am deeply indebted to my advisor Professor R. D. Middlebrook and my co-advisor Professor Slobodan Ćuk for accepting me into the Power Electronics group, and for their encouragement, guidance, and support during my years at Caltech.

I also wish to acknowledge the financial support of the California Institute of Technology by way of several Graduate Teaching Assistantships, the Garrett Corporation, the NASA Lewis Research Center, the International Business Machines Corporation, and General Dynamics for Graduate Research Assistantships.

To my friends who made my stay a more pleasant and productive experience, I am very grateful.

Finally, of great personal importance to me have been the understanding, encouragement and support of my parents and my wife Yasmin during my years at Caltech.

ABSTRACT

A new modelling method for magnetic circuits is presented in this thesis. This method can be used to model magnetic circuits with any number of windings. The models incorporate adequate information about the correct distribution of leakage energy, the presence of gaps throughout the core, the arrangement of the windings, and the type of core used.

These new electric circuit models (*physical models*) are "physically natural"; i.e., the elements in the models have a one-to-one relationship with corresponding physical quantities in the original magnetic structure.

Several commonly used arrangements such as toroids with uniformly distributed turns, and bobbin core structures with multiple windings were modelled with the new technique. The measured electric circuit model values always compared favorably with the predicted physical values derived with the new method.

By breaking the windings of the magnetic circuit into their separate layers, a more elaborate and accurate set of models (layer-to-layer models) can be obtained. These models incorporate additional information about the correct distribution of the windings and interwinding self-capacitances. Because of the complicated nature of these elaborate models, they are more suitable for computer analysis of magnetic circuits.

TABLE OF CONTENTS

CHAPTER 1

INTRODUCTION

In recent years, the use of magnetic components in switching converters has been greatly affected by new developments in the disciplines that form the basis for power electronics.

In the field of semiconductor devices, the development of new high-power switching devices (FET's etc.) prompted designers of power conversion equipment to increase the switching frequency at which the main semiconductor devices are operated. In consequence, the size and weight of the magnetics, and therefore of the entire power supply have been considerably reduced.

As the switching frequency is increased, a point is reached at which the bottleneck of such designs is not in the semiconductor devices but, on the contrary, in the magnetics design.

For example, even after careful layout of the isolation transformer in a switching power supply, a small residual leakage inductance can have severe adverse effects on the power supply operation and design, from requiring sizable power dissipative networks to making the design completely inoperable when the switching frequency is sufficiently increased.

The development of new topologies for switching power converters, together with the discovery of the *zero-ripple phenomena* in coupled inductors and integrated magnetic structures [1, 2, 3], has

also played a very important role in the development of new magnetic circuits for switching power converters.

For example, in many multiple-output switching converters, the output and input inductors can be combined into a single magnetic structure [4]. The resultant savings in the cost and reduced size of the converters are further augmented by improved performance through reduced ripple currents. However, the actual ripple current distribution among the various output windings is, to first-order, dependent on the distribution of leakage energy in the windings of the magnetic structure. Hence, in these coupled-inductors and recently proposed integrated magnetic structures, the magnetic leakages also play a first-order role, improving the performance of such converters by reducing the amount of current ripple in some of the windings.

Because leakage can have both positive and negative effects in different applications, it is important to know, for each case, the correct distribution of leakage energy in the windings of the magnetic structure under investigation.

In the case of transformers, this can lead to further improvements in the selection and design of transformers with minimum leakage.

For coupled-inductors and integrated magnetic structures where leakage has positive effects, a better assessment of the improvements can be made.

Unfortunately, conventional modelling methods for magnetic circuits have always fallen short of predicting the correct

distribution of leakage energy in the windings of a magnetic structure.

A new modelling method for magnetic circuits is introduced in this thesis. The technique involves determination of the approximate flux pattern inside the actual magnetic structure under investigation, and the analytic determination of all the parameter values in the electric circuit model derived from the flux pattern.

This method can be used to model magnetic circuits with any number of windings. The models contain adequate information about the correct distribution of leakage energy, the arrangement of the windings, the presence of gaps throughout the core, and the type of core used.

The electric circuit models (*physical models*) obtained with this method are *physically natural*; i.e., the elements in these models have a one-to-one relationship with corresponding *physical* quantities in the original magnetic structure. This simplifies the task of finding analytic expressions for all the elements in the models, and it also makes it easy to relate these elements to their corresponding physical parameters in the original magnetic structure.

These models can be particularly useful in prediction of the effects of second-order parasitics on switching converters. For example, for a particular application, different arrangements can be studied through their *physical models*, and the one that gives the best performance can easily be chosen. All this can be accomplished without going through the usual "trial and error" process.

CHAPTER 2

MAGNETIC DEVICES IN SWITCHING CONVERTERS

One of the principal goals of any switched-mode power converter is to process power at the maximum possible efficiency, which is why resistors, and semiconductor devices operated in their linear-mode, are avoided in the power stage of any switching converter. Only lossless elements such as magnetic components (transformers, inductors, etc.), capacitors, and switches are used in power processing circuits.

This chapter reviews some of the basic magnetic components commonly used in switching converters.

2.1 Inductors

Inductors are used as energy storage elements to transfer energy from one point in the switching circuit to another.

Figure 2.1 illustrates a simple buck-boost converter. During the first part of the cycle (DT_s), energy is transferred from the source V_g to the inductor L, and this energy is then released into the load during the reminder of the cycle $D'T_s$. The inductor current waveform is illustrated in Fig. 2.1.

2.2 Coupled-Inductors

Sometimes it is possible to couple several inductors into a single magnetic component, resulting typically in considerable savings in magnetic material, size, weight, and cost of the power supply.

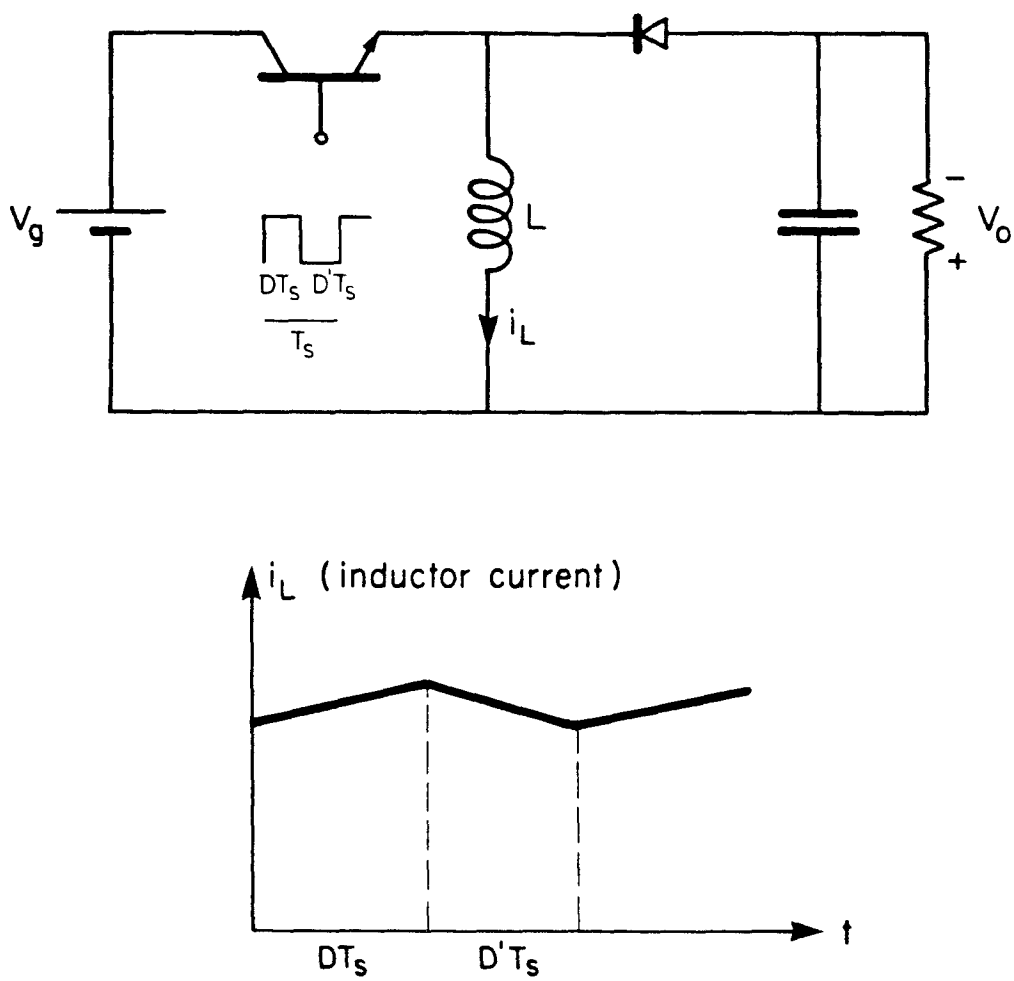

Fig. 2.1. Buck-boost dc-to-dc converter.

For example, in the Ćuk dc-to-dc converter in Fig. 2.2a, since the inductor voltages v_1 and v_2 are identical, then, in principle, the two inductors can be combined into a single magnetic component as illustrated in Fig. 2.2b.

In general, it can be shown that any number of inductors can be coupled into a single coupled-inductor structure, if all the uncoupled inductor voltages are proportional to each other [3, 4, 5].

2.3 Transformers

Transformers provide electric isolation between the input and the output(s) of a switching converter. Also, because of the natural transformer turns ratio, the voltage and current gains can be either stepped up or down by proper selection of this ratio.

The non-isolated and isolated versions of the four basic dc-to-dc converters (buck, boost, buck-boost, and Ćuk) are illustrated in Fig. 2.3. Notice that in all the isolated versions the voltage gain M is proportional to the transformer turns ratio N.

The isolation transformer used in the buck-boost (flyback) converter (Fig. 2.3c) is significantly different from those in the buck, the boost, and the Ćuk converters. The transformers in these three converters are transparent to the energy transfer process; i.e., no significant amount of energy is stored in them. The flyback transformer, on the other hand, is the energy storage and transfer element itself.

In general, the four isolated converters can be easily extended to give multiple isolated outputs. For example, a multiple-output version of the Ćuk converter is shown in Fig. 2.4.

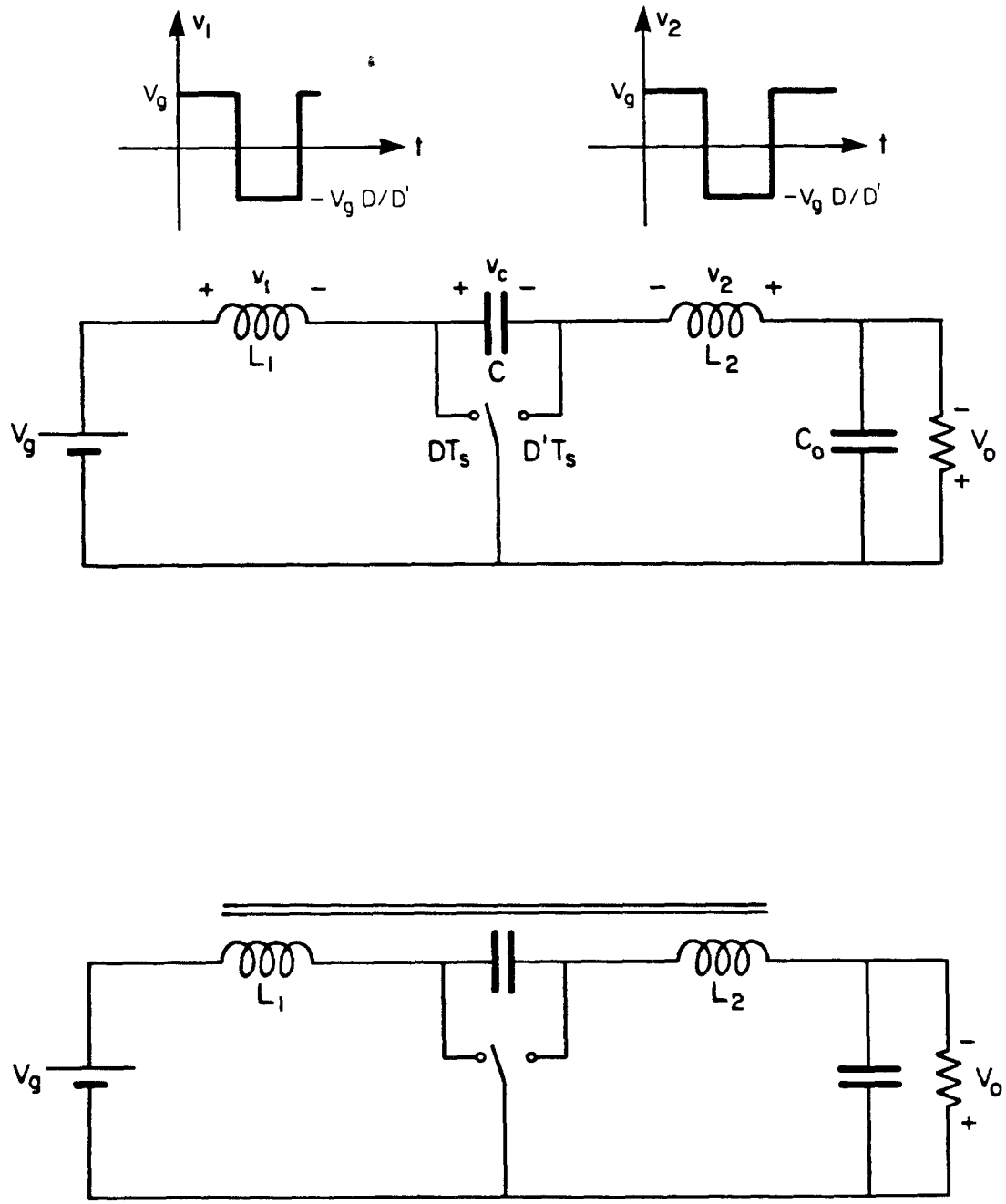

Fig. 2.2. Ćuk *dc-to-dc converter, (a) with uncoupled inductors, (b) with coupled inductors.*

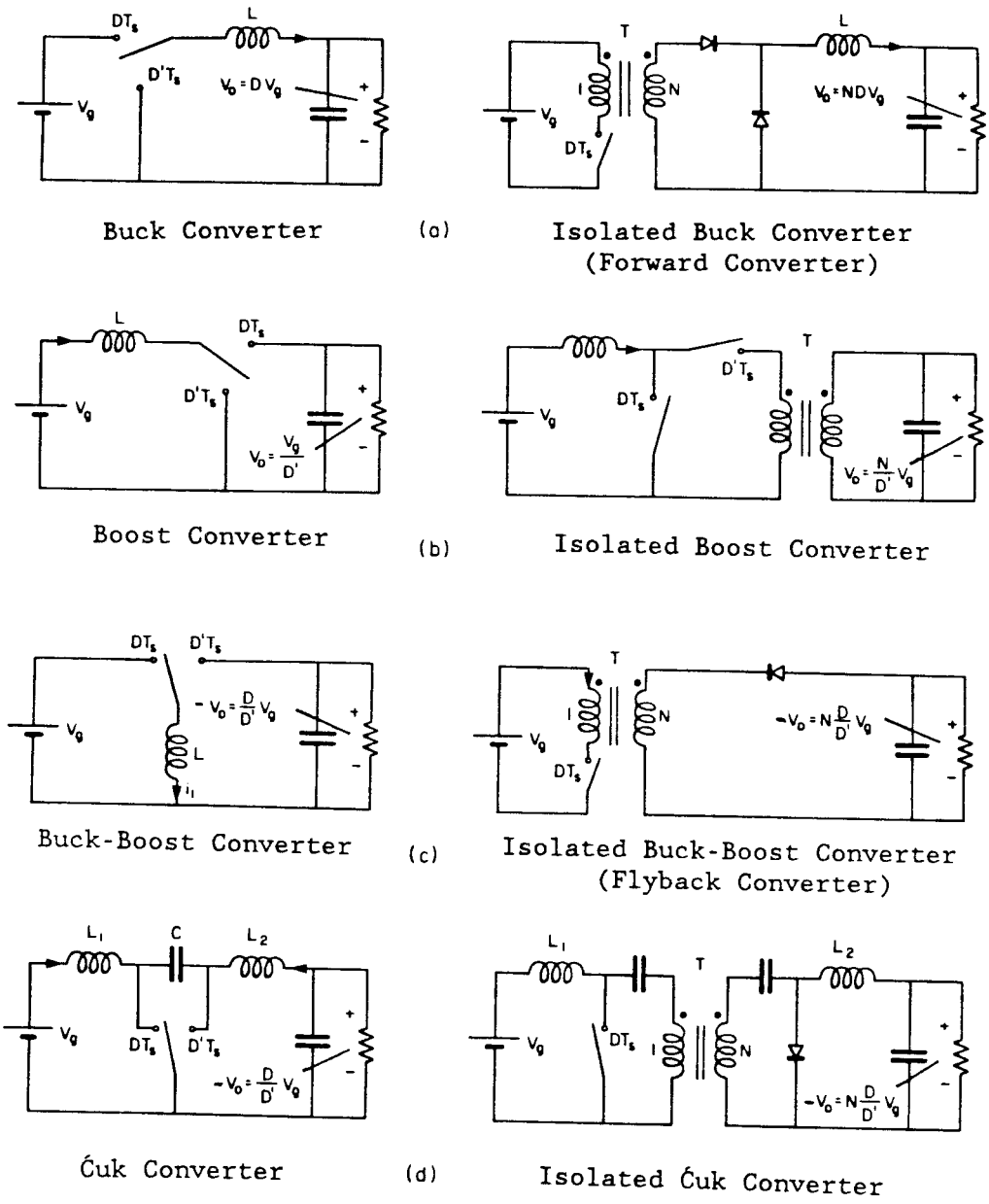

Fig. 2.3. Four basic dc-to-dc converters and their corresponding isolated versions (a) buck, (b) boost, (c) buck-boost, (d) Ćuk.

2.4 Integrated Magnetic Structures

In the same way that it is sometimes possible to couple several inductors into a single piece of magnetics, it is also possible to integrate several inductors and transformers into a single magnetic component [3, 5]. Again, substantial savings in magnetic material, size, weight and costs result from the integration.

For example, careful examination of the isolated Ćuk converter in Fig. 2.4 shows that the inductors and transformer voltage waveforms are all proportional to each other [3, 5]. Therefore, these separate elements can be integrated into a single magnetic structure as shown in Fig. 2.5.

In the next chapter, some of the same magnetic components and converters that were briefly discussed in this chapter are used to illustrate how leakage, a second-order parasitic phenomenon in magnetic circuits, can have first-order effects on some of these converters.

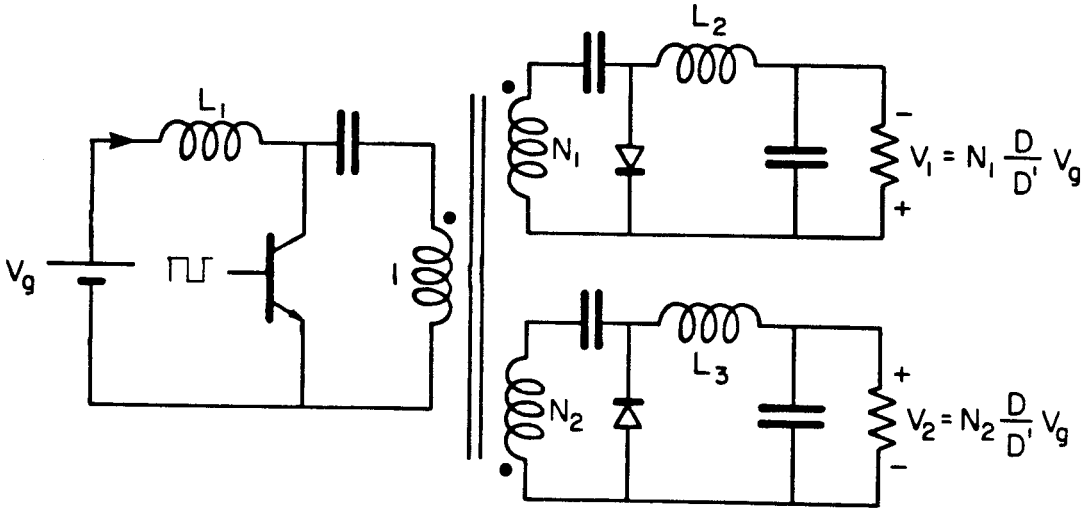

Fig. 2.4. Multiple outputs in Ćuk converter.

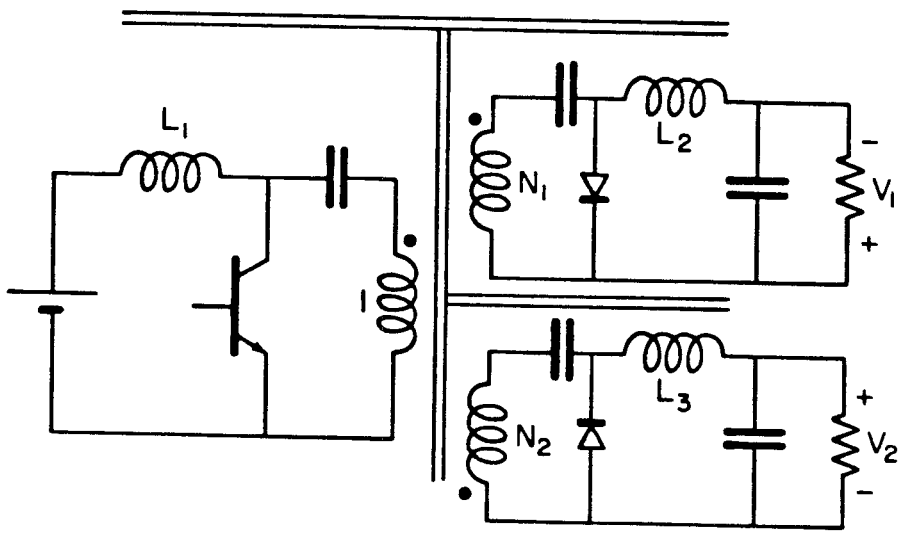

Fig. 2.5. Ćuk converter with integrated magnetic structure.

CHAPTER 3

LEAKAGE PHENOMENA IN SWITCHING CONVERTERS

Some of the basic magnetic components commonly used in switching converters were reviewed in the previous chapter.

In this chapter, it is shown how *magnetic leakage*, usually considered to be a second-order parasitic phenomenon in magnetic circuits, can have first-order useful effects in switching applications.

3.1 Adverse Leakage Effects in Transformers

Transformers provide isolation, step ratios and, sometimes, energy storage capabilities in switching converters. The transformer in the isolated *flyback* converter in Fig. 3.1 has these three properties.

During the time DT_s, the transistor is turned on, and energy is stored in the inductance of the transformer. During $D'T_s$, when the transistor is off, the inductance energy *flies-back* to the output, turns the diode on, and releases energy into the load. The ideal current and voltage waveforms of the transistor switch are illustrated in Fig. 3.1.

Application of volt-second balance [6] across the inductance of the transformer results in

$$M = \frac{V_o}{V_g} = N \frac{D}{D'} \tag{3.1}$$

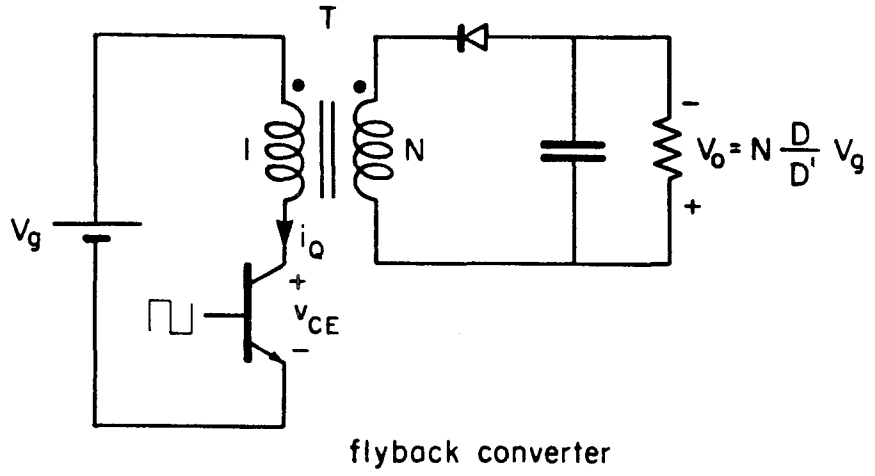

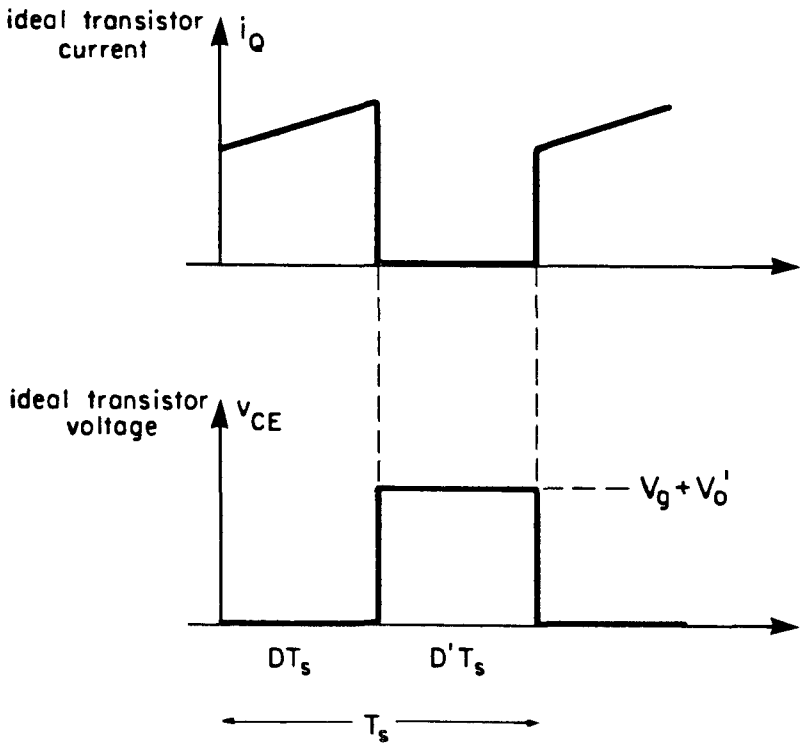

Fig. 3.1. Illustration of ideal transistor voltage and current waveforms in flyback converter.

Mathematically, the input-output characteristics of any magnetic circuit with two windings can be represented by the electric circuit model shown in Fig. 3.2 [7]. If the mutual inductance L_m of the transformer is much larger than the "leakage inductances" ℓ_1, and ℓ_2, the electric circuit model in Fig. 3.2 can be reduced to that in Fig. 3.3, where

$$\ell = \ell_1 + \frac{\ell_2}{N^2} \tag{3.2}$$

This approximate model can be used to find the actual (non-ideal) voltage and current waveforms of the transistor switch, as shown in Fig. 3.4.

On the assumption that a *steady-state* condition has been reached by the circuit after a few switching cycles, every time the transistor is turned off, the mutual inductance L_m releases its energy into the load, but the "leakage inductance" ℓ, which carries the same current as the mutual inductance during the on-time of the switch, does not have a path into which to release its energy. However, since the transistor switch is not ideal, it does not turn off in zero time. During the very small turn-off time of the transistor, the leakage inductance has a path through which it can discharge, namely, the transistor collector-emitter junction.

If the transistor turn-off time is Δt, and the leakage inductance current at turn-off is I, then a voltage spike of approximate value

$$V_s = \ell \frac{di}{dt} \approx \ell \frac{I}{\Delta t} \tag{3.3}$$

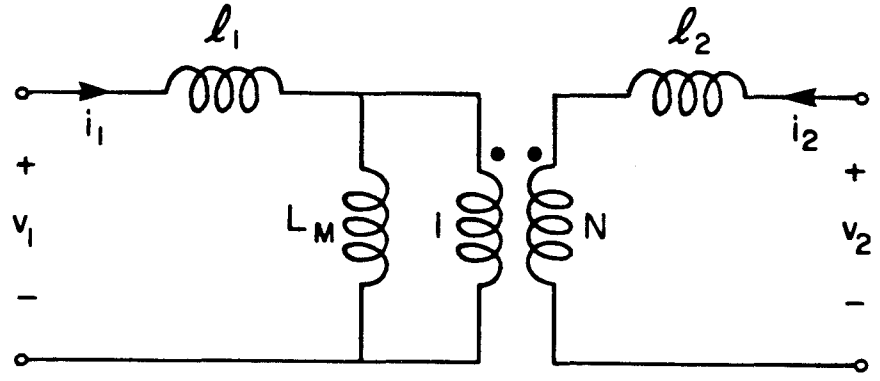

Fig. 3.2. π-model for two-winding magnetic circuits.

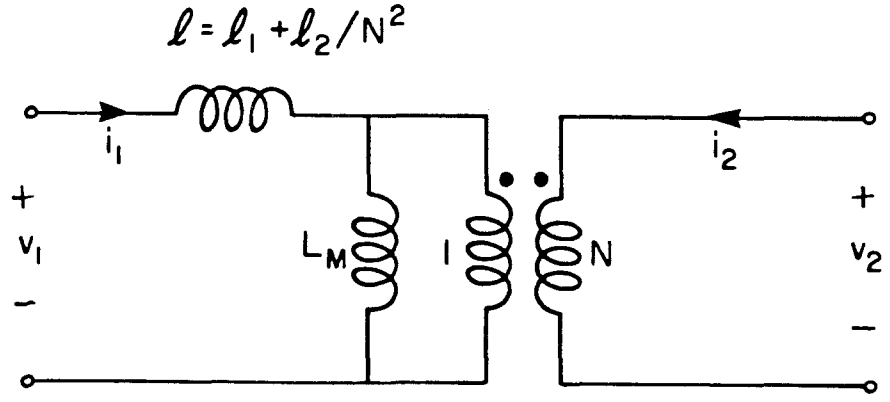

Fig. 3.3. Approximate π-model for two-winding magnetic circuit with $L_M >> \ell_1\ \ell_2$.

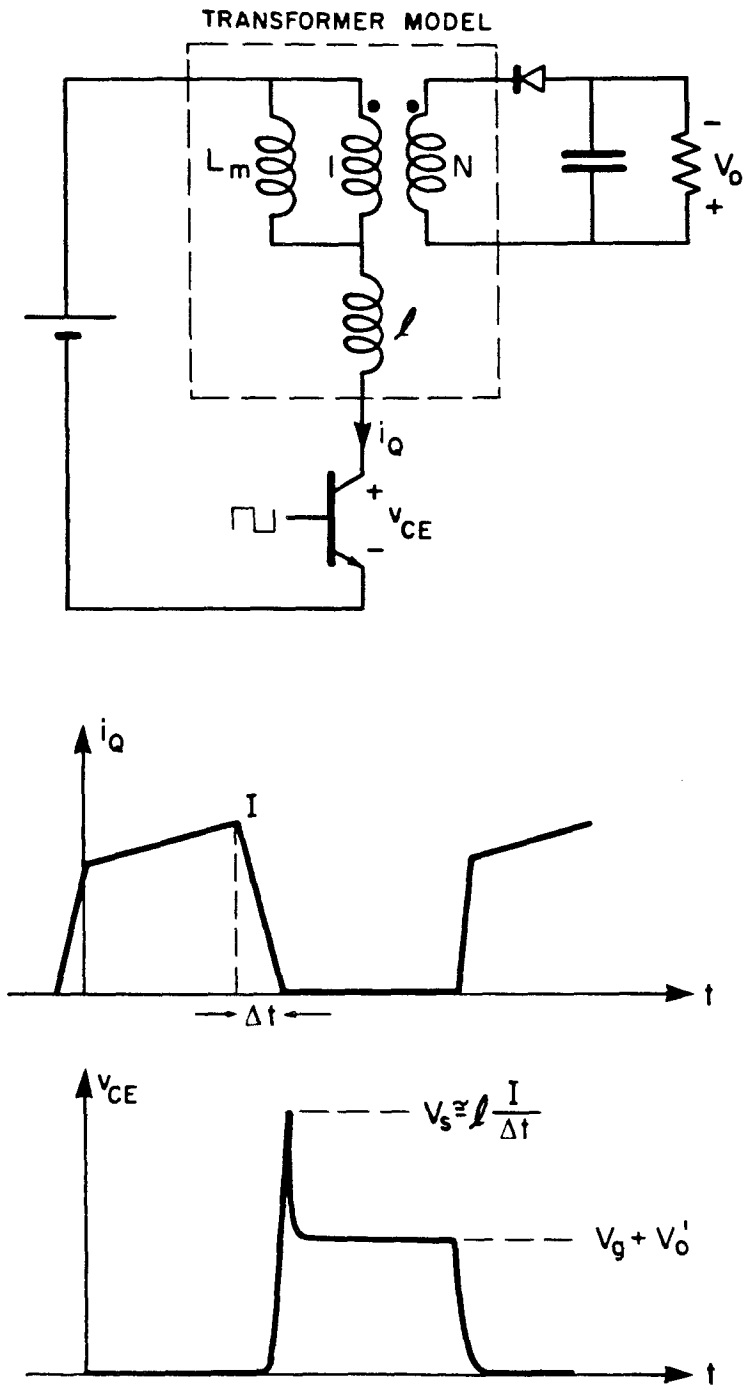

Fig. 3.4. Flyback converter with approximate transformer model. The non-ideal voltage and current waveforms of the transistor illustrate the adverse effects of the leakage inductance on the switching element.

appears across the collector-emitter terminals of the transistor. The approximate current and voltage waveforms of the transistor are shown in Fig. 3.4b.

For example, for a turn-off time of 0.5 μS, a leakage inductance of 100 μH, and an input current of 1 A at turn-off, a voltage spike of about 200 volts is generated across the collector-emitter junction of the transistor. This can be fatal for almost any low-to-medium power switching transistor.

By increasing the switching frequency, the size and weight of the transformer can be decreased. In Chapter 14, it is shown that this also results in an increase in the transformer's *leakage ratio*. Also, with the development of new faster semiconductor devices (FET's etc.), the turn-off time of the switches (Δt in Eq.(3.3)), can be dramatically reduced. All this results in an increase of the spikes generated across the switching elements.

Several methods for protecting the switches from spurious turn-off voltage spikes due to leakage inductances have been developed in the past. They range from using special winding techniques to reduce the leakage inductance of the transformers, to introducing extra elements in the circuit to protect the switches. These extra elements absorb most of the energy in the turn-off voltage spikes. A commonly used protection circuit known as a snubber is illustrated in Fig. 3.5.

During the turn-off time of the switch (Fig. 3.5b), the snubber diode turns on, the leakage current flows through the diode (away from the transistor), and charges the capacitor C. This capacitor absorbs all the energy that otherwise would be released through the transistor

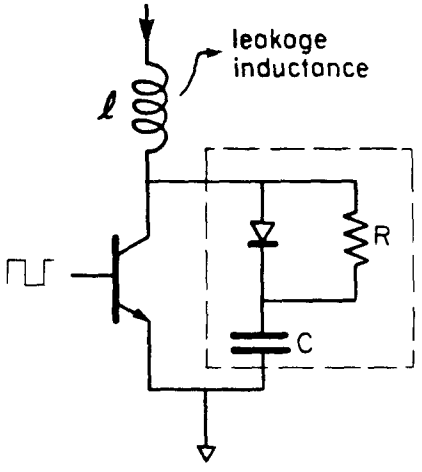

(a) Turn-off Snubber Circuit.

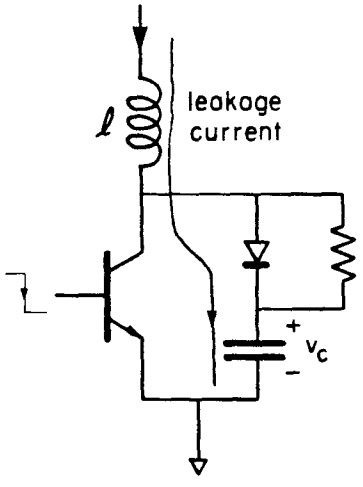

(b) At turn-off the leakage current flows away from the transistor and charges the capacitor C.

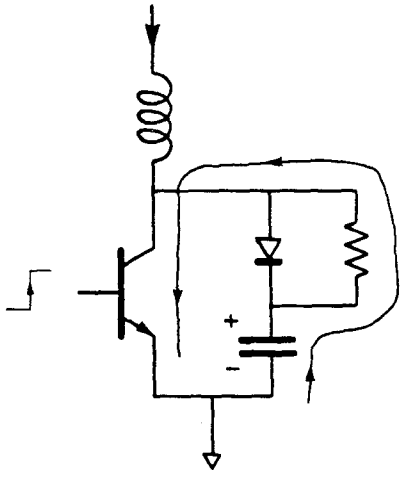

(c) Capacitor discharge during turn-on.

Fig. 3.5. Turn-off snubber circuit.

in a very short period of time. When the transistor is turned back on, the capacitor energy is released through the resistor R and, finally, through the transistor to ground as shown in Fig. 3.5c.

As the switching frequency is increased, the size and weight of the additional circuits necessary to protect the switches can eventually overcome any savings obtained by reducing the size of the magnetics. Obviously, there most be some switching frequency at which no further reduction in size or weight of the power supply is obtained. The problem of finding the optimum switching frequency is illustrated with more detail in Chapter 14.

3.2 Leakage Effects in Coupled Inductors

Power electronics engineers usually associate leakage with the adverse effects it produces in transformers. The discovery of the "zero current-ripple phenomena" in coupled-inductors [1] changed this unique perception. It is now very well understood that this second-order phenomenon can have not only negative effects (as in transformers), but also positive and very desirable effects in coupled-inductor applications.

Coupled inductors can be used in a variety of switching dc-to-dc converters. The following example illustrates how leakage in the coupled inductors of the dc-to-dc converter can drastically change the performance of the converter.

Application of volt-second balance across the inductors, and current-second balance across the energy transfer capacitor of the Ćuk converter in Fig. 2.2, results in

$$M = \frac{V_o}{V_g} = \frac{D}{D'} \tag{3.4}$$

$$V_c = \frac{1}{D'} V_g \tag{3.5}$$

Since both the inductors voltages and currents are known, the flux in each inductor can be determined. The inductor fluxes are illustrated in Fig. 3.6. Since ϕ_1 and ϕ_2 are identical, if the two inductors are brought together as shown in Fig. 3.7a, the two fluxes in the center legs add to zero. The center legs can therefore be removed as shown in Fig. 3.7b. The new magnetic structure is a simple two-winding coupled inductor, which is smaller and weighs less than the two separate inductors in Fig. 3.7a.

3.2.1 Analysis of Current Ripple in Coupled Inductors

The following analysis shows how proper design of the parameters in the coupled inductors (including the leakage inductances), can lead to substantial reduction of the ripple currents.

Since the electric circuit model in Fig. 3.2 can be used to model the input-output characteristics of any two-winding magnetic structure, it can be used to model the coupled inductors in Fig. 3.7b. This in turn can be used to investigate the effects of the leakage inductances ℓ_1 and ℓ_2 on the a-c ripple currents i_1 and i_2.

Since the voltages applied to the input and output inductors are equal (Fig. 2.2), the ac ripple currents i_1 and i_2 can be obtained using the circuit model shown in Fig. 3.8, where the coupled inductors have been substituted by the electric circuit model in Fig. 3.2.

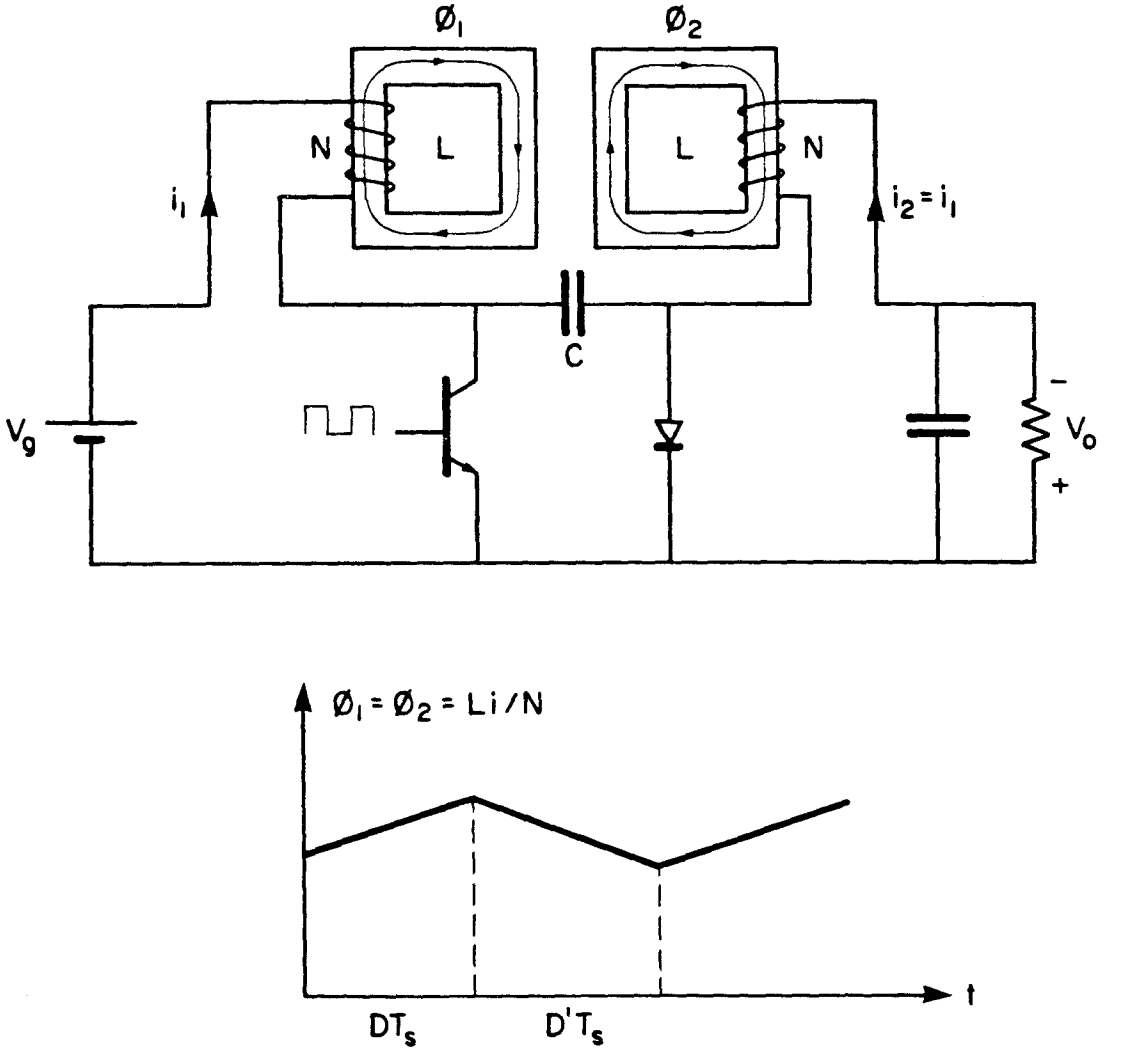

Fig. 3.6. Flux inside the inductors of the Ćuk converter.

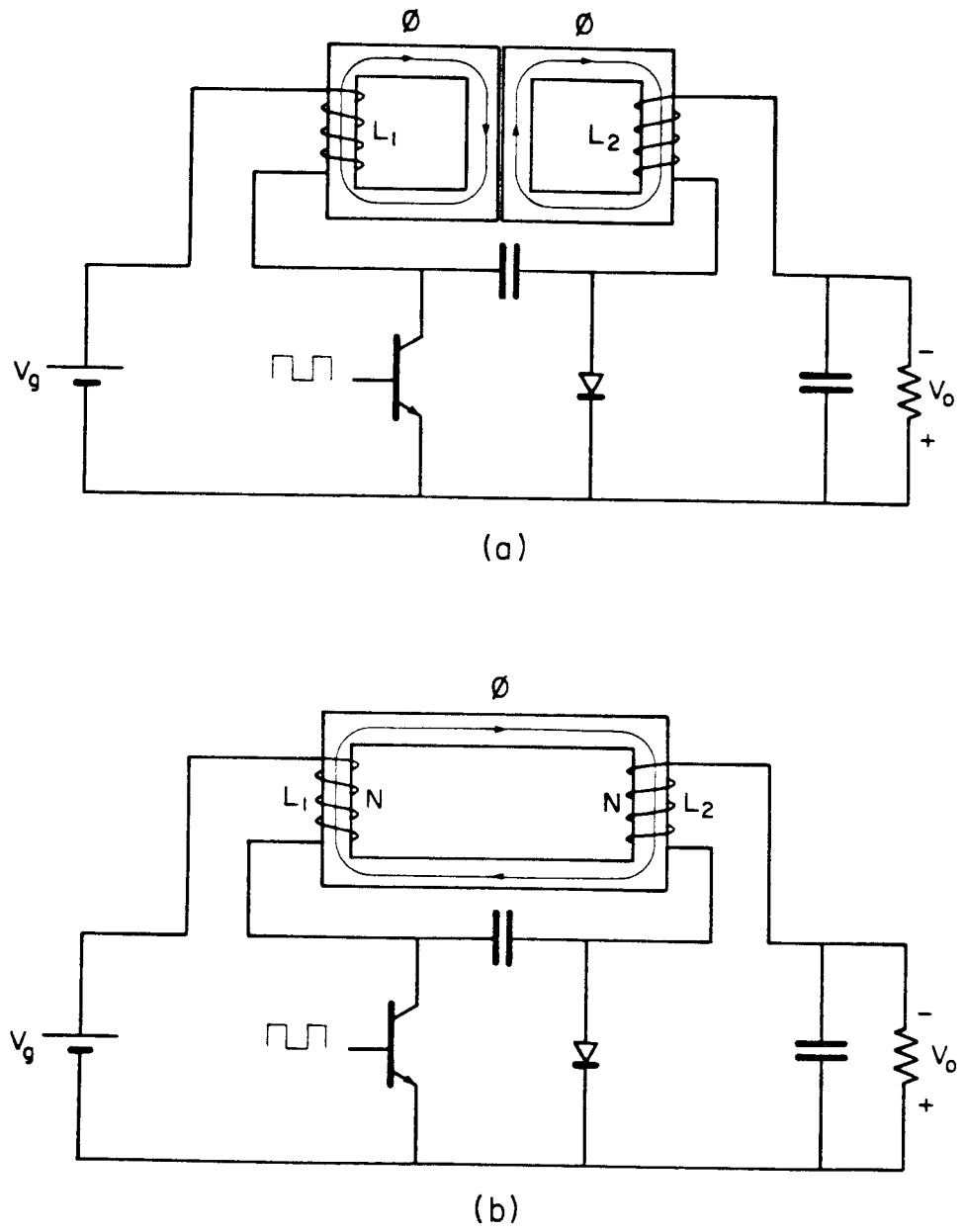

Fig. 3.7. Illustration of physical implementation of coupled-inductors in Ćuk converter. The coupled-inductors in (b) have less weight, size and volume than the two separate inductors in (a).

From the circuit in Fig. 3.8,

$$i_1 \left(\frac{\ell_1}{L_m(N-1)} - 1 \right) = i_2 \left(N - \frac{\ell_2}{L_m(1-N)} \right) \tag{3.6}$$

Now if

$$N = 1 + \frac{\ell_1}{L_m} \tag{3.7}$$

then

$$i_2 = 0 \tag{3.8}$$

Condition (3.7) is known as the "zero output ripple condition."

Similarly, if

$$\frac{1}{N} = 1 + \frac{\ell_2}{N^2 L_m} \tag{3.9}$$

then

$$i_1 = 0 \tag{3.10}$$

Equation (3.9) is the "zero input ripple condition."

This example illustrates how proper selection (design) of the parameters in the magnetic circuit can lead to a drastic reduction of the ripple currents in a switching converter. One of these parameters is the coupled inductor's leakage inductance.

3.3 Conclusions

Although leakage in magnetic circuits has always been considered a second-order parasitic phenomenon, it can have first-order effects in switching applications.

In transformers, leakage can generate spurious turn-off voltage spikes across the switches, which in turn will need to be

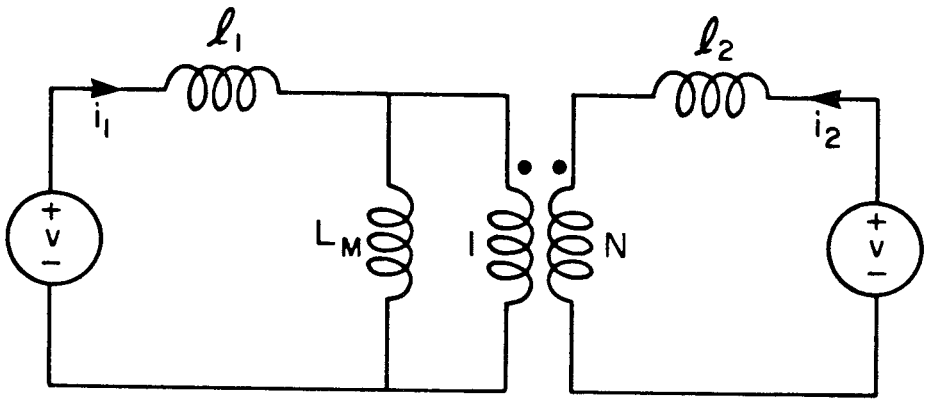

Fig. 3.8. The π-model for two-winding magnetic circuits can be used to investigate the ac ripple currents i_1 and i_2 in the Ćuk *converter with coupled-inductors.*

protected. As the switching frequency is increased, the increasing relative size and weight of the protection circuits might overcome any savings obtained by reducing the size of the magnetics.

In coupled inductors the leakage inductances in the magnetic circuit can be used to reduce, and sometimes even eliminate, the current ripple in either the input or the outputs of a switching converter. This is not an adverse, but a very positive and desirable effect.

The development of new models for magnetic circuits that incorporate information about the correct distribution of the leakage energy in the windings of the magnetic circuit, can have important implications on either of these applications. In transformers, these models can serve as a tool for designing transformers with minimum leakage and, in coupled inductors and zero current ripple applications, they can be used to design magnetic structures that should satisfy some ripple conditions. All this can be accomplished without going through the usual trial and error process generally associated with such design problems.

CHAPTER 4

FUNDAMENTAL ELECTROMAGNETICS

4.1 Introduction

In general, solution of the leakage problem involves determination of the leakage flux intensity throughout the windings of the magnetic structure. After all the fluxes inside the structure have been determined, a reluctance model is constructed based on the approximate *flux pattern* inside the core and windings.

To determine the leakage flux intensity throughout the windings requires the use of some of Maxwell's equations, in particular, those derived from Ampere's and Faraday's laws. Also, to find reluctance models, the relation between the magnetic flux density **B** and the magnetic field intensity **H**, and the electromagnetic energy equations are used.

This chapter reviews these fundamental relations, which constitute the mathematical background for the rest of this thesis.

4.2 Maxwell's Equations

Maxwell's equations, together with boundary and other auxiliary relations, form the basic tool of analysis for most electromagnetic problems, and in integral form are:

$$\oint_C \mathbf{H}\cdot d\ell = \iint \left(\mathbf{J} + \frac{\partial \mathbf{D}}{\partial t}\right) ds \qquad (4.1)$$

$$\oint_c \mathbf{E}\cdot d\ell = -\iint \frac{\partial \mathbf{B}}{\partial t}\cdot ds \tag{4.2}$$

$$\oiint \mathbf{B}\cdot ds = 0 \tag{4.3}$$

$$\oiint \mathbf{D}\cdot ds = \iiint \rho dv \tag{4.4}$$

Equation (4.1), *Maxwell's equation as derived from Ampere's law*, relates the field intensity **H** to the total current enclosed by the integration path *c*.

Equation (4.2), *Maxwell's equation as derived from Faraday's law*, relates the electric field intensity **E** to the magnetic flux density **B**. This field relation is a generalization of Faraday's circuit law.

Equations (4.3 and 4.4) are *Maxwell's field equations derived from Gauss' law*.

These equations will be used throughout this thesis under the following assumptions:

1. Displacement currents are negligible compared to conduction currents.

2. The frequencies of the time-varying quantities involved are low enough so that quasi-static approximations and lumped parameter models apply.

3. The material of which the magnetic structures are made is homogeneous and isotropic [8].

4.3 Ampere's Law

Under the previous assumptions, Eq. (4.1) can be written as

$$\oint_c \mathbf{H}\cdot d\ell = \iint \mathbf{J} ds \tag{4.5}$$

This relation is known as Ampere's law. It states basically that the closed line integral of **H** is equal to the total current enclosed by the integration path *c*. Figure 4.1 illustrates this relation with a simple example in which the integration path *c* goes along the center of the toroid. The toroid is surrounded by N uniformly distributed turns, each of which carries a current I. The total current enclosed by *c* is therefore

$$\iint \mathbf{J}\cdot d\mathbf{s} = NI \tag{4.6}$$

If the toroid is made of ferromagnetic material, the field intensity **H** can be assumed "almost" uniform throughout the toroid and parallel to the path *c*. Under these conditions, Eqs. (4.5) and (4.6) give

$$H(2\pi R_m) = NI \tag{4.7}$$

which yields

$$H = \frac{NI}{2\pi R_m} \tag{4.8}$$

where R_m is the mean radius of the toroid.

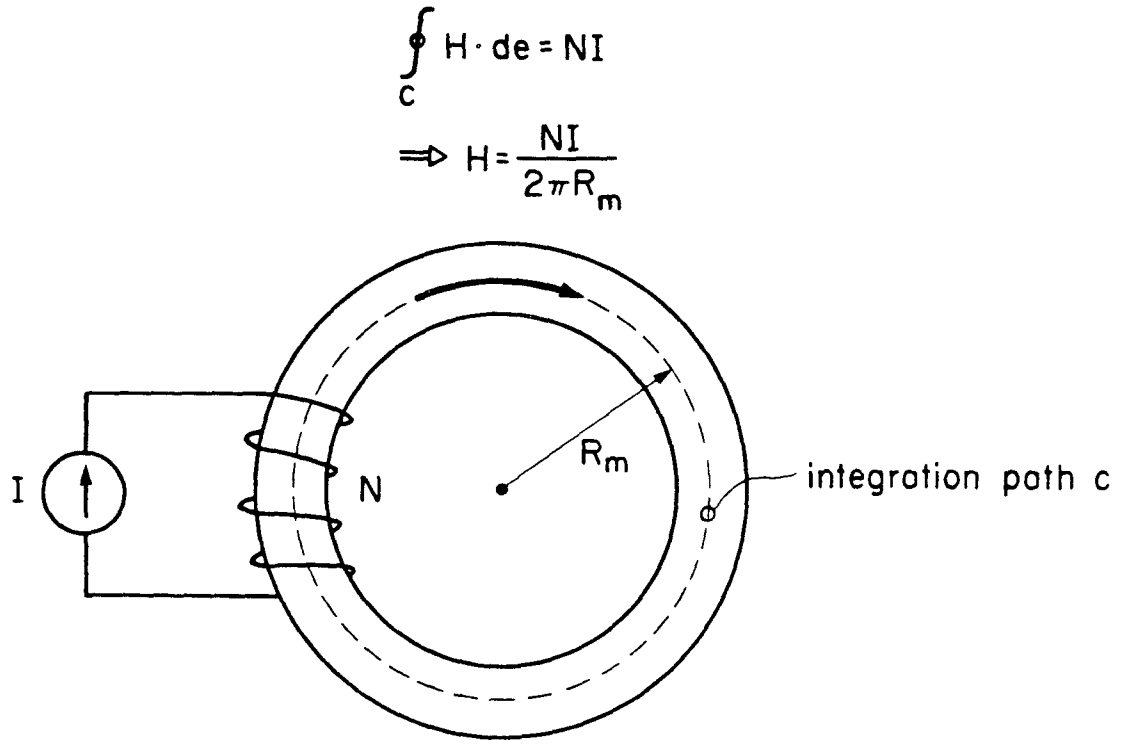

Fig. 4.1. Illustration of the use of Ampere's law to compute the field intensity H inside a toroid.

In Chapter 5, a more accurate solution of the field intensity H inside the toroid is obtained. It is also compared to this simple approximation.

4.4 Faraday's Law

According to this law, if a magnetic flux ϕ links N turns of a conductor, a time-varying voltage v is induced at the terminals of the conductor. The relation between v and ϕ is given by

$$v = N \frac{d\phi}{dt} \tag{4.9}$$

Conversely, if a voltage v is applied across the terminals of the N turns conductor, a magnetic flux ϕ is induced, and it is related to v by

$$\phi = \frac{1}{N} \int v(t)dt \tag{4.10}$$

4.5 Relation Between B and H

4.5.1 Free space

In free space, the relation between the field density B and the field intensity H is linear.

$$B = \mu_o H \tag{4.11}$$

where μ_o is the permeability of free space

$$\mu_o = 4\pi \times 10^{-7} \quad H/m \tag{4.12}$$

4.5.2 Ferromagnetic Materials

If **H** is considered the cause and **B** the effect, ferromagnetic materials can be defined as those that are capable of producing a larger effect (larger **B**, hence more flux), with a smaller means (smaller **H**, hence smaller current).

If the material is homogeneous, isotropic and linear, the relation between **B** and **H** is given by

$$\mathbf{B} = \mu_o \mu_r \mathbf{H} \tag{4.13}$$

where μ_r is the relative permeability of the material, which is typically in the range of 100 to 100,000. In other words, ferromagnetic materials are capable of producing 100 to 100,000 more flux than free space for the same amount of **H**.

Equation (4.13) can also be written as

$$\mathbf{B} = \mu \mathbf{H} \tag{4.14}$$

where

$$\mu = \mu_o \mu_r \tag{4.15}$$

4.5.3 Saturation and Hysteresis in Ferromagnetic Materials

Ferromagnetic materials are not perfectly linear as expressed by (4.15). After a certain amount of flux density **B** is reached, the material saturates, and further increase in **H** produces only a small increase in **B**. This saturation phenomenon is illustrated in Fig. 4.2b.

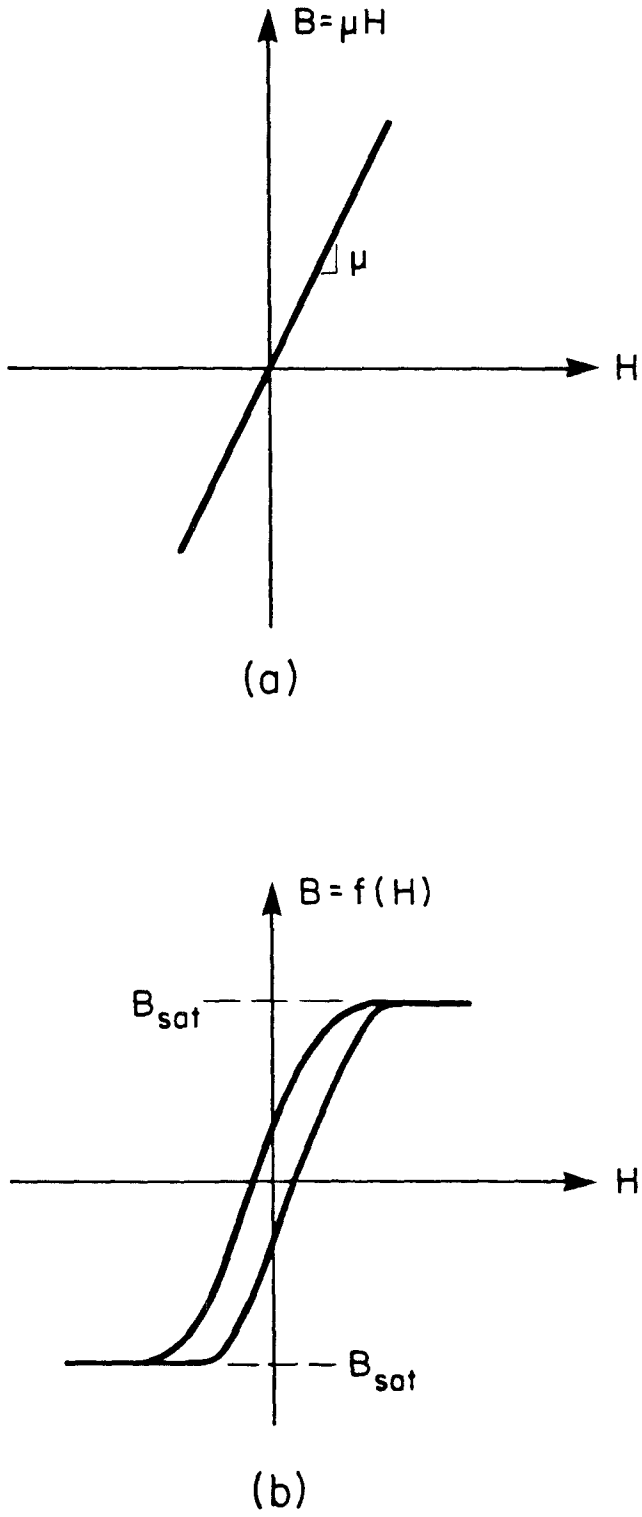

Fig. 4.2. Ideally linear (a) and actual (b) B-H characteristics of ferromagnetic materials.

Saturation is not the only non-linear characteristic of ferromagnetic materials; the relation between **B** and **H** is not a single-valued function. The non-linear phenomenon that causes **B** to lag behind **H** is called *hysteresis*.

Figure 4.2 illustrates the differences between the ideal and the non-ideal **B-H** relations for ferromagnetic materials.

In general, the width of the *hysteresis loop* and the saturation flux density B_{sat}, are functions of the operating temperature, the excitation frequency, and other external parameters. Soft materials, like ferrites, usually have a very thin *hysteresis loop*, and their **B-H** characteristics are in general considered piecewise linear.

Only the ideally linear characteristics will be used in this thesis, and it will also be assumed that the magnetic structures are operated below saturation.

4.6 Energy in Magnetic Fields

In general, the energy possessed by any form of inductance is stored in its magnetic field. If the value of the inductance is L and the current in the inductor is I, the energy stored in the inductor is given by

$$E = \frac{1}{2} LI^2 \tag{4.16}$$

If the magnetic field intensity **H** inside the inductor is known, the energy stored in the inductor can also be computed as

$$E = \frac{\mu}{2} \iiint H^2 \, dv \tag{4.17}$$

The above volume integral should be evaluated throughout the volume of the inductor. For example, for the toroid in Fig. 4.1, it was found before, that

$$\mathbf{H} = \frac{NI}{2\pi R_m} \tag{4.8}$$

Substitution of this equation into (4.17) and evaluation of the integral throughout the volume of the toroid gives

$$E = \frac{1}{2}\left(\frac{\mu N^2}{2\pi R_m}\right) I^2 \tag{4.18}$$

If the quantity in parenthesis is defined as L, Eq. (4.18) reduces to Eq. (4.16).

The above example illustrates the equivalence of Eqs.(4.16) and (4.17), but these two equations can also be used to obtain the "equivalent" or "effective inductance" of some volume of material with a known field intensity **H**. For instance, equating (4.16) to (4.17) gives

$$L = \frac{\mu}{I^2} \iiint \mathbf{H}^2 \, dv \tag{4.19}$$

Again, using the toroid in Fig. 4.1 as an example, substitution of (4.8) into (4.19) results in

$$L = \frac{\mu N^2 S}{2\pi R_m} \tag{4.20}$$

Equation (4.19) will be used often in this thesis to compute the "effective inductance" of some part of a magnetic structure for which the field intensity **H** has previously been determined.

4.7 Magnetic Circuits and The Reluctance Concept

Circuit models for magnetic structures can be constructed, based on the analogy that exists between the equations that describe electric and magnetic fields.

$$I = \iint \mathbf{J}\,d\mathbf{s} \qquad\qquad \phi = \iint \mathbf{B}\,d\mathbf{s} \tag{4.21}$$

$$v = \oint \mathbf{E}\cdot d\boldsymbol{\ell} \qquad\qquad F = NI = \oint \mathbf{H}\cdot d\boldsymbol{\ell} \tag{4.22}$$

$$\mathbf{J} = \sigma\mathbf{E} \qquad\qquad \mathbf{B} = \mu\mathbf{H} \tag{4.23}$$

Electric circuits are based on the three equations on the left and, because of the perfect analogy, the same laws and relations that apply to electric circuits also apply to magnetic circuits, which can be defined based on Eqs. (4.21) through (4.23).

4.7.1 The Reluctance Concept

From Eqs. (4.21) through (4.23), if a voltage v is applied across a cylindrical conductor of length ℓ, cross section S, and conductivity σ, the resultant current I through the conductor can be determined using the left sides of (4.21) through (4.23).

$$I = JS = \sigma ES = \frac{\sigma S}{\ell}\,V \tag{4.24}$$

The quantity $\ell/\sigma S = R$ is the electrical resistance of the conductor, and Eq. (4.24) can be written as

$$I = \frac{V}{R} \tag{4.25}$$

which is Ohm's law. The same procedure can be used to obtain relations that involve magnetic quantities. For example, from Fig. 4.3, if the field intensity inside the toroid is uniform, the resultant flux ϕ due to the *magnetomotive force* NI can be obtained using the magnetic field relations (4.21) through (4.23):

$$\phi = BS = \mu HS = \frac{\mu S}{\ell_m} NI \tag{4.26}$$

where $\ell_m = 2\pi R_m$ is the mean length of the toroid.

The field equations can be completely bypassed, and the flux ϕ could be obtained as

$$\phi = \frac{NI}{R} \tag{4.27}$$

where

$$R = \frac{\ell_m}{\mu S} \tag{4.28}$$

Equation (4.27) is Ohm's law applied to magnetic circuits, where R is defined as the *reluctance*, and $\mathcal{P} = 1/R$ is the *permeance* of the magnetic path. *Reluctance circuits* can be constructed based on these analogies. The *reluctance circuit* for the toroid is illustrated in

Fig. 4.3b. In general, the laws and relations used in electric circuit analysis can also be used in magnetic circuits.

4.7.2 Air Gaps in Magnetic Components

If a small air gap is introduced along the magnetic path of the toroid as shown in Fig. 4.4a, the effect of the gap can be modelled as illustrated in Fig. 4.4b, where

$$R_m = \frac{\ell_m}{\mu S} \qquad R_g = \frac{\ell_g}{\mu_o S} \tag{4.29}$$

The flux ϕ can then be obtained as

$$\phi = \frac{NI}{R_m + R_g} \tag{4.30}$$

In general, $R_g >>> R_m$, and (4.30) reduces to

$$\phi \approx \frac{NI}{R_g} \tag{4.31}$$

The inductance of the toroid is then

$$L = \frac{N\phi}{I} = \frac{N^2}{R_g} \tag{4.32}$$

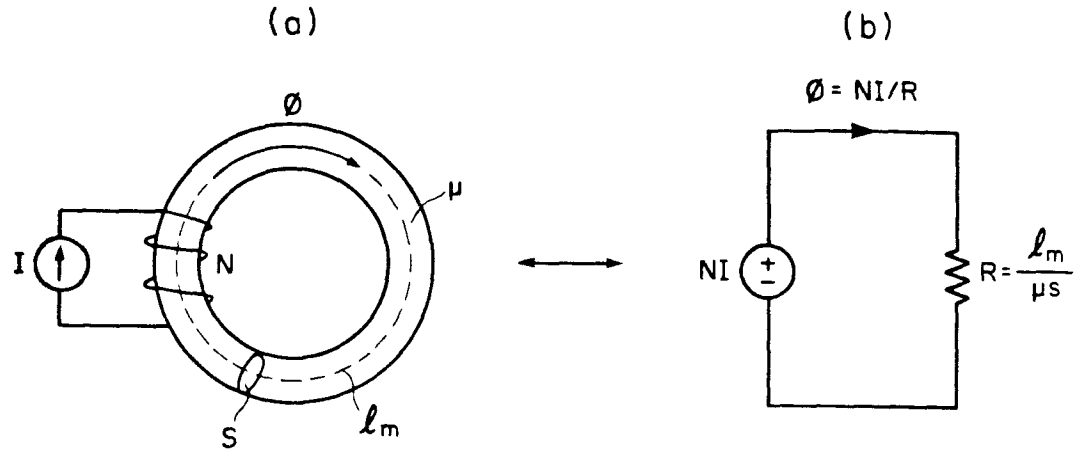

Fig. 4.3. Reluctance model for toroid with N turns cross section S and mean length ℓ_m.

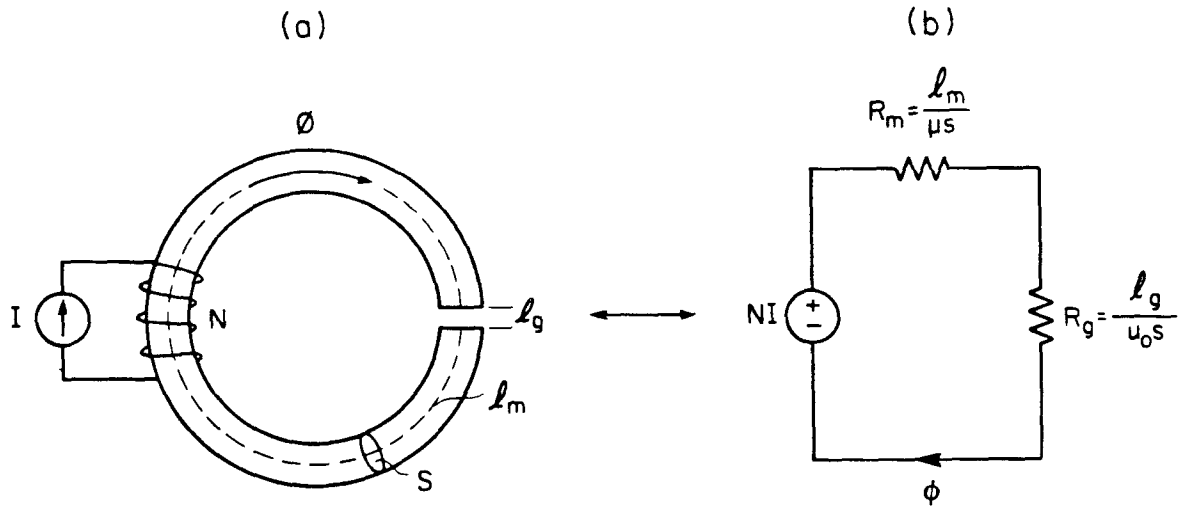

Fig. 4.4. Reluctance model for gapped toroid.

CHAPTER 5

A SIMPLE LEAKAGE ESTIMATION PROBLEM: THE ONE-TURN INDUCTOR

The leakage flux in the neighborhood of a one-turn inductor is investigated. The attempt that is made in this chapter to solve this "simple" problem mathematically serves to illustrate some basic approximations that are used throughout this thesis, and also to motivate the much simpler estimation method discussed in the next chapter.

5.1 Infinitely Small Wire

Figure 5.1 shows a simple toroid with one turn of infinitely small wire. The energy stored in the magnetic field inside the toroid can be associated with the inductance of the toroid L and can be computed as

$$E_L = \frac{\mu}{2} \iiint H_i^2 \, dv \tag{5.1}$$

where H_i is the magnetic field intensity inside the toroid.

The energy stored in the magnetic field outside the toroid can be associated with the *leakage inductance* ℓ and can be computed as

$$E_\ell = \frac{\mu_o}{2} \iiint H_o^2 \, dv \tag{5.2}$$

where H_o is the magnetic field intensity outside the toroid.

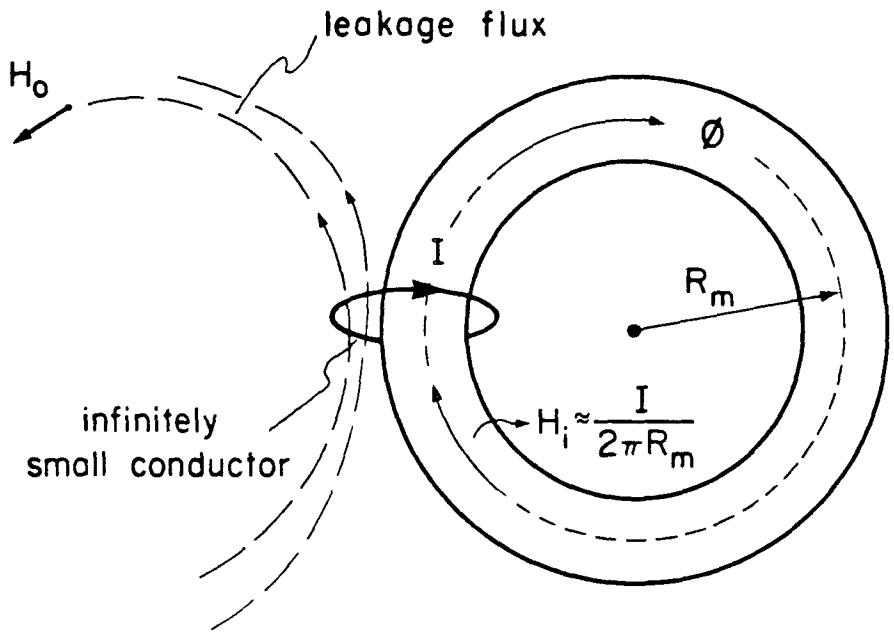

Fig. 5.1. Toroid with one turn of infinitely small wire.

Evaluation of these two integrals requires the determination of the field intensities H_i and H_o. In general, if the toroid is made of ferromagnetic material, the field intensity inside the toroid H_i can be considered almost constant throughout the volume of the toroid, which in the previous chapter was found to be approximately

$$H_i = \frac{I}{2\pi R_m} \tag{5.3}$$

A more accurate solution can be obtained if it is assumed that the field intensity is constant only along a radial line around the toroid but changes as this line gets closer or farther from the center of the toroid. This is illustrated in Fig. 5.2. The field intensity H_i can then be obtained by substitution of R_x for R_m in Eq. (5.3). That is,

$$H_i = \frac{I}{2\pi R_x} \tag{5.4}$$

where R_x can be written in terms of the coordinates (r,θ) as illustrated in Fig. 5.2.

$$R_x = (R_m^2 + r^2 + 2R_m r\cos\theta)^{1/2} \tag{5.5}$$

Substitution of Eq. (5.5) into (5.4) gives

$$H_i(r,\theta) = \frac{I}{2\pi(R_m^2 + r^2 + 2R_m r\cos\theta)^{1/2}} \tag{5.6}$$

Equation (5.6) gives the field intensity everywhere inside the toroid as a function of the coordinates r, θ. For example, at the boundary $r=r_o$, H_i is only a function of θ and is given by

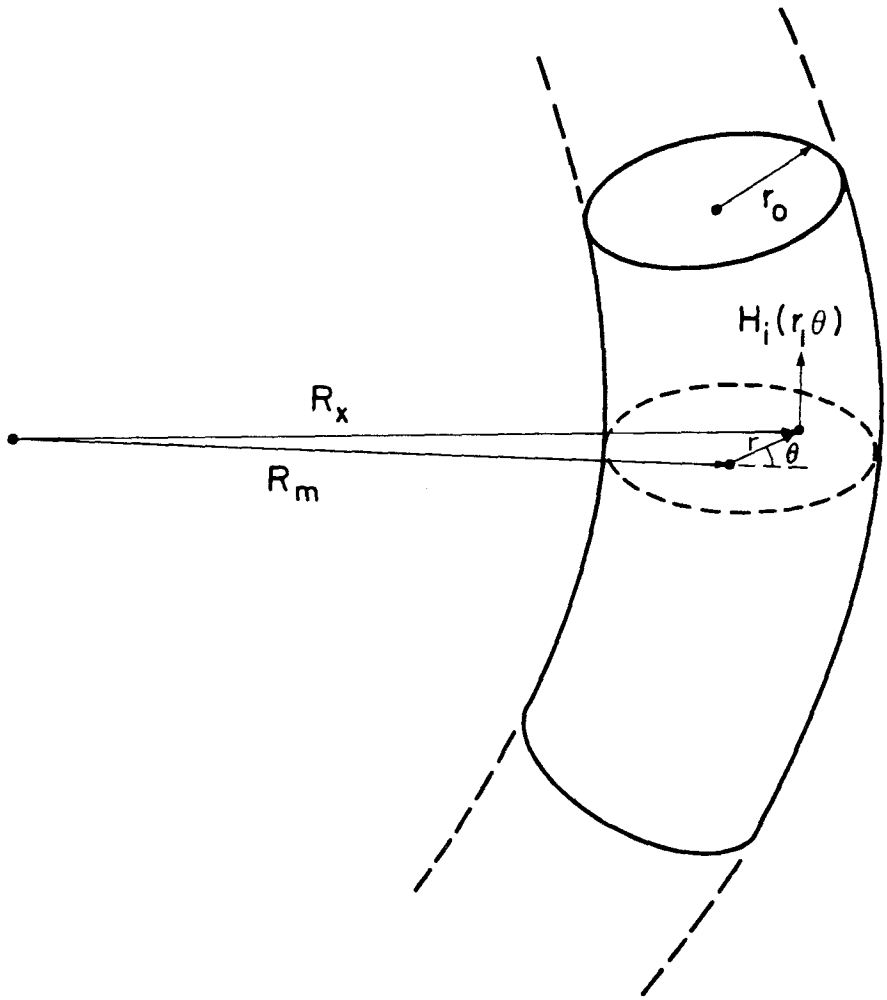

Fig. 5.2. The field intensity $H_i(r,\theta)$ can be obtained more accurately if it is assumed to change as the coordinates r and θ change inside the toroid.

$$H_i(\theta) = \frac{I}{2\pi(R_m^2 + r_o^2 + 2R_m r_o \cos\theta)^{\frac{1}{2}}} \tag{5.7}$$

This function is plotted as a function of θ in Fig. 5.3. The field intensity is strongest at the inner section of the toroid ($\theta=\pi$), where

$$H_{max} = \frac{I}{2\pi R_m(1 + (r_o/R_m)^2)^{\frac{1}{2}}}$$

and weakest at the outer-most section ($\theta=0,2\pi$), where

$$H_{min} = \frac{I}{2\pi R_m(1 + r_o/R_m)}$$

The deviation of the maximum and minimum values from the average H_{avg} is a function of the geometric ratio of the toroid r_o/R_m.
If $r_o/R_m \ll 1$, H_i can be approximated to

$$H_i \approx \frac{I}{2\pi R_m} \tag{5.8}$$

This approximation will be used in the analysis that follows as the field intensity at the boundary of the toroid.

5.1.1 Flux Density Outside Toroid

Figure 5.4 shows a magnified view of a small section of the toroid that contains the current-carrying conductor. The flux density **B** at any point P outside the toroid can be obtained as

$$\mathbf{B} = \mathbf{B}_p + \mathbf{B}_h \tag{5.9}$$

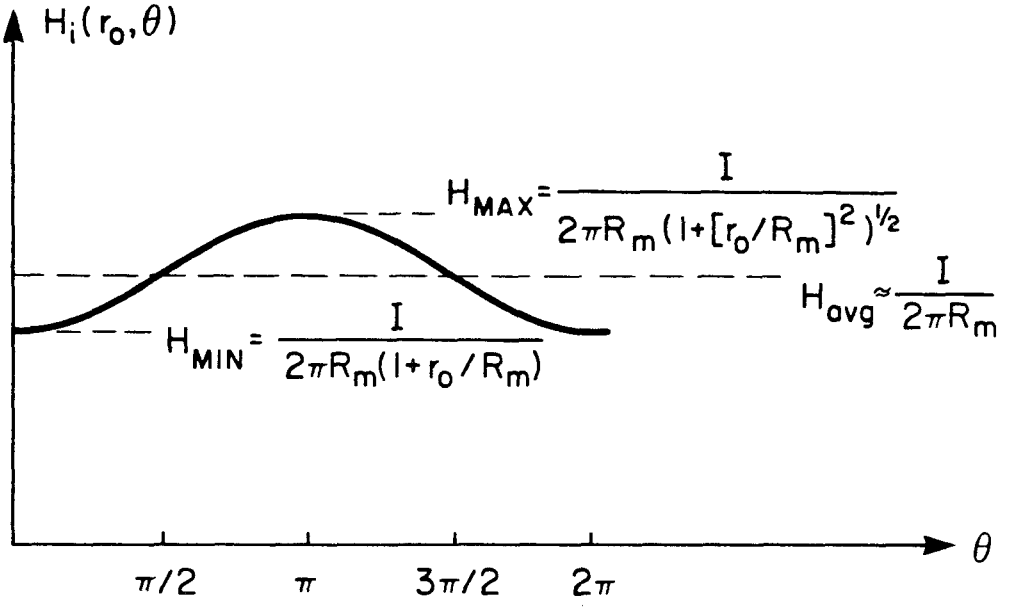

Fig. 5.3. Plot of the field intensity at the boundary of the toroid ($r = r_0$). The deviation of the maximum and minimum values from the average is a function of the geometric ratio of the toroid r_0/R_m. If $r_0/R_m \ll 1$, $H_i(r_0,\theta) \approx I/2\pi R_m = H_{avg}$.

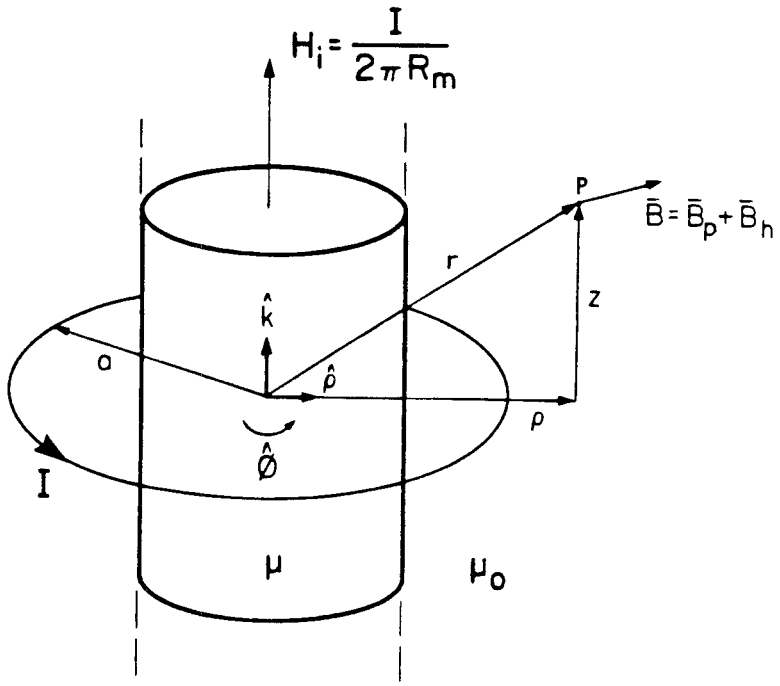

Fig. 5.4. Illustration of coordinate system used to determine the flux density B outside toroid.

where $\mathbf{B}_p$ is derived from the particular solution of the magnetic vector potential (which satisfies Poisson's equation), and is given in [9, 10] as

$$\mathbf{B}_p = \hat{\rho} B_\rho + \hat{\kappa} B_z \tag{5.10}$$

where

$$B_\rho = \frac{\mu_o I}{2\pi} \frac{z}{\rho[(a+\rho)^2 + z^2]^{1/2}} \left[-K + \frac{a^2 + \rho^2 + z^2}{(a-\rho)^2 + z^2} E \right] \tag{5.11}$$

and

$$B_z = \frac{\mu_o I}{2\pi} \frac{1}{[(a+\rho)^2 + z^2]^{1/2}} \left[K + \frac{a^2 - \rho^2 - z^2}{(a-\rho)^2 + z^2} E \right] \tag{5.12}$$

where K and E are elliptic integrals of the first and second kind, which are given by

$$K = \int_0^{\pi/2} \frac{d\theta}{(1 - k^2 \sin\theta)^{1/2}} \qquad E = \int_0^{\pi/2} (1 - k^2 \sin\theta)^{1/2} \, d\theta$$

with

$$k^2 = \frac{4a\rho}{[(a+\rho)^2 + z^2]}$$

The homogeneous solution $\mathbf{B}_h$ can be obtained solving the equation

$$\mathbf{B}_h = -\nabla\Phi \tag{5.13}$$

where Φ is a solution of

$$\nabla^2\Phi = 0 \tag{5.14}$$

From Eqs. (5.13) and (5.14),

$$\mathbf{B}_h = \hat{\rho} C_1 e^{-\alpha z} J_1(\alpha\rho) + \hat{\kappa} C_2 e^{-\alpha z} J_o(\alpha\rho) \tag{5.15}$$

where

$$J_n(\alpha\rho) = \sum_{i=0}^{\infty} \frac{(-1)^i (\alpha\rho/2)^{n+2i}}{i!(n+i)!} \tag{5.16}$$

The constants C_1 and C_2 are evaluated using Eq. (5.9) and the boundary condition given in Eq. (5.8).

The particular solution B_p when evaluated at any point on the wire loop is infinite. In other words, the energy density at any point on the wire is infinite. This is due to the original assumption that the wire's cross-sectional area is infinitely small, which in turn means that the total energy in the winding of the toroid (leakage energy) is infinite.

Although the solution given by Eqs. (5.9) through (5.16) is mathematically correct, it is of little practical importance, since in any practical situation the wires are of finite size, and so is the magnetic leakage energy.

5.2 Finite Wire Size

The infinitely small wire loop in Fig. 5.1 can be replaced by the wire loop of finite size shown in Fig. 5.5. The magnetic field intensity inside the toroid remains the same as before, and so does the homogeneous solution B_h of flux density outside the toroid. However, the particular solution B_p in Eq. (5.9) becomes mathematically intractable and can be solved only numerically.

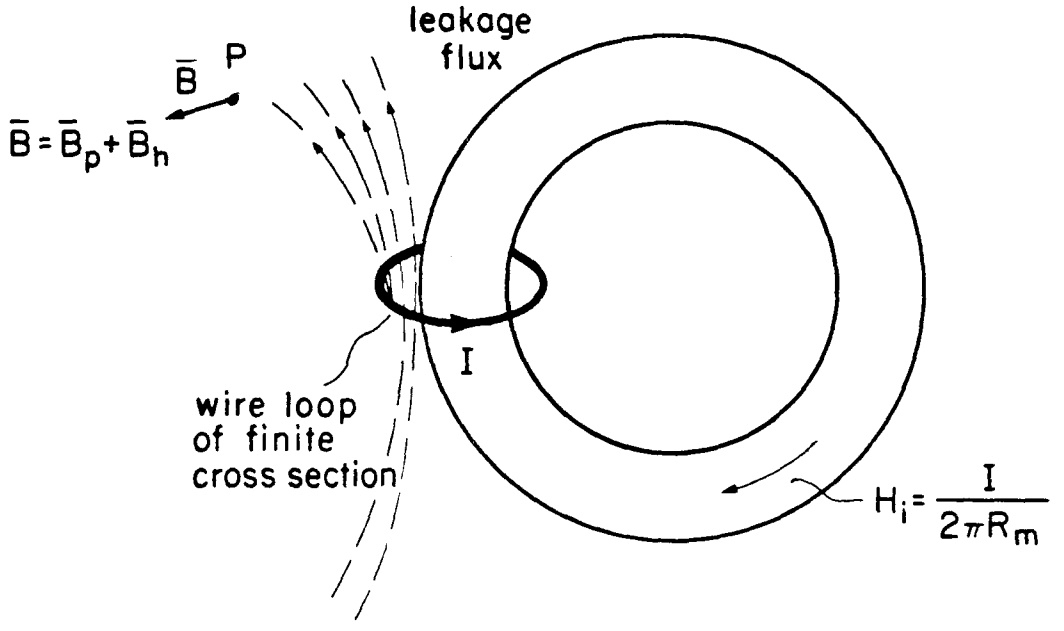

Fig. 5.5. The infinitely small wire loop in Fig. 5.1 is replaced by a wire loop of finite cross-section. The field intensity inside the toroid remains the same as before, as well as the homogeneous solution B_h of the flux density outside the toroid, but the particular solution B_p is now mathematically intractable.

5.3 Superposition and the "N" Turns Inductor

Magnetic components in general contain many turns for every winding in the structure. Superposition can in general be used to find the field intensity in the windings of such structure. For instance, at any given point outside the core, the field intensity due to each turn is calculated and the total intensity at that point is the vector sum of all the separate components of the field due to each turn. But as before, the flux density due to each turn of wire of finite size can be solved only numerically.

5.4 Conclusions

The complicated nature of the field solutions for the one-turn inductor suggests that a simpler approach must be used to find simple analytic expressions for the field quantities in the windings of practical magnetic structures. A simplified method to estimate this energy is discussed in the next chapter.

CHAPTER 6

SIMPLIFIED METHOD FOR ESTIMATING THE LEAKAGE ENERGY IN THE WINDINGS OF A MAGNETIC STRUCTURE

6.1 Introduction

The single-turn inductor discussed in the previous chapter illustrated that although analytic or numerical solutions can be obtained for certain simple field problems, the nature of the solutions can be so complicated that any possible use of such solutions in the process of designing magnetic circuits is almost hopeless.

Fortunately, the windings of most practical magnetic structures consist of large numbers of turns which are, with very few exceptions, arranged in an organized manner.

In this chapter a simplified method for estimating the field intensity inside the windings of practical magnetic structures is discussed. The method is based on the following assumptions:

1. The windings are made of large numbers of turns with all the turns very close to each other, and each turn is made of very thin wire compared to the total area of the winding.
2. The field intensity inside the ferromagnetic materials is uniform and constant.

6.2 Toroid with Uniformly Distributed Turns

To illustrate the method, a simple toroidal core with N uniformly distributed turns is used. This is illustrated in Fig. 6.1.

6.2.1 Field Intensity Inside the Toroid and Winding

The field intensity inside the toroid was obtained in Chapter 5 and is given by

$$H_i = \frac{NI}{\ell_m} \tag{6.1}$$

where $\ell_m = 2\pi R_m$ is the mean length of the magnetic path of the toroid. Since the turns are made of thin wires, the shape of the winding can be assumed to be that of a thick uniform layer around the toroid that carries a total current NI. This is illustrated in Fig. 6.2.

To visualize the next steps better, the toroid is "cut" and stretched open as shown in Fig. 6.3. The winding is now a cylindrical conductor of thickness h and of internal radius r_o, which surrounds the toroid.

The field intensity H inside the winding (leakage field intensity) can be obtained using Ampere's law in its most general form,

$$\oint_C H \cdot d\ell = \iint J ds \tag{6.2}$$

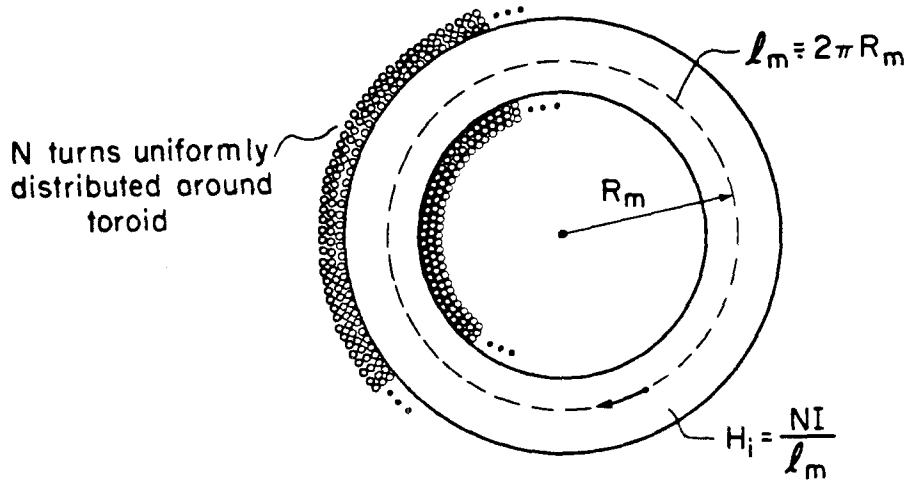

Fig. 6.1. Toroid with N uniformly distributed turns.

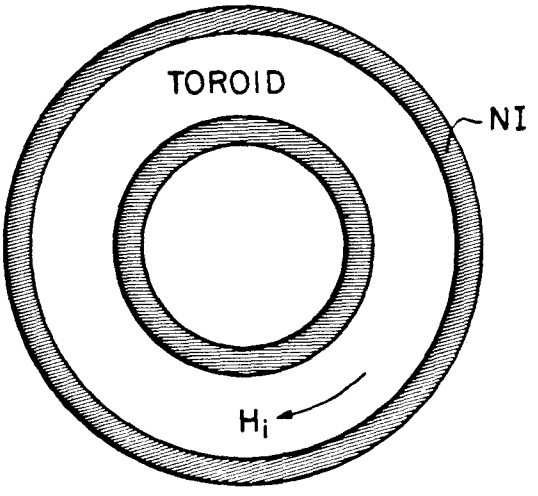

Fig. 6.2. The shape of the winding in Fig. 6.1 can be considered to be a thick uniform layer which carries a total current NI.

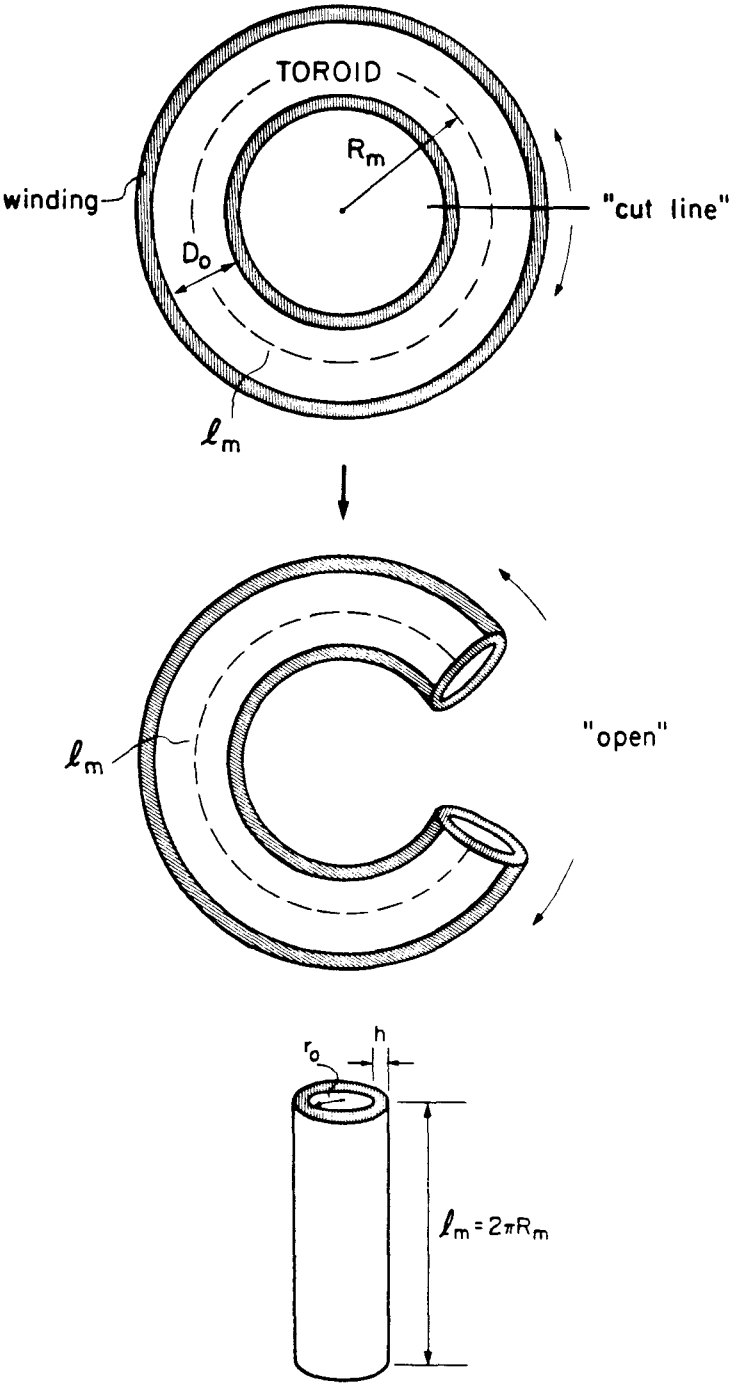

Fig. 6.3. The original circular toroid in (a) is "cut" and stretched open into the shape shown in (b). The winding is now a cylinder surrounding the toroid.

The integration path c can be selected as shown in Fig. 6.4, which is closed because the bottom of the figure is actually connected to the top.

If $H(\rho)$ is assumed normal to the current density J, the left side of Eq. (6.2) becomes

$$\oint_c H \cdot d\ell = \int_{\ell=0}^{\ell=\ell_m} H(\rho) d\ell = H(\rho)\ell_m \tag{6.3}$$

The right-hand side of Eq. (6.2) is the total current enclosed by the integration path c. If the current density J is constant throughout the entire cross section of the conductor cylinder, the total current enclosed by c is then

$$I_c = J(h-\rho)\ell_m \tag{6.4}$$

where

$$J = \frac{NI}{h\ell_m} \tag{6.5}$$

where $h\ell_m$ is the area of the cross section of the conductor cylinder. Substitution of Eq. (6.5) into (6.4) gives

$$I_c = NI \left(1 - \frac{\rho}{h} \right) \tag{6.6}$$

Finally, from Eqs. (6.3) and (6.6)

$$H(\rho) = \frac{NI}{\ell_m} \left(1 - \frac{\rho}{h} \right) \tag{6.7}$$

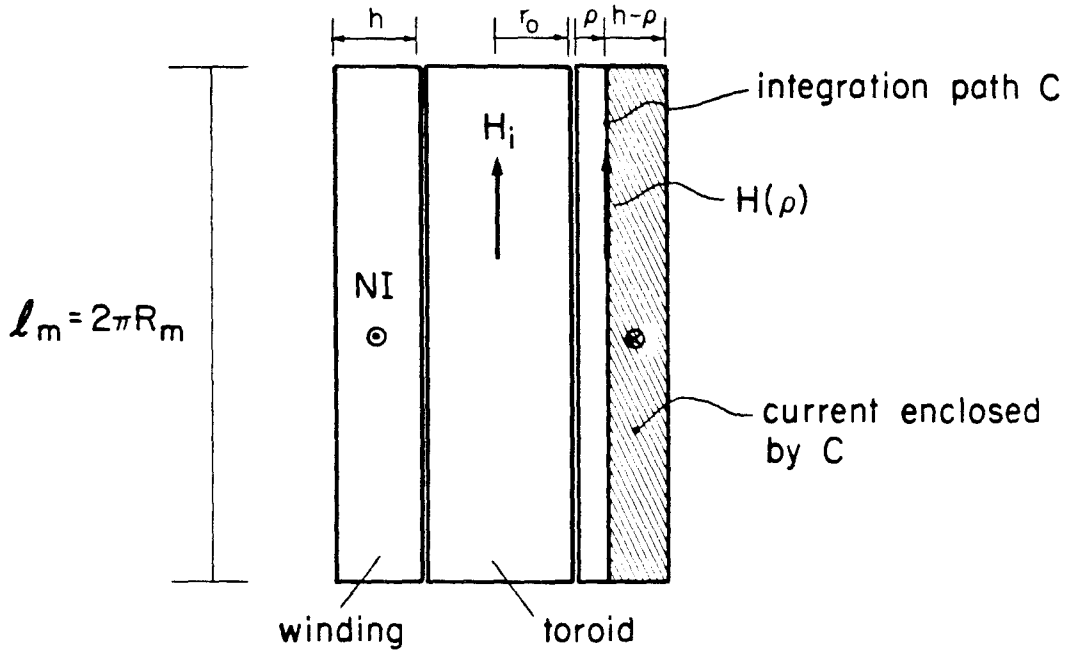

Fig. 6.4. Illustration of the integration path used to evaluate Ampere's law to obtain the field intensity $H(\rho)$ across the winding and the toroid.

or

$$H(\rho) = H_i \left(1 - \frac{\rho}{h} \right) \tag{6.8}$$

where $H_i = NI/\ell_m$ is the field intensity inside the toroid.

Figure 6.5 illustrates the variation of the field intensity H inside and outside the toroid. At the boundary between the toroid and the winding (ρ=0), the field intensity is H_i. This is as expected since one of the boundary conditions for magnetic fields is that *tangential components of the field intensity are equal on both sides of a boundary*. Finally, at the end of the winding (ρ=h), the field intensity reduces to zero.

If the toroid is closed into its original circular form, it is possible to draw the direction of the fluxes inside the winding and the toroid. This is shown in Fig. 6.6. In the figure, except for a very small amount of flux that might escape the outer layers of the winding, the leakage flux (winding flux) as well as the toroid's flux is self contained inside the structure. In other words, this inductor configuration generates very little directly radiated electromagnetic interference (EMI). Other inductor configurations such as the EI core shown in Fig. 6.7 have part of their winding outside the core, and the leakage flux that goes through this section of the winding is directly radiated towards the outside of the structure.

6.2.2 Inductance Calculation

In Chapter 4 it was shown that the inductance of any volume of material for which the field intensity H has previously been determined can be obtained as

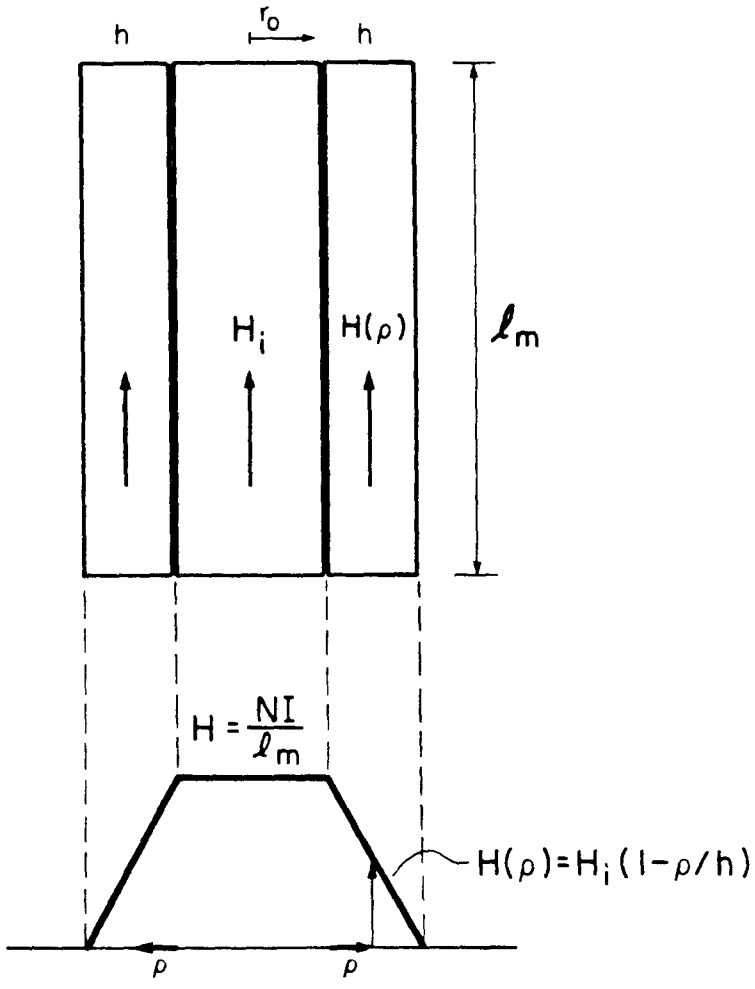

Fig. 6.5. Plot of the field intensity inside the toroid and the winding.

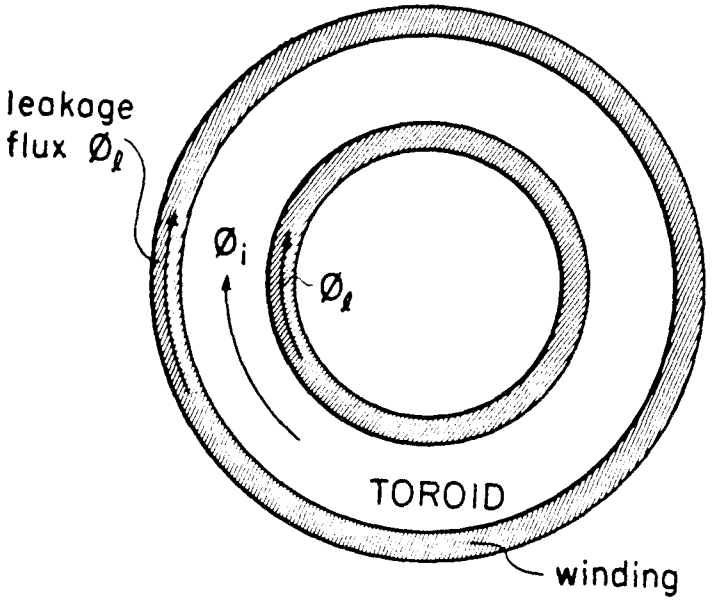

Fig. 6.6. The toroid and the winding in Fig. 6.5 can be closed back into their original circular shape to illustrate the direction of the flux inside the toroid ϕ_i and the leakage flux ϕ_ℓ.

$$L = \frac{\mu}{I^2} \iiint H^2 \, dv \tag{4.19}$$

This equation can now be used to find both the inductance of the toroid as well as the "equivalent" or "effective" inductance of the winding, i.e., the leakage inductance. The inductance of the toroid was found in Chapter 4 and is given by

$$L = \frac{N^2}{R_m} \tag{6.9}$$

where $R_m = \mu S/\ell_m$ is the reluctance of the toroid.

The effective (leakage) inductance of the winding is computed using

$$\ell = \frac{\mu_o}{I^2} \iiint H^2(\rho) \, dv \tag{6.10}$$

where it has been assumed that the magnetic permeability of the winding is that of air μ_o, which is very closely the case if the winding is made of copper wire ($\mu_{copper} = 0.999991\mu_o$).

Substitution of $H(\rho)$ from Eq. (6.8) into Eq. (6.10) gives

$$\ell = \frac{\mu_o}{I^2} \int_{\rho=0}^{\rho=h} \left(H_i \left(1 - \frac{\rho}{h}\right) \right)^2 2\pi \ell_m (\rho + r_o) \, d\rho \tag{6.11}$$

Evaluation of the integral gives

$$\ell = \frac{2}{3} N^2 \pi \mu_o \frac{h}{\ell_m} \left(r_o + \frac{h}{4} \right) \tag{6.12}$$

where ℓ is the *effective leakage inductance* of the winding. The total inductance of the toroid is the sum of the inductance of the toroid L and the leakage inductance ℓ.

6.3 Other Inductor Configurations

Figures 6.7 and 6.8 illustrate other commonly used inductor configurations. The field intensity and the *flux pattern* inside the core and the winding of a pot core are illustrated in Fig. 6.8. Equation (4.19) can again be used to compute the inductances of the core and the winding. As before, the total inductance of the structure is the sum of these two.

From the circuit point of view, the only effect that magnetic leakage has in inductors is to increase the total inductance of the structure. Other than that, it is of little importance. The effects of leakage are far more important in multiple-winding structures such as transformers and coupled-inductors.

6.4 Multiple-Winding Structures and the General Solution to the Leakage Problem

The previous inductor examples illustrated how to obtain simple analytic approximations for the field intensity inside the windings of a magnetic circuit. It also showed how Eq. (4.19) can be used to compute the effective inductance of some volume of material for which the field intensity has been previously determined.

However, for multiple-winding structures not only is it necessary to estimate the energy of the magnetic fields inside the windings but also it is very important to know how this energy is distributed among the different windings.

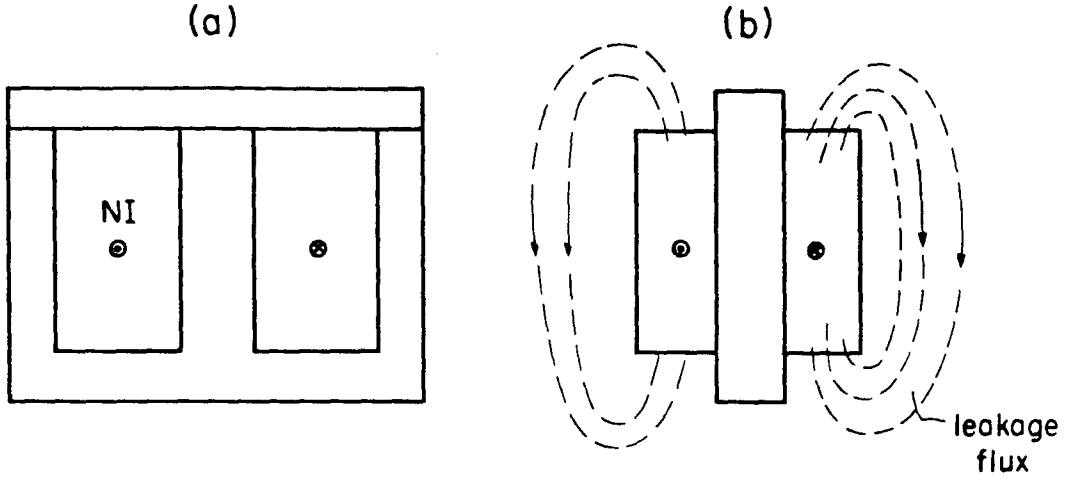

Fig. 6.7. Another common inductor configuration is the EI core arrangement shown. As illustrated in (b), part of the leakage flux is directly radiated towards the outside of the structure.

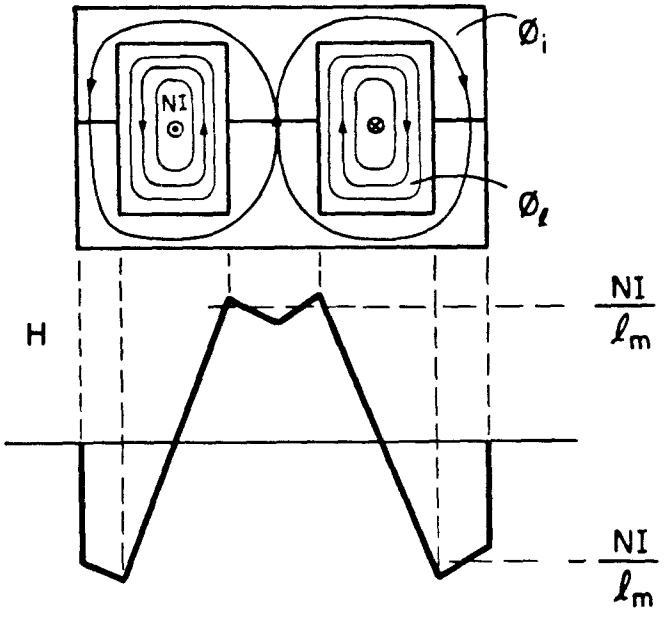

Fig. 6.8 Pot core configuration with field intensity inside the core and the winding illustrated.

The general solution to the leakage problem is divided in various steps. First, the intensity of the fields inside the structure is determined so that an approximate *flux pattern* can be established. Based on this "pattern," a reluctance or electric circuit model is constructed. Finally, the elements of the electric circuit model are analytically determined including all leakage parameters.

This process generates electric circuit models that are *physically natural*. The elements in these *Physical Models* have a one-to-one relationship with corresponding physical parameters in the original magnetic structure. The complete method for obtaining the physical model of a magnetic circuit is described in detail in Chapter 8.

In the past, magnetic circuits have been modelled based on mathematical descriptions of "generic" magnetic circuits with the same number of windings [7]. Unfortunately, these *mathematical models* have always fallen short of predicting the correct distribution of leakage energy in the windings of a magnetic structure. The next chapter reviews the concepts and steps involved in the determination of these *mathematical models*.

CHAPTER 7

MATHEMATICAL DESCRIPTION OF MAGNETIC CIRCUITS: MATHEMATICAL MODELS

The conventional method for modelling magnetic circuits [7] is reviewed in this chapter. It is shown with some examples that although these models are conceptually right, the meaning of the models and its elements can sometimes be reduced to mere mathematical abstractions with no physical interpretation.

7.1 Mathematical Description of Magnetic Circuits

The input-output characteristics of any magnetic circuit can be described in terms of simple differential equations. An electric circuit model can be constructed based on this *mathematical description*. The circuit model thus obtained is a *mathematical model* for the original magnetic structure.

7.1.1 Mathematical Models for Two-Winding Magnetic Circuits

Figure 7.1 shows a simple two-winding transformer. One possible way to model such a structure is to consider the two-winding toroid shown in Fig. 7.2 a "generic" case for all two-winding transformers. Figure 7.2 also illustrates the assumed *flux pattern* inside the generic toroid and its windings.

The total flux enclosed by N_1 is

$$\phi_{N1} = \phi_m + \phi_l \tag{7.1}$$

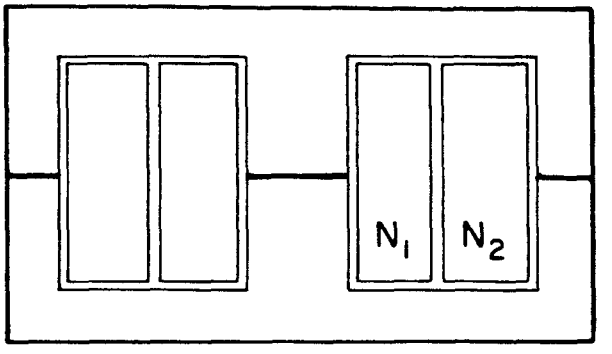

Fig. 7.1. Example of a two-winding bobbin core transformer.

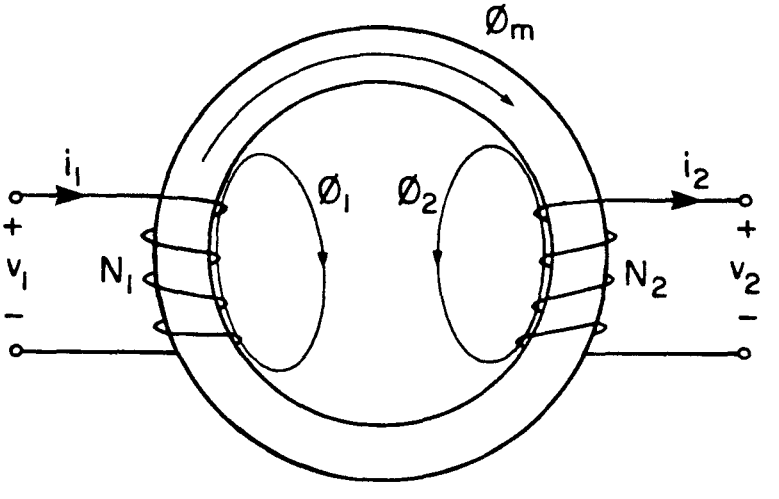

Fig. 7.2. Generic two-winding transformer.

Similarly, the total flux enclosed by N_2 is

$$\phi_{N2} = \phi_m - \phi_2 \tag{7.2}$$

Using Faraday's law, one can also write

$$v_1 = N_1 \frac{d\phi_{N1}}{dt} = N_1 \left(\frac{d\phi_m}{dt} + \frac{d\phi_1}{dt} \right) \tag{7.3}$$

$$v_2 = N_2 \frac{d\phi_{N2}}{dt} = N_2 \left(\frac{d\phi_m}{dt} - \frac{d\phi_2}{dt} \right) \tag{7.4}$$

The leakage fluxes ϕ_1 and ϕ_2 can also be expressed as

$$\phi_1 = N_1 \mathcal{P}_1 i_1 \tag{7.5}$$

$$\phi_2 = N_2 \mathcal{P}_2 i_2 \tag{7.6}$$

where $\mathcal{P}_1$ and $\mathcal{P}_2$ are the permeances of the magnetic paths of ϕ_1 and ϕ_2 [7].

By Lenz's law the relation between ϕ_m and the currents i_1 and i_2 can be written as

$$\phi_m = \mathcal{P}_m (N_1 i_1 - N_2 i_2) \tag{7.7}$$

where $\mathcal{P}_m$ is the permeance of the path of the magnetization flux ϕ_m [7]. Substitution of Eqs. (7.5), (7.6) and (7.7) into Eqs. (7.3) and (7.4) gives

$$v_1 = N_1 \left(\mathcal{P}_m \frac{d}{dt}[N_1 i_1 - N_2 i_2] + \mathcal{P}_1 \frac{di_1}{dt} \right) \tag{7.8}$$

$$v_2 = N_2 \left(\mathcal{P}_m \frac{d}{dt}[N_1 i_1 - N_2 i_2] - \mathcal{P}_2 \frac{di_2}{dt} \right) \tag{7.9}$$

which can be rearranged to

$$v_1 = N_1^2 \mathcal{P}_1 \frac{di_1}{dt} + N_1^2 \mathcal{P}_m \left(\frac{di_1}{dt} - \frac{N_2}{N_1} \frac{di_2}{dt} \right) \tag{7.10}$$

$$v_2 = -N_2^2 \mathcal{P}_2 \frac{di_2}{dt} + N_2 N_1 \mathcal{P}_m \left(\frac{di_1}{dt} - \frac{N_2}{N_1} \frac{di_2}{dt} \right) \tag{7.11}$$

The unit for permeance $\mathcal{P}$ is Henry/turns^2 and consequently the following inductances can be defined in terms of the permeances $\mathcal{P}_m$, $\mathcal{P}_1$, and $\mathcal{P}_2$:

$$L_m = N_1^2 \mathcal{P}_m \tag{7.12}$$

$$\ell_1 = N_1^2 \mathcal{P}_1 \tag{7.13}$$

$$\ell_2 = N_2^2 \mathcal{P}_2 \tag{7.14}$$

Substitution of Eqs. (7.12), (7.13) and (7.14) into Eqs. (7.10) and (7.11) gives

$$v_1 = \ell_1 \frac{di_1}{dt} + L_m \left(\frac{di_1}{dt} - \frac{N_2}{N_1} \frac{di_2}{dt} \right) \tag{7.15}$$

$$v_2 = -\ell_2 \frac{di_2}{dt} + \frac{N_2}{N_1} L_m \left(\frac{di_1}{dt} - \frac{N_2}{N_1} \frac{di_2}{dt} \right) \tag{7.16}$$

Equations (7.15) and (7.16) are a *mathematical description* of the input-output characteristics of the generic transformer in Fig. 7.2.

Electric Circuit Model

An equivalent electric circuit model that satisfies Eqs. (7.15) and (7.16) is illustrated in Fig. 7.3. This model is known as the π-model for a two-winding transformer.

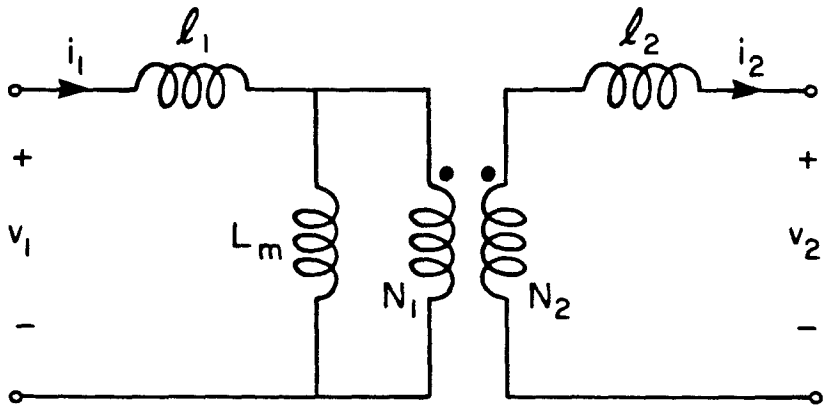

Fig. 7.3. Electric circuit model (π-model) for the generic two-winding transformer in Fig. 7.2. The leakage inductances ℓ_1 and ℓ_2 can be directly associated with the paths of the leakage fluxes ϕ_1 and ϕ_2 in Fig. 7.2. This circuit model can also be mathematically forced to satisfy the input-output characteristics of the two-winding transformer in Fig. 7.1, but the meanings of the elements in the model are reduced to mere mathematical abstractions with no physical interpretation.

The voltages across the *leakage inductances* ℓ_1 and ℓ_2 correspond to the leakage fluxes ϕ_1 and ϕ_2 in the generic toroid. The voltage across the *magnetizing inductance* L_m corresponds to the magnetization flux ϕ_m.

Because of the physical correspondence between the elements in the π-model and those in the generic two-winding transformer, this π-model can be called a physical model for the generic transformer in Fig. 7.2. However, for any other two-winding configuration, the elements in the π-model lose their physical meaning.

For instance, the π-model in Fig. 7.3 can be mathematically forced to satisfy the input-output characteristics of the two-winding transformer in Fig. 7.1. However, since the elements in this model represent physical quantities associated with the generic transformer in Fig. 7.2 and not the actual one in Fig. 7.1, the meanings of the elements in this model are reduced to mere mathematical abstractions with no physical interpretation.

In general, for any two-winding transformer configuration other than the generic two-winding transformer in Fig. 7.2, the π-model is just a mathematical description, i.e., a mathematical model of the transformer characteristics.

7.1.2 Mathematical Models for Three-Winding Magnetic Circuits

The same procedure used to model the generic two-winding transformer can be used to find an electric circuit model for the generic three-winding transformer shown in Fig. 7.4. Because of the

additional winding N_3 there are several additional flux components. The seven flux components are illustrated in Fig. 7.4.

The differential equations that relate the winding voltages and currents can be derived as before [7] and are given by

$$v_1 = \ell_1 \frac{di_1}{dt} + M_o \left[\frac{d}{dt} (i_1 - Ai_2 - Bi_3) \right] \tag{7.17}$$

$$v_2 = -\ell_2 \frac{di_2}{dt} + M_o A \left[\frac{d}{dt} (i_1 - Ai_2 - Bi_3) \right] \tag{7.18}$$

$$v_3 = -\ell_3 \frac{di_3}{dt} + M_o B \left[\frac{d}{dt} (i_1 - Ai_2 - Bi_3) \right] \tag{7.19}$$

where

$$\ell_1 = N_1^2 \frac{(\mathcal{P}_1 + \mathcal{P}_{23})\mathcal{P}_m + \mathcal{P}_{23}(\mathcal{P}_1 + \mathcal{P}_{12} + \mathcal{P}_{13}) - \mathcal{P}_{12}\mathcal{P}_{13}}{(\mathcal{P}_m + \mathcal{P}_{23})} \tag{7.20}$$

$$\ell_2 = N_2^2 \frac{(\mathcal{P}_2 + \mathcal{P}_{13})\mathcal{P}_m + \mathcal{P}_{13}(\mathcal{P}_2 + \mathcal{P}_{12} + \mathcal{P}_{23}) - \mathcal{P}_{23}\mathcal{P}_{12}}{(\mathcal{P}_m + \mathcal{P}_{13})} \tag{7.21}$$

$$\ell_3 = N_3^2 \frac{(\mathcal{P}_3 + \mathcal{P}_{12})\mathcal{P}_m + \mathcal{P}_{12}(\mathcal{P}_3 + \mathcal{P}_{13} + \mathcal{P}_{23}) - \mathcal{P}_{13}\mathcal{P}_{23}}{(\mathcal{P}_m + \mathcal{P}_{12})} \tag{7.22}$$

$$M_o = N_1^2 \frac{(\mathcal{P}_m + \mathcal{P}_{12})(\mathcal{P}_m + \mathcal{P}_{13})}{(\mathcal{P}_m + \mathcal{P}_{23})} \tag{7.23}$$

$$A = \frac{N_2}{N_1} \frac{(\mathcal{P}_m + \mathcal{P}_{23})}{(\mathcal{P}_m + \mathcal{P}_{13})} \tag{7.24}$$

$$B = \frac{N_3}{N_1} \frac{(\mathcal{P}_m + \mathcal{P}_{23})}{(\mathcal{P}_m + \mathcal{P}_{12})} \tag{7.25}$$

The $\mathcal{P}$'s are the permeances associated with the different flux paths shown in Fig. 7.4. The π-model that corresponds to Eqs. (7.20) through (7.22) is shown in Fig. 7.5. This time, though, a general and

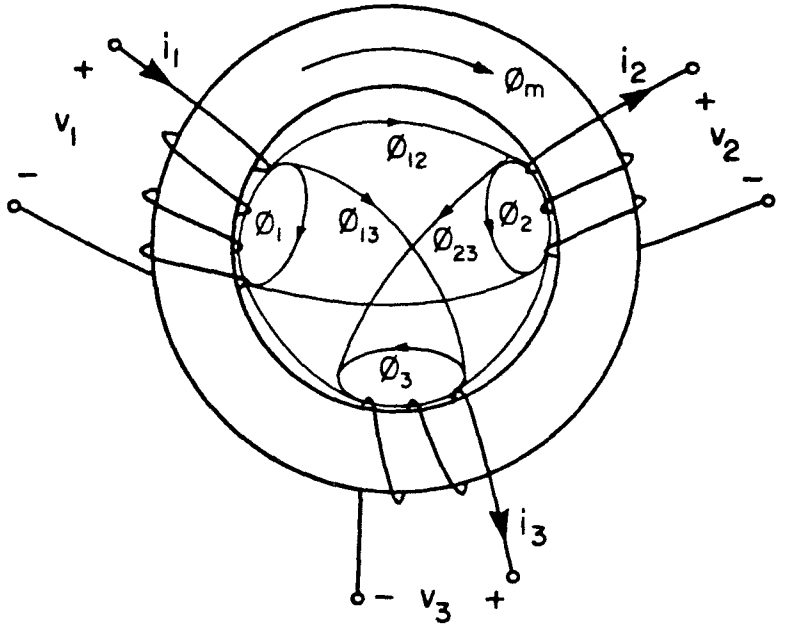

Fig. 7.4. Generic three-winding transformer with the seven flux components illustrated.

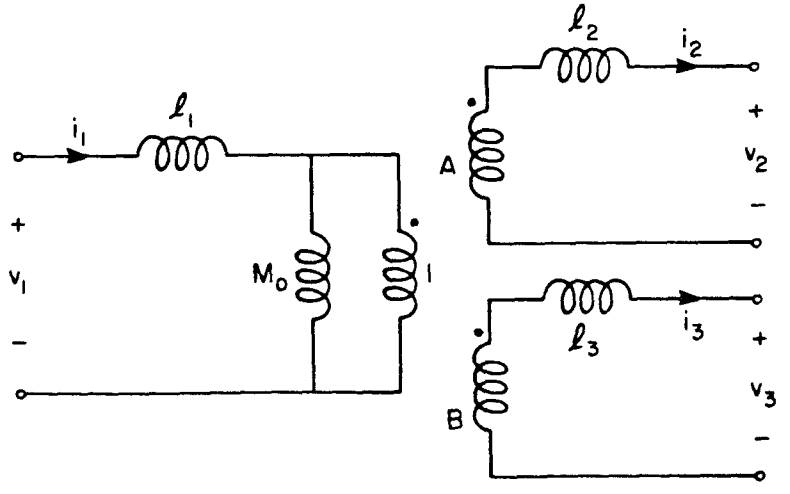

Fig. 7.5. Electric circuit model for the generic three-winding transformer in Fig. 7.4.

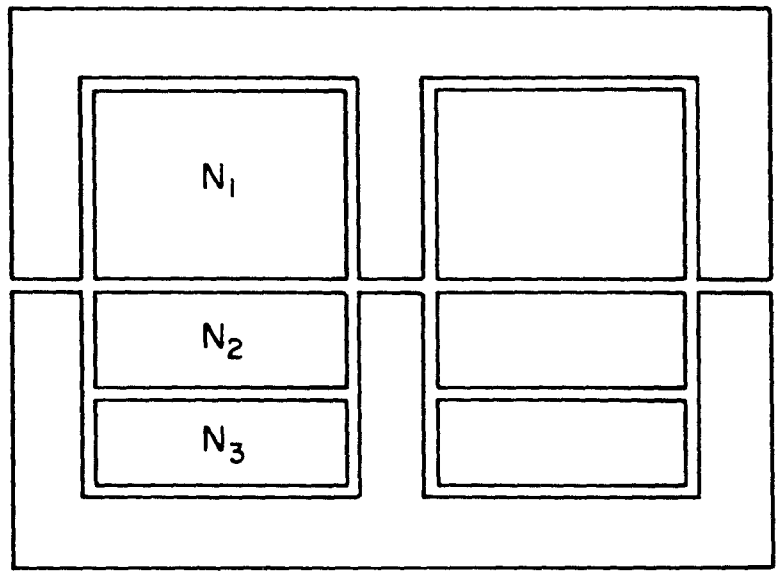

Fig. 7.6. Three-winding bobbin core transformer.

simple interpretation of the electric circuit model in terms of the generic three-winding transformer is not always possible.

Furthermore, if this model is used to characterize a "real" structure such as the one in Fig. 7.6, any interpretation is almost hopeless.

7.1.3 Mathematical Models for Four-Winding Magnetic Circuits

As more windings are added to the generic toroid, the mathematical description of the transformer becomes more complicated. For the four-winding toroid in Fig. 7.7, the electric circuit model can be derived as before. Unfortunately, for any transformer with more than three windings it is not possible to represent in general the input-output characteristics with a π-model.

The electric circuit model (mathematical model) for the generic transformer in Fig. 7.7 is shown in Fig. 7.8. As before, any interpretation from this model is almost hopeless.

7.2 Conclusions

Mathematical models for magnetic circuits can be used as an analysis tool in switching converters. For instance, the input-output characteristics of the coupled inductors in a Ćuk converter can be measured, the measurements can be associated with the corresponding *mathematical model*, and finally the parameters in the model can be estimated in terms of the measurements. The electric circuit model of the coupled inductors obtained this way can be used in the model of the entire converter to find other quantities of interest external to the magnetic structure.

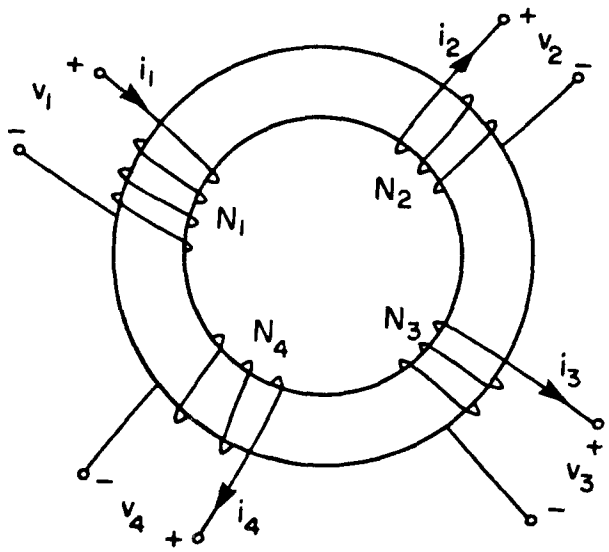

Fig. 7.7. Generic four-winding transformer.

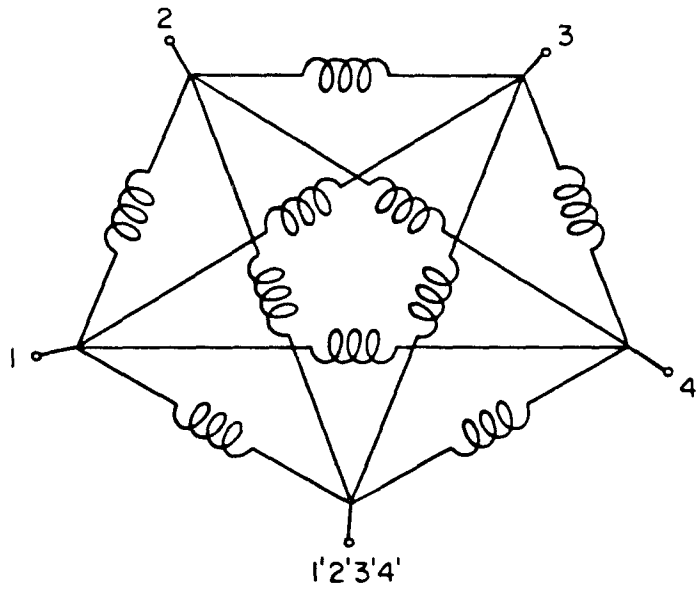

Fig. 7.8. Electric circuit model for the generic four-winding transformer in Fig. 7.7.

With respect to design of the magnetic structure, mathematical models are not very useful. They do not contain adequate information about the correct distribution of the leakage energy, about the presence of gaps throughout the core and, in general, about the geometric and structural properties of the magnetic component under investigation.

Electric circuit models that are derived from the actual magnetic structures under investigation and are such that the parameters in the models (leakage inductances, etc) have a one-to-one relationship with corresponding physical quantities in the original magnetic structure, can be used not only as analysis tools, but also as design-oriented tools for magnetic structures.

These models, which are *physically natural*, are the main topic of this thesis. The general method to obtain the *physical model* of a magnetic structure is discussed in the next chapter.

CHAPTER 8

PHYSICAL DESCRIPTION OF MAGNETIC CIRCUITS: PHYSICAL MODELS

8.1 Introduction

Mathematical models are based on generic magnetic circuits with the same number of windings as the original magnetic structure.

Physical models, on the other hand, are based fundamentally on a knowledge of the distribution and intensity of the fluxes inside the actual magnetic structure under investigation. To obtain the *physical model* of a magnetic structure, a new modelling technique is used.

The general modelling procedure for physical models is illustrated in Fig. 8.1. The first step involves the determination of the flux pattern inside the actual magnetic structure under investigation. Based on this pattern a set of algebraic flux equations is derived. These equations, which simply describe the distribution of the fluxes inside the structure, are used to construct the reluctance circuit model for the magnetic structure. The electric circuit model is then derived from the reluctance model using the principle of duality (Appendix A). Finally, all the parameter values in the electric circuit model are analytically determined in terms of the geometry of the structure.

The method is described next with the help of a simple example. The merits and limitations of this technique are also discussed.

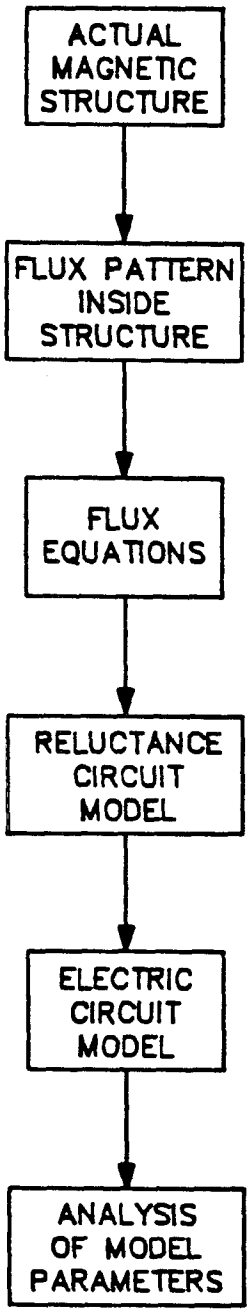

Fig. 8.1 General procedure to obtain the physical model of a magnetic structure.

8.2 Physical Description of Magnetic Circuits

The two-winding toroid in Fig. 8.2 is used as an example to illustrate the steps involved in the process of determination of the *physical model* of a magnetic structure.

The primary is wound first and it is uniformly distributed around the toroid. The secondary is wound on top of and uniformly around the primary. For simplicity, the space between the primary and the toroid and the space between the secondary and the primary, are assumed negligible when compared to the widths of the windings. In later chapters of this thesis some configurations are studied in which these spaces are accounted for.

It is easier to visualize the process if the toroid in Fig. 8.2 is "cut" and stretched open as shown in Fig. 8.3. This is similar to what was done before in the case of the toroid used for the inductor in Chapter 6.

The toroid and windings have now been "transformed" into cylinders of an average height $\ell_m=2\pi R_m$.

While the actual lengths of the inner sections of the windings are smaller than the lengths of the outer sections, all the integration steps involved go around the toroid and the windings, which to a large extent average out these differences and, since the "cut and stretched" toroid is assumed to be of average length $\ell_m=2\pi R_m$, the error in the calculations is very small.

What follows is a step-by-step description of the new modelling technique as it is used to model the two-winding transformer in Fig. 8.3.

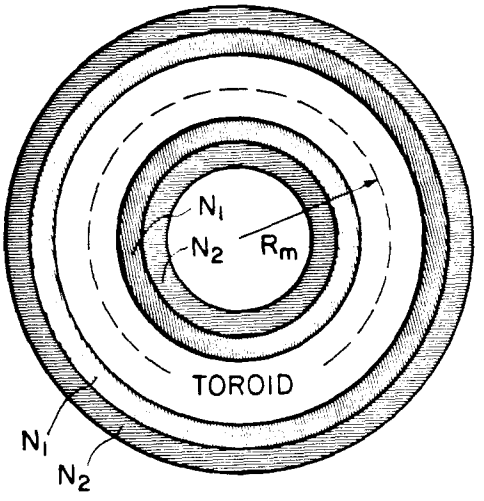

Fig. 8.2. Two-winding toroid with uniformly distributed turns.

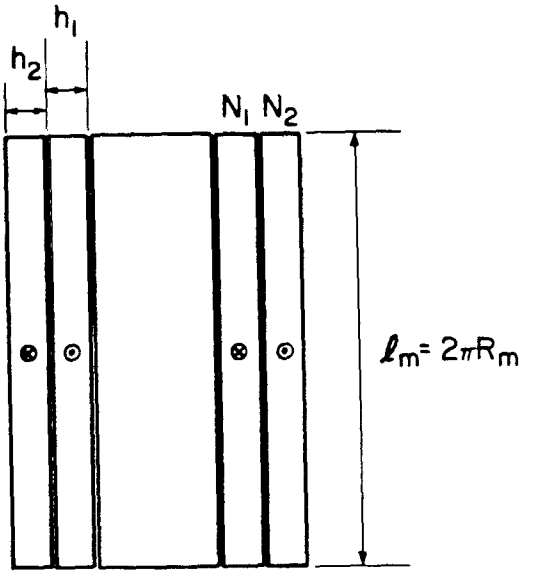

Fig. 8.3. Cut and stretched toroid. The primary N_1 surrounds the toroid, while the secondary N_2 surrounds both the primary and the toroid.

8.2.1 Approximate Flux Pattern Inside The Magnetic Structure

In the previous chapter it was shown how the electric circuit model (mathematical model) of a generic transformer was obtained based on an "assumed flux pattern" inside the generic structure and its windings.

To obtain the physical model of a magnetic structure, it is necessary to find approximately the flux pattern everywhere inside the actual structure under investigation. The flux pattern inside a magnetic structure can in general be obtained using Ampere's law in its most general form,

$$\oint_c \mathbf{H}\cdot d\ell = \iint \mathbf{J}\cdot d\mathbf{s} \qquad (4.5)$$

For the stretched toroid in Fig. 8.3 the integration path c in Eq. (4.5) can be selected as shown in Fig. 8.4, and since the bottom of the figure is actually connected to the top, the line c constitutes a closed integration path.

The right side of Eq. (4.5) represents the total current enclosed by c, which is indicated by the hatched area in Fig. 8.4 and can be computed as

$$\iint \mathbf{J}\cdot d\mathbf{s} = J_1(h_1-\rho)\ell_m - N_2 I_2 \qquad 0 \le \rho \le h_1 \qquad (8.1)$$

where J_1 is the current density in the primary, which for a uniform distribution of the turns can be written as

$$J_1 = \frac{N_1 I_1}{h_1 \ell_m} \tag{8.2}$$

Substitution of Eq. (8.2) into (8.1), gives

$$\iint J \cdot ds = N_1 I_1 \left(1 - \frac{\rho}{h_1} \right) - N_2 I_2 \qquad 0 \le \rho \le h_1 \tag{8.3}$$

If the field intensity H is constant along c, the left side of Eq. (4.5) can be computed as

$$\oint_c H \cdot d\ell = \int_{\ell=0}^{\ell=\ell_m} H(\rho) d\ell = H(\rho) \ell_m \tag{8.4}$$

where $H(\rho)$ is the unknown field intensity at a radial position ρ inside the primary as illustrated in Fig. 8.4.

Finally, combining Eqs. (8.3) and (8.4) results in

$$H(\rho) = \frac{1}{\ell_m} \left[N_1 I_1 \left(1 - \frac{\rho}{h_1} \right) - N_2 I_2 \right] \qquad 0 \le \rho \le h_1 \tag{8.5}$$

The field intensity H can be computed this way for any position inside the toroid or the windings. The result is plotted in Fig. 8.5.

On the plot the field intensity H_m corresponds to the magnetizing flux of the transformer, which is given by

$$H_m = \frac{N_1 I_1 - N_2 I_2}{\ell_m} \tag{8.6}$$

The boundary conditions are satisfied between the toroid and the primary and the primary and the secondary. For example, at the

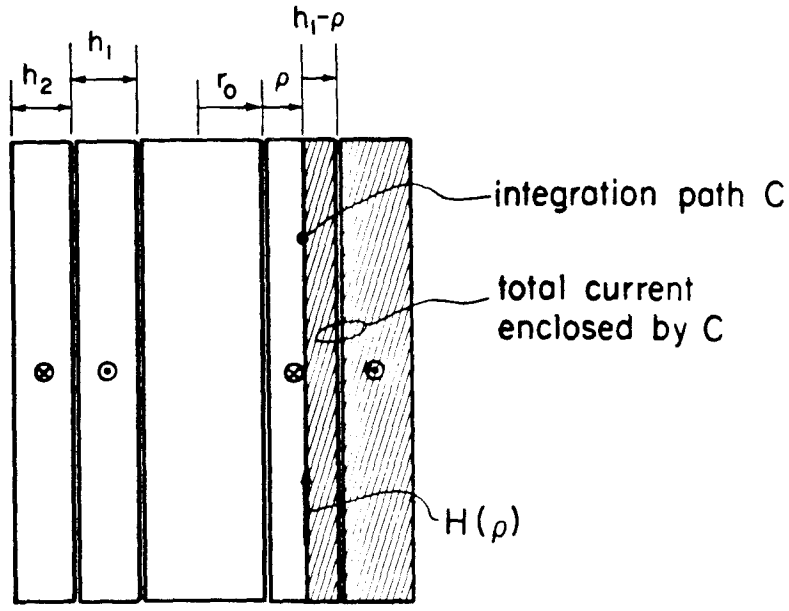

Fig. 8.4. Illustration of integration path used to determine the field intensity inside the windings and the toroid.

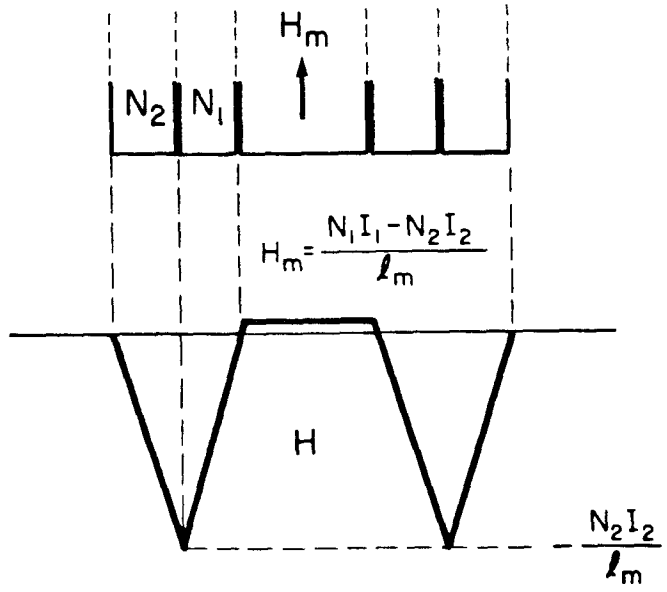

Fig. 8.5. Plot of the field intensity H inside the toroid and the windings.

boundary between the primary and the secondary the field intensity is the same on both sides of the boundary.

To solve for the field intensity in Eq. (4.5), it was assumed that the intensity in the windings and the toroid is constant in a direction along the integration path c. Part of the proof that this is approximately the case is the relatively strong field intensity that results from the integration process along such a direction for most of the winding's width with respect to other components of the field in different directions. For example, if a closed integration path is taken in a normal direction to c as shown in Fig. 8.6, the right side of Eq. (4.5) is reduced to zero, because the total current enclosed by any such path is zero. Consequently the field intensity along a direction normal to $H(\rho)$ is either very weak or zero.

Although this simple analysis does not constitute an exact proof, it is sufficient to justify the assumption that the field intensity inside the toroid and the windings is largely in a direction parallel to the integration path c. Other components of the field in different directions are very weak, and are not likely to change noticeably the direction of $H(\rho)$.

With the field intensity across the windings and toroid determined, the *flux pattern* inside the structure can be approximately established. This is illustrated in Fig. 8.7a. The sign of $H(\rho)$ in Fig. 8.7a indicates the direction of the fluxes inside the windings and the toroid.

The actual *flux pattern* inside the toroid in its original circular form can be obtained if the "stretched" toroid in Fig. 8.7a

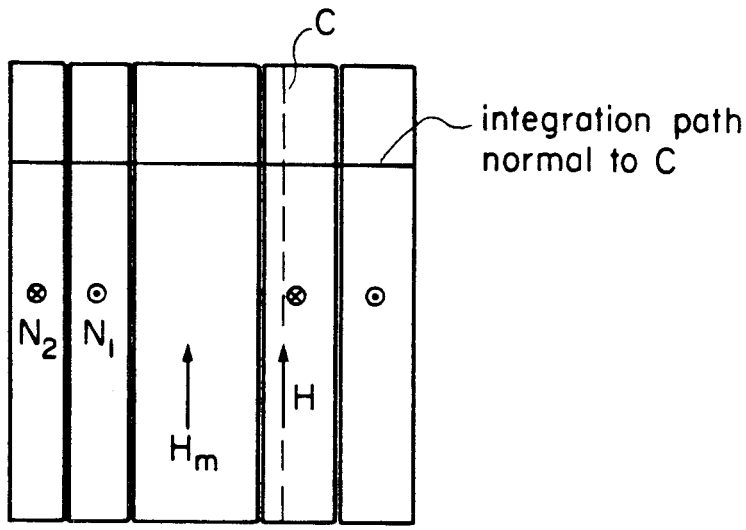

Fig. 8.6. Any integration path normal to c encloses zero net current.

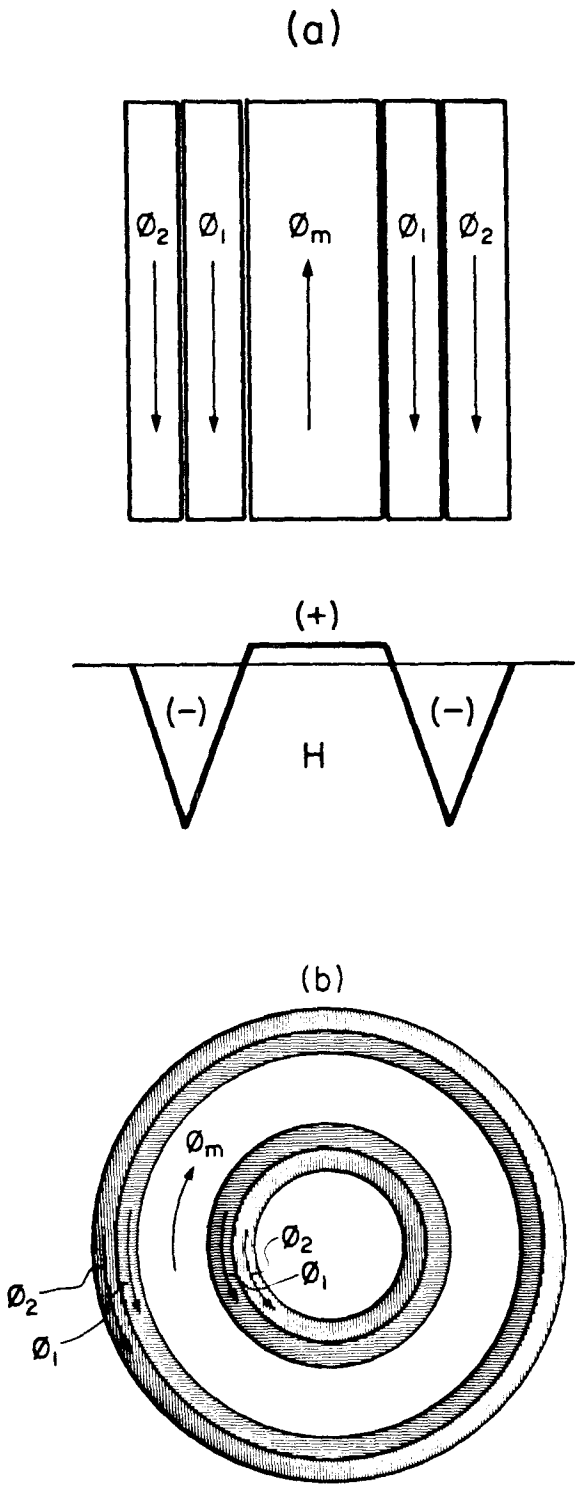

Fig. 8.7. Flux pattern inside two-winding toroid (a) cut and stretched version, (b) transformer in its original circular form.

is bent back into its original form as shown in Fig. 8.7b. The leakage flux inside the windings runs parallel to the toroid and, as in the case of the inductor discussed in Chapter 6, no significant amount of leakage flux leaves the windings, thus keeping the nearby environment free of directly radiated magnetic fields.

8.2.2 The Flux Equations

The next step to determine the *physical model* of a magnetic circuit is to write down a set of algebraic *flux equations* which are based on the *flux pattern* previously determined and on the following definitions.

The total flux enclosed by the primary winding is defined as that which is enclosed by the infinitely small source $N_1 I_1$ shown in Fig. 8.8.

$$\phi_{N1} \equiv \text{Total flux enclosed by } N_1 = \phi_m \tag{8.7}$$

Similarly, the total flux enclosed by the secondary N_2 is the sum of all the flux enclosed by the infinitely small source $N_2 I_2$ shown in Fig. 8.8.

$$\phi_{N2} \equiv \text{Total flux enclosed by } N_2 = \phi_m - (\phi_1 + \phi_2) \tag{8.8}$$

In defining these two equations two fundamental approximations are made. The first one incorporates all the mmf of the windings into the infinitely small sources $N_1 I_1$ and $N_2 I_2$. The ideal situation would be to consider each turn as a separate source of mmf. This can unnecessarily complicate the results and make the process intractable.

An intermediate solution is to break the windings into their separate layers as they are physically wound. Each layer would then be treated as a separated winding, each carrying a current $N_i I$, where N_i is the number of turns in the i^{th} layer, and I is the current of each turn in the layer. The case where the windings are broken into their separate layers is discussed in detail in Chapter 12.

The second approximation has to do with the position of the infinitely small sources $N_1 I_1$ and $N_2 I_2$ at the edges of the windings as indicated in Fig. 8.8. The purpose of this is to ensure that all the leakage fluxes ϕ_1 and ϕ_2 are contained within these two sources. If, for instance, the position of $N_1 I_1$ is selected somewhere in the middle of the primary as shown in Fig. 8.9, the amount of leakage inside $N_1 I_1$ can be mistakenly taken as part of the "mutual" flux of the transformer. This approximation can also be significantly improved by breaking the winding into layers.

Later in the thesis experimental results show that both of these approximations do not introduce significantly large errors in the predicted models. However, if more accurate models are desired, the layer-to-layer models discussed in Chapter 12 provide a better answer.

8.2.3 Construction of the Reluctance Model

The *reluctance model* is another intermediate step in the process of determining the electric circuit model (*physical model*) of a magnetic structure. The *reluctance model* gives a "circuit like" description of the flux distribution in the original magnetic structure.

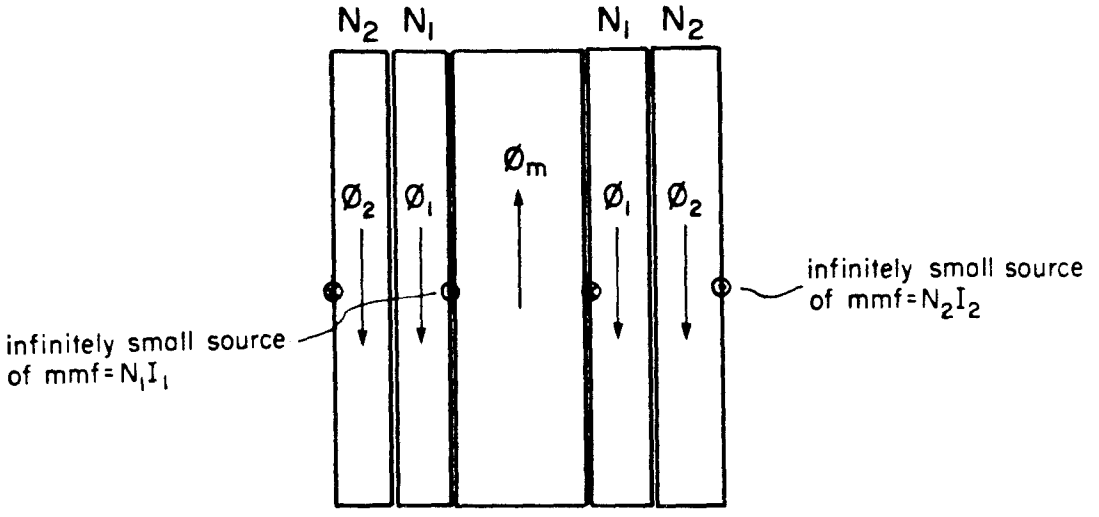

Fig. 8.8. Illustration of definition and positioning of the infinitely small sources of mmf $N_1 I_1$ and $N_2 I_2$.

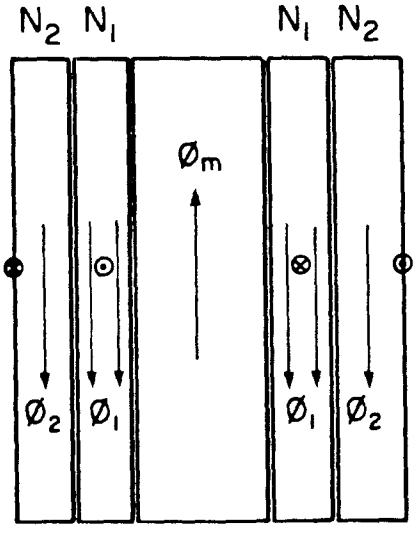

Fig. 8.9. If the position of the mmf source $N_1 I_1$ is selected somewhere in the middle of N_1, the amount of leakage flux inside $N_1 I_1$ can be mistakenly taken as part of the mutual flux of the transformer.

The currents in the reluctance circuit represent the different flux quantities in the magnetic structure which are also mathematically described by the *flux equations*. The mmf sources translate into voltage sources as described earlier in Chapter 4.

Each node in the reluctance model satisfies one of the *flux equations*, and each branch of the reluctance circuit is associated with the corresponding flux path in the magnetic structure. The reluctances represent the the ability of the structure to store magnetic energy along that particular path.

For the two-winding toroid in Fig. 8.2, the reluctance model is obtained as follows.

The flux quantities ϕ_{N1} and ϕ_{N2}, which were previously defined as

$$\phi_{N1} \equiv \text{Total flux enclosed by } N_1$$
$$\phi_{N2} \equiv \text{Total flux enclosed by } N_2$$

are the "currents" associated with the "voltage sources" $N_1 I_1$ and $N_2 I_2$, as illustrated in Fig. 8.10a. Notice that the "current" ϕ_{N2} in the figure, together with the sign of the "voltage source" $N_2 I_2$ indicates the "load nature" of $N_2 I_2$.

The first node in the reluctance circuit satisfies Eq. (8.7), which simply states that the mutual flux ϕ_m is the same as ϕ_{N1}.

For the second node, substitution of Eq. (8.7) into (8.8) gives

$$\phi_{N2} = \phi_{N1} - (\phi_1 + \phi_2) \tag{8.9}$$

This nodal equation can be used to connect the sources $N_1 I_1$ and $N_2 I_2$. Figure 8.10a illustrates the implementation of Eqs. (8.7) and (8.9) in the reluctance circuit.

The energy storage capabilities of each one of the flux paths in the flux pattern is represented in the reluctance circuit by reluctances in the different branches of the circuit. This is illustrated in Fig. 8.10b. The reluctance R_m represents the ability of the structure to store magnetic energy inside the toroid (energy stored in H_m). Similarly, the energy storage capability of the primary is represented by R_1, and that of the secondary by R_2.

Finally, Eq. (8.8) is used to close the reluctance model. The complete circuit is shown in Fig. 8.11. The circuit can be rearranged into a more conventional way as shown in Fig. 8.12.

8.2.4 Electric Circuit Model (Physical Model)

In Appendix A a method for obtaining the electric circuit model given the reluctance circuit is reviewed. The technique is known as the principle of duality. The electric circuit model derived from the reluctance model in Fig. 8.12 using the principle of duality is shown in Fig. 8.13. Since the two leakage reluctances R_1 and R_2 are in parallel in the reluctance model, their duals, the leakage inductances ℓ_1 and ℓ_2 appear in series in the electric circuit model.

The relations between the inductances in the electric circuit model and the reluctance elements in the reluctance model are given by

$$Lm = \frac{N_1^2}{R_m} \tag{8.10}$$

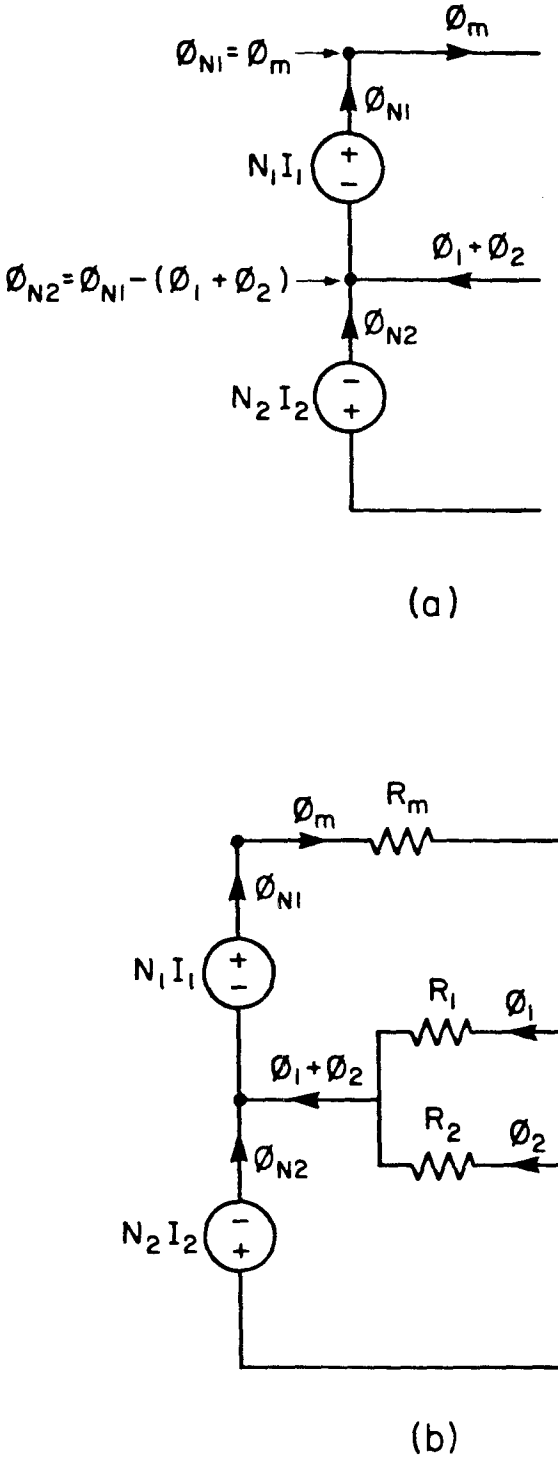

Fig. 8.10. Construction of reluctance model using the flux equations. Equations (8.7) and (8.9) are synthesized in (a). The reluctances associated with the different flux paths in the structure are introduced in the reluctance model as shown in (b).

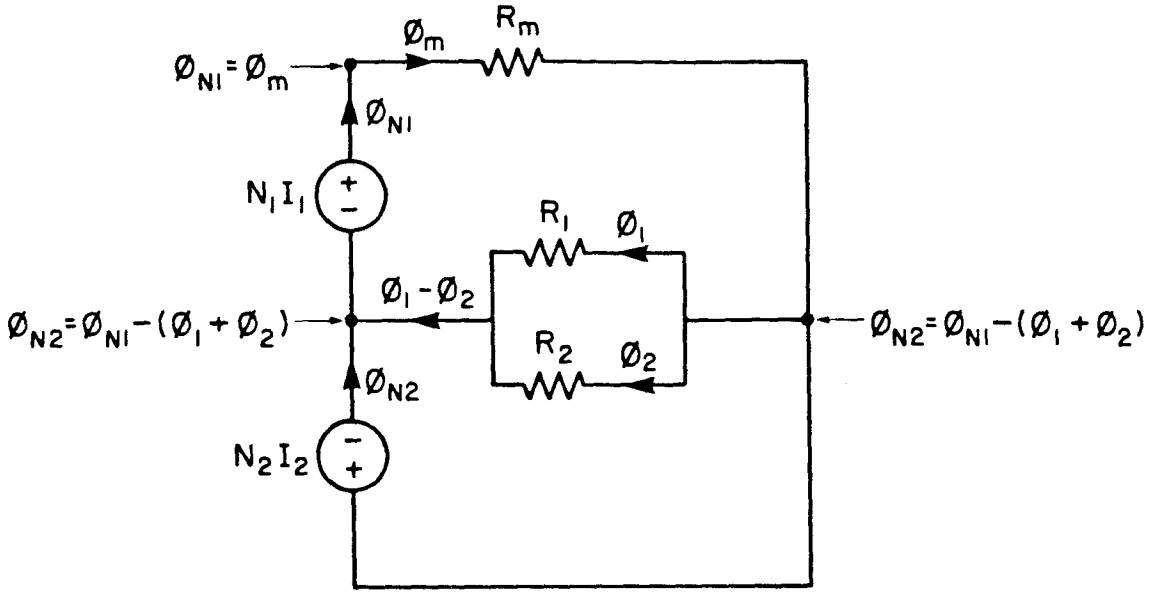

Fig. 8.11. Complete reluctance model for two-winding toroid.

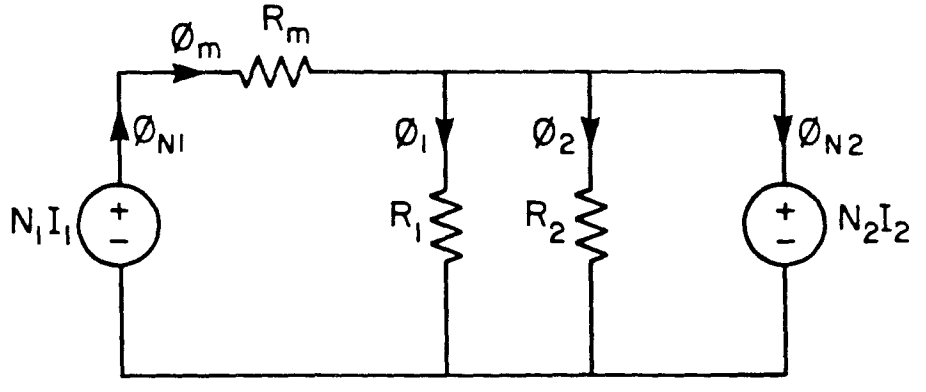

Fig. 8.12. The reluctance model in Fig. 8.10 can be rearranged into a more conventional way.

$$\ell_1 = \frac{N_1^2}{R_1} \tag{8.11}$$

$$\ell_2 = \frac{N_1^2}{R_2} \tag{8.12}$$

The two leakage inductances ℓ_1 and ℓ_2 can be combined into one inductance ℓ, as illustrated in Fig. 8.14, where

$$\ell = \ell_1 + \ell_2 \tag{8.13}$$

If the inductance of the toroid L_m is much larger than ℓ_1, the leakage inductance ℓ_1 in Fig. 8.13 can be "pushed" through the node of the mutual inductance L_m without significantly changing the other parameters in the model. This is illustrated in Fig. 8.15.

The electric circuit model shown in Fig. 8.15 is widely used by engineers in design and analysis of transformers. However, if the inductance of the toroid L_m is not large compared to ℓ_1, as can be the case in coupled inductors, the electric circuit model in Fig. 8.15 does not represent the characteristics of the structure.

For simplicity, the resistances of the windings were ignored but they can be easily accounted for in the usual form. The electric circuit model shown in Fig. 8.16 contains these additional elements.

8.2.5 Analytic Estimation of the Parameters in the Electric Circuit Model

To completely define the electric circuit model for the two-winding toroid, it is necessary to find approximate analytic expressions for all the inductances in the model L_m and ℓ.

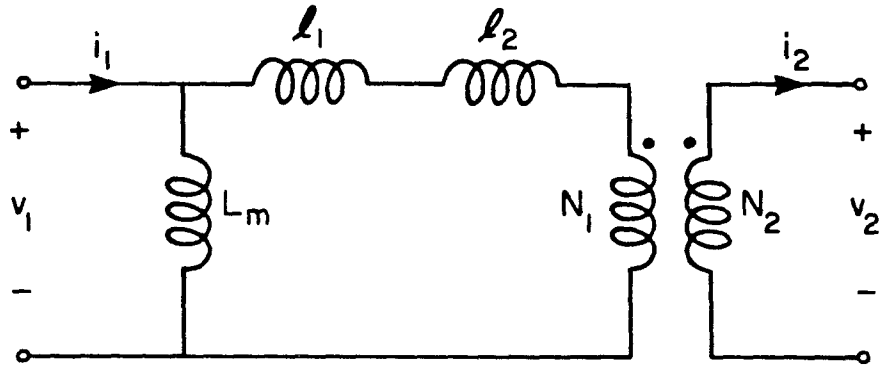

Fig. 8.13. Electric circuit model for two-winding toroid.

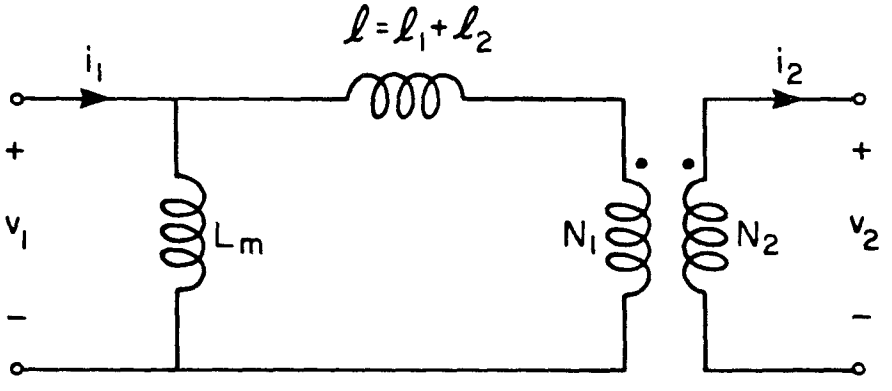

Fig. 8.14. The leakage inductances ℓ_1 and ℓ_2 in Fig. 8.13 can be combined into one single inductance $\ell = \ell_1 + \ell_2$.

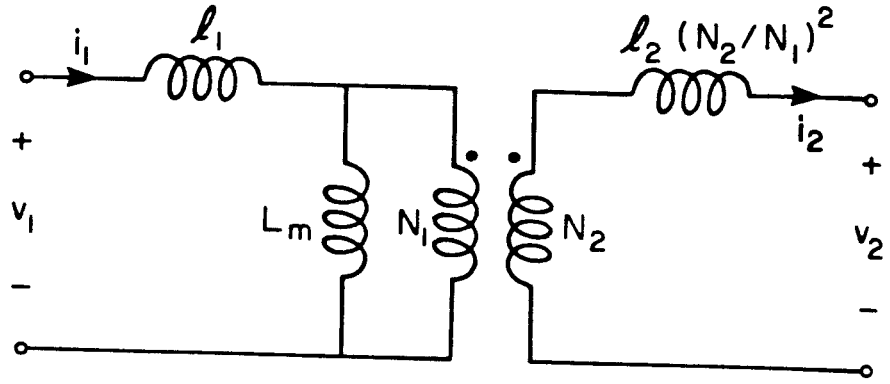

Fig. 8.15. If L_m >>> ℓ_1, the leakage inductance ℓ_1 can be pushed through the node of L_m without significantly changing any of the elements values. However, if L_m is not much larger than ℓ_1, this circuit does not represent the characteristics of the two-winding toroid.

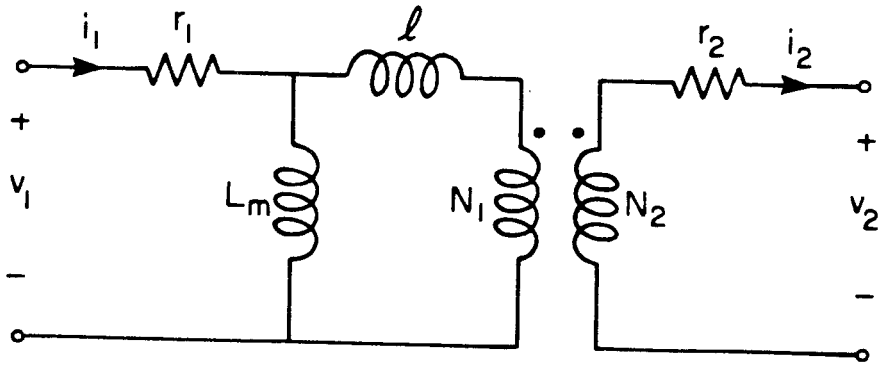

Fig. 8.16. Electric circuit model for the two-winding toroid with the windings resistances r_1 and r_2.

The inductance of the toroid L_m was obtained in Chapter 6 and is given by

$$L_m = \frac{N_1^2 \mu S}{\ell_m} \tag{8.14}$$

To estimate the value of the leakage inductance ℓ, it is sufficient to excite the circuit in such a way that most or all of the energy is stored in ℓ. For instance, if the primary is shorted and a current source is connected across the secondary as illustrated in Fig. 8.17, the voltage across the magnetizing inductance L_m is zero and all the energy from the current source I_2 is stored in ℓ. Also, since the voltage across the inductance Lm is zero, there is no flux inside the toroid as indicated in Fig. 8.18.

The field intensity through the windings can be determined as before, using Ampere's law. The only difference now is that because the primary is shorted, the magnetizing current is zero and consequently, $N_1 I_1 = N_2 I_2$.

A plot of the field intensity across the windings is shown in Fig. 8.18. The shaded area under the H plot corresponds to the energy stored in ℓ.

The leakage inductances ℓ can now be obtained by evaluation of Eq. (4.19) together with the plot of the field intensity given in Fig. 8.18 as

$$\ell = \frac{\mu_o}{I_1^2} \iiint H^2 \, dv \tag{8.15}$$

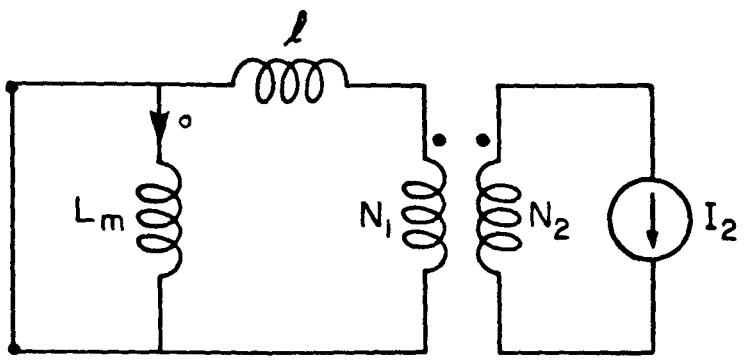

Fig. 8.17. With the primary side shorted, all the energy from I_2 is stored in the leakage inductance ℓ.

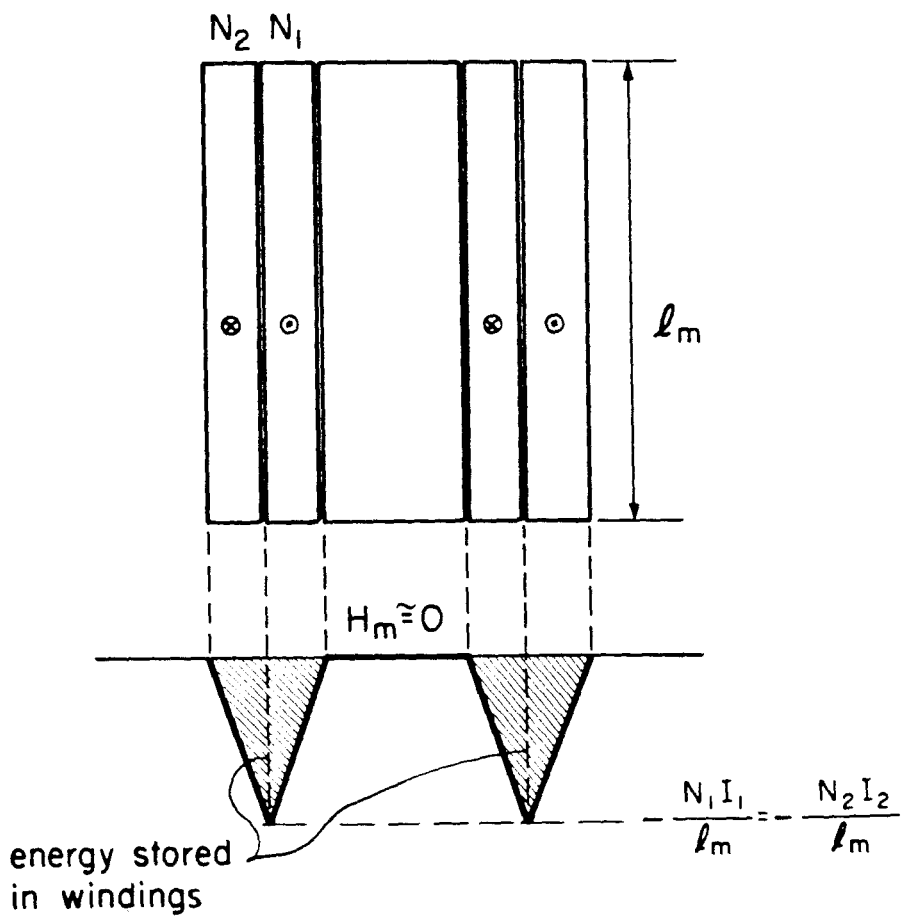

Fig. 8.18. Field intensity inside the windings with the primary shorted.

Solving the integral gives

$$\ell = \frac{2}{3} N_1^2 \pi \mu_o \frac{1}{\ell_m} \left[h_1 (r_o + \frac{3}{4} h_1) + h_2 (r_o + h_1 + \frac{h_2}{4}) \right] \qquad (8.16)$$

If the widths of the windings are the same ($h_1=h_2=h/2$), Eq. (8.16) reduces to

$$\ell = \frac{2}{3} N_1^2 \pi \mu_o \frac{h}{\ell_m} (r_o + h/2) \qquad (8.17)$$

The electric circuit model in Fig. 8.16 together with the expressions given by Eqs. (8.14) and (8.16) completely defines the *physical model* of the two-winding toroid in Fig. 8.2.

8.3 Interpretation of Physical Model of the Two-Winding Toroid

The physical model of a magnetic structure can be easily interpreted in terms of the parameters and the geometry of the magnetic structure.

For example, for the two-winding toroid in Fig. 8.2 the elements in the electric circuit model (physical model) shown in Fig. 8.13 can be associated with the structure in the following way. The magnetizing inductance L_m represents the energy storage capabilities of the toroid. The leakage inductances ℓ_1 and ℓ_2 represent the energy storage capabilities of the windings. Finally, because the primary, is physically "sandwiched" between the toroid and the secondary as illustrated in Fig. 8.2 or 8.3, any flux enclosed by the primary, is also enclosed by the secondary, which is why the leakage inductance ℓ_1 appears in series with ℓ_2 so that

$$v_2 = \frac{N_2}{N_1} \left[v_m + v_1 + v_2 \right] \tag{8.18}$$

or

$$v_2 = N_2 \left[\frac{d\phi_m}{dt} + \frac{d\phi_1}{dt} + \frac{d\phi_2}{dt} \right] \tag{8.19}$$

Stated in words, the voltage across the secondary winding N_2 is the sum of the voltages due to the magnetizing flux ϕ_m and the leakage fluxes ϕ_1 and ϕ_2.

The expression given by Eq. (8.16) for the leakage inductance ℓ in can also be related to the geometry of the windings and the toroid. For instance, if the toroid is longer and the winding widths h_1 and h_2 are reduced, the leakage inductance ℓ can be decreased. If on the other hand the toroid is shorter and the windings are made thicker, the leakage inductance ℓ can be increased. Both of these cases are important in switching applications. Some examples are discussed later in Chapter 11 and 13.

8.4 Experimental Results

A toroidal core (TDK T-19-31-8 H7C1) was wound as shown in Fig. 8.2. The primary consisted of one layer of 62 turns of #18 AWG copper wire. The secondary was also wound on one layer of #18 AWG copper wire with 52 turns.

Since the toroid was not gapped, the inductance of the toroid L_m is very high, and either the circuit model given in Fig. 8.14 or that in Fig. 8.15 can be used to model the characteristics of this transformer.

The values for the toroid and the windings dimensions are:

r_o = radius of the toroid = 0.43 cm

ℓ_m = mean length of the toroid = 7.55 cm

$h_1 = h_2$ = width of the windings = 0.1 cm

Substitution of these values into Eq. (8.17) gives

$$\ell \approx 1.4\ \mu H \tag{8.20}$$

Such a small value of inductance can only be directly measured using a very sophisticated inductance meter. An alternative way of accurately measuring small inductances is to use the HP Network Analyzer. The arrangement is illustrated in Fig. 8.19.

The resistances r_1 and r_2 are the primary and secondary winding resistances, and R_t is an external resistance of known value. With the primary shorted, the ratio of the voltages v_b and v_a is approximately given by

$$\frac{v_b}{v_a} = G_o \frac{\frac{s}{w_z} + 1}{\frac{s}{w_p} + 1} \tag{8.21}$$

where

$$G_o = \frac{r}{r + R_t} \tag{8.22}$$

$$f_z = \frac{w_z}{2\pi} = \frac{1}{2\pi} \frac{r}{(N_2/N_1)^2 \ell} \tag{8.23}$$

$$f_p = \frac{w_p}{2\pi} = \frac{1}{2\pi} \frac{r + R_t}{(N_2/N_1)^2 \ell} \tag{8.24}$$

and

$$r = r_1 \left(\frac{N_2}{N_1}\right)^2 + r_2 \tag{8.25}$$

The HP Network analyzer is used to measure the transfer function v_b/v_a and, since R_t is known, the low frequency gain G_o can be used to measure accurately the winding resistance r, which from Eq. (8.22) can be derived as

$$r = R_t \frac{G_o}{1 - G_o} \tag{8.26}$$

Finally, either the pole f_p or the zero f_z of the measured transfer function can be used to measure the leakage inductance ℓ. That is,

$$\ell = \frac{1}{2\pi} \frac{r}{f_z} (N_1/N_2)^2 \tag{8.27a}$$

or

$$\ell = \frac{1}{2\pi} \frac{r + R_t}{f_p} (N_1/N_2)^2 \tag{8.27b}$$

The measured transfer function v_b/v_a is illustrated in Fig. 8.20. From the measurements and using Eqs. (8.26) and (8.27a)

$$r = 0.151\ \Omega \tag{8.28}$$

$$\ell = 1.6\ \mu H \tag{8.29}$$

The value of the measured leakage inductance ℓ is in good agreement with the predicted value of 1.4 μH.

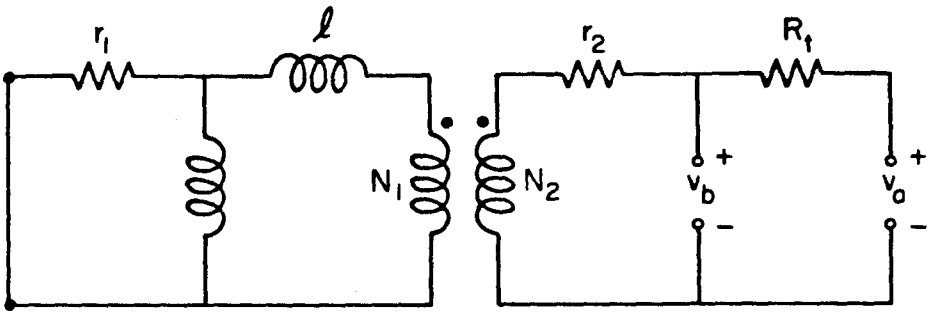

Fig. 8.19. Set up used to measure indirectly the leakage inductance ℓ. The HP-network analyzer measures the transfer function v_b/v_a from which ℓ can be determined.

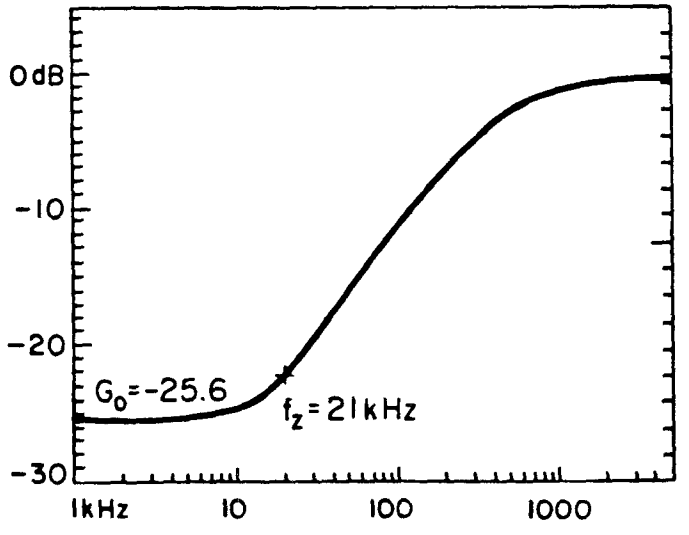

Fig. 8.20. Measured transfer function v_b/v_a. G_0 = -25.6 db, f_z = 21 kHz, R_t = 2.72 Ω.

8.5 Conclusions

In this chapter the general steps necessary to determine the electric circuit model (physical model) of a magnetic structure are described with the help of a simple example. The example also illustrates how the parameters in the physical model of a magnetic structure can be easily associated with corresponding quantities in the original magnetic structure.

In the next chapters this method is used to obtain the physical model of some commonly used arrangements.

CHAPTER 9

PHYSICAL MODELS FOR TWO-WINDING BOBBIN CORE MAGNETIC STRUCTURES

9.1 Introduction

In the previous chapter the method for obtaining the physical model of a magnetic structure is illustrated using a simple two-winding toroid as an example. Although this configuration is sometimes used in transformer and inductor designs, the closed nature of the core makes it very difficult to "thread" the windings through the toroid.

Figure 9.1 illustrates a different type of core in which the windings are first wound on a bobbin, and the bobbin is then put together with the two cut pieces of the core. The advantages of this type of configuration over the simple toroid are various. For instance, the windings can be wound much more easily on the bobbin than on a toroid, and also, gaps can be easily introduced along the magnetic path of the core as shown in the figure.

Bobbin core structures come in several shapes, some of which are illustrated in Fig. 9.2.

9.2 Open and Closed Cores

There is one noticeable difference between the cores illustrated in Fig. 9.2a and the one in Fig.9.2b. The shape of the pot core in Fig. 9.2b is closed, while that of the cores in Fig. 9.2a is partially open. Because of the closed nature of pot cores, the magnetic fields

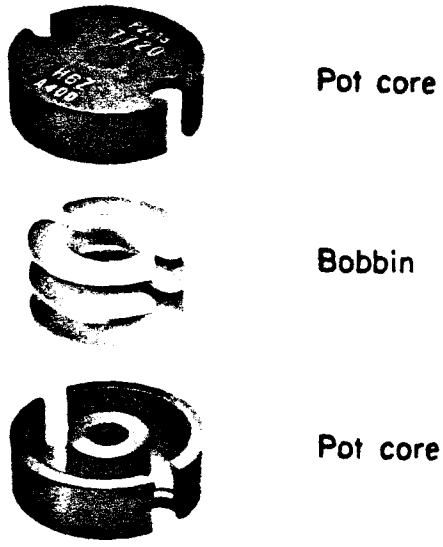

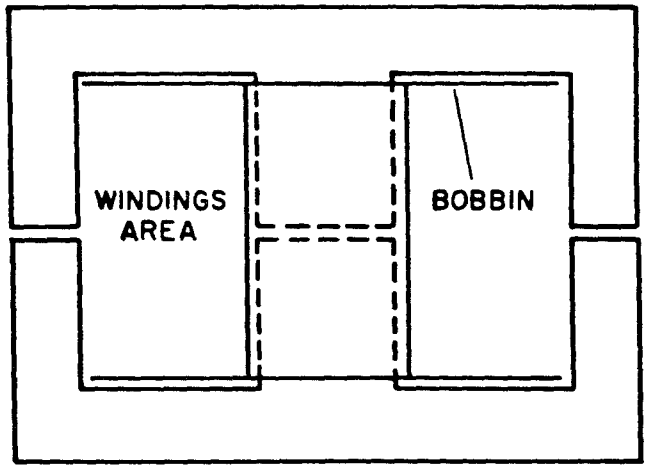

Fig. 9.1 Illustration of bobbin core structure. The windings are wound on a bobbin, which is then assembled with the two cut pieces of the core.

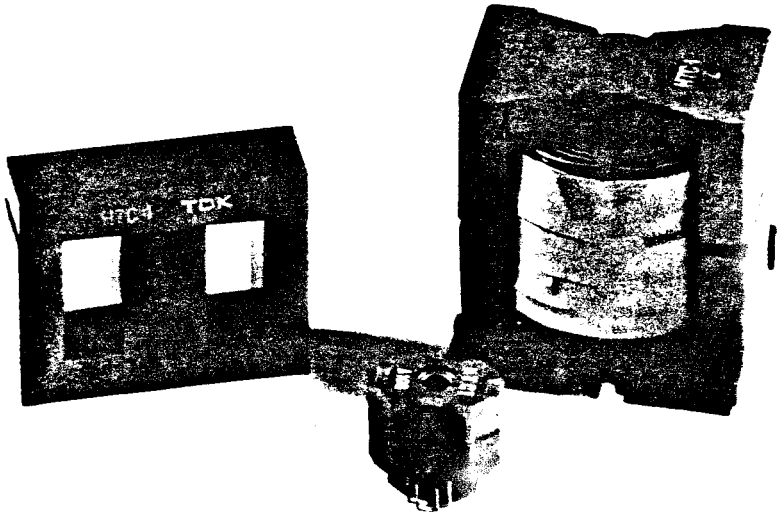

(a)

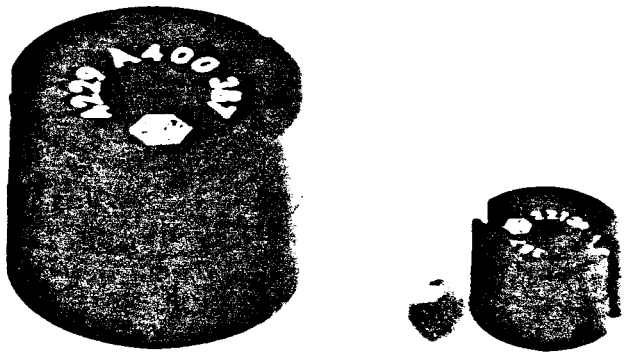

(b)

Fig. 9.2 *Examples of bobbin core structures. (a) Partially open cores, (b) closed pot cores.*

inside the structure (including the leakage flux) remain inside the core.

For the partially open cores, however, the leakage flux through the outside sections of the windings is partially radiated away from the structure. Although this might be an important qualitative difference between these two types of cores, quantitatively it makes no significant difference, which is why both types of cores have been classified under the same general category of bobbin core structures.

Of the many possible ways of arranging the windings on the bobbin of this type of core, two arrangements are the most widely used. The physical models for these arrangements are discussed in the sections that follow.

9.3 Two-Winding Side-by-Side Arrangement

Figure 9.3 illustrates what is probably the most common way of arranging the windings in a bobbin core. The primary is wound first on the bobbin, and the secondary is then wound on top of and around the primary. In the figure, the bobbin is omitted for clarity.

The two sections of the core are shown separated by a small gap. Although sometimes only the center leg is gapped, or a gap is not used at all (as might be the case in a transformer design), it is shown later that these two special cases are particular cases of the more general one shown in Fig. 9.3.

9.3.1 Flux Pattern inside the Structure

The flux pattern inside the windings of the structure in Fig. 9.3 is obtained using Ampere's law in its most general form. The

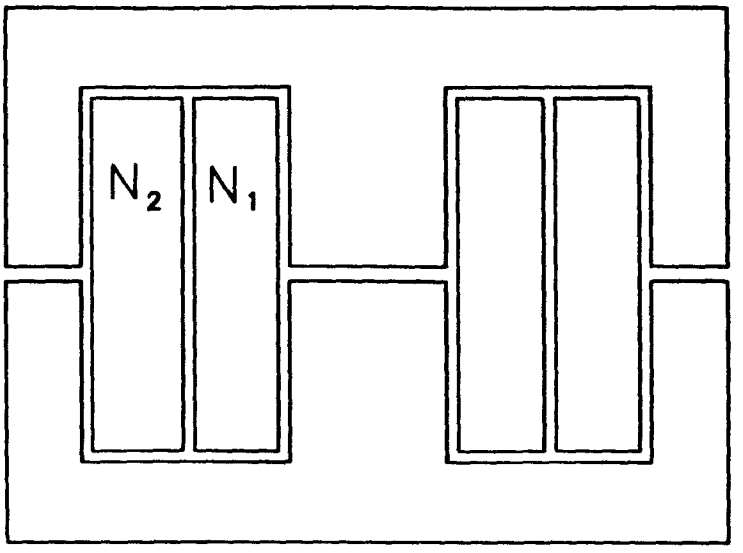

Fig. 9.3 Two-Winding side-by-side arrangement.

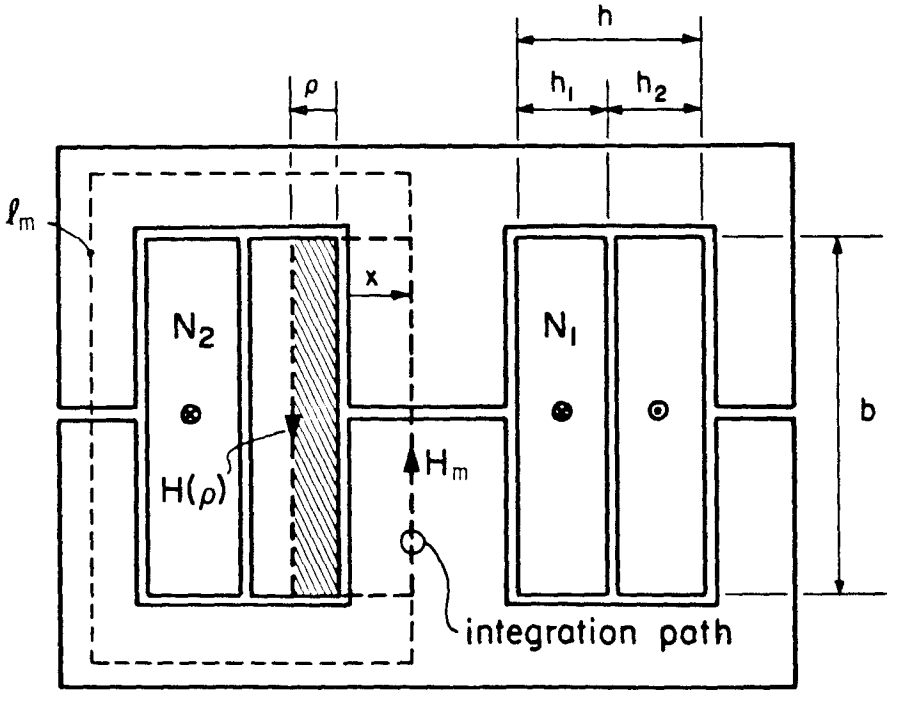

Fig. 9.4 Illustration of integration path used to obtain the field intensity inside the windings H(ρ). The hatched area is the total current enclosed by the integration path. Also illustrated is the mean length of the magnetic path of the core ℓ_m.

integration path can be selected as indicated in Fig. 9.4. This time, the windings are cylinders surrounding the center leg of the core, and therefore there is no need to transform or stretch the structure as was done for the toroid.

With use of the integration path shown in Fig. 9.4, Ampere's law can be written as

$$\oint_C H \cdot d\ell = \iint J \cdot ds \tag{9.1}$$

The right-hand side of this equation is the total current enclosed by the integration path; therefore Eq. (9.1) reduces to

$$\oint_C H \cdot d\ell = J_1 b \rho \tag{9.2}$$

where J_1 is the current density in the primary which is given by

$$J_1 = \frac{N_1 I_1}{h_1 b} \tag{9.3}$$

Substitution of Eq. (9.3) into (9.2) and evaluation of the integral on the left side gives

$$H(\rho) = H_m - \frac{N_1 I_1}{b} \frac{\rho}{h_1} \tag{9.4}$$

where $H(\rho)$ is the field intensity inside the primary at a radial distance $(\rho + r_o)$ from the center of the core, and H_m is the field intensity inside the core, which is approximately given by

$$H_m = \frac{N_1 I_1 - N_2 I_2}{\ell_m} \tag{9.5}$$

where ℓ_m is the mean length of the magnetic path of the core.

The field intensity through the secondary winding and the rest of the core is obtained in a similar way. The complete result is illustrated in Fig. 9.5. The sign of the field intensity determines the direction of the fluxes inside the windings and the rest of the core. This, in turn, is used to establish the approximate flux pattern inside the structure, which is also illustrated in Fig. 9.5.

9.3.2 The Flux Equations

Before writing the flux equations it is necessary to define the infinitely small sources of mmf that represent the windings N_1 and N_2. This is similar to what is done with the two-winding toroid.

The two sources of mmf are shown in Fig. 9.6. Again, they have been positioned at the extremes of the windings, so that all the leakage flux is contained within the two.

The flux equations can now be written according to the following definitions:

$$\phi_{N1} = \text{Total flux enclosed by } N_1 I_1 \tag{9.7}$$

$$\phi_{N2} = \text{Total flux enclosed by } N_2 I_2 \tag{9.8}$$

and the flux pattern in Fig. 9.5. This yields

$$\phi_{N1} = \phi_c \tag{9.9}$$

$$\phi_{N2} = \phi_c - (\phi_1 + \phi_\delta + \phi_2) \tag{9.10}$$

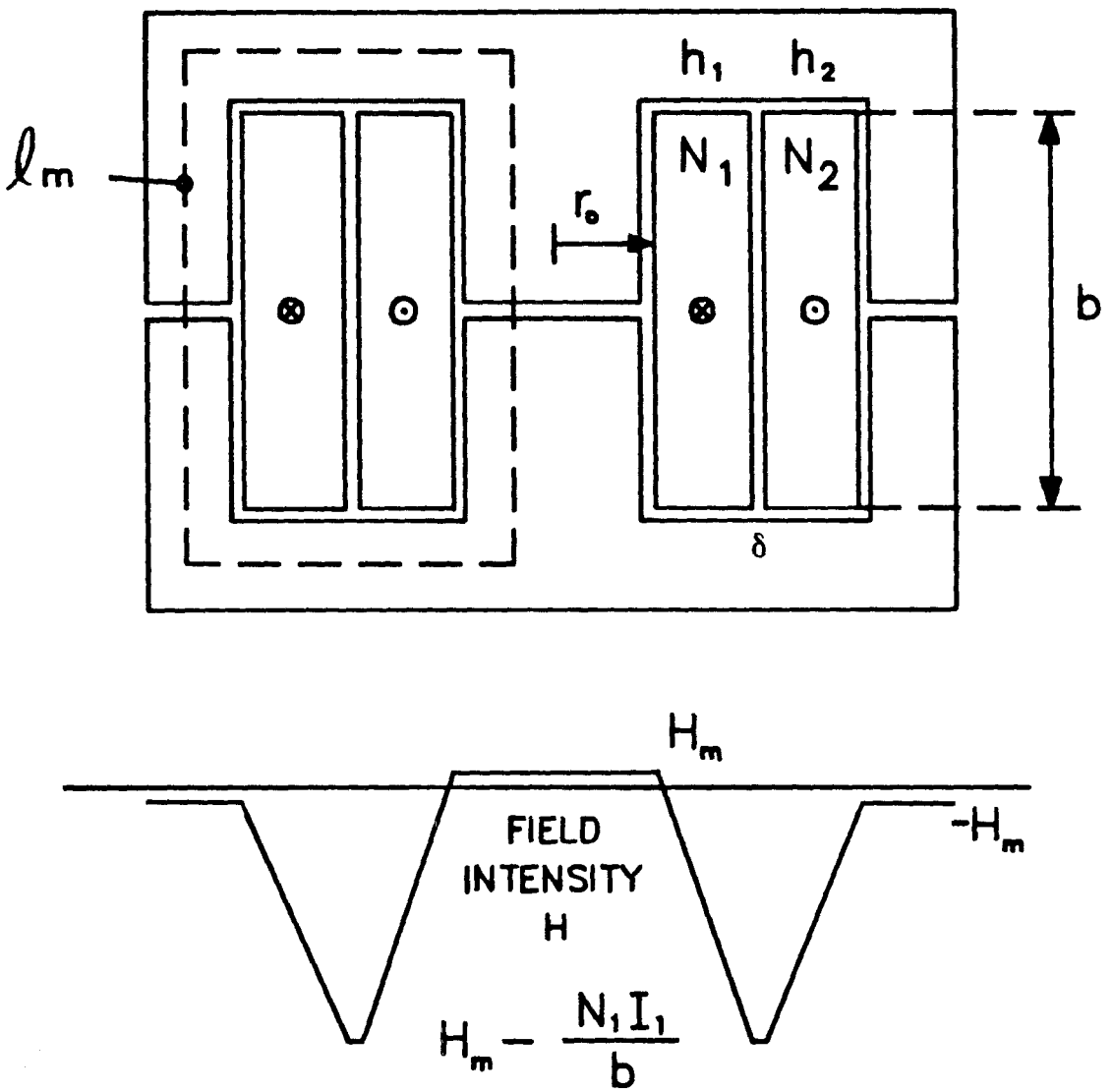

Fig. 9.5 Field intensity inside the windings and the core.

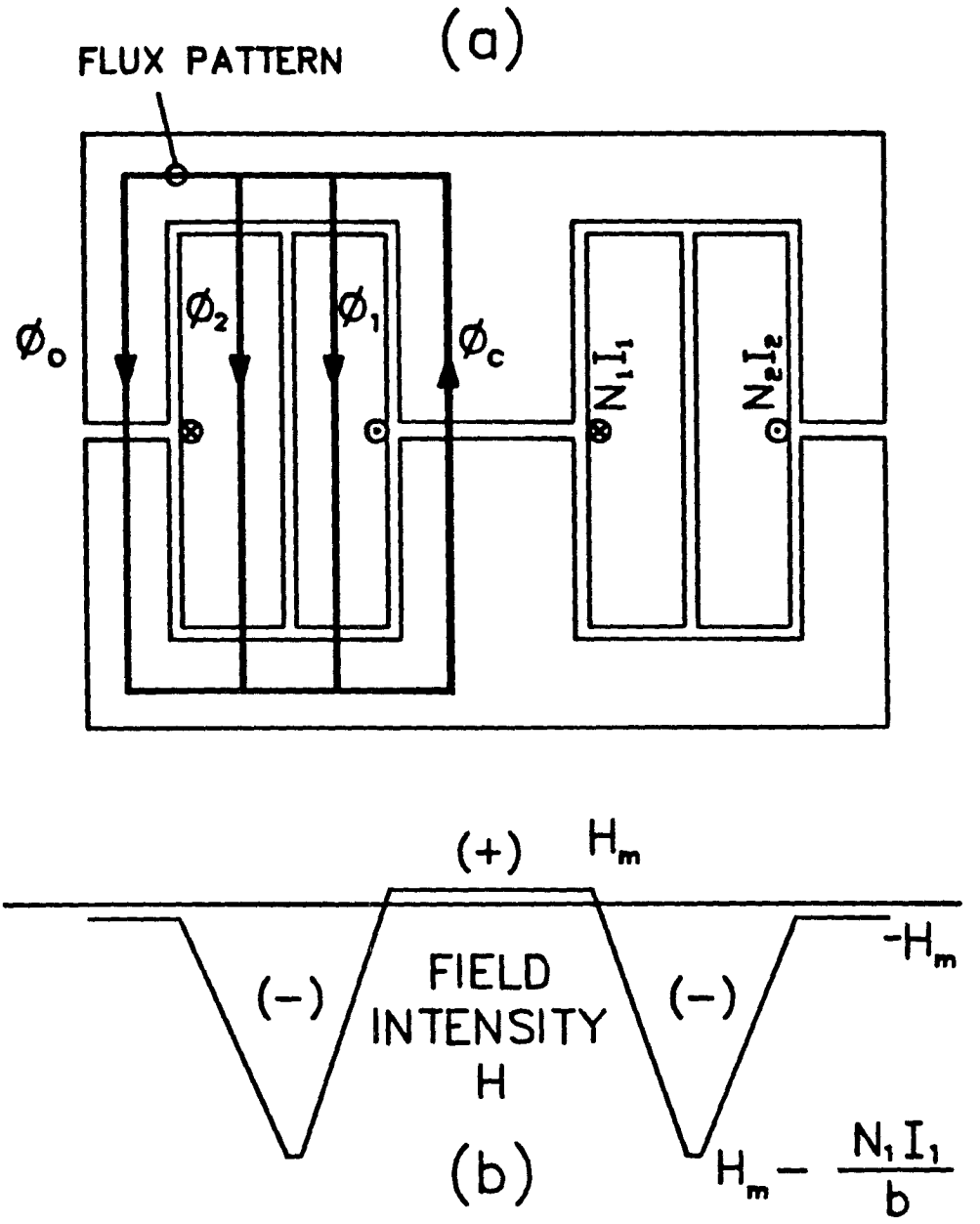

Fig. 9.6 Illustration of the flux pattern inside two-winding side-by-side arrangement. It is determined with the use of the field intensity plot. Also shown are the infinitely small sources of mmf N_1I_1 and N_2I_2.

Substitution of Eq. (9.9) into (9.10) gives

$$\phi_{N2} = \phi_{N1} - \phi_{\ell} \tag{9.11}$$

where $\phi_{\ell}=\phi_1+\phi_{\delta}+\phi_2$.

Finally, the last flux equation gives the relation between the flux through the center leg of the core ϕ_c, and the flux through the outer legs ϕ_o. That is,

$$\phi_o = \phi_c - \phi_{\ell} = \phi_{N2} \tag{9.12}$$

9.3.3 Construction of Reluctance Model

The reluctance circuit model is constructed using Eqs. (9.9) through (9.12). Each node in the reluctance circuit model satisfies one of these equations, and each branch in the circuit represents a corresponding flux path. The infinitely small sources of mmf $N_1 I_1$ and $N_2 I_2$ are represented by two voltage sources. The complete reluctance circuit model is illustrated in Fig. 9.7.

The reluctances in the circuit represent the ability of the structure to store energy along that particular path. For instance, R_{ℓ} represents the ability of the structure to store energy in the windings; R_c is the reluctance of the center leg gap and R_o, that of the outer legs.

9.3.4 Electric Circuit Model

The electric circuit model derived from the reluctance model using the principle of duality discussed in Appendix A is illustrated in Fig. 9.8. The relations between the inductances in the electric circuit model and the reluctances in the reluctance model are given by

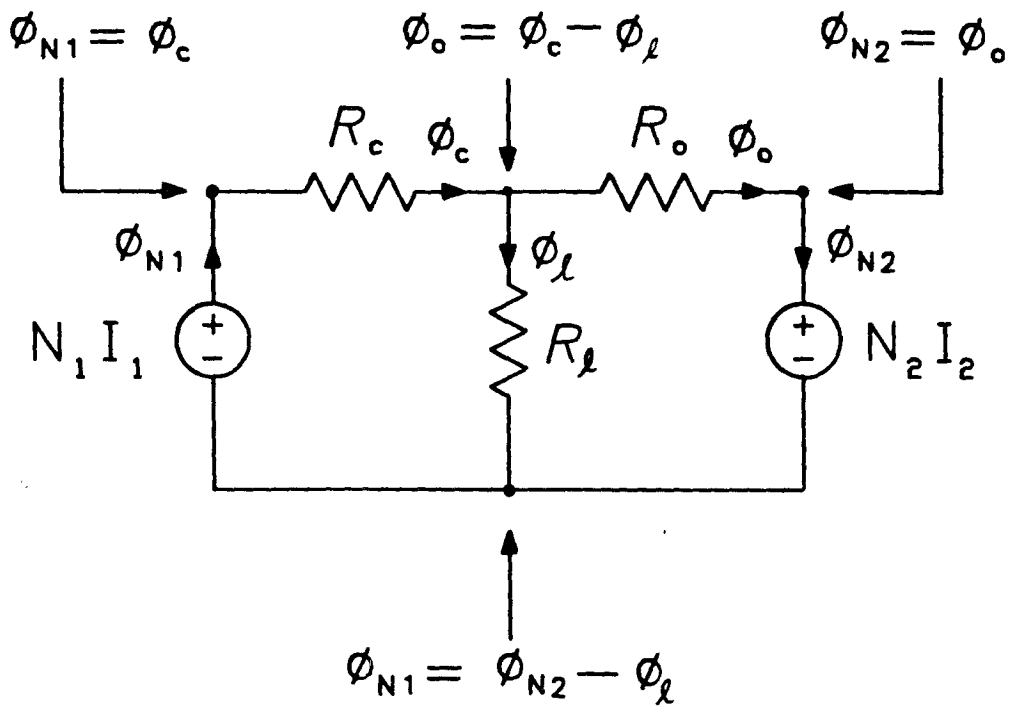

Fig. 9.7 Reluctance circuit model for two-winding side-by-side arrangement. The "voltage" sources represent the mmf sources $N_1 I_1$ and $N_2 I_2$ in Fig. 9.6, and the reluctances the energy storage capabilities of each path in the flux pattern. Each node in the reluctance circuit satisfies a flux equation.

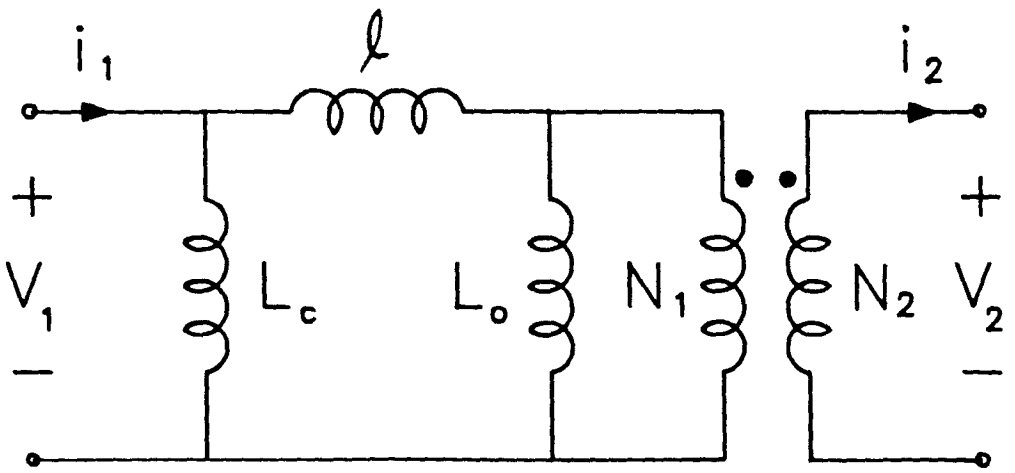

Fig. 9.8 Electric circuit model for two-winding side-by-side arrangement.

$$L_c = \frac{N_1^2}{R_c} \tag{9.13}$$

$$L_o = \frac{N_1^2}{R_o} \tag{9.14}$$

$$\ell = \frac{N_1^2}{R_\ell} \tag{9.15}$$

9.3.5 Estimation of Parameters in Electric Circuit Model

The two inductances L_c and L_o in the electric circuit model are easily obtained since they are directly associated with the center and outer leg gaps, respectively. That is,

$$L_c = \frac{N_1^2}{R_c} = \frac{N_1^2}{\ell_g/\mu_o S_c} \tag{9.16}$$

and

$$L_o = \frac{N_1^2}{R_o} = \frac{N_1^2}{\ell_g/\mu_o S_o} \tag{9.17}$$

where S_c is the effective area of the center leg of the core, S_o the total area of the outer legs, and ℓ_g the length of the spacer gap.

The leakage inductance ℓ can be calculated by shorting the secondary and exiting the primary with a current source. This is illustrated in Fig. 9.9.

If the leakage inductance ℓ is much smaller than L_c, most of the energy from the current source is stored in the leakage inductance ℓ and not in L_c. The field intensity inside the windings with the secondary shorted can be obtained using the same integration path that was used in Fig. 9.4. The result is illustrated in Fig. 9.10. Since

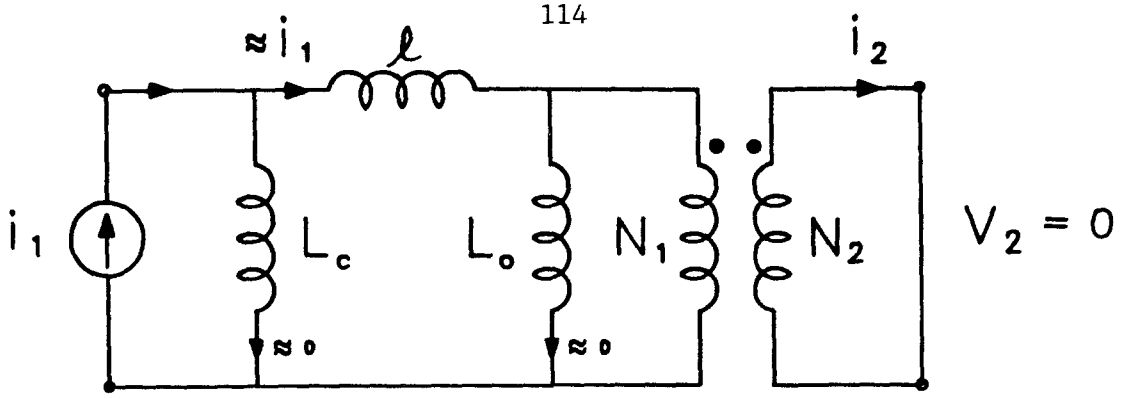

Fig. 9.9 With the secondary shorted, most of the energy from I_1 is stored in the leakage inductance ℓ.

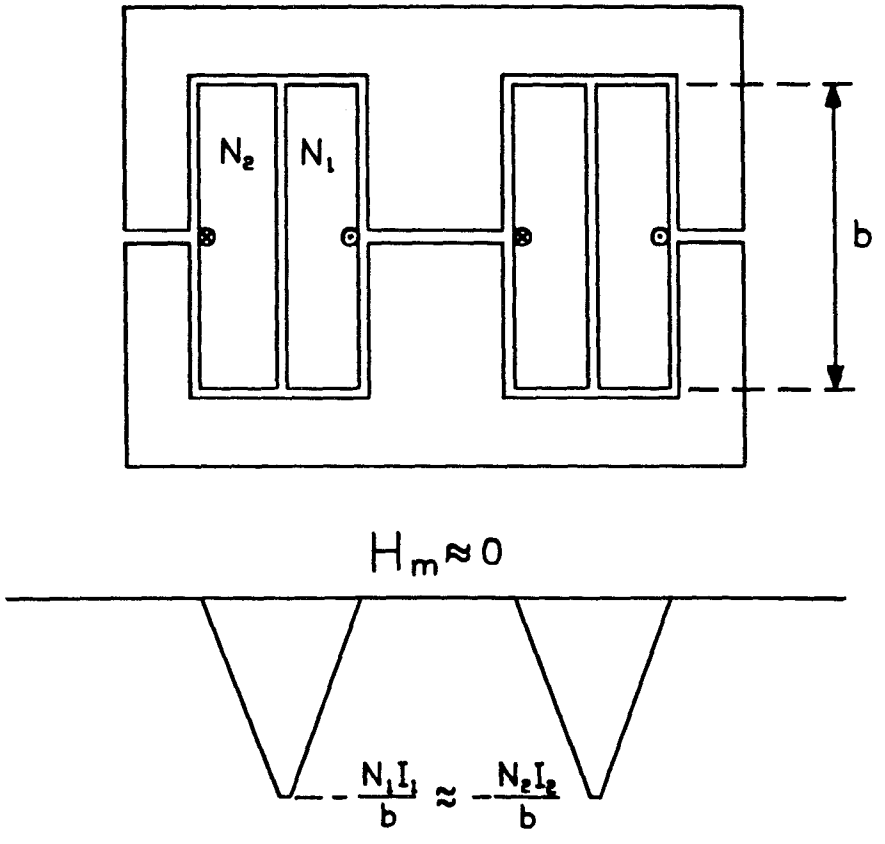

Fig. 9.10 Illustration of field intensity inside the two-winding side-by-side arrangement when the secondary is shorted. The field intensity inside the core H_m is reduced to almost zero.

the secondary is shorted, $N_1 I_1 \approx N_2 I_2$, therefore, the mutual flux ϕ_m is approximately zero.

The leakage inductance ℓ can now be computed by evaluation of

$$\ell = \frac{\mu_o}{I_1^2} \iiint H(\rho)^2 dv \tag{9.18}$$

throughout the volume of the windings, where $H(\rho)$ is given in Fig. 9.10. Evaluation of this integral gives

$$\ell = 2\pi\mu_o N_1^2 \frac{1}{b} \left[h_1 \left(\frac{r_o}{3} + \frac{h_1}{4} \right) + \delta \left(r_o + h_1 + \frac{\delta}{2} \right) + h_2 \left(\frac{r_o + h_1 + \delta}{3} + \frac{h_2}{12} \right) \right] \tag{9.19}$$

If the widths of the windings are the same, i.e., $h_1 = h_2 = h/2$, and $\delta \ll h$, Eq. (9.19) reduces to

$$\ell = \frac{2}{3} \pi\mu_o N_1^2 \frac{h}{b} (r_o + h/2) \tag{9.20}$$

or

$$\ell = \frac{1}{3} \mu_o N_1^2 \frac{h}{b} MLT \tag{9.21}$$

where $MLT = 2\pi(r_o + h/2)$ is the mean length per turn of the bobbin.

The electric circuit model in Fig. 9.8, together with Eqs. (9.16), (9.17) and (9.19) define the physical model for the two-winding transformer in Fig. 9.3.

9.3.6 Relation Between Physical Model and Mathematical Model

The electric circuit model (physical model) in Fig. 9.8 can be transformed to the mathematical model shown in Fig. 7.3 by performing a ∇-to-Y transformation as shown in in Figs. 9.11a and 9.11b. The relations between the elements in Fig. 9.11a and the ones in Fig. 9.11b are given by

$$\ell_1 = \frac{\ell L_c}{\ell + L_c + L_o} \tag{9.22}$$

$$\ell_2 = \frac{\ell L_o}{\ell + L_c + L_o} \tag{9.23}$$

$$L_m = \frac{L_c L_o}{\ell + L_c + L_o} \tag{9.24}$$

The elements in the mathematical model in Fig. 9.11b, ℓ_1, ℓ_2, and L_m are a mathematical function (Eqs. (9.22) through (9.24)) of the parameters in the physical model ℓ, L_c and L_o.

9.3.7 Special Cases of the Two-winding Side-by-Side Arrangement

The configuration in Fig. 9.3 can be considered a general case for the two-winding side-by-side arrangement. The case where the core is ungapped and the case where only a gap in the center leg is used can be considered special cases of the arrangement in Fig. 9.3.

If the core is ungapped, the two inductances L_c and L_o in Fig. 9.8 are very large compared to ℓ, and consequently, the electric circuit model can be reduced to that shown in Fig. 9.12. The

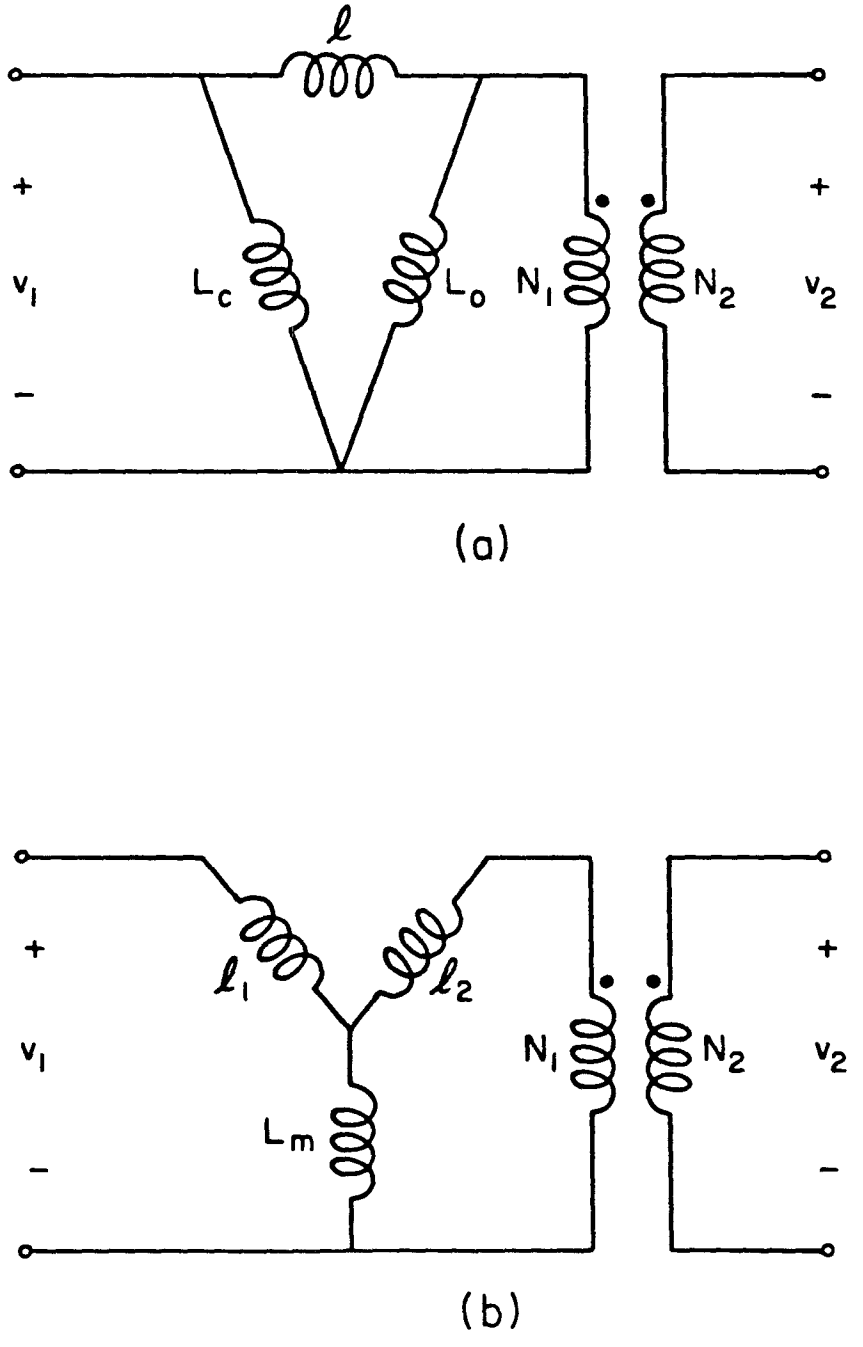

Fig. 9.11 The electric circuit model for the two-winding side-by-side arrangement in Fig. 9.8 is shown here (a) with the Δ connection of the inductances more explicit to illustrate how it can be transformed into the mathematical model in (b).

expression for the leakage inductance ℓ in this circuit is still given by Eq. (9.19), and the mutual inductance is now given by

$$L_m = \frac{N_1^2}{R_m} \tag{9.25}$$

where $R_m = \ell_m / \mu S$ is the reluctance of the magnetic path of the core.

If a gap is present in the center leg only, then $L_o >>> L_c$, and the electric circuit model in Fig. 9.8 can be approximated by that in Fig. 9.13. The expression for the inductance of the center leg is given by Eq. (9.16), and the leakage inductance, by Eq. (9.19).

9.3.8 Examples

Various bobbin cores of different sizes were wound as shown in Fig. 9.3. Two examples are given in this section to illustrate how the models are experimentally verified.

The first example is a small P-2213 pot core with a spacer gap. The length of the gap and the size of the windings and the core are summarized below.

$$\begin{aligned}
&N_1 = 65, \quad N_2 = 61 \\
&r_o = \text{radius of bobbin} = 0.5 \text{ cm} \\
&h = \text{width of each winding} = 0.2 \text{ cm} \\
&b = \text{height of the windings} = 0.8 \text{ cm} \\
&S_c = \text{effective area of the center leg} = 0.542 \text{ cm}^2 \\
&S_o = \text{effective area of the outer legs} = 1.04 \text{ cm}^2 \\
&\ell_g = \text{length of the spacer gap} = 0.28 \text{ mm}
\end{aligned} \tag{9.26}$$

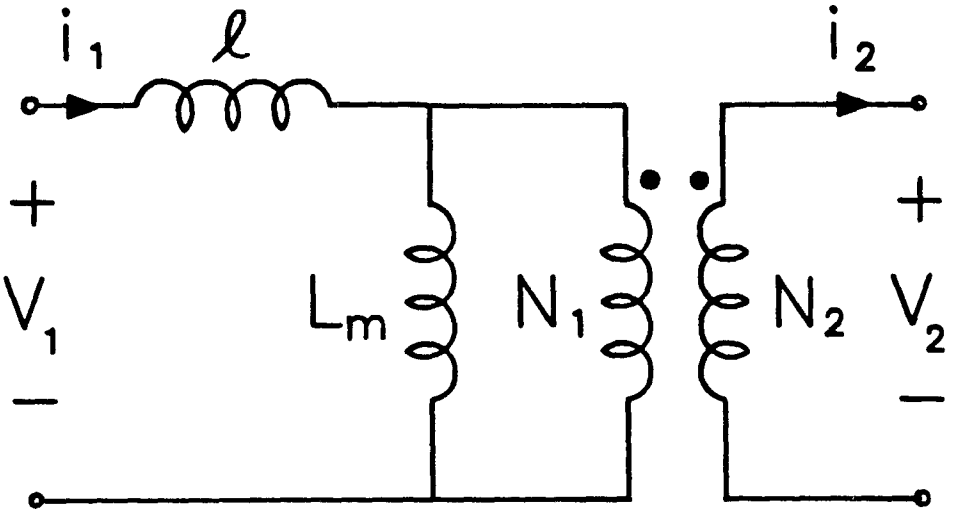

Fig. 9.12 Reduced electric circuit model for ungapped two-winding side-by-side arrangement.

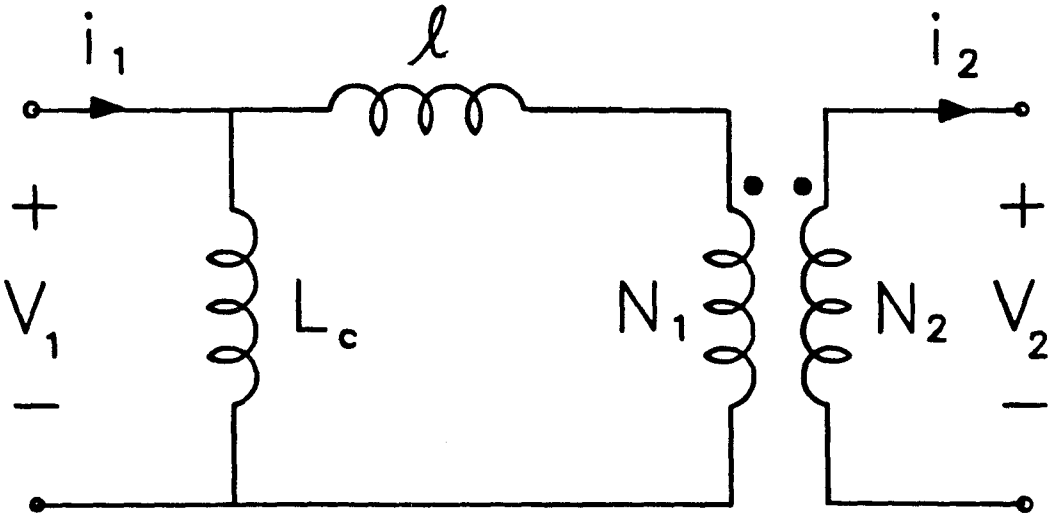

Fig. 9.13 Reduced electric circuit model for two-winding side-by-side arrangement with only a center leg gap.

The predicted electric circuit model (physical model) obtained by substitution of these values in Eqs. (9.16), (9.17), and (9.20) is shown in Fig. 9.14a.

To experimentally verify the model, the four parameters L_c, L_o, ℓ, and N can be derived from the following measurements.

With the secondary open, measure the impedance looking into the primary. This gives

$$s(L_c \| (L_s + \ell)) \tag{9.27}$$

Similarly, with the primary open, measure the impedance looking into the secondary, which gives

$$s \left(\frac{N_2}{N_1} \right)^2 (L_s \| (L_c + \ell) \tag{9.28}$$

Next, measure the impedance looking into the primary with the secondary shorted. This gives

$$s(L_c \| \ell) \tag{9.29}$$

Similarly, the impedance looking into the secondary with the primary shorted gives

$$s \left(\frac{N_2}{N_1} \right)^2 (L_s \| \ell) \tag{9.30}$$

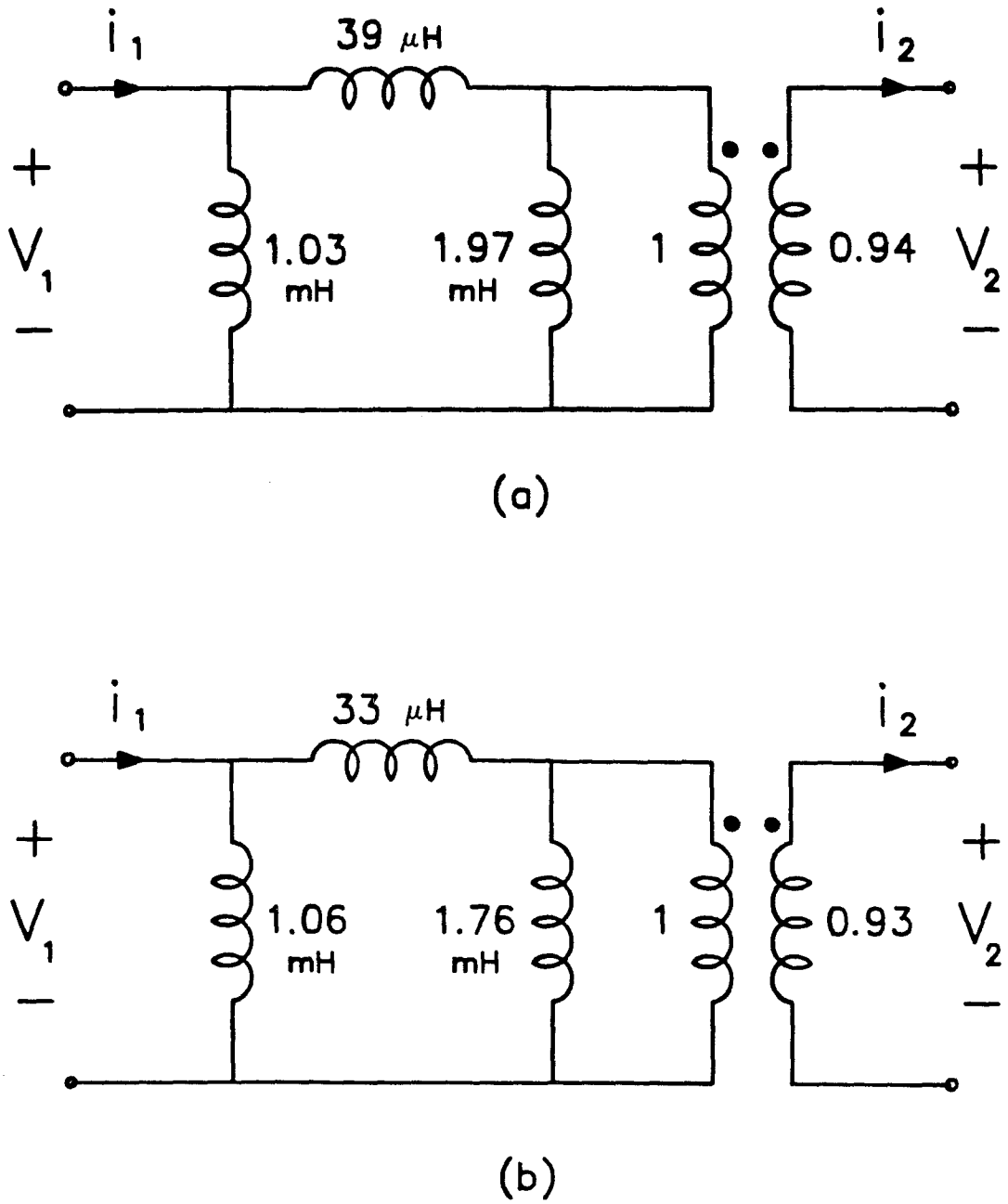

Fig. 9.14 (a) Predicted electric circuit model values for two-winding side-by-side arrangement on a P-2213 pot core with a 0.28 mm spacer gap. (b) Measured electric circuit model.

Finally, measure the open circuit voltage ratios

$$\frac{v_2}{v_1} = \frac{N_2}{N_1} \frac{L_s}{L_s + \ell} \tag{9.31}$$

$$\frac{v_1}{v_2} = \frac{N_1}{N_2} \frac{L_c}{L_c + \ell} \tag{9.32}$$

All the measurements are performed with the HP network analyzer. The frequency of the measurements is sufficiently high that the resistances of the windings are negligible when compared to the reactances of the inductances in the circuit.

The electric circuit model values derived from these measurements are illustrated in Fig. 9.14b and compare favorably with the predicted values in Fig. 9.14a.

The second example is a similar pot core (P-2213) but with a very large center leg gap only. The length of the gap is 1.2 mm, which for a core this size ($\approx$ 22 mm $\times$ 13 mm) is significantly large. The predicted electric circuit model is illustrated in Fig. 9.15a. The measurements are performed in a similar way by substitution of $L_o \approx \infty$ in Eqs. (9.27) through (9.32).

The measured electric circuit model values are shown in Fig. 9.15b. Although the errors between the measured and the predicted values have increased (probably due to the large size of the gap), the measurements still compare well with the predictions.

Other examples were also investigated, and the results always compared favorably with the predictions.

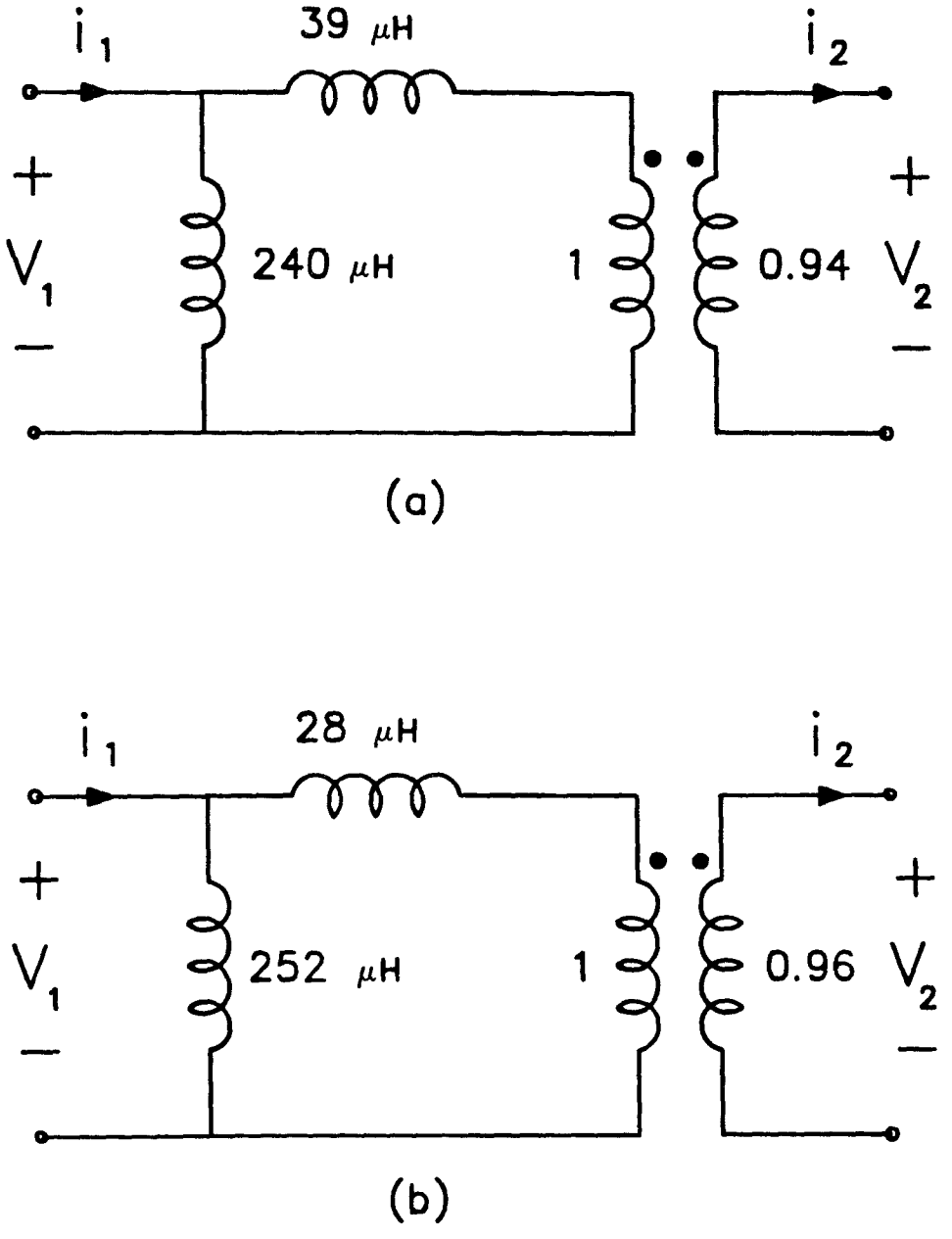

Fig 9.15 *(a) Predicted electric circuit model values for two-winding side-by-side arrangement on a P-2213 pot core with a 1.2 mm center leg gap. (b) Measured electric circuit model.*

9.4 Two-Winding Top-Bottom Arrangement

Another commonly used two-winding configuration is the top-bottom arrangement illustrated in Fig. 9.16. A special bobbin with a divider disk is required to arrange the windings this way. Most core manufacturers supply this type of bobbin for their cores.

9.4.1 Physical Model of Top-Bottom Arrangement

The physical model of this structure is obtained the same way as before. The flux pattern inside the core and the windings is derived using Ampere's law and the integration path shown in Fig. 9.17a. The field intensity throughout the core and the windings is illustrated in Fig. 9.17b.

The sign of the field intensity determines the direction of the fluxes inside the core and the windings. This in turn determines the flux pattern inside the structure that is illustrated in Fig. 9.17b.

The infinitely small sources $N_1 I_1$ and $N_2 I_2$ are positioned at the extremes of the windings as indicated in Fig. 9.17b. The fluxes enclosed by each one of these mmf sources (flux equations) are obtained from the flux pattern in Fig. 9.17b and are given by

$$\phi_{N1} = \text{Total flux enclosed by } N_1 I_1 = \phi_c + \phi_1 \tag{9.33}$$

$$\phi_{N2} = \text{Total flux enclosed by } N_2 I_2 = \phi_o - \phi_2 \tag{9.34}$$

and also, from the figure

$$\phi_c = \phi_o \tag{9.35}$$

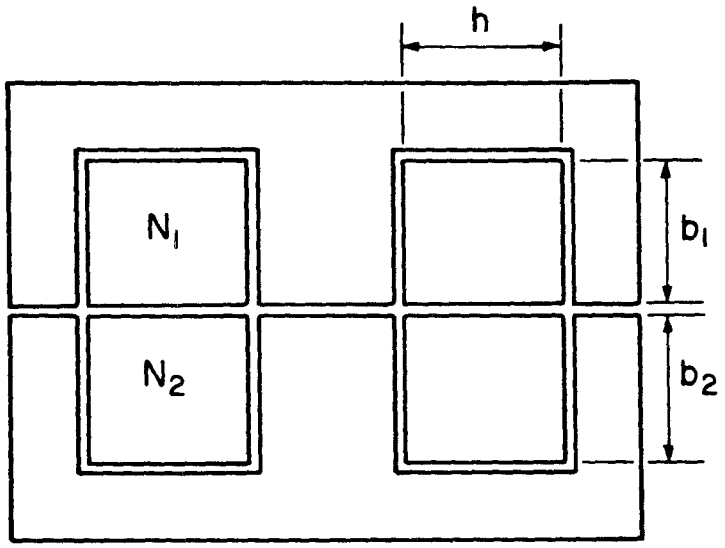

Fig. 9.16 Two-winding top-bottom arrangement.

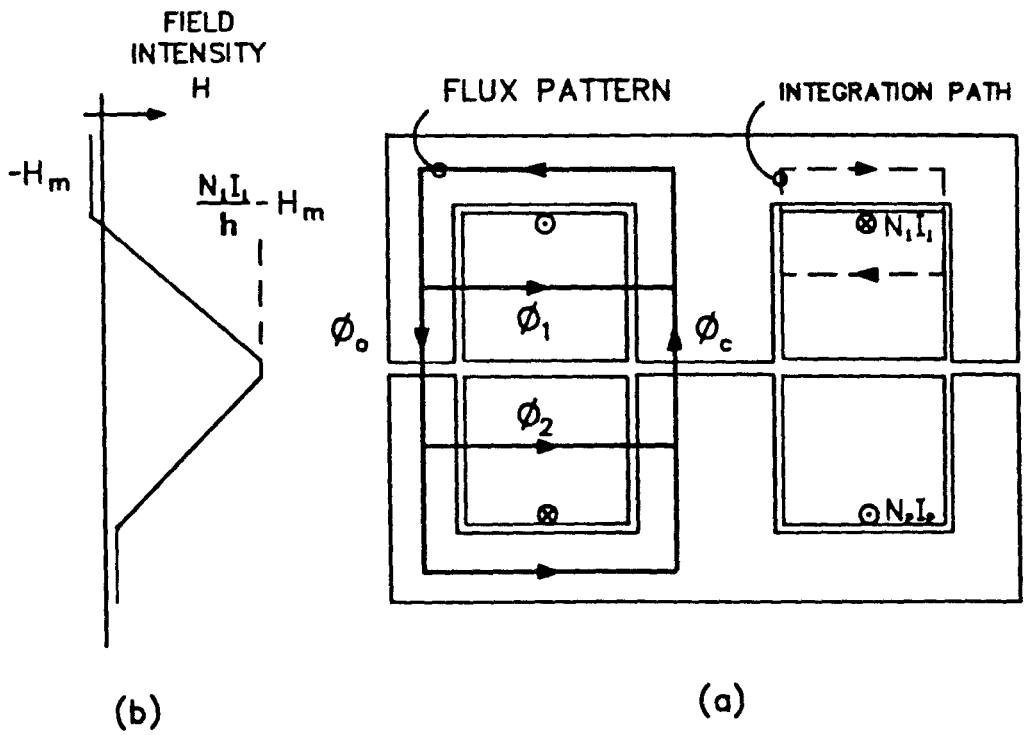

Fig. 9.17 Illustration of integration path (a) used to determine the field intensity (b) in the windings. The flux pattern inside the structure is also illustrated in (a).

Equations (9.33) through (9.35) are used to construct the reluctance circuit model shown in Fig. 9.18. The electric circuit model derived from the reluctance model is illustrated in Fig. 9.19.

Because of the series connection of R_c and R_o in the reluctance circuit, the corresponding inductances L_c and L_o in the electric circuit model appear as a parallel combination.

The expressions for L_c and L_o are again given by Eqs. (9.16) and (9.17), since they also represent the inductances of the center and the outer leg gaps, respectively.

The leakage inductances ℓ_1 and ℓ_2 can be estimated by "mathematically" shorting the secondary and calculating the amount of energy stored in each one of the windings. The field intensity with the secondary shorted is similar to that in Fig. 9.17b, with the mutual flux ϕ_m reduced to approximately zero. The leakage inductance ℓ_1 is calculated by evaluation of

$$\ell_1 = \frac{\mu_o}{I_1^2} \iiint H(\rho)^2 dv \tag{9.36}$$

throughout the volume of N_1.

Similarly, ℓ_2 is obtained by evaluation of

$$\ell_2 = \frac{\mu_o}{I_1^2} \iiint H(\rho)^2 dv \tag{9.37}$$

throughout the volume of N_2.

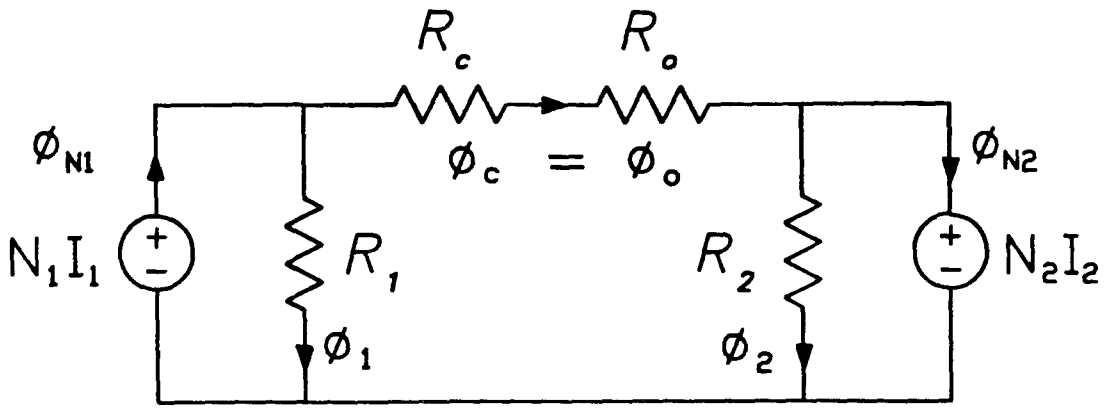

Fig. 9.18 Reluctance circuit model for two-winding top-bottom arrangement.

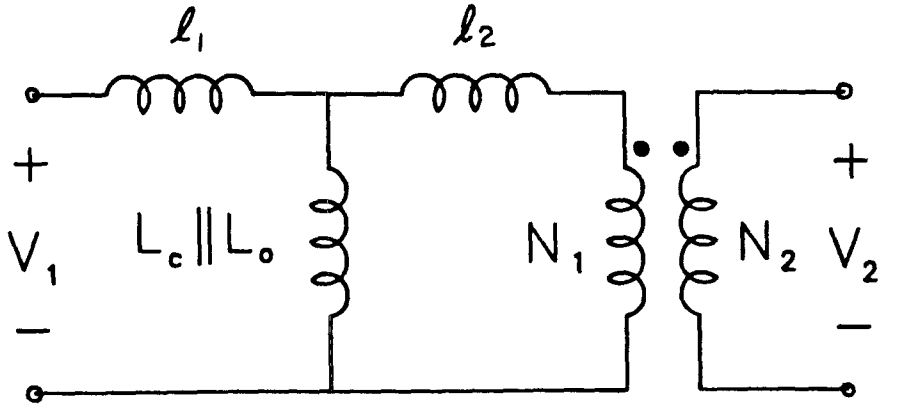

Fig. 9.19 Electric circuit model for two-winding top-bottom arrangement.

Evaluation of Eqs. (9.36) and (9.37) gives

$$\ell_1 = \frac{\mu_o}{3} N_1^2 \frac{b_1}{h} MLT \tag{9.38}$$

$$\ell_2 = \frac{\mu_o}{3} N_1^2 \frac{b_2}{h} MLT \tag{9.39}$$

where $MLT = 2\pi(r_o + h/2)$ is the mean length per turn of the bobbin.

The electric circuit model (physical model) of the top-bottom arrangement (Fig. 9.19), is the same as the mathematical model, i.e., the π-model for a two-winding structure. This is only an exception, not a general result.

9.4.2 Special cases of Top-Bottom arrangement

If the core of the transformer in Fig. 9.16 is ungapped, the mutual inductance in Fig. 9.19 is given by Eq. (9.25). Also, since $L_m >>> \ell_2$, ℓ_2 can be pushed through the node of the mutual inductance L_m, and the circuit model reduces to that in Fig. 9.12. The value of the leakage inductance ℓ is the sum of ℓ_1 and ℓ_2 which are given by Eqs. (9.38) and (9.39). That is,

$$\ell = \ell_1 + \ell_2 = \mu_o N_1^2 \frac{1}{h} \left(\frac{b_1 + b_2}{3} \right) MLT \tag{9.40}$$

or

$$\ell = \frac{1}{3} \mu_o N_1^2 \frac{b}{h} MLT \tag{9.41}$$

where $b=(b_1+b_2)$.

The other special case considered is the one in which only the center leg is gapped. In this case the electric circuit model remains

basically the same as that in Fig. 9.19, with $L_o \approx \infty$, which results in $L_o \| L_c \approx L_c$.

9.4.3 Examples

A small pot core (P-2213) with a center leg gap was used for this example. The windings are wound on a split bobbin as shown in Fig. 9.16. The dimensions of the windings and the core are

$$\begin{aligned} N_1 &= N_2 = 65 \\ r_o &= 0.5 \text{ cm} \\ b_1 &= b_2 = 0.36 \text{ cm} \\ h &= 0.36 \\ S_c &= 0.542 \\ \ell_g &= 0.45 \text{ mm} \end{aligned} \tag{9.42}$$

Substitution of these values in Eqs. (9.16), (9.38), and (9.39), results in the predicted circuit model shown in Fig. 9.20a.

The model is experimentally verified, performing a similar set of impedance and voltage ratios measurements on the circuit. The electric circuit model values calculated from these measurements are illustrated in Fig. 9.20b. The measurements compare favorably with the predictions.

Other examples were also experimentally verified, but since all the circuit models for this arrangement are similar, very little additional information is derived from these examples. In all the cases, the measurements always followed the predictions closely.

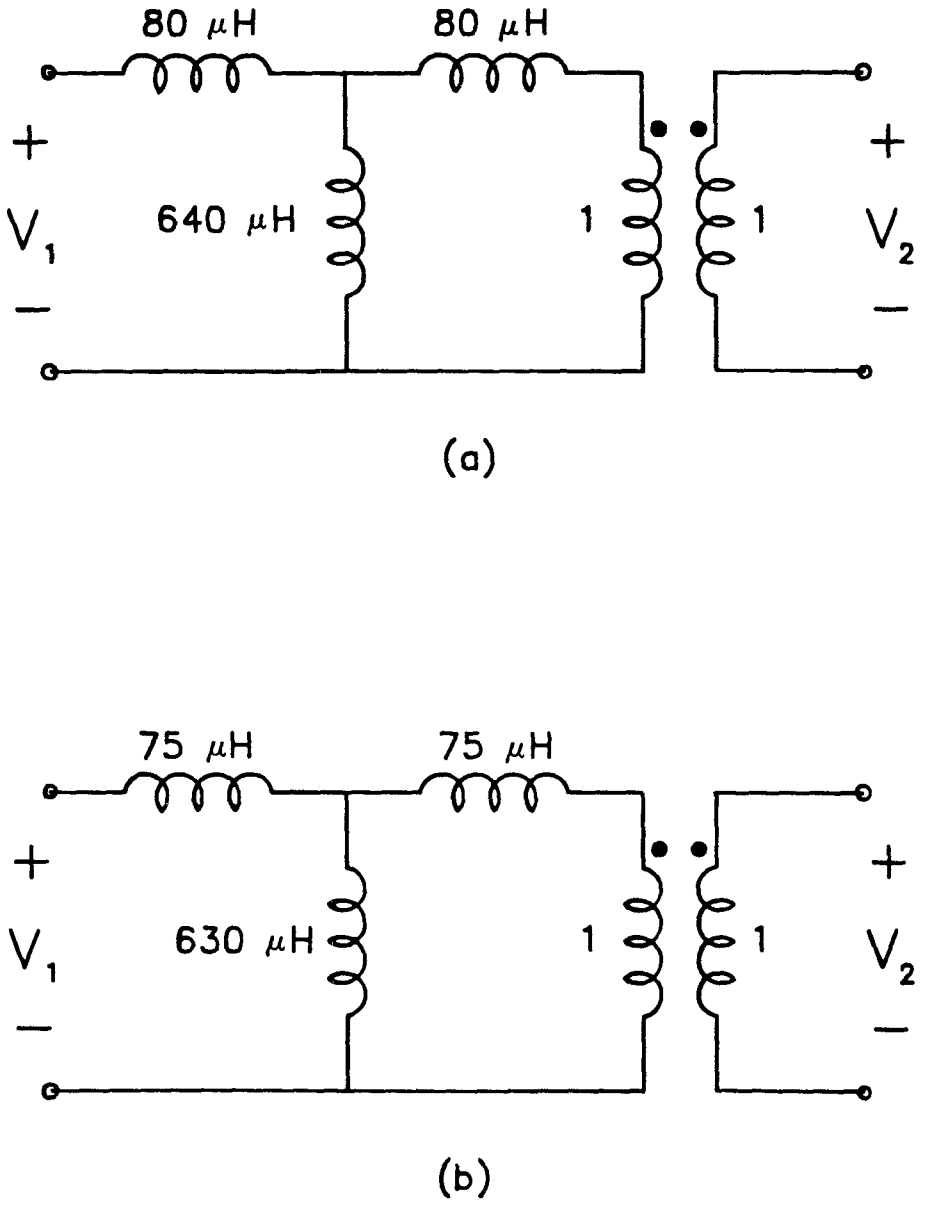

Fig. 9.20 (a) Predicted electric circuit model values for two-winding top-bottom arrangement on a P-2213 pot core with a 0.45 mm center leg gap. (b) Measured electric circuit model.

9.5 Conclusions

In this chapter the method for obtaining the physical model of a magnetic structure is used to determine the electric circuit model (physical model) of two commonly used arrangements.

It is also shown how the physical model of a magnetic circuit differs from the mathematical model (π-model for a two-winding structure). In general, the parameters in the mathematical model are a mathematical function of the parameters in the physical models.

The physical models of the two arrangements discussed illustrate how it is possible with this modelling technique to predict the correct distribution of leakage energy in a magnetic circuit. This is particularly important in the design of coupled inductors, where gaps are always used, and means of controlling the distribution of the leakage energy in the circuit model can assure an optimal performance of the converter.

In the next chapter the new modelling technique is used to obtain the physical model of some three- and four-winding structures.

CHAPTER 10

PHYSICAL MODEL FOR THREE AND FOUR-WINDING MAGNETIC STRUCTURES

In this chapter the same procedure used to obtain the physical models for two-winding structures is used to derive the physical models of some three- and four-winding configurations.

The configurations treated in this chapter are three and four-winding extensions of the two-winding arrangements discussed in Chapters 8 and 9.

10.1 Three-Winding Magnetic Structures

10.1.1 Three-Winding Toroid with Uniformly Distributed Turns

Figure 10.1 illustrates the first three-winding arrangement. It is simply a three-winding extension of the two-winding toroid discussed in Chapter 8. The third winding N_3 is wound on top of and around N_2.

Since the relative positions of N_2 and N_1 have not changed, the electric circuit model (physical model) between N_2 and N_1 remains the same as it was in the two-winding case, i.e., Fig. 8.12.

The toroid in Fig. 10.1 can be cut and stretched the same way as the two-winding toroid. The cut and stretched three-winding toroid is illustrated in Fig. 10.2a.

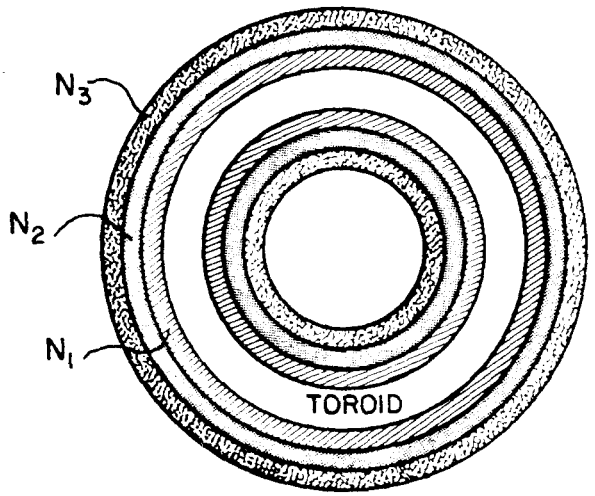

Fig. 10.1 Three-winding toroid with uniformly distributed turns.

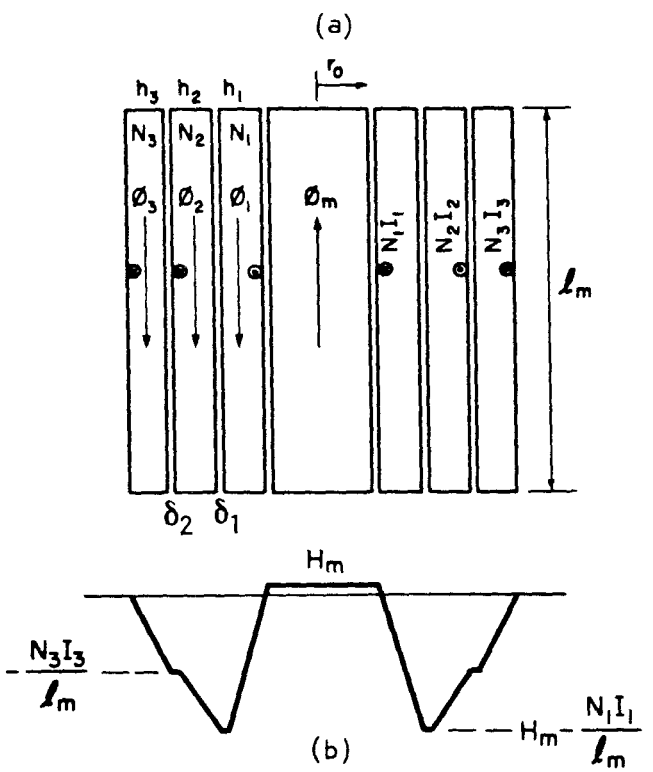

Fig. 10.2 (a) "Cut" and stretched three-winding toroid. (b) Field intensity and flux pattern inside the windings and toroid. Also illustrated are the mmf sources $N_1 I_1$, $N_2 I_2$, and $N_3 I_3$.

The field intensity throughout the toroid and the three windings is obtained in the same way as it is in the two-winding case. The result is illustrated in Fig. 10.2b.

The direction (sign) of the field intensity is used to establish the flux pattern inside the toroid and the windings. This flux pattern is also illustrated in Fig. 10.2a.

The flux equations are defined by the flux pattern and the usual definitions for the infinitely small sources of mmf $N_1 I_1$, $N_2 I_2$, and $N_3 I_3$, which are positioned at the extremes of the windings as indicated in Fig. 10.2a. The flux equations according to these definitions are given by

$$\phi_{N1} = \text{Total flux enclosed by } N_1 I_1 = \phi_m \tag{10.1}$$

$$\phi_{N2} = \text{Total flux enclosed by } N_2 I_2 = \phi_m - (\phi_1 + \phi_2) \tag{10.2}$$

$$\phi_{N3} = \text{Total flux enclosed by } N_3 I_3 = \phi_m - (\phi_1 + \phi_2 + \phi_3) \tag{10.3}$$

Substitution of Eq. (10.1) into Eqs. (10.2) and (10.3) gives

$$\phi_{N2} = \phi_{N1} - (\phi_1 + \phi_2) \tag{10.4}$$

$$\phi_{N3} = \phi_{N2} - \phi_3 \tag{10.5}$$

Equations (10.1) through (10.5) are used to construct the reluctance circuit model illustrated in Fig. 10.3a. Each node in the reluctance circuit satisfies one of these equations, and the reluctances represent the ability of the structure to store magnetic energy along each path. The reluctance circuit in Fig. 10.3a can be rearranged in a more conventional way as shown in Fig. 10.3b.

The electric circuit model derived from the reluctance model using the principle of duality (Appendix A) is illustrated in

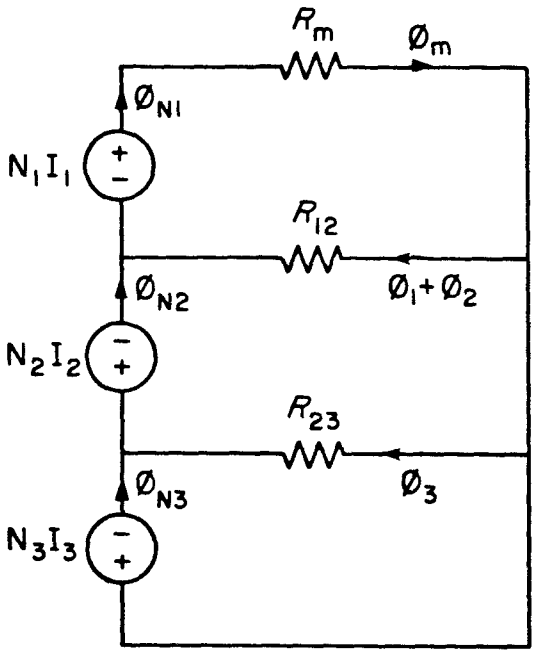

(a)

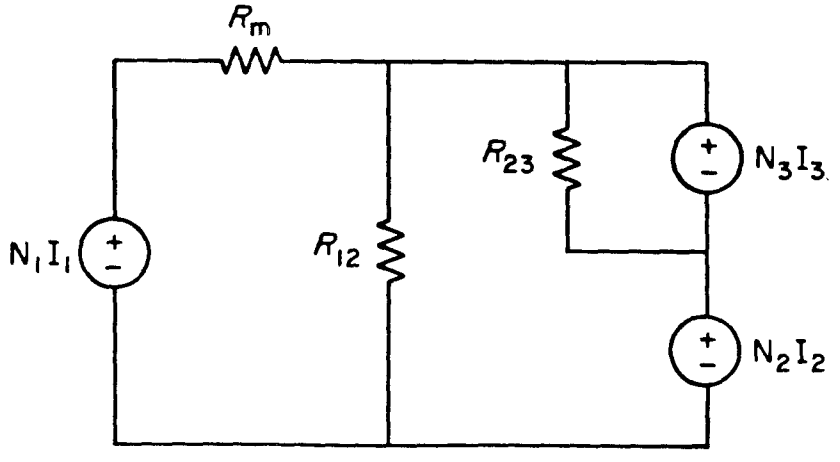

(b)

Fig. 10.3 The reluctance circuit for three-winding toroid (a) can be rearranged as shown in (b).

Fig. 10.4a. It can also be rearranged as shown in Fig. 10.4b where the leakage inductance element ℓ_{23} has been reflected to N_3, and therefore,

$$\ell_{23}' = \left(\frac{N_3}{N_1} \right)^2 \ell_{23}$$

Note that the electric circuit model between N_2 and N_1 (with N_3 open) is the same one in Fig. 8.12. In other words, if N_3 is left open, it is the same as not being there at all, and the structure is basically the same as the two-winding toroid in Chapter 8. Therefore, the electric circuit model (physical model) between N_1 and N_2 with N_3 open is also the same.

The mutual inductance L_m corresponds to the inductance of the toroid which is given by

$$L_m = \frac{N_1^2}{R_m} \tag{10.6}$$

where $R_m = \ell_m / \mu S$ is the reluctance of the toroid.

Since the model between N_2 and N_1 is the same as that of the two-winding toroid in Chapter 8, the expression for the leakage inductance element ℓ_{12} is given by Eq. 8.16; i.e.,

$$\ell_{12} = 2\pi\mu_o N_1^2 \frac{1}{\ell_m} \left[h_1 \left(\frac{r_o}{3} + \frac{h_1}{4} \right) + \delta_1 \left(r_o + h_1 + \frac{\delta_1}{2} \right) + h_2 \left(\frac{r_o + h_1 + \delta_1}{3} + \frac{h_2}{12} \right) \right] \tag{10.7}$$

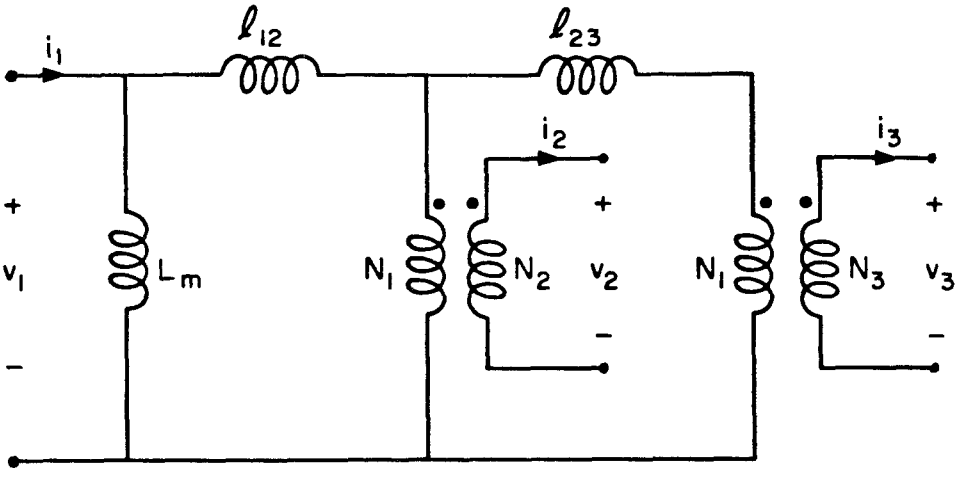

(a)

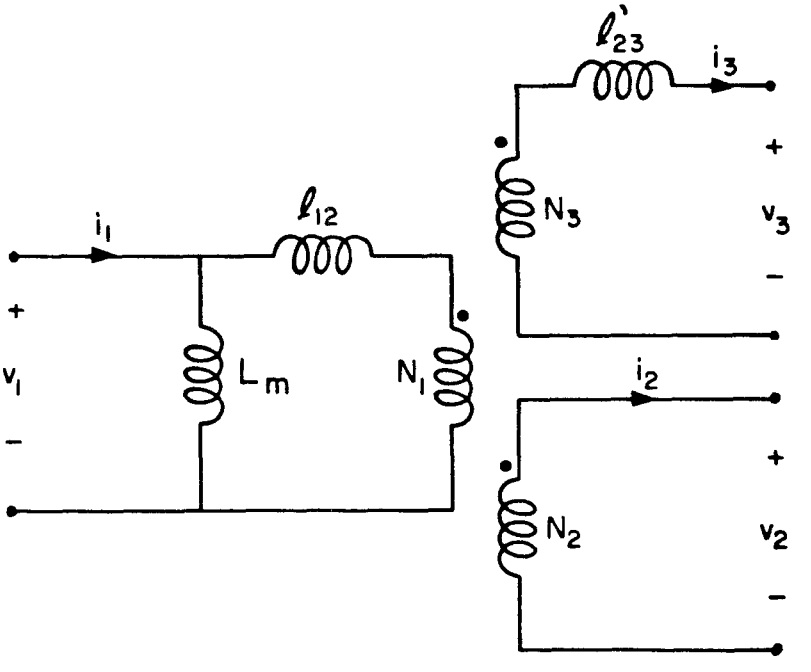

(b)

Fig. 10.4 (a) Electric circuit model for three-winding toroid. It can be rearranged as shown in (b) by reflecting ℓ_{23} to N_3.

where the space δ_1 between N_1 and N_2 is now accounted for.

Finally, the leakage inductance element ℓ_{23}' can be estimated by opening the primary N_1, shorting the secondary N_2, and exciting N_3 with a current source. This is illustrated in Fig. 10.5. Since N_2 is shorted, all the energy from the current source I_3 is approximately stored in the leakage element ℓ_{23}'.

The field intensity throughout the windings under this condition (N_1 open, N_2 shorted) is illustrated in Fig. 10.6. Since all the energy is approximately stored in ℓ_{23}', ℓ_{23}' can be estimated by evaluation of

$$\ell_{23}' = \frac{\mu_o}{I_3^2} \iiint H^2(\rho)\,dv \tag{10.8}$$

where $H(\rho)$ is given in Fig. 10.6. Evaluation of this integral gives

$$\ell_{23}' = 2\pi\mu_o N_3^2 \frac{1}{\ell_m} \left[h_2 \left(\frac{r_o + h_1 + \delta_1}{3} + \frac{h_2}{4} \right) + \right.$$

$$+ \delta_2 \left(r_o + h_1 + \delta_1 + h_2 + \frac{\delta_2}{2} \right) +$$

$$\left. + h_3 \left(\frac{r_o + h_1 + \delta_1 + h_2 + \delta_2}{3} + \frac{h_3}{12} \right) \right] \tag{10.9}$$

If $h_1 = h_2 = h_3 = h/3$, and δ_1, $\delta_2 \ll h$, Eqs. (10.7) and (10.9) reduce to

$$\ell_{12} = \frac{4}{9} \pi\mu_o N_1^2 \frac{h}{\ell_m} (r_o + h/3) \tag{10.10}$$

$$\ell_{23}' = \frac{4}{9} \pi\mu_o N_3^2 \frac{h}{\ell_m} (r_o + 2h/3) \tag{10.11}$$

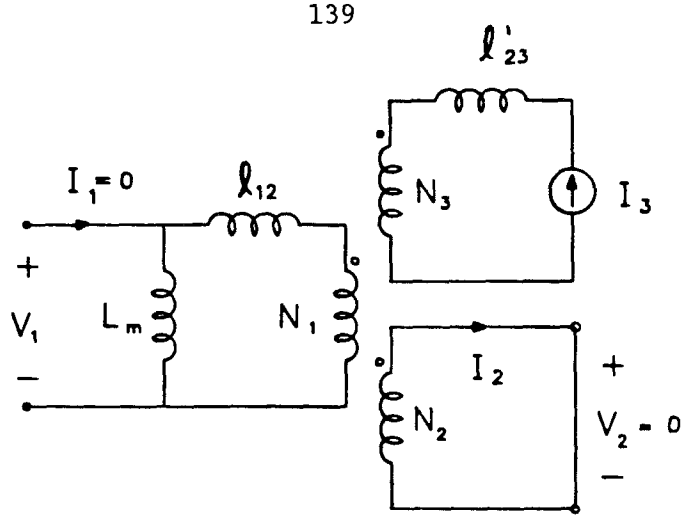

Fig. 10.5 With the primary open and the secondary N_2 shorted, all the energy from the current source I_3 is stored in ℓ_{23}'.

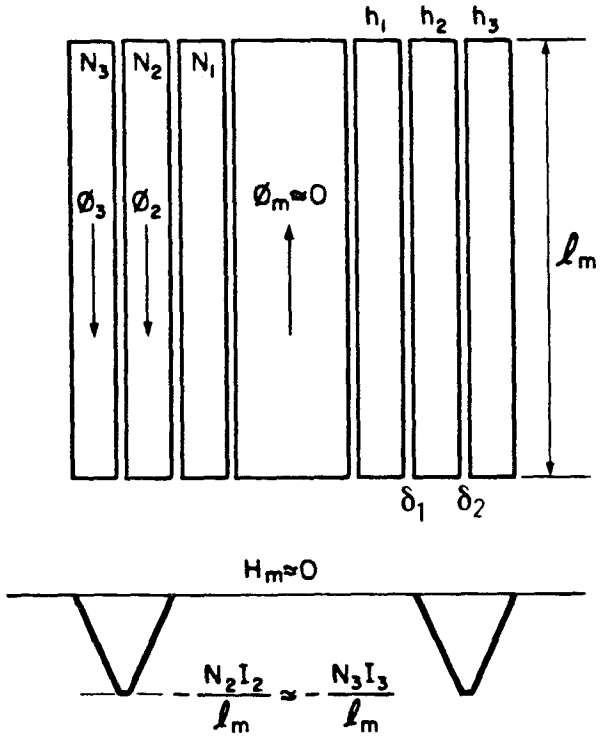

Fig. 10.6 Field intensity in three-winding toroid with the primary open and the secondary shorted.

Finally, it may be noted from the electric circuit model in Fig. 10.4b that there is no leakage inductance element in series with N_2, which is because, physically, N_2 is "sandwiched" between N_1 and N_3, as illustrated in Fig. 10.1. Therefore, any flux enclosed by N_2 is also approximately enclosed by either N_1 or N_3.

However, the energy storage capability of N_2 is represented in the electric circuit model by ℓ_{12}, and ℓ_{23}'. For example, if N_3 is left open, ℓ_{12} simply becomes the leakage inductance between N_1 and N_2. If N_1 is open, ℓ_{23}' is the leakage inductance between N_2 and N_3. This is also reflected in the expressions for ℓ_{12} and ℓ_{23}'.

10.1.2 Three-Winding Bobbin Core Arrangements

Side-by Side-Arrangement

Figure 10.7 illustrates a three-winding extension of the side-by-side arrangement discussed in Chapter 9. Again, the general case occurs when a spacer gap is used as illustrated in the figure. The field intensity and the flux pattern inside the structure are determined in the same way as the previous examples. The result is illustrated in Fig. 10.8.

The flux equations based on the flux pattern in Fig. 10.8 are given by

$$\phi_{N1} = \phi_c \tag{10.12}$$

$$\phi_{N2} = \phi_c - (\phi_1 + \phi_2) \tag{10.13}$$

$$\phi_{N3} = \phi_c - (\phi_1 + \phi_2 + \phi_3) \tag{10.14}$$

$$\phi_c = \phi_o + \phi_1 + \phi_2 + \phi_3 \tag{10.15}$$

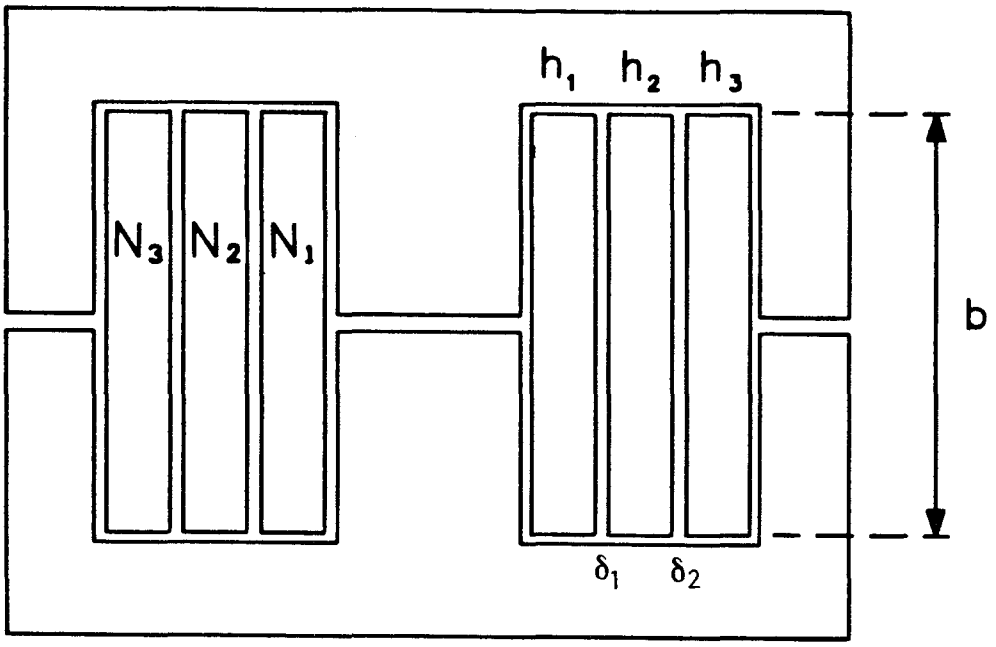

Fig. 10.7 Three-winding side-by-side arrangement.

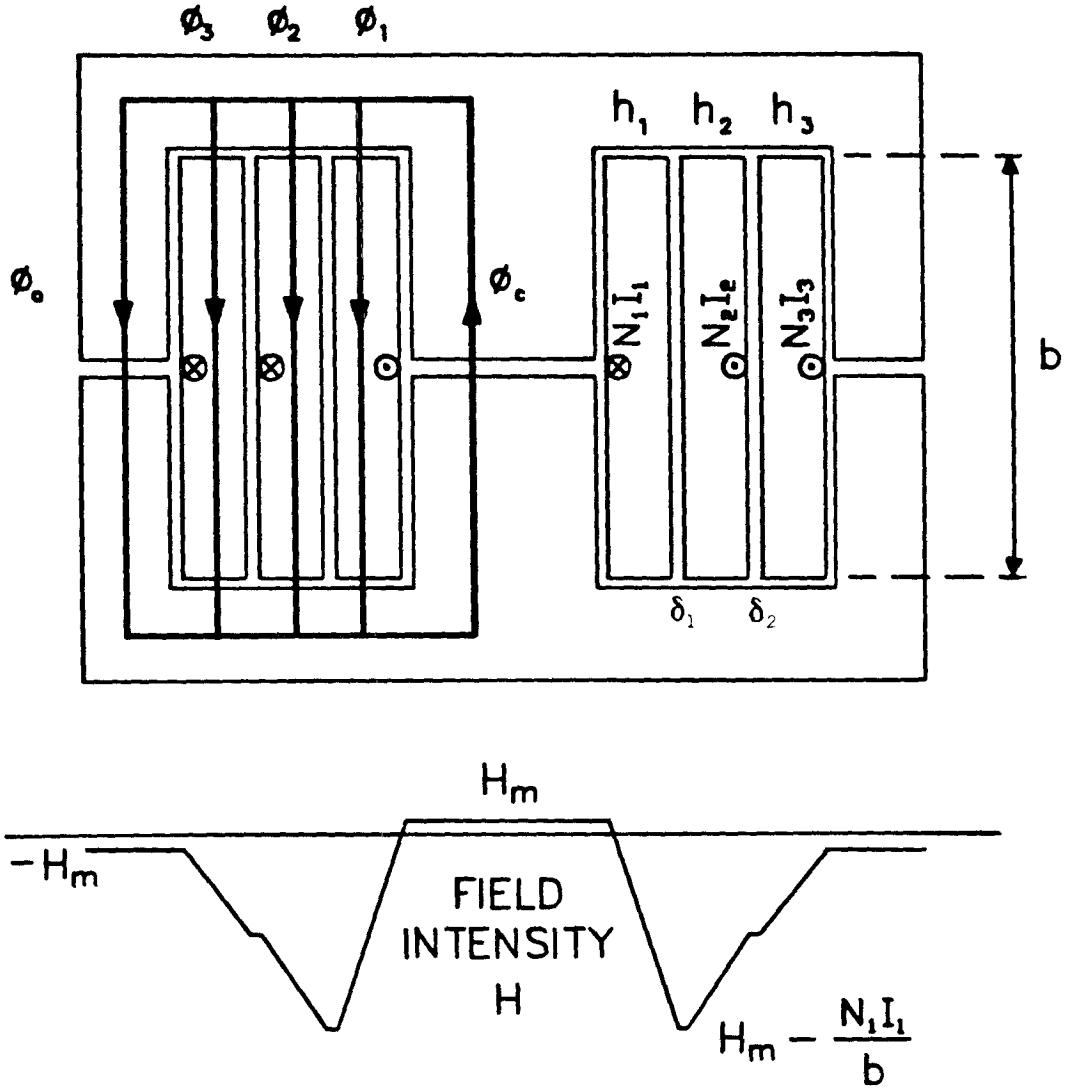

Fig. 10.8 Field intensity and flux pattern inside three-winding side-by-side structure. Also illustrated are the infinitely small sources of mmf N_1I_1, N_2I_2 and N_3I_3.

Substitution of Eq. (10.15) into Eqs. (10.12) through (10.14) gives the additional equations

$$\phi_{N1} = \phi_o + \phi_1 + \phi_2 + \phi_3 \tag{10.16}$$

$$\phi_{N2} = \phi_o - \phi_3 \tag{10.17}$$

$$\phi_{N3} = \phi_o \tag{10.18}$$

Equations (10.12) through (10.18) are used to construct the reluctance model illustrated in Fig. 10.9. The corresponding electric circuit model is shown in Fig. 10.10a and can be rearranged as in Fig. 10.10b.

The inductance L_c in the electric circuit model corresponds to the center leg gap and is given by Eq. (9.16). Similarly, L_o represents the inductance of the outer legs and is given by Eq. (9.17).

The leakage inductance elements ℓ_{12} and ℓ_{23}' can be estimated in a similar way as the leakage elements in the three-winding toroid previously discussed. For example, ℓ_{12} is the leakage inductance between the primary N_1 and the secondary N_2, which is basically the same as the leakage inductance of the two-winding side-by-side arrangement given in Eq. (9.19); that is,

$$\ell_{12} = 2\pi\mu_o N_1^2 \frac{1}{b}\left[h_1\left(\frac{r_o}{3} + \frac{h_1}{4} \right) + \delta_1\left(r_o + h_1 + \frac{\delta_1}{2} \right) + h_2\left(\frac{r_o + h_1 + \delta_1}{3} + \frac{h_2}{12} \right) \right] \tag{10.19}$$

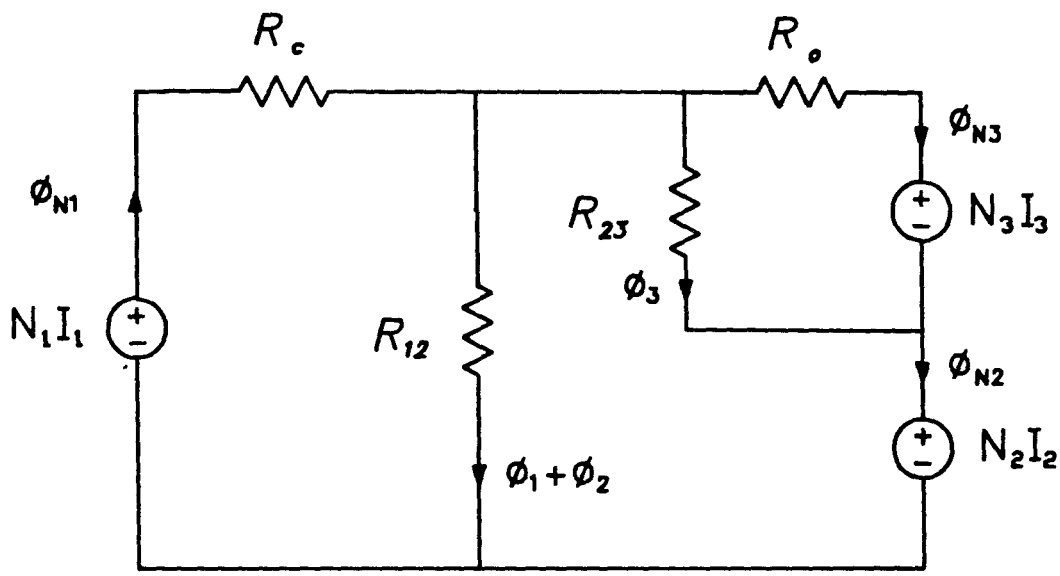

Fig. 10.9 Reluctance model for three-winding side-by-side arrangement.

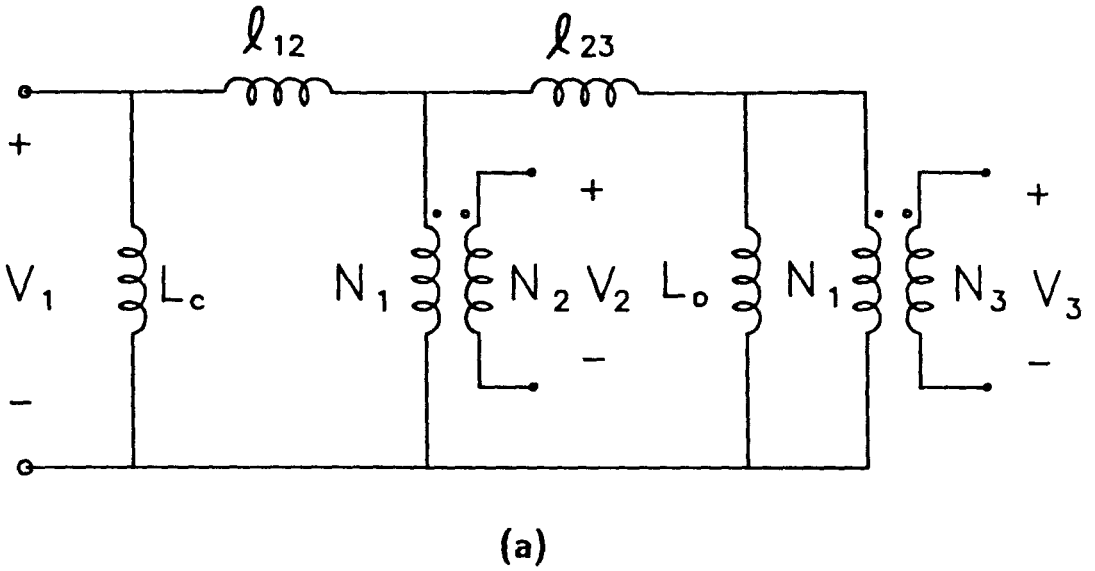

(a)

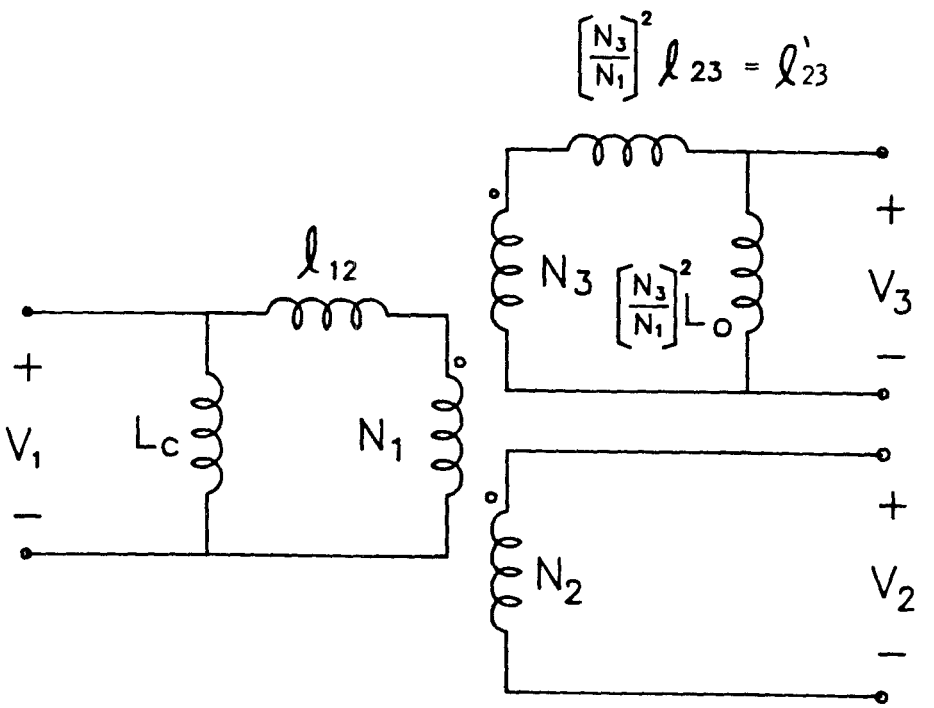

(b)

Fig. 10.10 (a) Electric circuit model for three-winding side-by-side arrangement. By reflecting the inductances L_o and ℓ_{23} to N3, the electric circuit model can be rearranged as shown in (b).

The leakage inductance ℓ_{23}' in Fig. 10.10b represents the energy storage capabilities of N_2 and N_3. It can be computed by opening the primary N_1, shorting the secondary N_2, and exciting N_3 with a current source as shown in Fig. 10.11. Evaluation of the total energy stored in ℓ_{23}' gives

$$\ell_{23}' = 2\pi\mu_o N_3^2 \frac{1}{b}\left[h_2\left(\frac{r_o + h_1 + \delta_1}{3} + \frac{h_2}{4} \right) + \right.$$

$$+ \delta_2\left(r_o + h_1 + \delta_1 + h_2 + \frac{\delta_2}{2} \right) +$$

$$\left. + h_3\left(\frac{r_o + h_1 + \delta_1 + h_2 + \delta_2}{3} + \frac{h_3}{12} \right) \right] \qquad (10.20)$$

If $h_1=h_2=h_3=h/3$, and δ_1, $\delta_2 \ll h$, Eqs. (10.19) and (10.20) reduce to

$$\ell_{12} = \frac{4}{9}\pi\mu_o N_1^2 \frac{h}{b}(r_o + h/3) \qquad (10.21)$$

$$\ell_{23}' = \frac{4}{9}\pi\mu_o N_3^2 \frac{h}{b}(r_o + 2h/3) \qquad (10.22)$$

The similarities between these two equations and the equations for the leakage parameters of the three-winding toroid, Eqs. (10.10) and (10.11), are due to the similarities of the windings arrangement in both cases, the stretched three-winding toroid (Fig. 10.2), and the three-winding side-by-side arrangement (Fig. 10.7). Note that in this case also, there is no leakage inductance element in series with the "sandwiched" winding N_2, but as before, the energy storage capability of N_2 is represented in the circuit model by ℓ_{12}, and ℓ_{23}'.

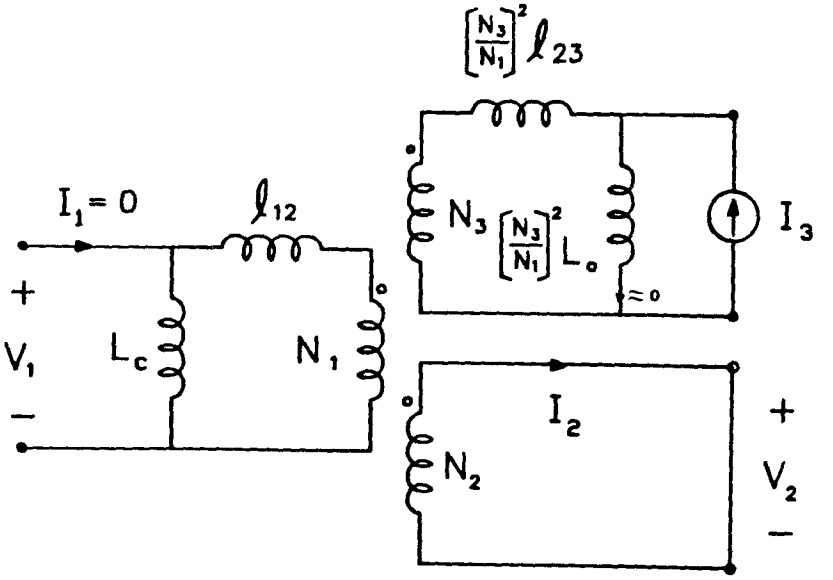

Fig. 10.11 With the primary open and the secondary N_2 shorted, all the energy from the current source I_3 is approximately stored in ℓ_{23}'. This condition can be used to estimate the value of the leakage inductance ℓ_{23}'.

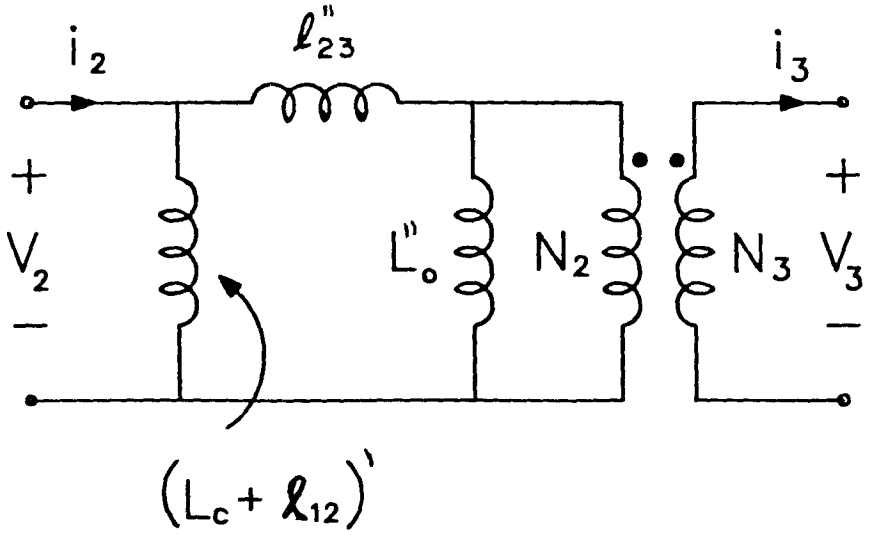

Fig. 10.12 Reduced electric circuit model between N_2 and N_3 with N_1 open.

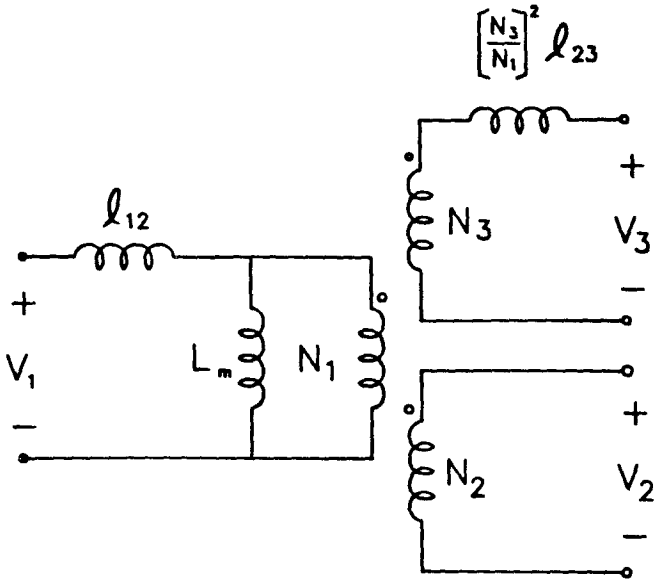

Fig. 10.13 Approximate electric circuit model for ungapped three-winding side-by-side arrangement.

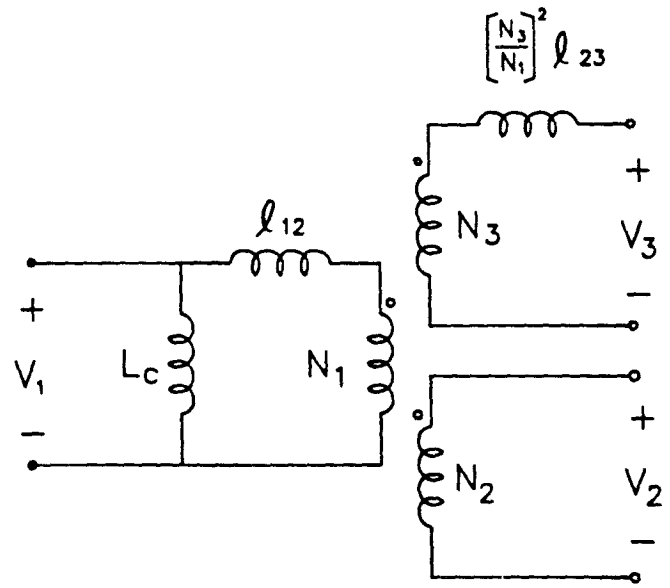

Fig. 10.14 Electric circuit model for three-winding side-by-side arrangement with a center leg gap.

Also, if either winding is left open, the electric circuit model between the other two windings is reduced to a circuit similar to the one in Fig. 9.8, i.e., the electric circuit model for a two-winding side-by-side arrangement.

For example, if N_1 is left open, the electric circuit model between N_2 and N_3 is reduced to the one in Fig. 10.12, where

$$(L_c + \ell_{12})' = \left(\frac{N_2}{N_1} \right)^2 (L_c + \ell_{12}) \tag{10.23}$$

$$\ell_3'' = \left(\frac{N_2}{N_1} \right)^2 \ell_3 \tag{10.24}$$

and

$$L_o'' = \left(\frac{N_2}{N_1} \right)^2 L_o \tag{10.25}$$

Some special cases of this arrangement are the ungapped and the center leg gapped cores. The corresponding electric circuit model for each of these cases is illustrated in Fig. 10.13 and 10.14.

Three-Winding Top-Bottom Arrangement

One possible three-winding extension of the two-winding arrangement in Fig. 9.16 is illustrated in Fig. 10.15. The method for obtaining the physical model for this arrangement is straightforward and follows the same path of all the previous cases. The electric circuit model (physical model) is illustrated in Fig. 10.16a and can be rearranged as shown Fig. 10.16b.

The expressions for the leakage inductance parameters in the circuit model are given by

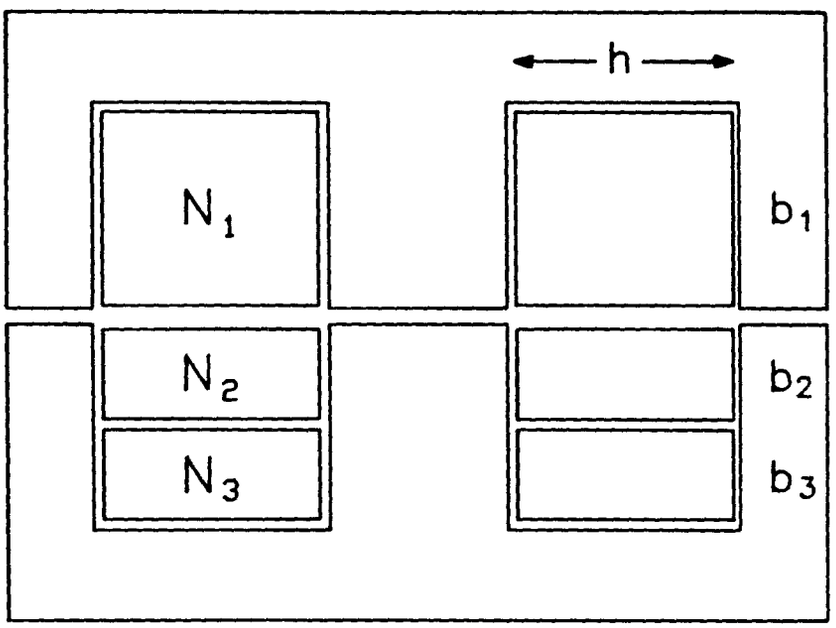

Fig. 10.15 Three-winding top-bottom arrangement.

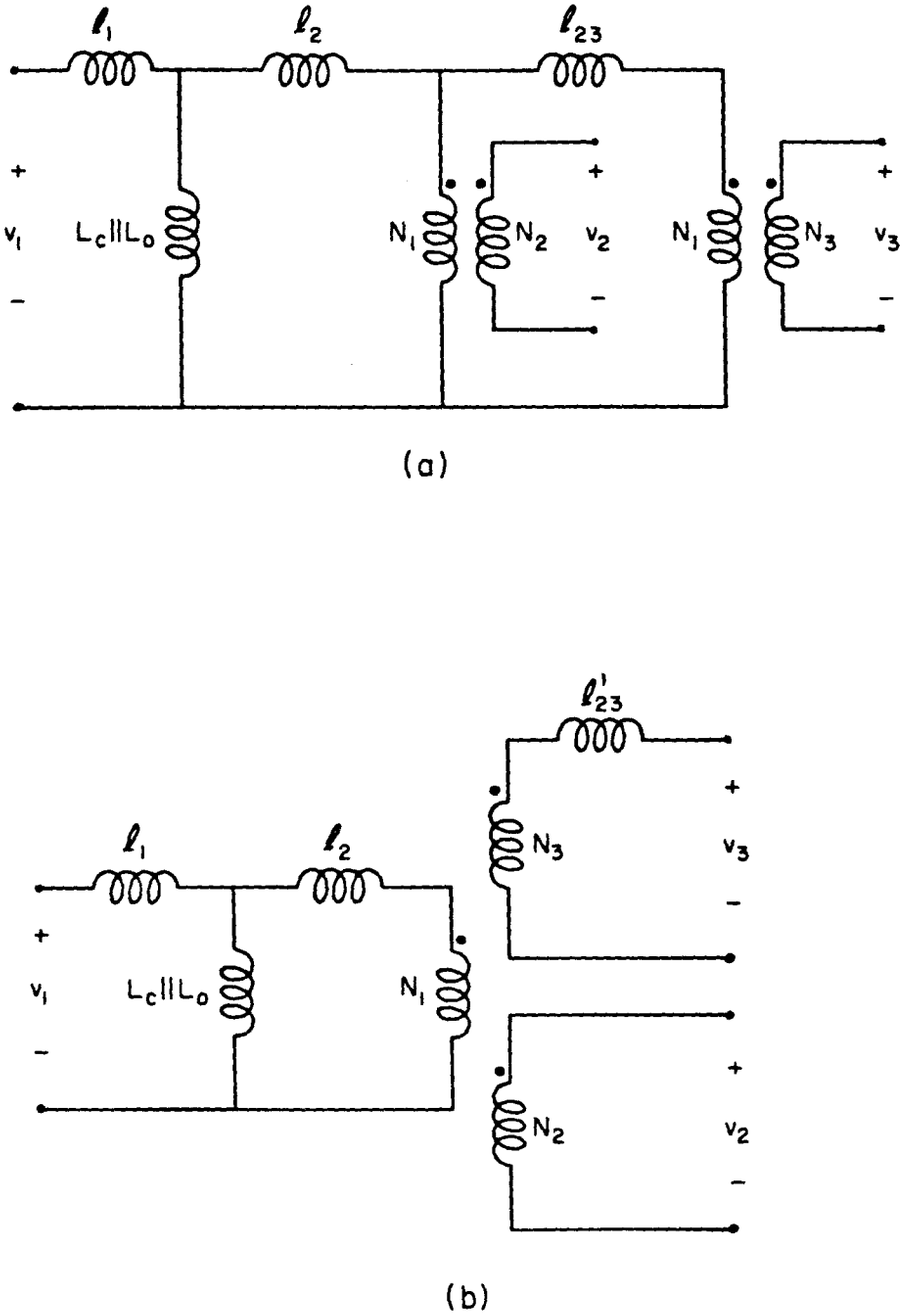

Fig. 10.16 The electric circuit model for the three-winding top-bottom arrangement in (a) can be easily rearranged as shown in (b) by reflecting ℓ_{23} to N3.

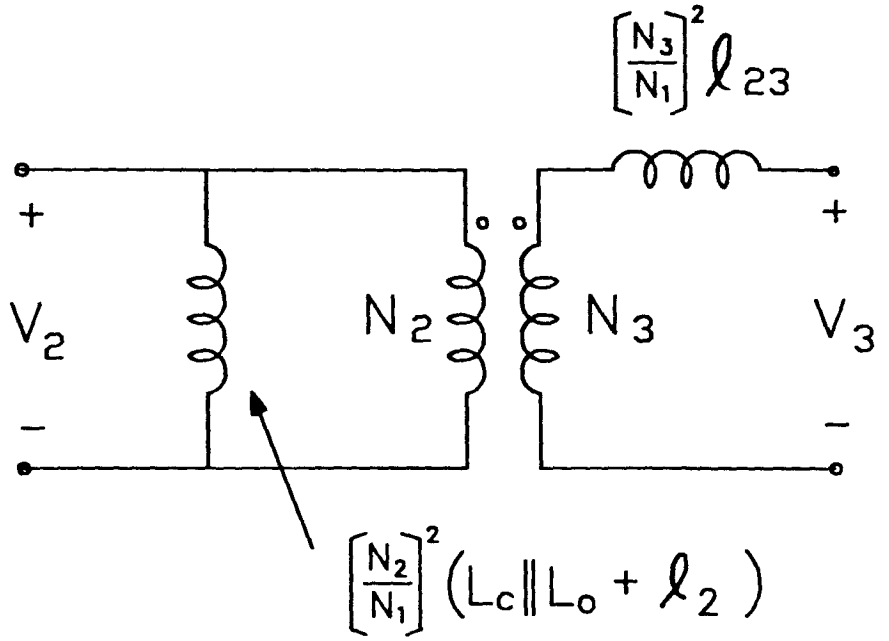

Fig. 10.17 Reduced electric circuit model between N_2 and N_3 with the primary open.

$$\ell_1 = \frac{\mu_o}{3} N_1^2 \frac{b_1}{h} MLT \tag{10.26}$$

$$\ell_2 = \frac{\mu_o}{3} N_1^2 \frac{b_2}{h} MLT \tag{10.27}$$

$$\ell_{23}' = \frac{\mu_o}{3} N_3^2 \frac{b_2 + b_3}{h} MLT \tag{10.28}$$

The inductances L_c and L_o are, once more, the inductances of the center and outer leg gaps, respectively.

Owing to the asymmetry of the winding positions with respect to that of the gaps, the circuit models between any pair of windings are not necessarily similar. For example, the reduced electric circuit model between N_1 and N_2, with N_3 open, is similar to the circuit model of the two-winding arrangement in Fig. 9.16, which is given in Fig. 9.19. However, the reduced electric circuit model between N_2 and N_3 with N_1 open (Fig. 10.17) is not similar to the one in Fig. 9.19. This is because the relative positions of the windings with respect to the gaps are not similar for these cases.

Note that the gaps are between N_1 and N_2 but not between N_2 and N_3. In the same way, one can also say that the gaps are positioned between N_1 and N_3; therefore, the electric circuit model between N_1 and N_3 with N_2 open should be similar to the model of the two-winding top-bottom arrangement in Fig. 9.19. This is easily verified by inspection of the electric circuit model in Fig. 10.16b.

10.2 Four-Winding Magnetic Structures

The four-winding extensions of the side-by-side and the top-bottom arrangements are illustrated in Figs. 10.18a and 10.19a. The

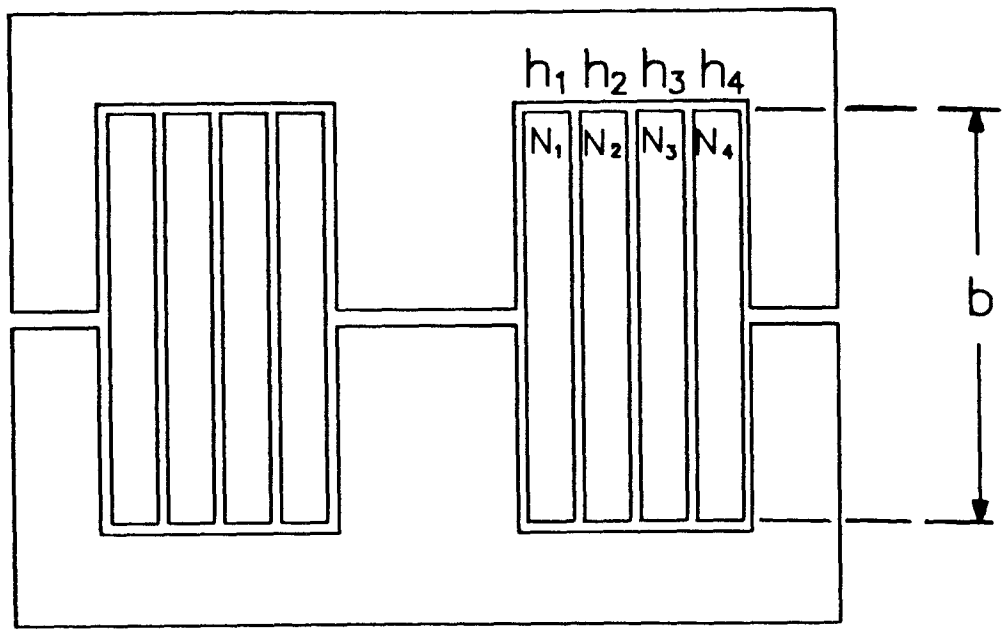

(a)

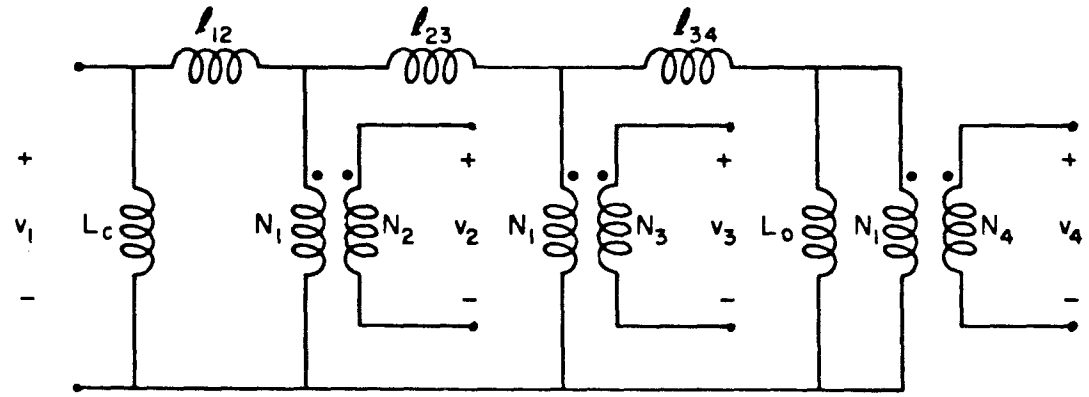

(b)

Fig. 10.18 Four-winding extension of the side-by-side arrangement (a) and the corresponding electric circuit model (b).

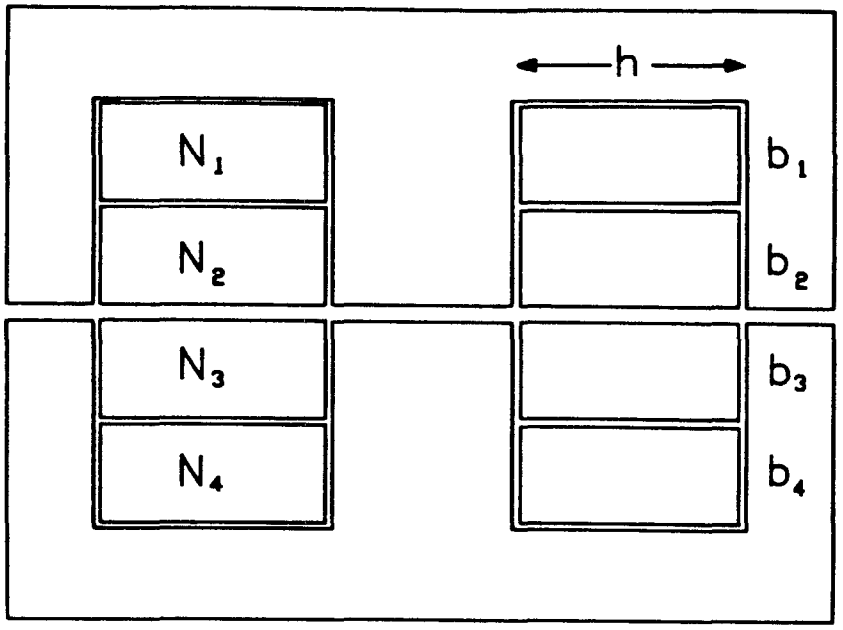

(a)

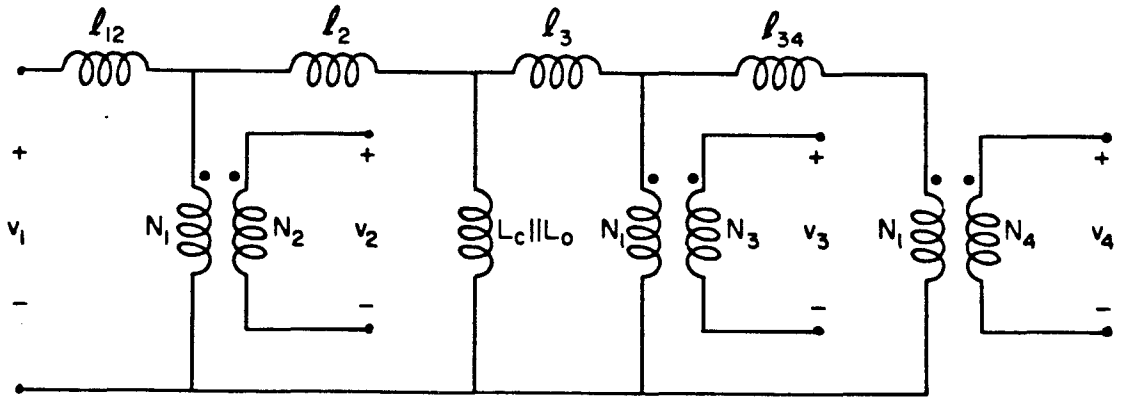

(b)

Fig. 10.19 Four-winding extension of the top-bottom arrangement (a) and the corresponding electric circuit model (b). Note the symmetry of the electric circuit model around the inductance $L_c \| L_o$. This is due to the physical symmetry of the arrangement in (a) with respect to the position of the gaps, which are represented in the circuit by L_c and L_0.

electric circuit models (physical models) for each of these arrangements are shown in Figs. 10.18b and 10.19b. The process for determination of these models is the same one used in all the previous cases.

The expressions for the leakage parameters of the four-winding side-by-side arrangement in Fig. 10.18 are given by

$$\ell_{12} = 2\pi\mu_o N_1^2 \frac{1}{b}\left[h_1\left(\frac{r_o}{3} + \frac{h_1}{4} \right) + h_2\left(\frac{r_o+h_1}{3} + \frac{h_2}{12} \right) \right] \tag{10.29}$$

$$\ell_{23} = 2\pi\mu_o N_1^2 \frac{1}{b}\left[h_2\left(\frac{r_o+h_1}{3} + \frac{h_2}{4} \right) + h_3\left(\frac{r_o+h_1+h_2}{3} + \frac{h_3}{12} \right) \right] \tag{10.30}$$

$$\ell_{34} = 2\pi\mu_o N_1^2 \frac{1}{b}\left[h_3\left(\frac{r_o+h_1+h_2}{3} + \frac{h_3}{4} \right) + h_4\left(\frac{r_o+h_1+h_2+h_3}{3} + \frac{h_4}{12} \right) \right] \tag{10.31}$$

where the spaces between the windings were neglected but, in general, can be accounted for in the usual way.

Similarly, the expressions for the leakage parameters of the four-winding top-bottom arrangement in Fig. 10.19 are given by

$$\ell_{12} = \frac{\mu_o}{3} N_1^2 \frac{b_1 + b_2}{h} \text{ MLT} \tag{10.32}$$

$$\ell_2 = \frac{\mu_o}{3} N_1^2 \frac{b_2}{h} \text{ MLT} \tag{10.33}$$

$$\ell_3 = \frac{\mu_o}{3} N_1^2 \frac{b_3}{h} \text{ MLT} \tag{10.34}$$

$$\ell_{34} = \frac{\mu_o}{3} N_1^2 \frac{b_3 + b_4}{h} \text{ MLT} \tag{10.35}$$

Further extensions of these arrangements are possible and are, in general, treated the same way as in all the previous cases. The general results are similar, and further investigations of these give no additional qualitative information.

10.3 Examples

The first example is a three-winding side-by-side arrangement on a large P-4229 ferrite pot core with a 1.4 mm spacer gap. The three windings are of the same width, and the separations between them are negligible.

The dimensions of the windings and the core are

$$\begin{aligned} &N_1 = 56,\ N_2 = 55,\ N_3 = 53 \\ &h = .26 \text{ cm} \\ &b = 1.8 \text{ cm} \\ &r_o = 1 \text{ cm} \\ &S_c = 2.23 \text{ cm}^2 \\ &S_o = 3.85 \text{ cm}^2 \end{aligned} \tag{10.36}$$

The predicted electric circuit model values obtained by substitution of these values into Eqs. (10.20), (10.21), (9.16) and (9.17) are shown in Fig. 10.20a.

The measurements for three- and four-winding structures are more complicated because of the additional windings, and if the process of open and short circuit measurement is followed, the number of equations involved can make the calculations almost hopeless.

To simplify the measurement process, a few assumptions are made. For instance, if a voltage source is connected across the primary N_1,

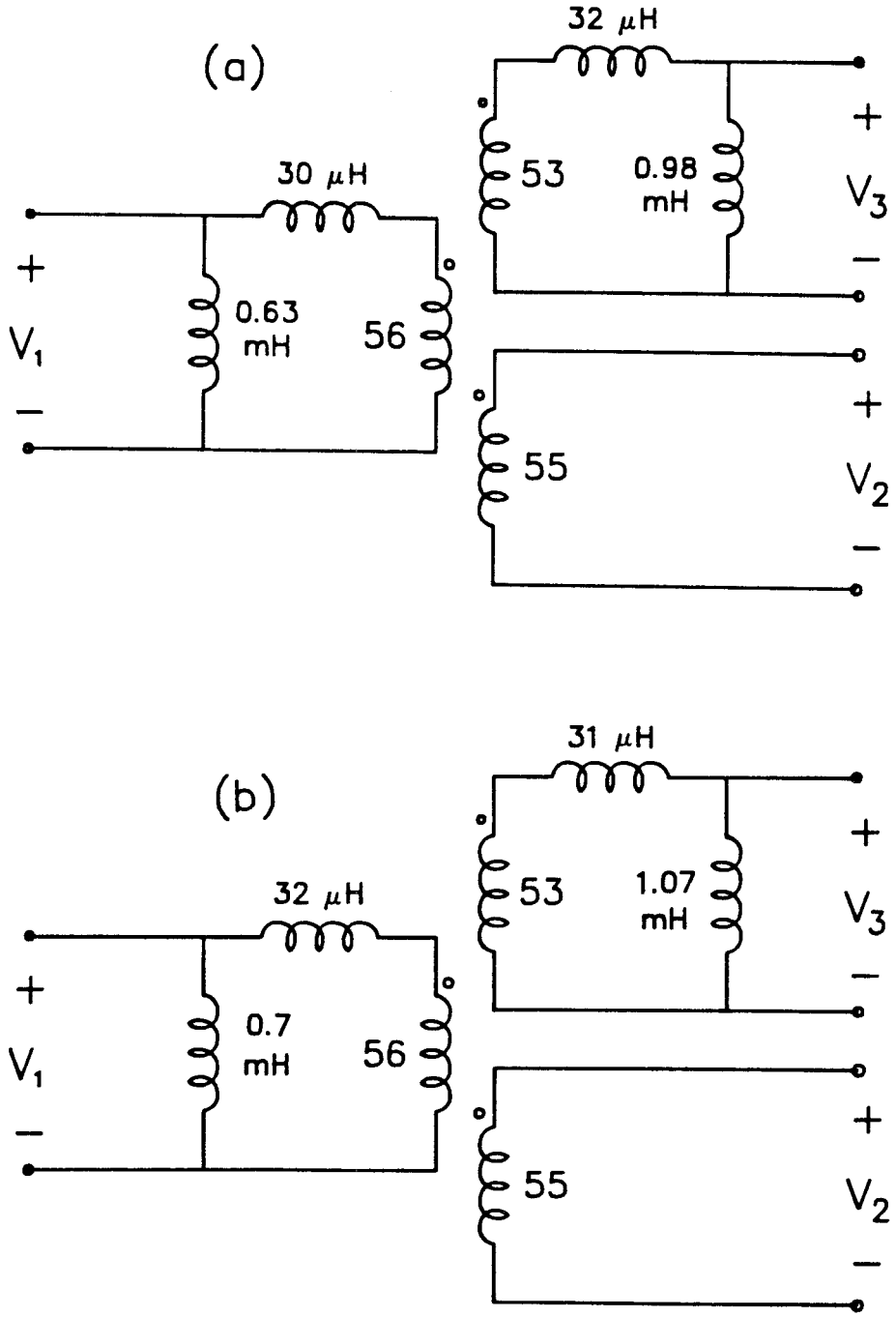

Fig. 10.20 (a) Predicted electric circuit model values for three-winding side-by-side arrangement on a P-4229 pot core with a 1.4 mm spacer gap. (b) Measured electric circuit model.

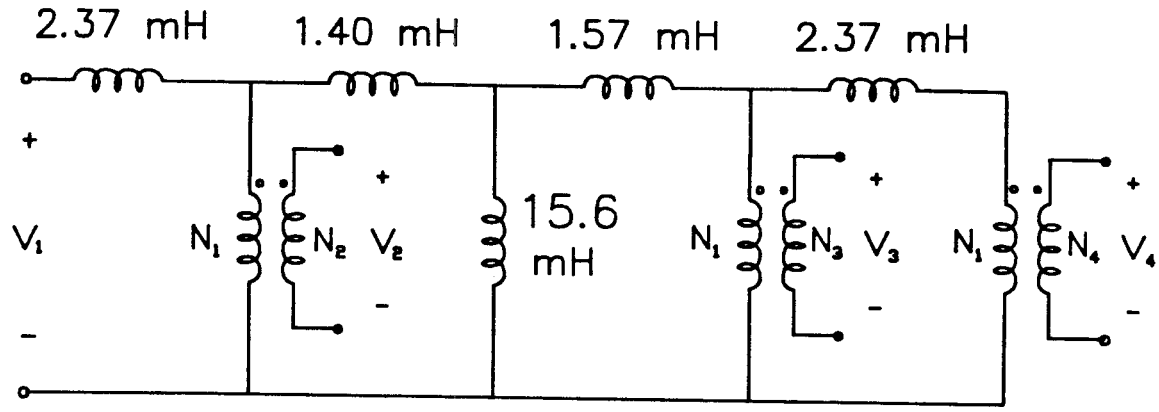

(a)

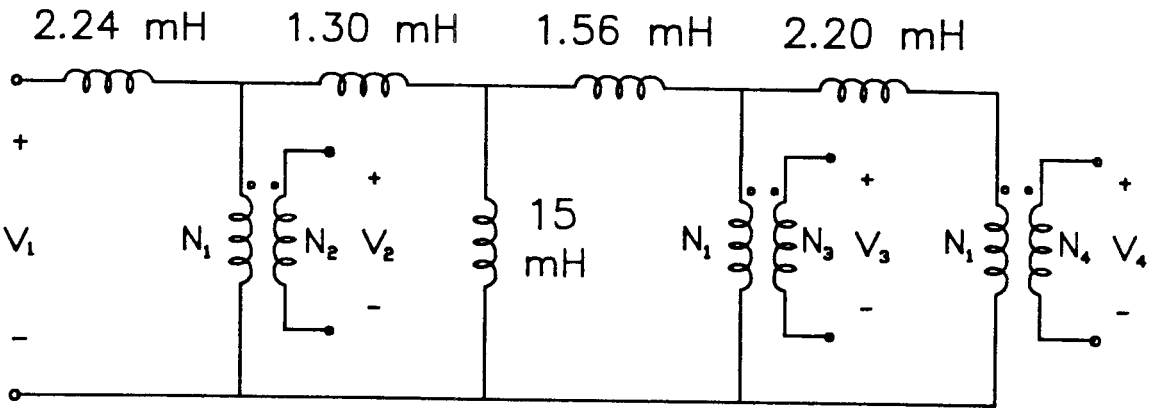

(b)

Fig 10.21 (a) Predicted electric circuit model values for four-winding top-bottom arrangement on a P-4229 pot core with a 0.8 mm spacer gap. (b) Measured electric circuit model.

the open circuit voltage ratio between the other two windings N_2 and N_3 is, from the circuit in Fig. 10.10b,

$$\frac{v_3}{v_2} = \frac{N_3}{N_2} \frac{L_o}{L_o + \ell_{23}} \tag{10.37}$$

which from the predicted circuit model in Fig. 10.21a gives

$$\frac{v_3}{v_2} = 0.94 \tag{10.37}$$

The actual measured voltage ratio is approximately 0.95. The error between the measured and the predicted value is very small. Since this is the case in all the other similar voltage ratio measurements made on multiple-winding structures, it is assumed that the turns (N_1, N_2, N_3, etc.) of the ideal transformers in the measured electric circuit models are equal to those in the predicted ones. This simplifies the measurement process and does not introduce significant errors.

In any case, the extra number of measurements that can be performed on the circuit and are not needed for determination of the inductance parameters, are used to verify that the ideal turns assumptions do not introduce significant errors on the measurements.

The electric circuit model parameter values for the three-winding pot core derived from a number of open and shorted circuit impedance measurements are illustrated in Fig. 10.20b.

A second example is a four-winding top-bottom arrangement such as that in Fig. 10.19a. A P-4229 ferrite pot core with a 0.8 mm

spacer gap was also used in this example. The predicted and measured electric circuit models are illustrated in Fig. 10.21.

In both examples, the three-winding side-by-side and the four-winding top-bottom arrangements, the measurements compare favorably with the predictions. The ideal turns assumptions for the the measured circuit models did not introduce significant errors in either case.

10.4 Conclusions

The physical models of the three- and four-winding extensions of the two-winding toroid, the side by side and top-bottom bobbin core arrangements, were obtained using the same modelling method previously used in the two-winding cases.

The physical model of these multiple-winding structures illustrates how these models can approximately predict the correct distribution of the leakage energy in the windings, and how the different gaps and their relative positions in the core are represented in the electric circuit model.

It is also illustrated how, if some of the windings of a multiple-winding configuration are left open, the electric circuit model between the other windings is the same that would be obtained on a similar arrangement where the open windings are not present.

CHAPTER 11

SPECIAL WINDING TECHNIQUES

11.1 Introduction

In the previous chapters some conventional winding arrangements that are commonly used in transformers as well as in coupled inductor applications are discussed. Sometimes, however, it is necessary to use a special winding technique to achieve a better performance.

For example, it is possible that in a low leakage transformer design, neither of the configurations discussed in Chapters 8 or 9 meets the requirements of the design. In this case, a special winding technique that minimizes the leakage inductance of the transformer must be used.

Similarly, a coupled inductor application might require more leakage inductance than that already "built into" some of the configurations previously discussed. In this case, a winding technique that maximizes the amount of leakage inductance should be used.

This chapter reviews some special winding techniques for minimizing the leakage inductance in transformers, investigating why and how they work, and how they can be modelled.

Also, one of the arrangements discussed in the previous chapters is demonstrated to be a very good candidate for high-leakage coupled inductor designs.

11.2 Minimization of Leakage Inductance in Two-Winding Transformers

Chapter 4 illustrates how the leakage inductance of the isolation transformer in a switching power supply can have severe adverse effects on the converter's operation.

This is the main reason why in a switching converter, where an isolation transformer is used, the leakage inductance of the transformer is kept at the minimum possible.

Several winding techniques that minimize the leakage inductance in transformers have been developed in the past. They are all based on the fact that the amount of leakage energy in a winding is directly associated with the magnitude of the magnetic field inside the winding.

That is,

$$E = \frac{\mu_o}{2} \iiint H^2 \, dv \qquad (11.1)$$

where E is the energy stored in the winding, and H is the field intensity inside the volume of the winding.

Consequently, any winding technique that minimizes the field intensity in the windings will also minimize the leakage energy, i.e., the leakage inductance of the transformer.

Some of the special winding techniques that minimize magnetic leakage in transformers are investigated in this section.

11.2.1 Sectionalized Windings

A simple way to reduce the field intensity throughout the windings of a magnetic structure is to break the windings into smaller sections. The sections of one winding are then *interleaved* with sections of the other winding.

The proximity of conductors carrying current in opposite directions reduces effectively the magnetic field intensity inside the windings.

For example, the windings of the two-winding transformer in Fig. 11.1a can be sectionalized as shown in Fig. 11.2a. The primary and the secondary windings have been broken into two sections each. The field intensity throughout the windings of the sectionalized transformer in Fig. 11.2a is illustrated in Fig. 11.2b, which should be compared to the field intensity plot for the non-sectionalized case illustrated in Fig. 11.1b. Because of the sectionalization of the windings the field intensity is considerably reduced.

The electric circuit model for the non-sectionalized arrangement in Fig. 11.1a is given in Chapter 9 and is illustrated in Fig. 9.12. The expression for the leakage inductance ℓ_n is given by

$$\ell_n = \frac{2}{3}\pi\mu_o N_1^2 \frac{h}{b}(r_o + h/2)$$

$$= \frac{1}{3}\mu_o N_1^2 \frac{h}{b} MLT \qquad (11.2)$$

where $MLT=2\pi(r_o + h/2)$.

The electric circuit model for the sectionalized transformer in Fig. 11.2a can be obtained simply by assuming that this transformer is

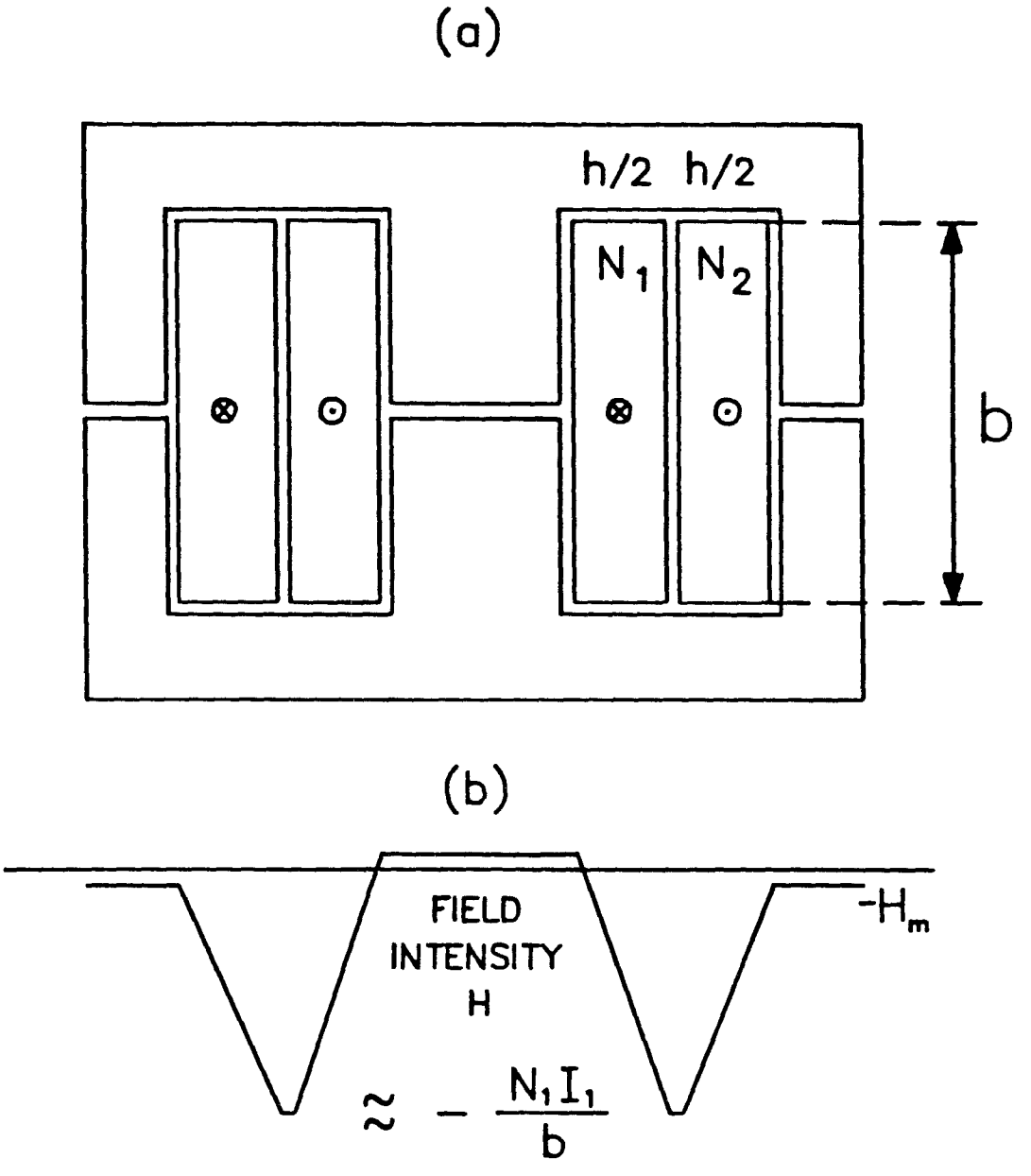

Fig 11.1 Two-winding side-by-side arrangement (a) and approximate field intensity through the windings (b).

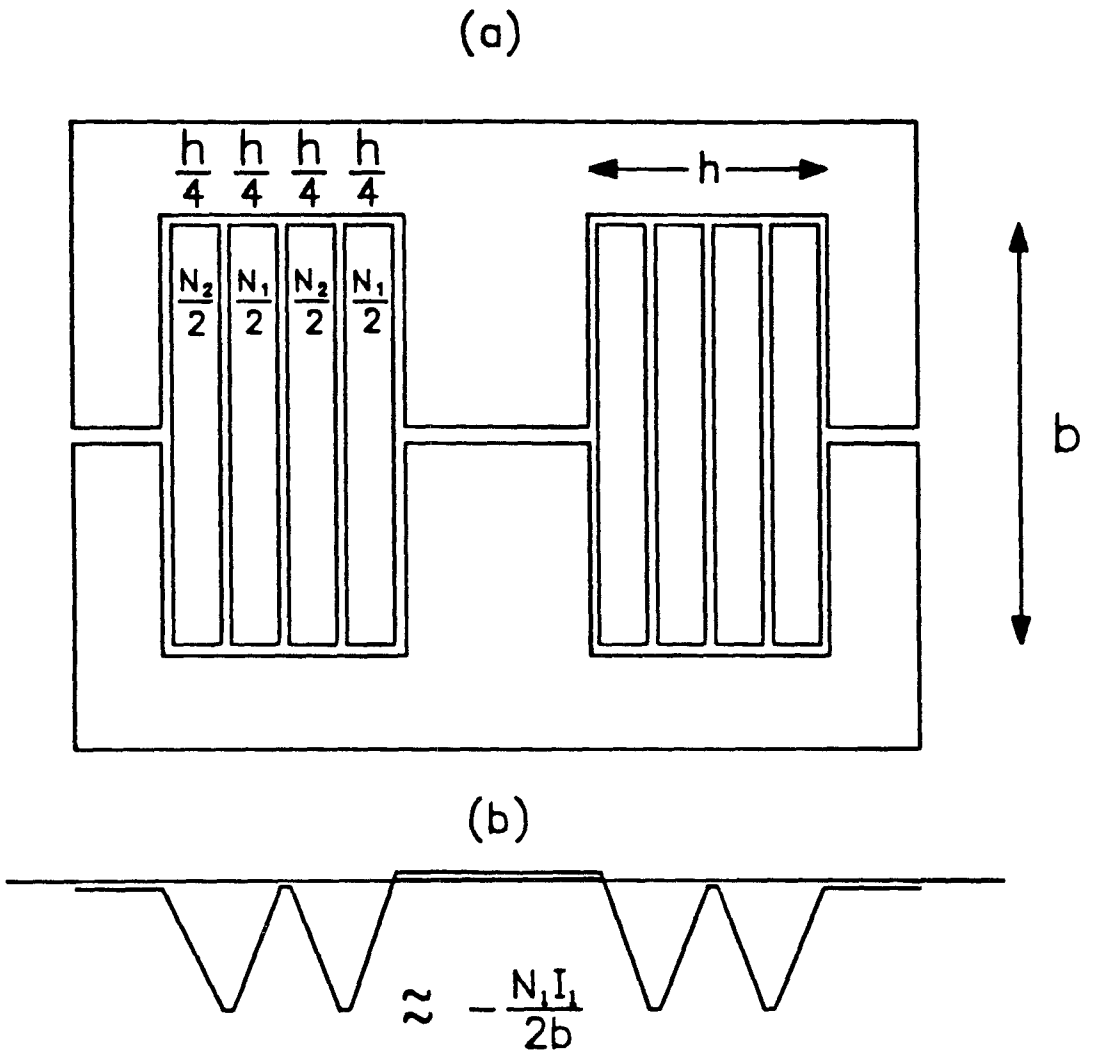

Fig. 11.2 The primary and the secondary of the transformer in Fig. 11.1 can be sectionalized as shown in (a). The two sections of the primary are interleaved with the two sections of the secondary, effectively reducing the field intensity (b) throughout the windings.

a four-winding structure with a side-by-side arrangement. This case is similar to that discussed in Chapter 10. The electric circuit model is obtained in the same way and is shown in Fig. 11.3a.

The different windings in the electric circuit model in Fig. 11.3a represent the four sections of the transformer in Fig. 11.2a, which are physically connected inside the structure. Therefore, the end points of each section of each winding in the electric circuit model in Fig. 11.3a should be similarly connected at the appropriate ends. This is illustrated in Fig. 11.3b.

Careful examination of the electric circuit model in Fig 11.3b shows that under the assumption L_c, L_o >>> ℓ_{12}, ℓ_{23}, ℓ_{34}, the current through the leakage inductance element ℓ_{23}, is almost zero. Therefore, the circuit model in Fig. 11.3b can be reduced to the more familiar circuit in Fig. 11.3c, where

$$\ell_s = \ell_{12} + \ell_{34} \tag{11.3}$$

The leakage inductances ℓ_{12} and ℓ_{34} are estimated in the same way as before, and are given by

$$\ell_{12} = 2\pi\mu_o \frac{N_1^2}{4} \frac{1}{b} \left[h_1 \left(\frac{r_o}{3} + \frac{h_1}{4} \right) + h_2 \left(\frac{r_o+h_1}{3} + \frac{h_2}{12} \right) \right] \tag{11.4}$$

$$\ell_{34} = 2\pi\mu_o \frac{N_1^2}{4} \frac{1}{b} \left[h_3 \left(\frac{r_o+h_1+h_2}{3} + \frac{h_3}{4} \right) + h_4 \left(\frac{r_o+h_1+h_2+h_3}{3} + \frac{h_4}{12} \right) \right] \tag{11.5}$$

Substitution of Eqs. (11.4) and (11.5) into (11.3), and assuming $h_1=h_2=h_3=h_4=h/4$, result in

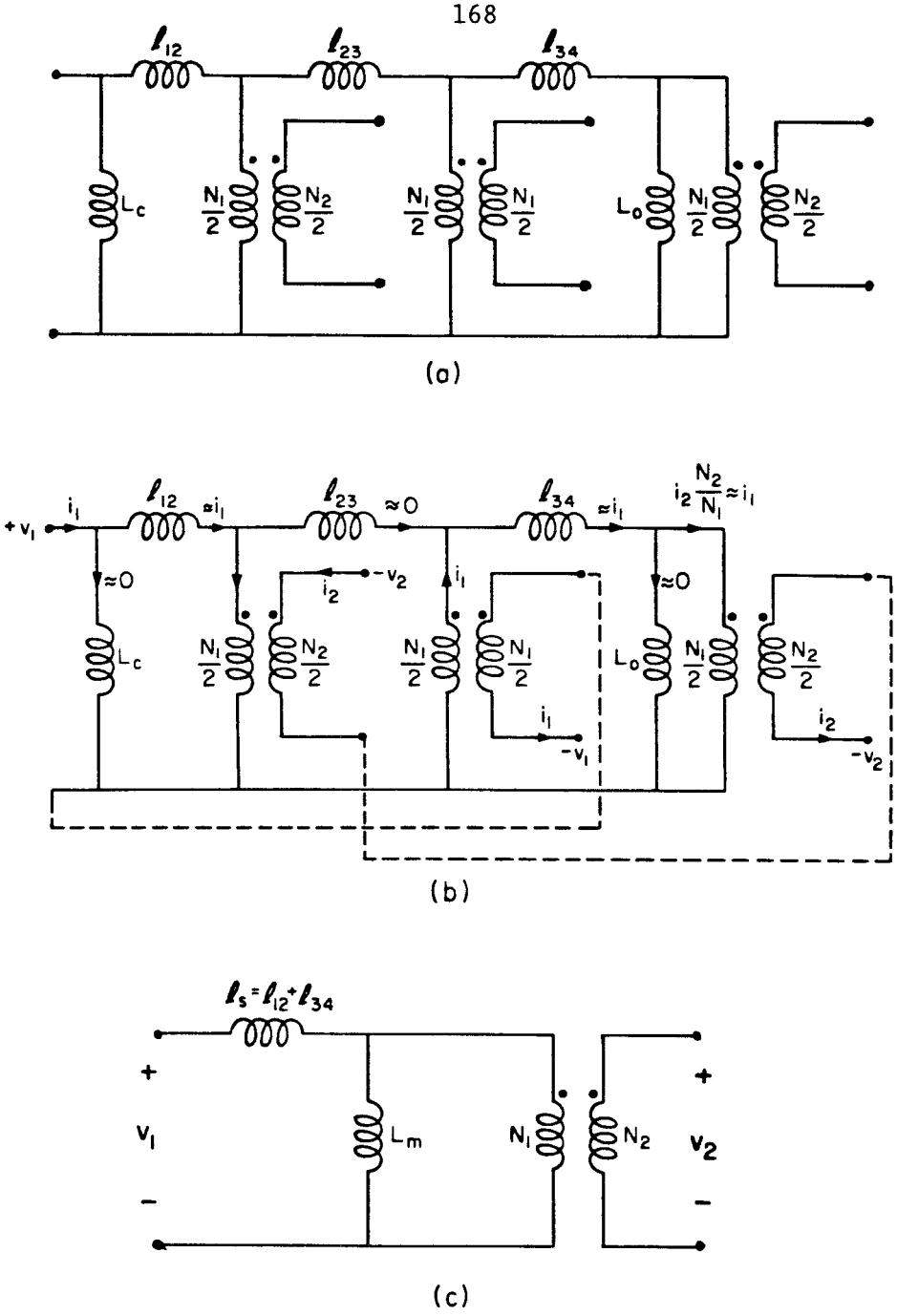

Fig. 11.3 The "windings" in the electric circuit model in (a) represent the different sections of the sectionalized transformer in Fig. 11.2a. Since the end points of the two sections of each winding are connected, similar connections are made on the electric circuit model (b). Examination of the circuit model in (b) shows that the current through ℓ_{23} is approximately zero. Therefore, the circuit model in (b) can be reduced to the simple model in (c).

$$\ell_s = \frac{1}{6} \pi \mu_o N_1^2 \frac{h}{b} (r_o + h/2)$$

$$= \frac{1}{12} \mu_o N_1^2 \frac{h}{b} MLT \qquad (11.6)$$

where $MLT=2\pi(r_o + h/2)$.

This is the same result that is obtained if the leakage inductance ℓ_s is evaluated using

$$\ell_s = \frac{\mu_o}{I_1^2} \iiint H^2 dv \qquad (11.7)$$

where H is the field intensity throughout the windings given in Fig. 11.2b with $H_m \approx 0$.

Comparison of the expressions for the leakage inductance of the non-sectionalized arrangement ℓ_n (Eq. (11.2)) against that of the sectionalized case ℓ_s (Eq. (11.6) gives

$$\ell_s = \frac{\ell_n}{4} \qquad (11.8)$$

Therefore, by sectionalization of the windings as shown in Fig. 11.2a, the leakage inductance of the transformer is reduced by a factor of 4 with respect to the conventional non-sectionalized case.

This can easily be traced back to the reduction of the field intensity throughout the windings where, as shown in Fig. 11.2b, the peak value of the field intensity H inside the sectionalized windings is half the peak value of the intensity in the non-sectionalized windings (Fig. 11.1b). Since the leakage inductance is a function of

the square of the field intensity, the leakage inductance is reduced by a factor of 4.

This does not constitute a mathematical proof because of the integration steps involved in the determination of the leakage inductance, but the general mathematical proof is simple and need not be demonstrated here.

Further sectionalization of the windings results in further reduction of the leakage inductance of the transformer. The general result for the side-by-side arrangement can be stated as follows.

Assuming that the spaces between the different sections of the windings are negligible (as is usually the case in low leakage transformer designs), and if the windings are sectionalized such that:

1. The absolute value of the peaks of the field intensity are the same throughout all the sections of the windings

and,

2. The peaks are reduced by a factor **K** with respect to the peak value of the field intensity in the non-sectionalized winding arrangement,

the leakage inductance is reduced by a factor of approximately K^2.

For example, if the windings are sectionalized as shown in Fig. 11.4a, where the corresponding field intensity plot is as shown in Fig. 11.4b, the conditions stated above are satisfied, and the reduction of the field intensity peak value with respect to the non-sectionalized arrangement is $K = 4$. Therefore, the leakage inductance ℓ is reduced by a factor of 16.

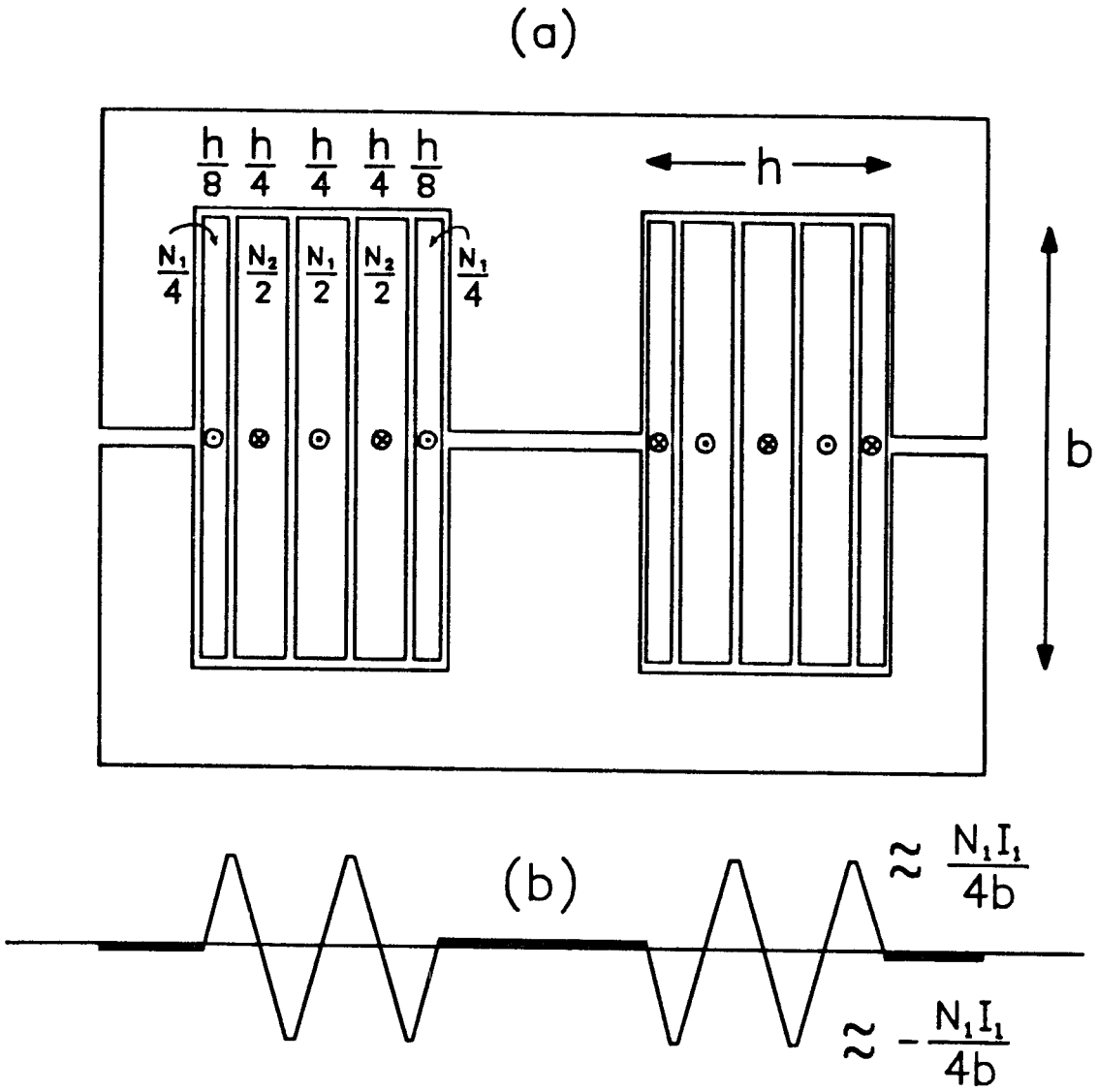

Fig. 11.4 *If the primary of the transformer in Fig. 11.1 is split in three sections and the secondary in two as shown in (a), the absolute value of the peaks in field intensity (b) through the windings are reduced by a factor of 4 with respect to the non-sectionalized case in Fig. 11.1.*

It can also be proven that the largest reduction is obtained when the windings are sectionalized such that the field intensity throughout the windings swings in both directions (positive and negative), with the absolute value of the peaks equal on all sections.

This is why in the example in Fig. 11.4, with five "smartly" selected sections (three for the primary, and two for the secondary), a reduction factor of 16 is achieved, while on the example with four sections in Fig. 11.2, only a reduction factor of four is obtained.

It may be noted that on the example in Fig. 11.2 the field intensity plot (Fig. 11.2b) swings in only one direction, while on the one in Fig. 11.4b (five sections), the field intensity swings in both directions.

11.2.2 Bifilar Foils

The limit of the sectionalization method previously discussed occurs when each section of the winding becomes just one turn. This is what is usually known as bifilar foils arrangement. The reason for the name is that the windings of this arrangement are layers of foils wound bifilarly.

If the separation between the foils is negligible, the peak of the field intensity is 1/b compared to N/b for the non-sectionalized arrangement; therefore, the leakage inductance of the bifilar foils arrangement is reduced by a factor of N^2 with respect to the non-sectionalized arrangement. Therefore, dividing Eq. (11.2) by N_1^2 gives

$$\ell = \frac{1}{3} \mu_o \frac{h}{b} MLT \qquad (11.9)$$

where ℓ is the leakage inductance of the bifilar foils arrangement.

11.2.3 Bifilar Wires

Perhaps the most commonly used low leakage transformer design is the bifilar arrangement where the primary and the secondary are a twisted pair of wires.

The principle is still the same; namely, a reduction of the magnetic field inside the windings yields a reduction of the leakage inductance of the transformer.

In the sectionalized arrangements previously discussed, this reduction is achieved by bringing sections of the primary next to sections of the secondary. This reduces effectively the overall field intensity throughout the windings and therefore, the leakage inductance.

If instead of foils, regular wires are used, the field intensity inside the windings can also be reduced significantly. For instance, the wires can be twisted together all through the length of the windings. The field intensity immediately outside the wires is cancelled by the opposing currents.

Since the field is cancelled by the opposing currents in the wires, and not by the geometric properties of the arrangement, the leakage inductance of the transformer is almost independent of the type of core used. It depends only on the length of the wires and the

separation between them, which on twisted pairs is usually controlled by the thickness of the dielectric that covers the wires.

For example, two meters of twisted wires looped around a toroid have approximately the same leakage inductance as the same two meters of twisted wires around a bobbin core structure.

There is usually a tendency to believe that this technique yields better results than the bifilar foils method. However, because of the better utilization factor of the window area using foils, lower leakage inductances can be obtained with the foils rather than with the usual twisted pair of wires. The price to be paid is the higher cost of thin foils.

11.3 Maximization of Leakage Inductance in Two-Winding Coupled Inductors

Chapter 3 it is illustrates how the leakage inductance of a coupled inductor in a switching application can dramatically improve the performance of the converter by reducing or even eliminating the a.c. ripple currents from the input or the outputs of a switching converter.

For example, if the coupled inductors of the Ćuk converter in Fig. 2.2b are wound on a bobbin core as in Fig. 9.16, the electric circuit model for the coupled inductors is then given by Fig. 9.19, where

$$L_c = \frac{N_1^2}{R_c} = \frac{N_1^2}{\ell_g/\mu_o S_c} \tag{9.16}$$

$$L_o = \frac{N_1^2}{R_o} = \frac{N_1^2}{\ell_g/\mu_o S_o} \tag{9.17}$$

$$\ell_1 = \frac{\mu_o}{3} N_1^2 \frac{b_1}{h} MLT \tag{9.38}$$

and

$$\ell_2' = \frac{\mu_o}{3} N_2^2 \frac{b_2}{h} MLT \tag{9.39}$$

where ℓ_2' is the leakage inductance element ℓ_2 reflected to the secondary N_2.

It is also shown in Chapter 3 that the zero output ripple condition for this converter is given by

$$N = 1 + \frac{\ell_1}{L_m} \tag{3.7}$$

where $N=N_2/N_1$, and $L_m=L_c \| L_o$.

From Eq. (3.7) it is clear that the leakage inductance ℓ_1 plays a primary role in the zero output ripple condition. A relative increase in the value of ℓ_1 can make the design of the zero output ripple condition into the coupled inductors a lot easier because of added freedom in the selection of the turns ratio.

If the coupled inductors is a low leakage structure (tightly coupled), Eq. (3.7) can be written as

$$\frac{N_2}{N_1} = 1 + \alpha \tag{11.10}$$

where $\alpha \ll 1$; therefore, the selection of the turns ratio is made more difficult since $N_2 \approx N_1$. For example, N_1 might even have to be less than one turn apart from N_2.

The sensitivity of the zero ripple condition is also worsened if tight coupling is used, since small variations in N_1, N_2 or ℓ_1 can produce large changes in the amount of ripple currents.

In the next section it is demonstrated how, given the window aspect ratio of a bobbin, an arrangement can be selected to give the maximum amount of leakage inductance.

11.3.1 Leakage Inductance and The Window Aspect Ratio

If the leakage inductances for the ungapped cases of the two-winding side-by-side (Eq. 9.21) and the top-bottom (Eq. 9.41) arrangements are compared, the result is

$$\frac{\ell_{tb}}{\ell_{ss}} = \left(\frac{b}{h}\right)^2 = \beta^2 \qquad (11.11)$$

where ℓ_{ss} and ℓ_{tb} are the leakage inductances of the side by side and the top-bottom arrangements, respectively, and β=b/h is the aspect ratio of the windings window area as shown in Fig. 11.5a.

If the bobbin has a square window area, β=1, $\ell_{ss} = \ell_{tb}$. However, most of the commercially available bobbin cores have a rectangular window area with $\beta > 1$; therefore, $\ell_{tb} > \ell_{ss}$ by a factor of β^2.

The actual ratios of some common bobbin cores are given in Fig. 11.5b. The LP-3213 ferrite core has the largest ratio we found ($\beta \approx 6$, or $\ell_{tb} \approx 36\ell_{ss}$). On an actual sample, the measured ratio was approximately 27.

Although LP-3213 cores offer a very large amount of leakage inductance using a top-bottom arrangement, other ferrite cores such as

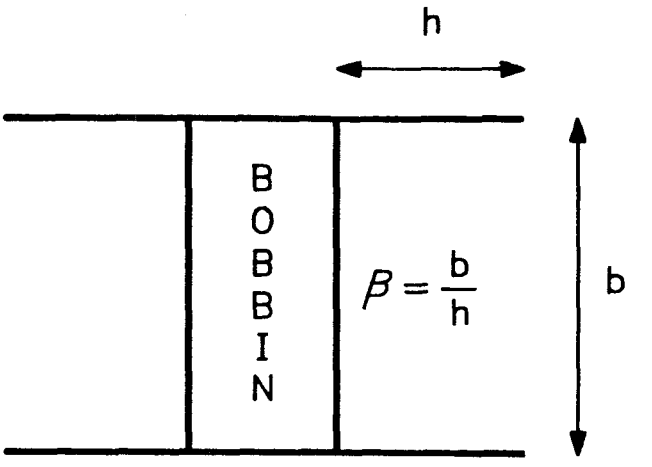

(a)

CORE	β
P–2213	2
RM–10	2.5
EE–12	3
LP–3213	6

(b)

Fig. 11.5 (a) Illustration of the window aspect ratio of a bobbin. The approximate aspect ratio of some actual bobbins are given in (b).

PQ, EE, pot cores etc, have a $\beta \approx 2$, which also gives a reasonably large leakage inductance when wound in a similar way.

The usual problem associated with the top-bottom arrangement is the difficulty of setting up the windings on the bobbin. However, most manufacturers of ferrite cores offer bobbins that are already split for such an arrangement.

11.4 Conclusions

Some conventional techniques for minimizing leakage inductance in two-winding transformers have been reviewed in this chapter. It is illustrated, with the use of physical models, how and why these techniques work.

Also, the two-winding top-bottom bobbin core arrangement is demonstrated to be a very good candidate for high leakage coupled inductor designs, as might be required in switching applications with minimum ac ripple currents.

In many switching converters, however, more than two windings are required. For example, in the forward converter with three isolated outputs shown in Fig. 11.6, a five-winding isolation transformer and a three-winding coupled inductor are required. The effects of the leakage parameters on structures such as these are not so well understood. The main reason for this is the lack of proper electric circuit models for multiple-winding magnetic circuits.

The newly developed physical models can be used to model adequately multiple-winding structures such as those in Fig. 11.6, and to further understand the effects of the different leakage parameters in the electric circuit model on the operation of the converter.

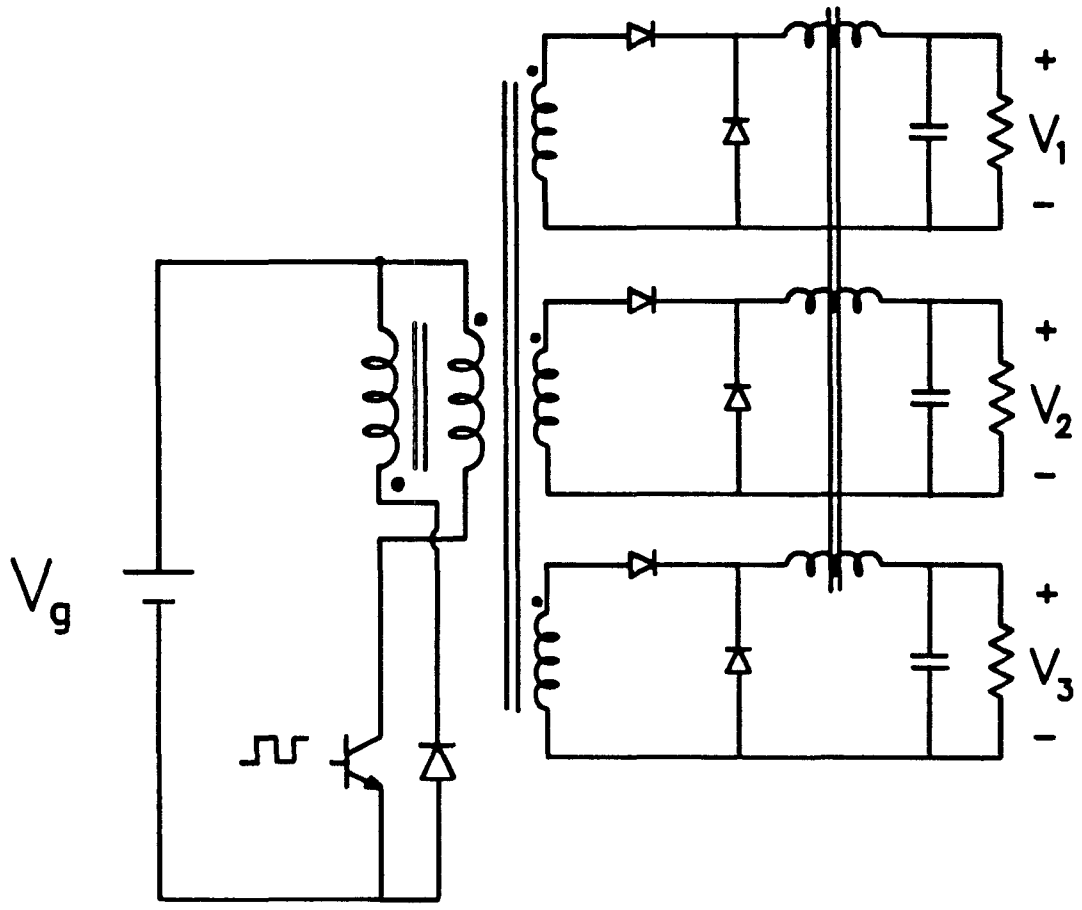

Fig. 11.6 Multiple-output isolated forward converter with output inductors coupled.

Further research in this area is necessary, but the initial step of developing a proper tool for analysis has already been undertaken, namely, the development of physical models for magnetic circuits.

CHAPTER 12

LAYER-TO-LAYER PHYSICAL MODELS AND THE WINDINGS AND INTERWINDING CAPACITANCE PROBLEM

12.1 Introduction

In all the previous cases where the physical model of a magnetic structure is determined, the windings are represented by infinitely small sources of mmf. Although the physical models obtained this way yield reliable results, sometimes more accurate solutions are required.

If the windings of the magnetic structure are laid out in an organized manner it is possible to represent the characteristics of the structure more accurately. For example, the primary and the secondary of the two-winding side by side arrangement in Fig. 12.1 are wound with three layers each.

This is not the only example in which the windings of a magnetic structure are organized in layers, but most of the commonly used configurations such as the side-by-side and the top-bottom arrangements discussed in the previous chapters are usually organized in a similar manner.

12.2 Layer-to-Layer Physical Models

If each layer of every winding is treated as a separate winding, and the physical model of this "multiple-winding" (multiple-layer)

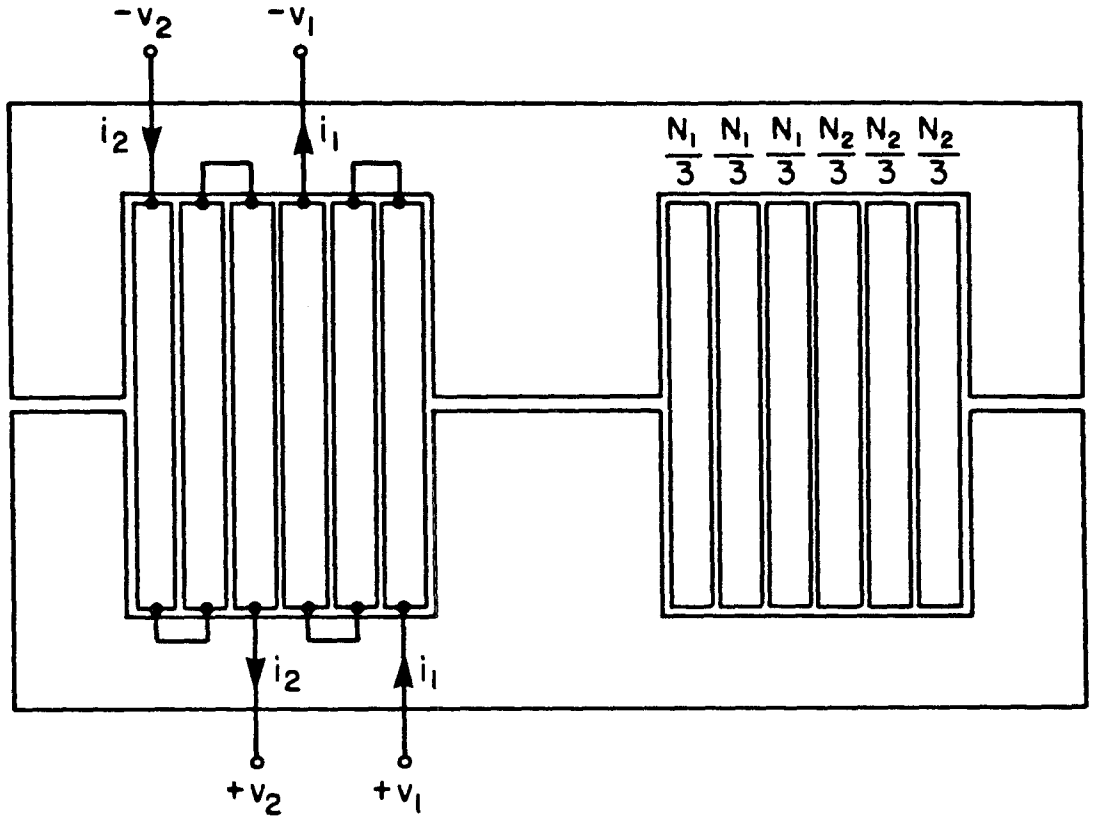

Fig. 12.1 Two-winding side-by-side arrangement. Both the primary and the secondary are wound with three layers each, with the layers connected as shown in the figure.

arrangement is determined, the result is a more accurate representation of the characteristics of the structure.

The separate "windings" in the electric circuit model represent the different layers and should be connected in the same way as the layers are on the actual windings.

This is very similar to the modelling method discussed in the previous chapter when the windings are sectionalized, and each section of the windings is treated as a separate winding.

12.2.1 Layer-to-Layer Physical Model of Two-Winding Side-by-Side Arrangement

The layer-to-layer physical model of the two-winding arrangement in Fig. 12.1, where each winding consists of three layers, is obtained by assuming that this is a six-winding side-by-side arrangement with the "windings" connected as shown in Fig. 12.1.

The flux pattern inside the structure illustrated in Fig. 12.2a is obtained in the usual way with the help of the field intensity plot throughout the windings illustrated in Fig. 12.2b.

The flux equations are defined by the flux pattern and the infinitely small sources of mmf illustrated in Fig. 12.2a, where each one of the sources represents a single layer. The flux equations determined this way are given by

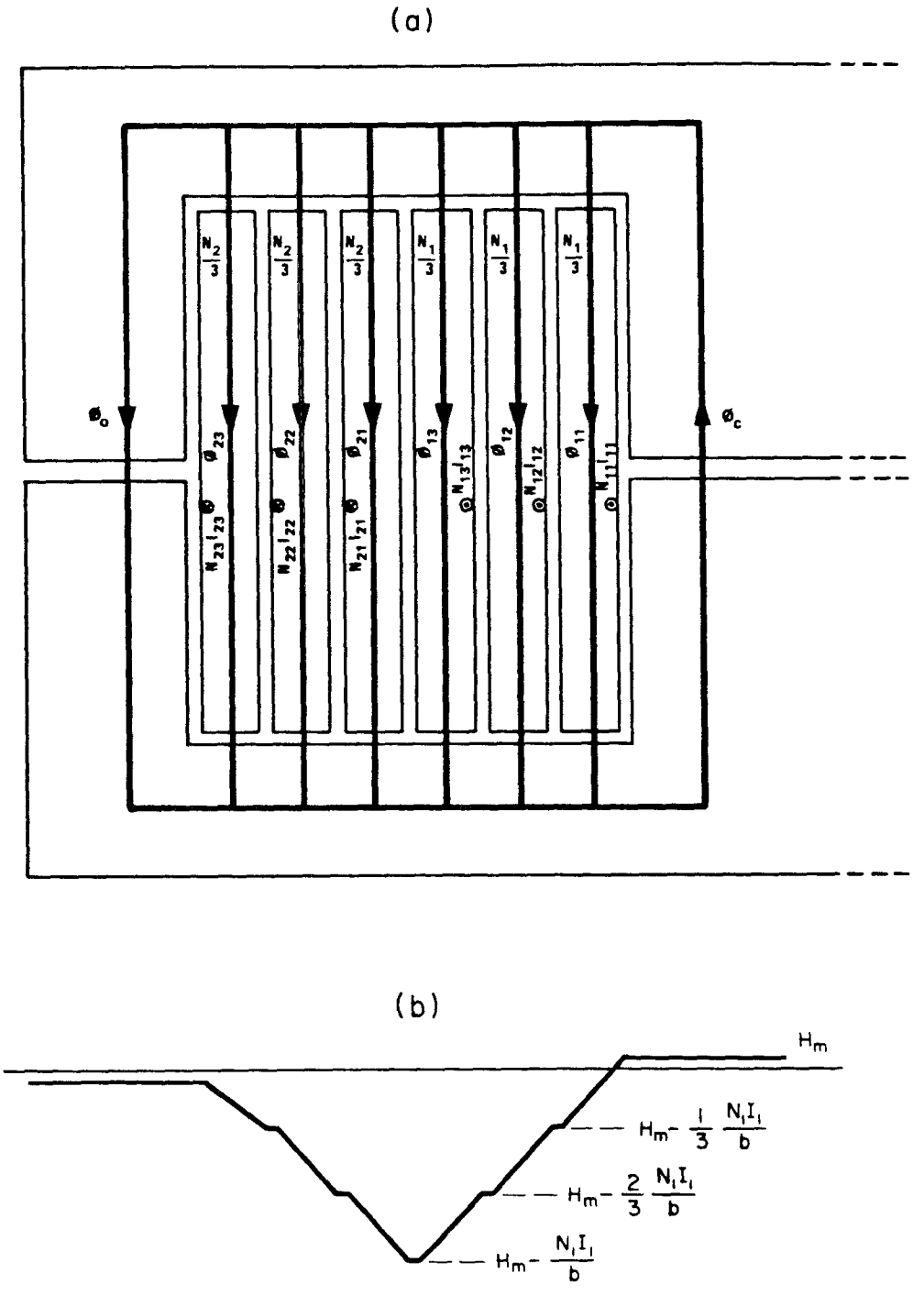

Fig. 12.2 Flux pattern (a) inside the six-layer (two-winding) structure side-by-side arrangement. The field intensity inside the layers and the core is shown in (b).

$$\phi_{N11} = \phi_c \tag{12.1}$$

$$\phi_{N12} = \phi_c - \phi_{11} \tag{12.2}$$

$$\phi_{N13} = \phi_c - (\phi_{11} + \phi_{12}) \tag{12.3}$$

$$\phi_{N21} = \phi_c - (\phi_{11} + \phi_{12} + \phi_{13} + \phi_{21}) \tag{12.4}$$

$$\phi_{N22} = \phi_c - (\phi_{11} + \phi_{12} + \phi_{13} + \phi_{21} + \phi_{22}) \tag{12.5}$$

$$\phi_{N23} = \phi_c - (\phi_{11} + \phi_{12} + \phi_{13} + \phi_{21} + \phi_{22} + \phi_{23}) \tag{12.6}$$

and

$$\phi_s = \phi_c - (\phi_{11} + \phi_{12} + \phi_{13} + \phi_{21} + \phi_{22} + \phi_{23}) \tag{12.6}$$

The reluctance circuit model is built around these equations and is illustrated in Fig. 12.3.

Finally, the electric circuit model derived from the reluctance circuit is illustrated in Fig. 12.4.

Since the three layers of each winding are connected as indicated in Fig. 12.1, the corresponding points in the electric circuit model should also be connected. The result after the connections are made is illustrated in Fig. 12.5. The electric circuit model in Fig. 12.5 can be rearranged as shown in Fig. 12.6.

The parameter values in the electric circuit model are determined in the same way as in all the previous cases. For example, the leakage inductance $\ell_{13} + \ell_{21}$ represents the energy storage capabilities of the two adjacent layers N_{13} and N_{21} in Fig. 12.1.

12.2.2 Layer-to-Layer Physical model of Two-Winding Top-Bottom Arrangement

Another common arrangement wound in layers is the two-winding top-bottom arrangement in Fig. 12.7. The flux pattern is illustrated in Fig. 12.8 to indicate how the mmf sources representing each layer are selected in this case. The reluctance model is illustrated in

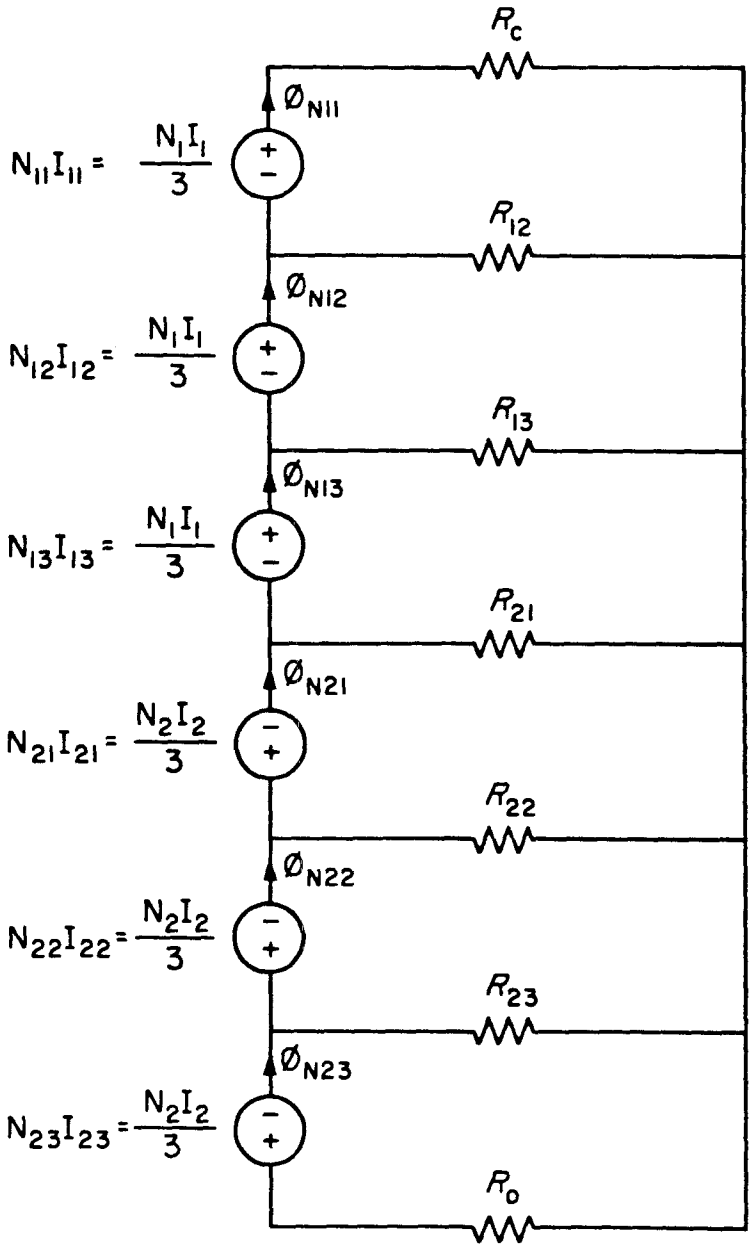

Fig. 12.3 Reluctance circuit model for six-layer structure. Each source of mmf represents one of the layers.

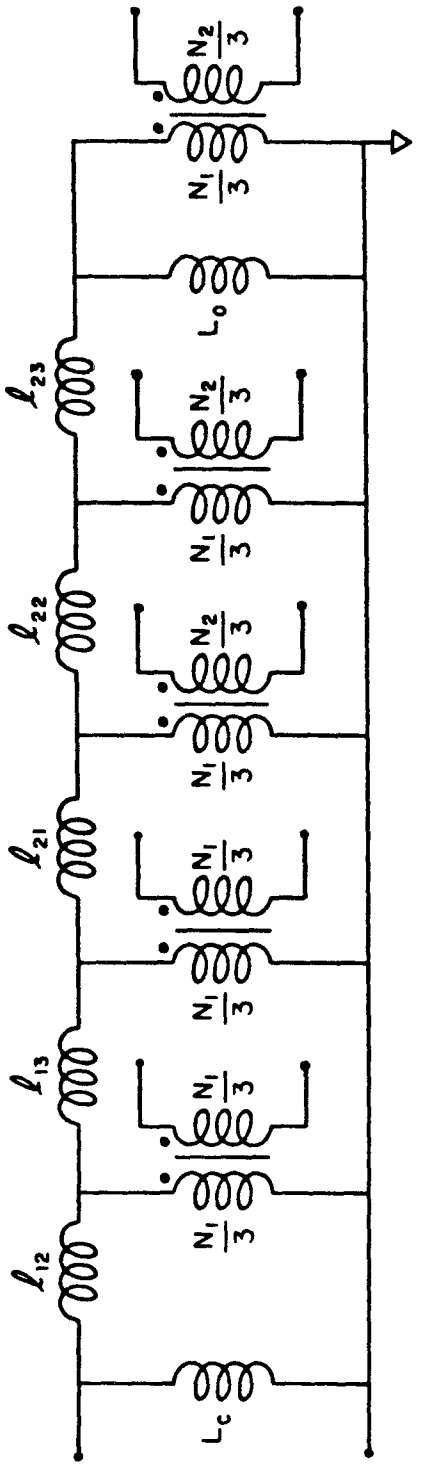

Fig. 12.4 Electric circuit model for six-layer side-by-side arrangement. Each layer is represented as an individual winding.

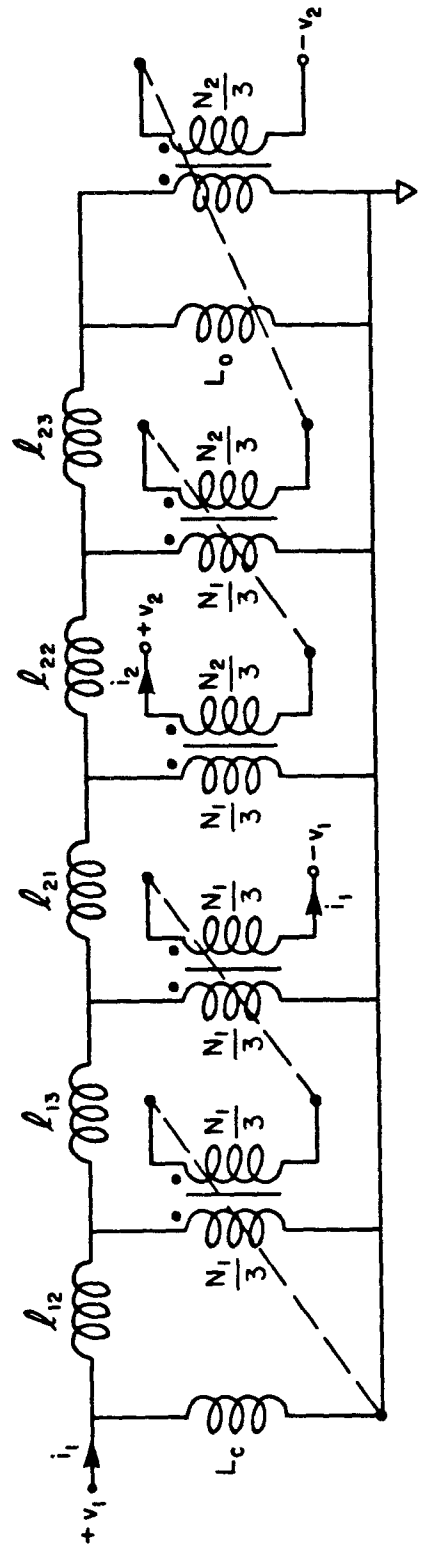

Fig. 12.5 Since the layers are physically connected in the structure (Fig. 12.1), similar connections are made at the corresponding points in the electric circuit model.

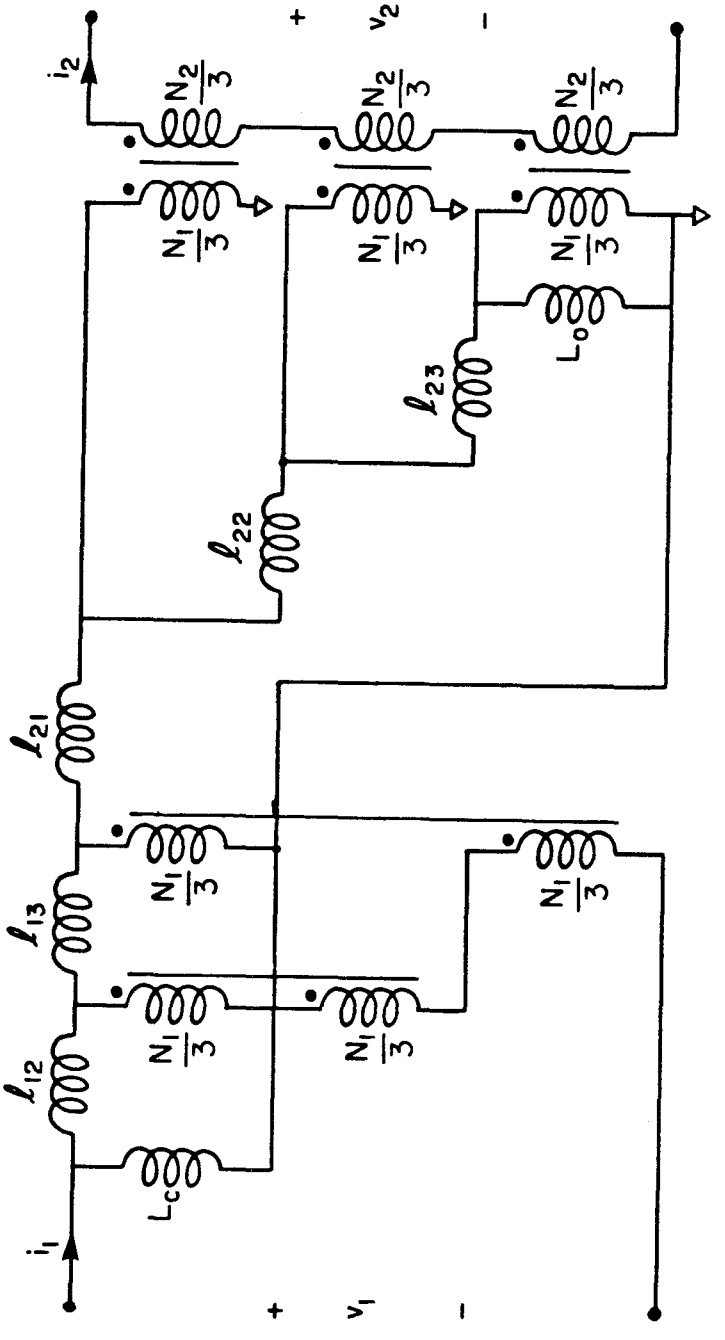

Fig.12.6 *The electric circuit model in Fig. 12.5 can be rearranged as shown in the figure. This circuit reflects the "transformer quality" of the magnetic component in Fig. 12.1 more than does the circuit model in Fig. 12.5.*

Fig. 12.9. The electric circuit model derived from the reluctance model is shown in Fig. 12.10.

It may be noted that because of the series connection of the leakage reluctances in the reluctance model, the corresponding leakage inductances appear in parallel in the electric circuit model.

The inductances associated with the center and outer leg gaps L_c and L_o are given by

$$L_c = \left(\frac{N_1}{3} \right)^2 \frac{1}{R_c} \tag{12.7}$$

$$L_o = \left(\frac{N_1}{3} \right)^2 \frac{1}{R_o} \tag{12.8}$$

where R_c and R_o are the reluctances of the center and outer legs respectively.

The leakage inductance parameters in the electric circuit model are computed as usual, but because of the similarities between this and the electric circuit model for the two-winding top-bottom arrangement in Fig. 9.19, the leakage inductances ℓ_1 and ℓ_2 in Fig. 9.19 have to be scaled only by the proper turns ratio, $(N_1/3)^2$, instead of by N_1^2. This is exactly the same procedure used to calculate the inductances L_c and L_o in Eqs. (12.7) and (12.8).

There are other possible configurations where the windings are wound in layers. The electric circuit models for these are obtained in the same way as in the previous two examples.

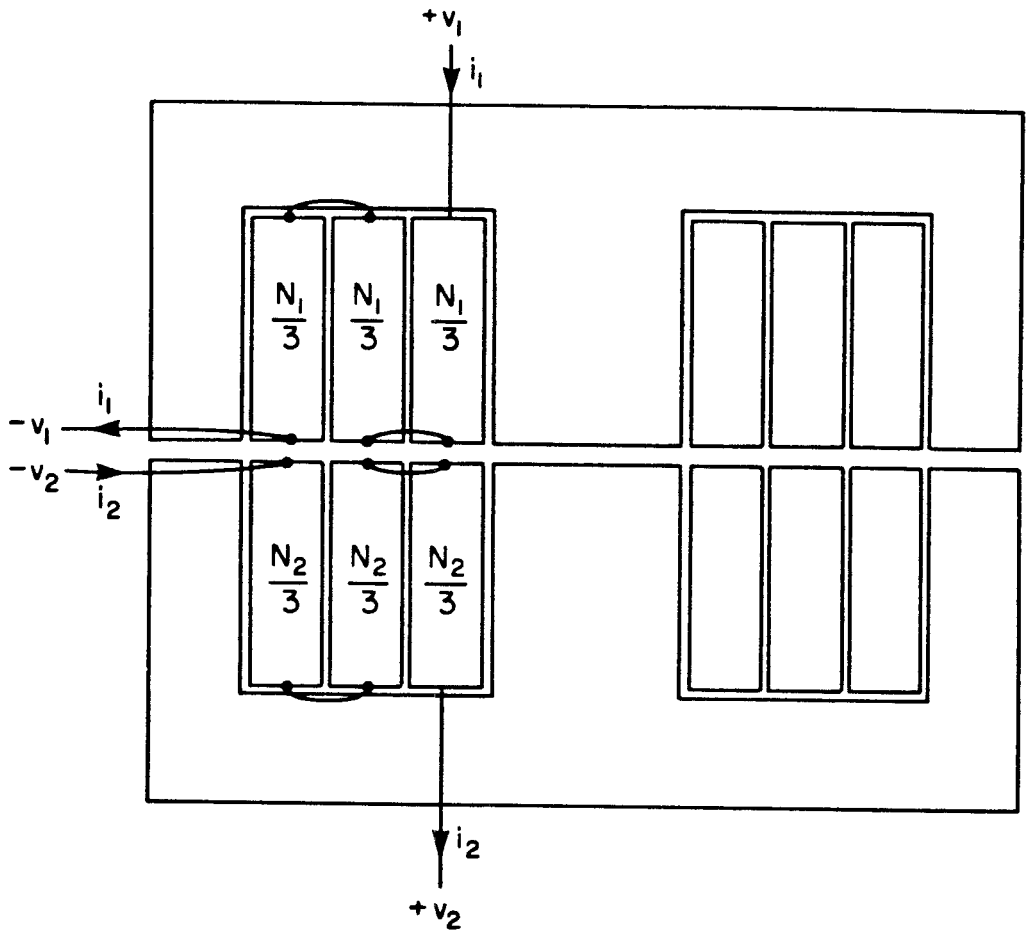

Fig. 12.7 Six-layer two-winding top-bottom arrangement.

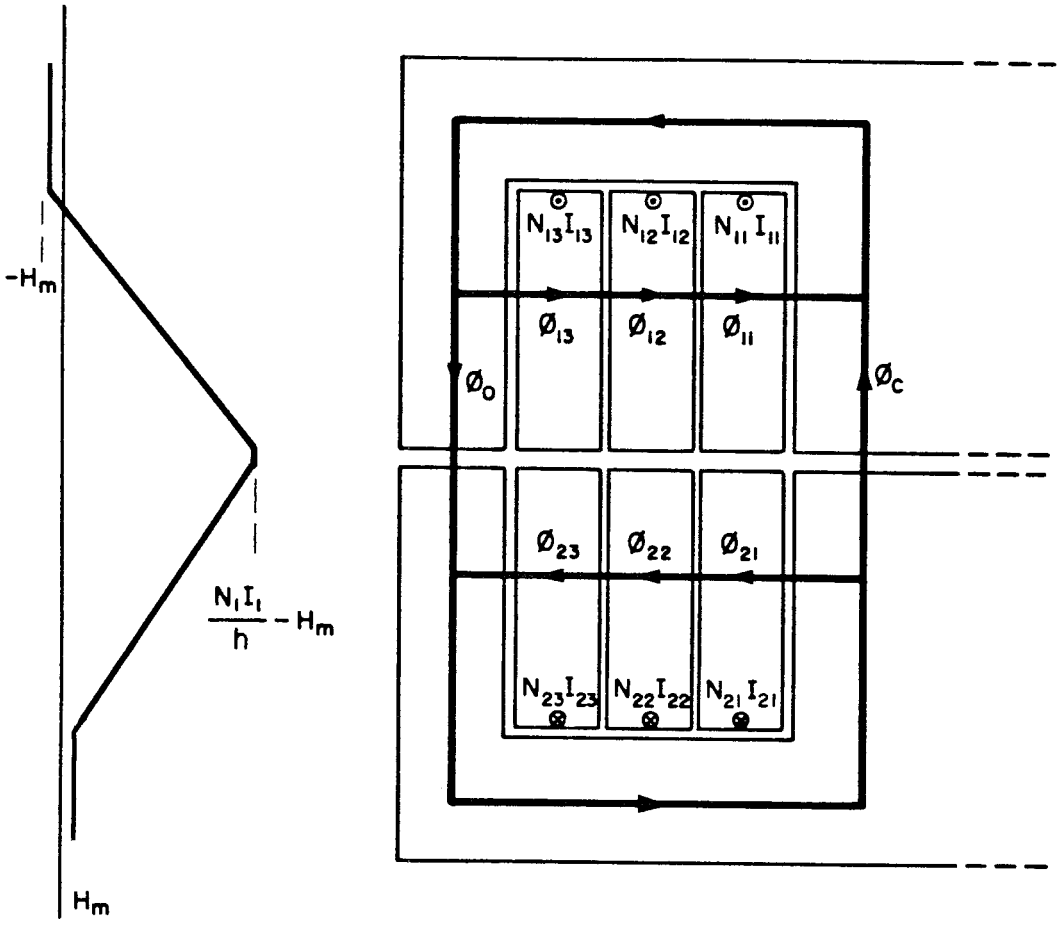

Fig. 12.8 Flux pattern and field intensity inside the windings of the six-layer top-bottom arrangement.

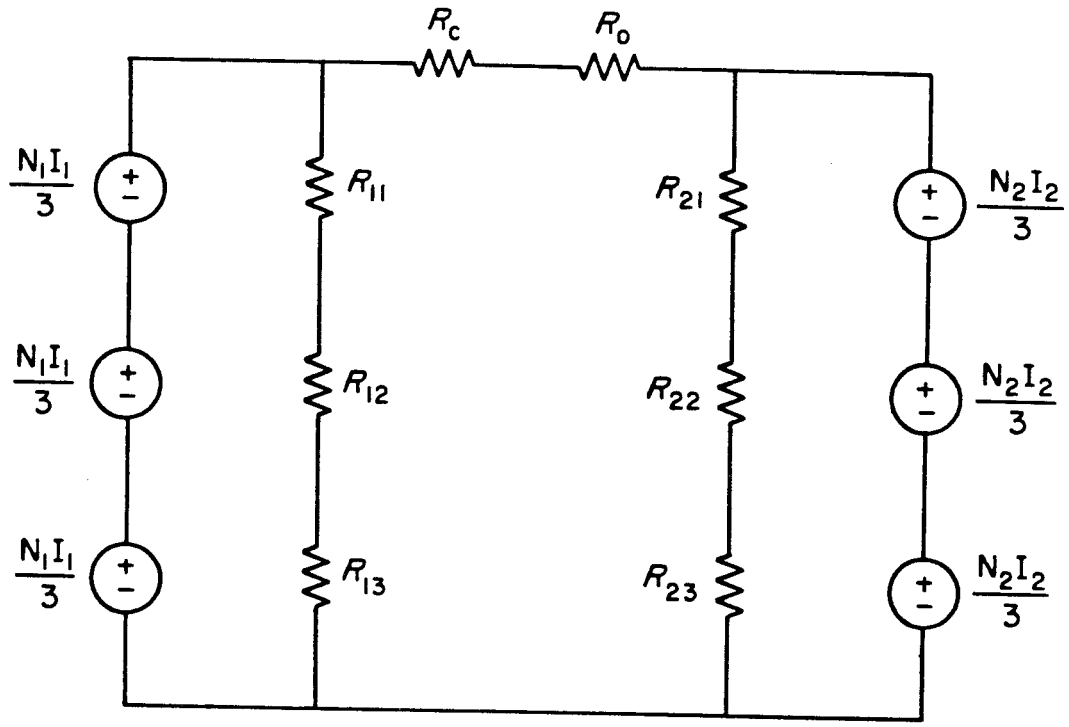

Fig. 12.9 Reluctance circuit model for six-layer two-winding top-bottom arrangement.

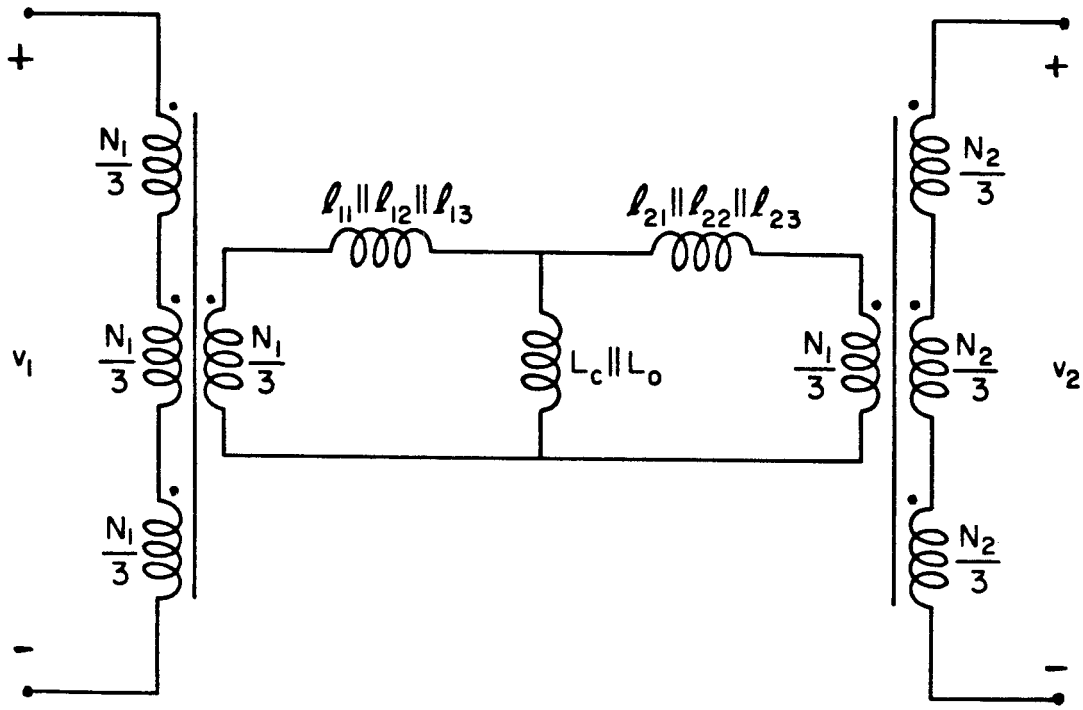

Fig. 12.10 Electric circuit model for six-layer top-bottom arrangement with the layers connected.

12.3 Modelling and Estimation of Windings and Interwinding Capacitance in Magnetic Circuits

The layer-to-layer models previously discussed give an accurate description of the leakage energy distribution inside the windings of a magnetic structure. Another advantage that these models offer is the ability to properly model other parasitic phenomena such as the distribution of the windings and interwinding capacitance in a magnetic circuit.

In the past, the windings and interwinding capacitances in two-winding transformers have always been modelled by a single parasitic capacitance element usually connected across the primary of the transformer model [11].

Although this method might provide reasonable answers in some cases of two-winding transformers, in general it falls short of predicting the correct distribution of the parasitic capacitances in cases of multiple-winding structures, and even in simple two-winding configurations where gaps are present, such as in coupled inductors.

The layer-to-layer physical models discussed in the previous section already contain adequate information about the correct distribution of leakage energy in the windings even in the presence of gaps. It is now illustrated how these models can be easily manipulated to incorporate additional information about the correct distribution of parasitic capacitances.

12.3.1 Windings and Interwinding Capacitances in Magnetic Circuits

There are several parts of a magnetic structure where energy can be stored in electric fields usually associated with capacitance

effects. One example is the separation space between the windings of a magnetic structure. Other parts of the windings can also store significant amounts of electrical energy as well, for instance, the space between two adjacent layers of a winding, the space between successive turns, and also, the spaces between the windings and the core.

For the analysis that follows, the capacitance between successive turns will be ignored. This does not introduce a significant error since these capacitances are very small owing to the small voltage difference between successive turns. Only in cases of windings with very few turns should this be considered.

What follows is a description of the method by which layer-to-layer physical models can be extended to incorporate additional information about the correct distribution of all the capacitance elements considered.

12.3.2 Modelling Procedure

To illustrate the method, the two-winding side-by-side arrangement in Fig. 12.1 is used as an example. All the relevant parasitic capacitance elements are represented in Fig. 12.11. The total capacitance between two adjacent layers is represented by a capacitance at the terminals of the layers.

The modelling method is simply an extension of the layer-to-layer modelling technique previously discussed. Basically, the capacitance elements in Fig. 12.11 are represented by similar capacitance elements at the proper terminals in the electric circuit model.

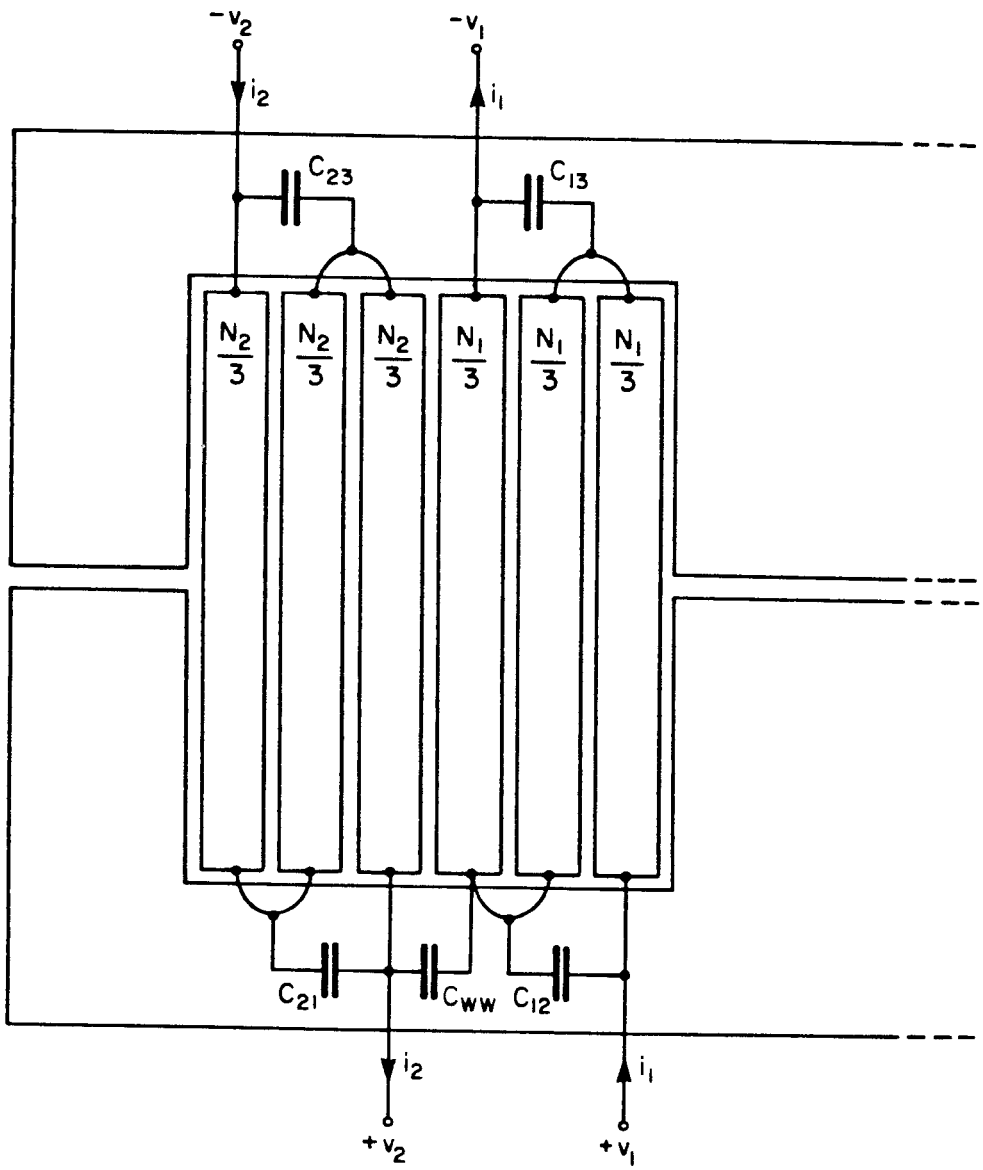

Fig. 12.11 Illustration of the parasitic capacitances in the six-layer two-winding side-by-side arrangement.

Layer-to-Layer Capacitances

Since the layer-to-layer models already provide the end points of each layer, it is easy to place the corresponding layer-to-layer capacitances in the electric circuit model. This is illustrated in Fig. 12.12.

Interwinding Capacitances

The capacitance between the two windings is just a special case of layer-to-layer capacitance and can be represented in the electric circuit model by the capacitance element C_{ww} in Fig. 12.12.

Sometimes screens are used to provide decoupling between the windings. In that case, the capacitance C_{ww} is split in two and the common point is the point to which the screen is connected (usually ground).

Windings to Core Capacitances

The capacitances between the windings and the core are usually ignored because of the thickness and the good isolation properties of the bobbin. In general, these can also be considered in a similar way as in the two previous cases.

12.3.3 Estimation of Parasitic Capacitances

There is extensive information in the literature [7], [11], [12], [13], that covers the subject of estimating the effective capacitance of the kind previously discussed. The analysis is straightforward, and only two examples will be discussed for illustration purposes.

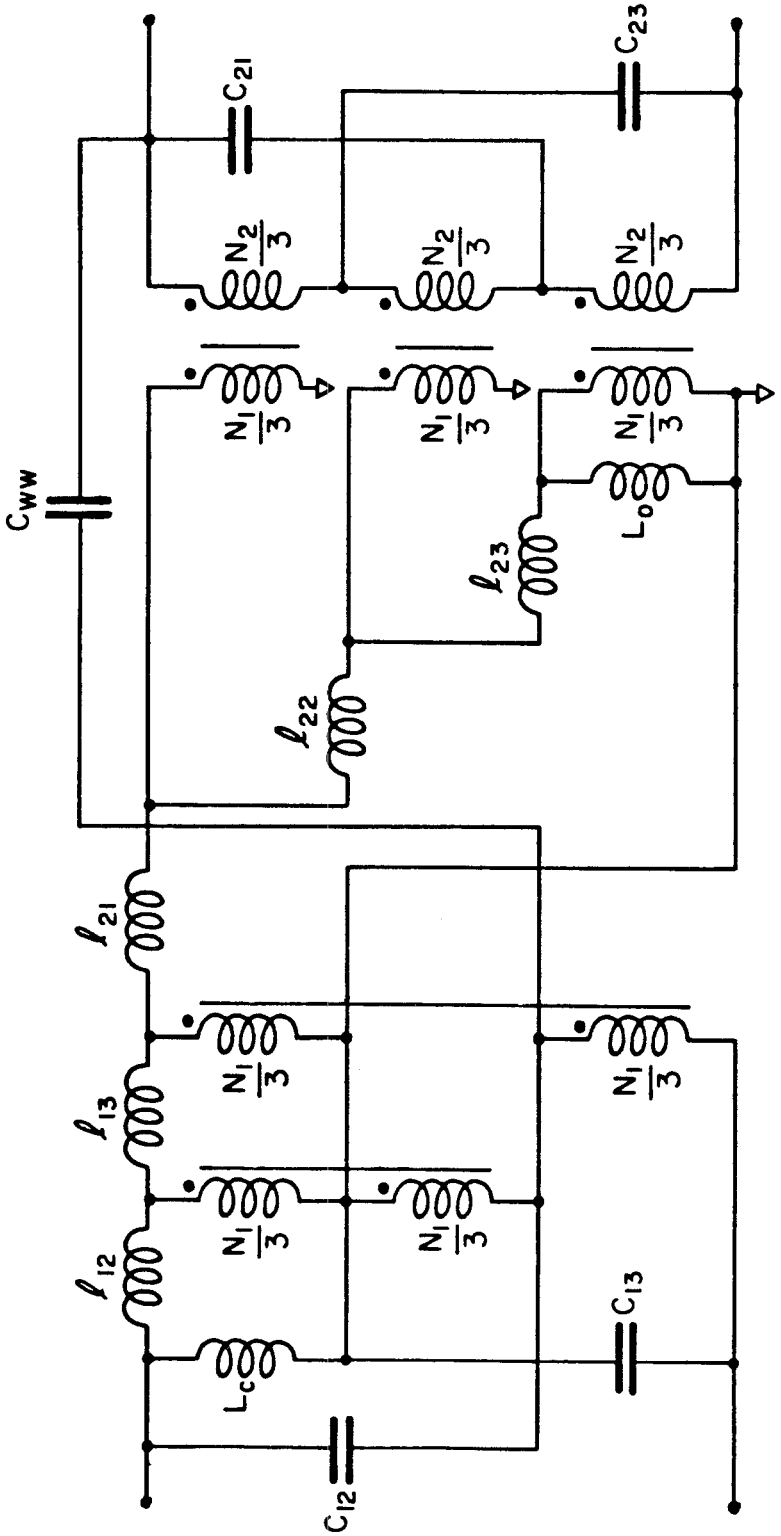

Fig. 12.12 Electric circuit model with additional information about the windings and interwinding parasitic capacitances.

Parallel Plate Capacitance

The effective or equivalent capacitance between two parallel plates shown in Fig. 12.13 can be estimated by computing the amount of electrical energy stored in the volume between the plates. That is,

$$W = \frac{\epsilon}{2} \iiint E^2 dv \tag{12.8}$$

where ϵ is the permittivity of the medium between the plates, and E, the electric field intensity.

This energy can also be written in terms of the *energy storage capability* (capacitance) of the volume between the plates. That is,

$$W = \frac{1}{2} CV^2 \tag{12.9}$$

Equations (12.8) and (12.9) are now combined to give

$$C = \frac{\epsilon}{V^2} \iiint E^2 dv \tag{12.10}$$

where V is the uniform potential difference between the plates.

The electric field intensity E in Eq. (12.10) can be evaluated as

$$E = V/d \tag{12.11}$$

where d is the separation between the plates.

Substitution of Eq. (12.11) into (12.10) and evaluation of the integral throughout the volume between the plates gives

$$C = \epsilon \frac{A}{d} \tag{12.12}$$

where A is the area of the plates.

Capacitance between two adjacent layers

The second example is illustrated in Fig. 12.14a. These are basically two adjacent layers as they are typically connected inside the windings of a magnetic structure.

This is a special case of the parallel plates, since the two layers run parallel to each other all around the core. The fact that they are cylinders and not flat plates makes no difference.

The potential difference across the layers, however, is not uniform. Assuming that the turns are very small compared to the height of the layers, the potential difference between the layers is a linear function of position as shown in Fig. 12.14b.

The total energy stored in a small differential piece of the layers as shown in Fig. 12.14 is approximately given by

$$dW = \frac{1}{2} \left(C_p \frac{dy}{b} \right) V(y)^2 \tag{12.13}$$

where C_p is the capacitance between the two layers considered as a parallel plate capacitor with uniform distribution of potential; i.e.,

$$C_p = \epsilon \frac{A}{d} \tag{12.14}$$

The quantity $(C_p dy/b)$ in Eq. (12.13) is the differential capacitance of the element dy.

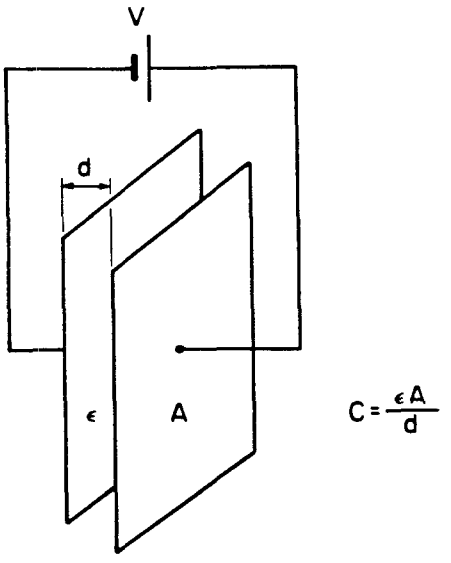

Fig. 12.13 Parallel plate capacitor.

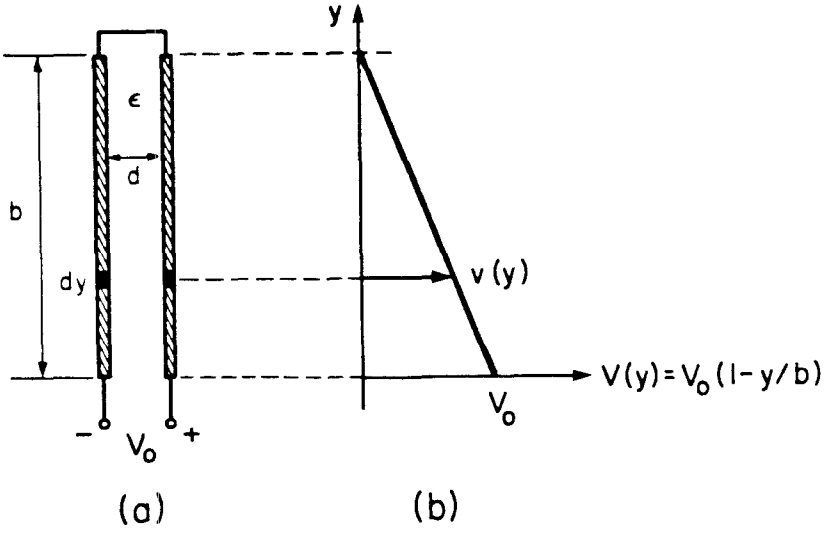

Fig. 12.14 Illustration of cross section of two adjacent layers as they are typically connected (a). The potential difference (b) is approximately a linear function of the position y.

In Eq. (12.14), it is necessary to know approximately the separation between the layers d. If enameled round copper wires are used, the determination of d is not straightforward. Several empirical methods have been used successfully in the past to determine this parameter [14].

Integration of Eq. (12.13) throughout the height of the layers gives

$$W = \frac{1}{2b} C_p \int_{y=0}^{y=b} \left[V_o \left(1 - \frac{y}{b}\right) \right]^2 dy \qquad (12.15)$$

which gives

$$W = \frac{C_p}{6} V_o^2 \qquad (12.16)$$

Since the capacitance between the two layers is represented at the terminals where $V(y) = V_o$, the total energy stored in it can also be expressed as

$$W = \frac{1}{2} C_{11} V_o^2 \qquad (12.17)$$

where C_{11} is the effective layer-to-layer capacitance.

Finally, comparison of Eqs.(12.16) and (12.17) results in

$$C_{11} = \frac{C_p}{3} \qquad (12.18)$$

This method can be easily extended to compute all the other capacitances in the circuit. It can also be used if screens are used to decouple the windings or the layers.

12.4 Distributed Windings Resistance

Already layer-to-layer physical models can incorporate adequate information about the correct distribution of leakage energy and parasitic capacitances.

The winding resistances which have almost been ignored so far can also be more accurately modelled using layer-to-layer models. Usually they are represented in the electric circuit model by a single resistance element for each winding.

Since an electric circuit model (layer-to-layer model) is now available in which the layers are independently represented, the separate layer resistances can be incorporated as well.

The procedure is straightforward, and it only amounts to introduction of the layer resistances at the proper position in the layer-to-layer electric circuit model.

For example, the resistances of every layer in each winding of the side-by-side arrangement in Fig. 12.1 can be introduced in the electric circuit model in Fig. 12.12 as shown in Fig. 12.15.

12.5 Conclusions

By breaking the windings into their separate layers, a more elaborate and accurate description of the characteristics of the magnetic structure can be obtained.

These extended layer-to-layer physical models can also be used to incorporate additional information about the correct distribution of the windings and interwinding parasitic capacitances and resistances.

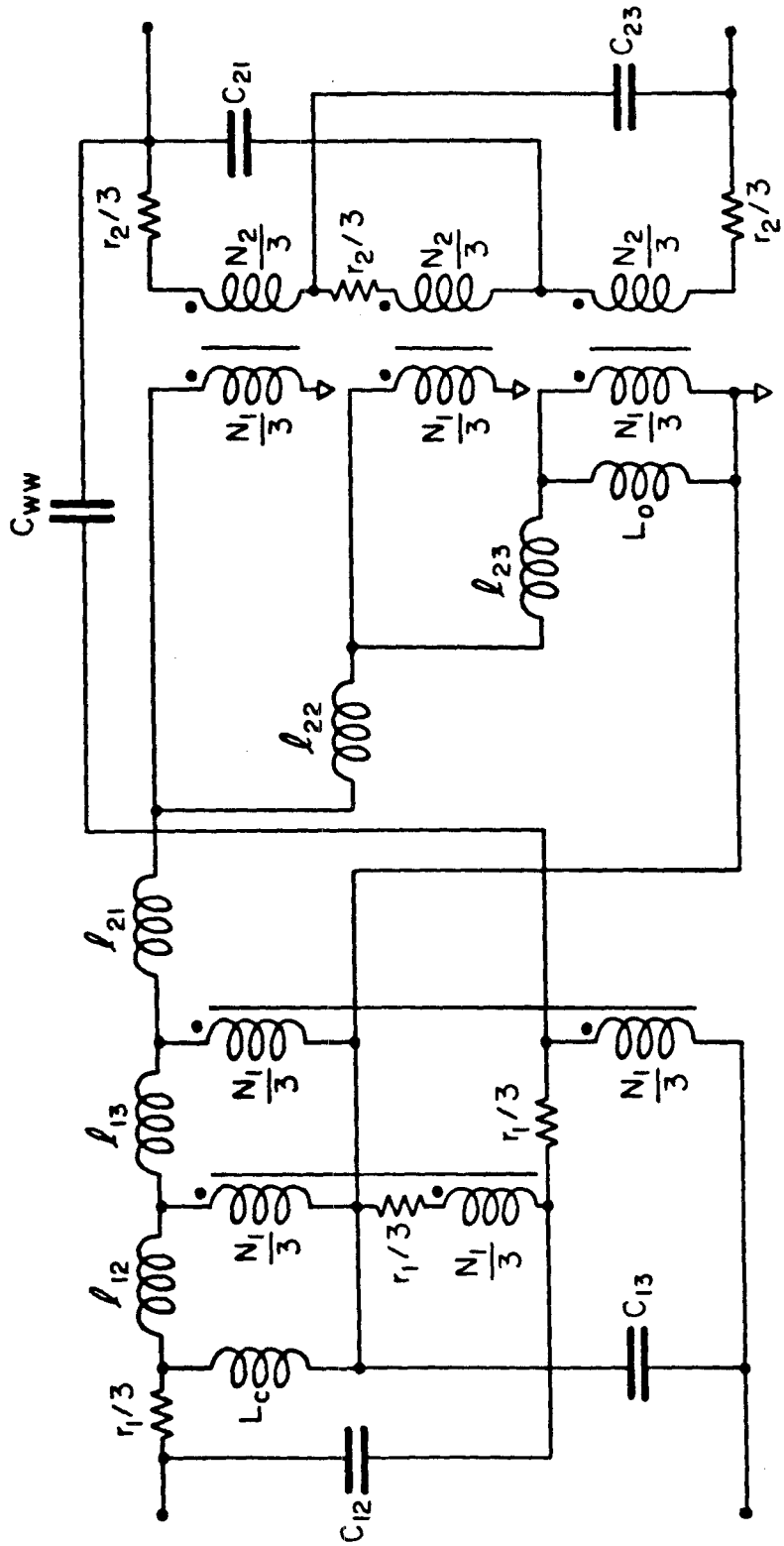

Fig. 12.15 Complete electric circuit model with additional information about the layers resistances.

Because of the complicated nature and the number of parameters in these elaborate models, they are more suitable for computer analysis.

CHAPTER 13

APPLICATIONS FOR PHYSICAL MODELS IN SWITCHING CONVERTERS

Several applications can be enhanced by the use of the newly developed physical models for magnetic circuits. Some of these applications are described in this chapter.

13.1 Minimization and Maximization of Leakage Phenomena in Switching Converters

Several examples throughout this thesis have illustrated how the newly developed physical models can be used to enhance the design and performance of a switching converter.

In converters where isolation transformers are used, leakage inductance can have severe adverse effects on the operation of the converter. Physical models can be used to investigate how these adverse effects can be minimized.

This is particularly important in multiple-winding transformers where the effects of the different leakage parameters are not so well understood owing to a lack of proper electric circuit models.

In converters where coupled inductors or integrated magnetic structures are used, physical models can be used to investigate and enhance the design of the magnetic structure so that the a.c. ripple currents in the different windings can be minimized.

Minimization of the ripple currents usually involve maximization of leakage parameters. Design guidelines for structures that maximize leakage parameters can be investigated through physical models.

13.2 Leakage Ratio and The Optimal Switching Frequency

The constant drive towards reducing the size and weight of power supplies leads inevitably to an increase in the frequency at which the main semiconductor devices are switched. Some designs operating in the megahertz range are already starting to appear.

As the switching frequency is increased, a point is reached at which the bottleneck of such designs lies not in the semiconductor devices but, on the contrary, in the magnetics design.

For example, even after careful layout of the isolation transformer in a switching power supply, a small residual leakage inductance can have severe adverse effects on the power supplies operation and design, from requiring sizable power dissipative networks to making the design completively inoperable if the switching frequency is sufficiently increased.

A design problem often encountered by power electronics engineers is the selection of the switching frequency at which a power converter is to be operated.

If the switching frequency is too low, the design can be unacceptably heavy and large. If, on the contrary, the switching frequency is too high, the parasitics in the magnetics can bring about a design just as heavy and large.

There must then be some *optimal switching frequency* between these two ranges at which no further decrease of the size or weight of the power supply is obtained.

Some of the factors that should be considered in an optimization process of this kind are illustrated in this section.

13.2.1 Leakage Ratio and Surface-to-Volume Ratio

Figure 13.1 illustrates a forward converter. The isolation transformer can be designed on a toroid with uniformly distributed turns as shown in Fig. 13.2. The reset winding has been omitted for simplicity.

If the power handled by the transformer remains constant, it can be easily demonstrated that the size of the toroid is inversely proportional to the switching frequency. That is,

$$S = \frac{k}{F_s} \tag{13.1}$$

where $S=\pi r_o^2$ is the cross-sectional area of the toroid, k is a proportionality constant, and F_s, the switching frequency.

Clearly, an increase in the switching frequency F_s yields a decrease in the size of the toroid. However, at the same time, two other important parameters also experience an increase, namely, the *leakage ratio* and the *surface-to-volume ratio* of the transformer. The increase of *leakage ratio* is proven to be a consequence of the increase in the *surface-to-volume ratio*.

The relations between these two quantities and the switching frequency are now discussed using the transformer of the forward converter in Fig. 13.1 as an example.

Leakage Ratio of toroid

The leakage ratio of any two-winding transformer can be defined as

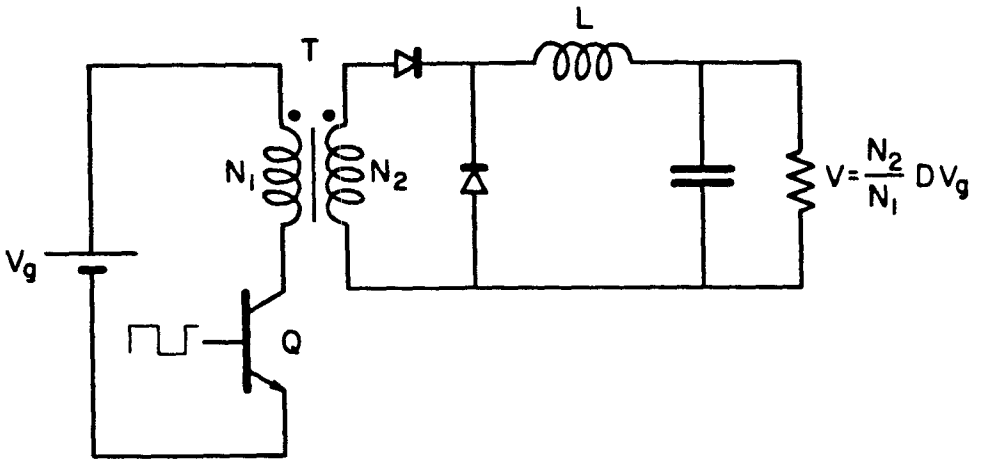

Fig. 13.1 Isolated forward converter.

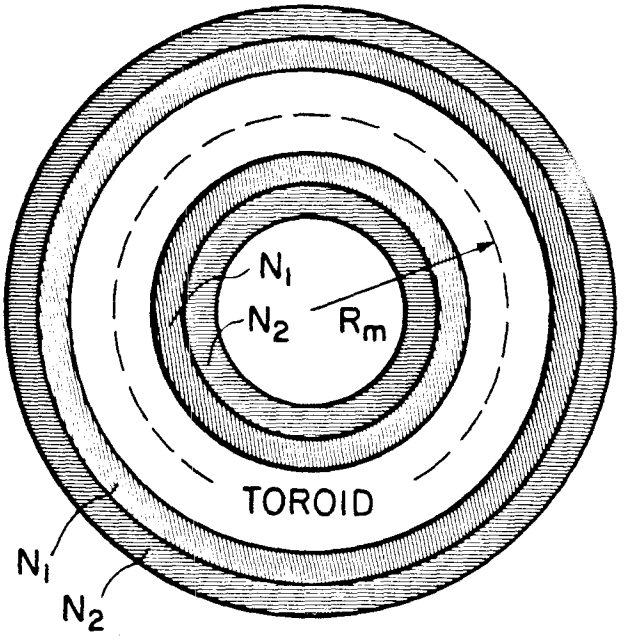

Fig. 13.2 A two-winding toroid with uniformly distributed turns can be used for the transformer in the forward converter.

$$\alpha \equiv \frac{\ell}{L_m} \tag{13.2}$$

where ℓ is the leakage inductance of the transformer, and L_m the mutual inductance. For the ungapped toroid in Fig. 13.2, the expressions for ℓ and L_m were previously obtained in Chapter 8 and are given by

$$L_m = \frac{N_1^2 \mu S}{\ell_m} \tag{8.14}$$

and

$$\ell = \frac{2}{3} N_1^2 \pi \mu_o \frac{h}{\ell_m} (r_o + h/2) \tag{8.17}$$

If ro >> h, Eq. (8.17) reduces to

$$\ell \approx \frac{2}{3} N_1^2 \pi \mu_o \frac{h}{\ell_m} r_o \tag{13.3}$$

Substitution of Eqs. (8.14) and (13.3) into Eq. (13.2) gives

$$\alpha = \left(\frac{2}{3} \frac{\mu o}{\mu} h \right) \frac{1}{r_o} \tag{13.4}$$

where the quantity in parenthesis can be regarded as a constant.

Surface-to-Volume Ratio of Toroid

The surface-to-volume ratio of the toroid is defined as

$$\beta = \frac{S_e}{V} \tag{13.5}$$

where S_e is the external surface area of the toroid and V the internal volume. This ratio can be easily obtained in terms of the internal radius of the toroid r_o, and is given by

$$\beta = \frac{2}{r_o} \tag{13.6}$$

Also from Eq. (13.1),

$$r_o = k_1 (F_s)^{\frac{1}{2}} \tag{13.7}$$

where $k_1 = (k/\pi)^{\frac{1}{4}}$.

Substitution of Eq. (13.7) into (13.6) gives

$$\beta = \frac{k_2}{(F_s)^{\frac{1}{2}}} \tag{13.8}$$

where $k_2 = 2/k_1$.

Finally, substitution of Eq. (13.6) into (13.4) gives

$$\alpha = k_3 \beta \tag{13.9}$$

where k_3 is a constant given by

$$k_3 = \frac{1}{3} \frac{\mu o}{\mu} h \tag{13.10}$$

Equations (13.8) and (13.9) can be plotted against each other as shown in Fig. 13.3, where the square root of the switching frequency is the tracing parameter of the curve.

The plot can be qualitatively interpreted in the following way: An increase in the switching frequency F_s produces an increase of the

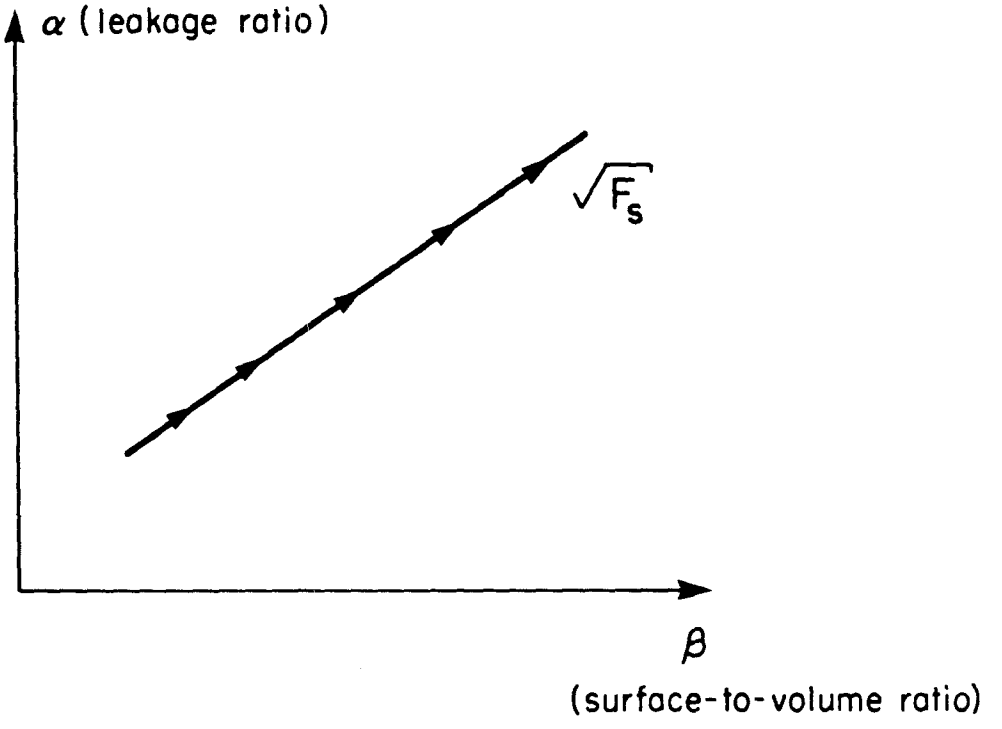

Fig. 13.3 As the switching frequency F_s is increased, the surface-to-volume ratio β of the transformer increases, consequently increasing the leakage ratio α.

surface-to-volume ratio β of the transformer and consequently, an increase in the leakage ratio α.

The qualitative nature of this statement, although proven true only for the toroid with uniformly distributed turns, is true in general for any magnetic structure [15].

Another interpretation of this result is that, since the leakage phenomenon is to a large extent a surface effect, an increase in the surface-to-volume ratio of the magnetic structure will increase the leakage ratio as well.

If the leakage ratio of the transformer is increased, additional protection for the switching elements is necessary. This inevitably increases the size of the power supply.

There is clearly an orthogonality of events related to an increase in switching frequency. On one hand, increasing it reduces the size and weight of the magnetic component, but on the other, it worsens the leakage ratio, which ultimately results in an increase in the size of the converter owing to the additional protection circuits.

The plots in Figs. 13.4a, 13.4b and 13.4c give a graphical description of the effects that are triggered by an increase in switching frequency, and how they affect the overall weight of the power converter.

In Fig. 13.4a, the size and weight of the magnetic components in the converter are decreased as the switching frequency is increased. At the same time, as indicated in Fig. 13.4b, the size and weight of the protection circuits are increased owing to an increase in the

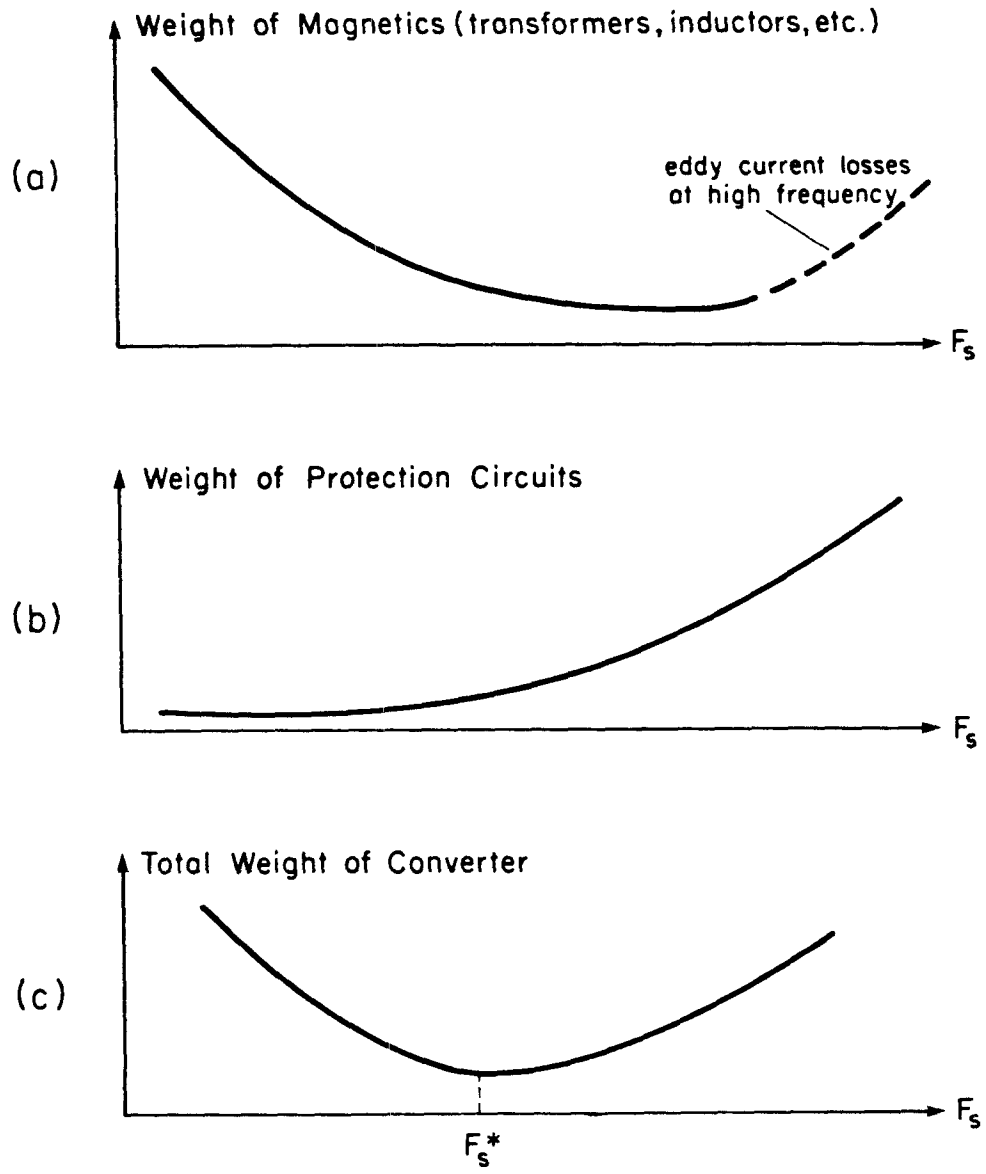

Fig. 13.4 *As the switching frequency is increased, the weight of the magnetic components in the switching converter is decreased (a), but at the same time, owing to an increase in leakage ratio, the size of the protection circuits is increased (b). The total weight of the power converter (c) reaches a minimum at the optimal switching frequency* F_s^*. *Further increase of the switching frequency effectively increases the size of the power supply.*

leakage ratio. The sum of these two curves given in Fig. 13.4c represents the total weight of the converter.

It is clear from Fig. 13.4c that for any switching frequency $F_s \neq F_s^*$ the overall weight of the converter is larger than the minimum weight at $F_s=F_s^*$. The frequency F_s^* at which no further reduction of the size of the converter is possible is the *optimal switching frequency*.

Another factor illustrated in the graph that has not been mentioned so far is the core losses usually associated with very high switching frequencies.

Basically, as the switching frequency is increased, the eddy current losses in the ferromagnetic material also increase. At very high frequencies these losses can be significant, and the associated heat must be dissipated somewhere. Typically, the size of the structure is increased to dissipate the heat before a breakdown of the material can occur.

The net increase in the size of the magnetics due to eddy current losses at very high frequencies is indicated in Fig. 13.4a with the dashed lines.

In some new designs that are starting to appear operating in the megahertz range, this is probably the determining factor, not additional protection circuits for the switches. But the end result is still the same, an overall increase in the size of the converter.

The *optimal switching frequency* is in general a function of the converter's topology, the protection schemes used, the ferromagnetic material, and various other factors. The problem of determination of

the *optimal switching frequency* for a given converter is therefore very complex.

However, definition of the problem and some of the factors that should be considered in the optimization process served to illustrate an important principle that should not be overlooked by power electronics engineers.

13.3 Extended Characterization of Magnetic Components

The process of defining a set of consistent specifications for a magnetic component can sometimes be as demanding as building the part itself. This is especially the case in multiple-winding applications.

If, for example, a multiple-winding design has to meet not only the usual first-order design parameters such as power, voltage and current levels, but also some second-order quantities such as leakage parameters, the design of the magnetic component usually ends up in a lengthy and tedious trial-and-error process. The main reason for this is the lack of proper electric circuit models for multiple-winding magnetic structures.

The typical design process for multiple-winding structures is illustrated in Fig. 13.5. The major loop in the figure corresponds to the trial-and-error process usually associated with a failure to meet the second-order specifications.

The design process can be significantly simplified if physical models are used to design the first-order as well as the second-order specifications of the magnetic component.

Since the newly developed physical models incorporate adequate information about the correct distribution of second-order quantities

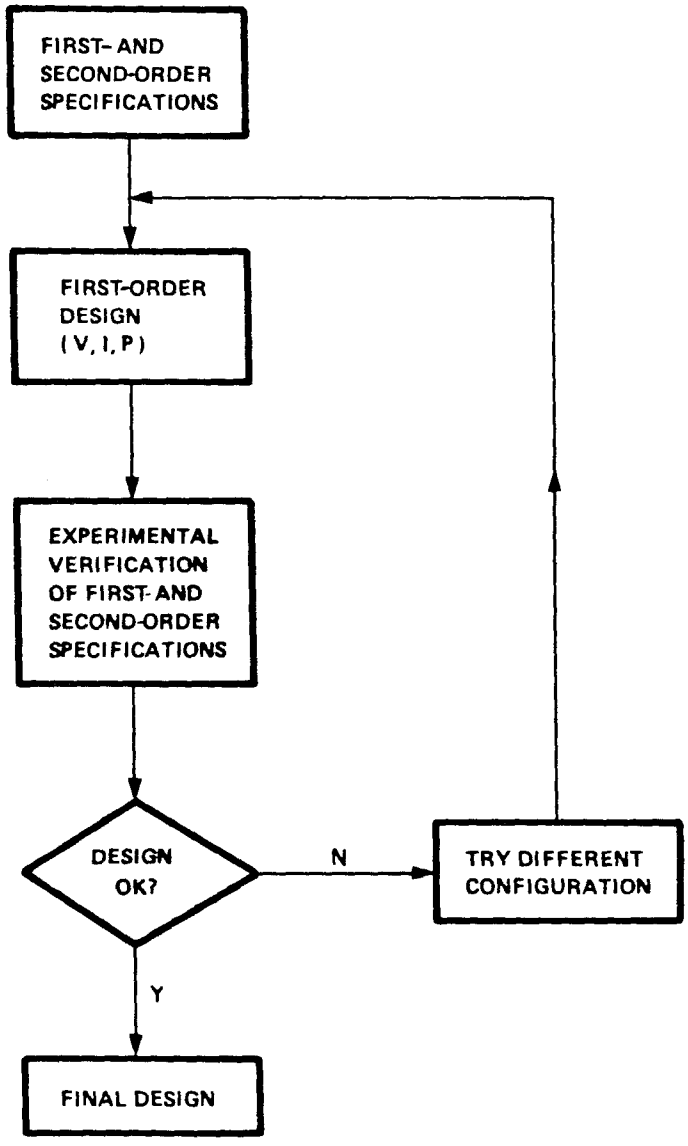

Fig. 13.5 Typical design process for multiple-winding magnetic structures. The major loop in the figure corresponds to the trial-and-error process usually associated with a failure to meet the second-order specifications.

such as leakage phenomena, a design of the magnetic component aimed at meeting not only first-order but also second-order specifications can be significantly simplified.

A possible simplified design procedure using physical models is illustrated in Fig. 13.6.

The more elaborate layer-to-layer physical models can also be used to investigate the effects of other parasitics such as the windings and interwinding capacitances. However, The complicated nature of these models, and the large number of parameters usually involved, make these models more suitable for computer analysis of switching converters.

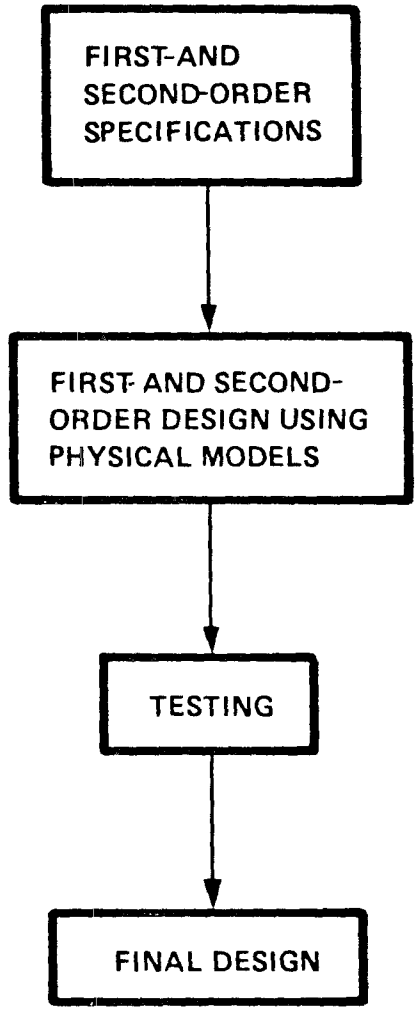

Fig. 13.6 The design process for multiple-winding structures can be significantly simplified with the use of physical models, since second-order parameters are adequately incorporated in these models.

CHAPTER 14

CONCLUSIONS

A new modelling method for magnetic circuits is presented in this thesis. The electric circuit models (physical models) obtained with this method incorporate adequate information about the correct distribution of leakage energy in the windings of a magnetic structure, the presence of gaps throughout the magnetic path of the core, and the type of cores used.

The electric circuit models obtained with this method are physically natural; i.e., there is a one-to-one correspondence between the elements in the model and corresponding physical parameters in the original magnetic structure.

Several commonly used arrangements such as toroids with uniformly distributed turns, and the conventional side-by-side and top-bottom bobbin core arrangements with multiple windings, have been modelled with the new technique. The measured electric circuit model values always compare favorably with the predicted physical values derived with the new method.

By breaking the windings of a magnetic structure into their separate layers, a more elaborate and accurate set of models can be obtained. These layer-to-layer physical models can be used to properly model the windings and interwinding capacitances as well as the windings' distributed resistances. These two "second-order" parameters, which have conventionally been modelled with single

elements, can now be more accurately represented in the electric circuit model.

Physical models for magnetic circuits can be used in a number of switching applications to enhance and facilitate what is usually a very lengthy and inefficient design process. This is especially the case when second-order specifications such as magnetic leakage are involved in the design process. Some of these applications are minimization of magnetic leakage effects in isolation transformers, minimization of current ripple in coupled inductors, and extended characterization of magnetic components.

The complicated nature and the large number of parameters in the more elaborate layer-to-layer physical models make them more suitable for computer analysis of magnetic circuits.

REFERENCES

[1] Slobodan Ćuk, "Switching Dc-to-Dc Converter with Zero Input or Output Current Ripple," IEEE Industry Applications Society Annual Meeting, 1978 Record, pp. 1131-1146.

[2] Slobodan Ćuk, "A New Zero-Ripple Switching DC-to-Dc Converter and Integrated Magnetics," IEEE Power Electronics Specialists Conference, 1980 Record, pp. 12-32.

[3] Slobodan Ćuk and William M. Polivka, "Analysis of Integrated Magnetics to Eliminate Current Ripple in Switching Converters," Proceedings of the Sixth International PCI'83 Conference, April 1983.

[4] R. D. Middlebrook and Slobodan Ćuk, "Isolation and Multiple Output Extensions of a New Optimum Topology Switching Dc-to-Dc Converter," IEEE Power Electronics Specialists Conference, 1978 Record, pp. 256-264.

[5] William M. Polivka, "Applications of Magnetics to Problems in Switched-Mode Power Converters," Ph.D. Thesis, California Institute of Technology, Department of Electrical Engineering, Pasadena, California, February 7, 1984.

[6] R. D. Middlebrook and Slobodan Ćuk, *Advances in Switched-Mode Power Conversion,* Volume II, pp. 279-310, TESLAco Power Electronics Series, Pasadena, California, 1981.

[7] Shi-Ping Hsu, "Problems in Analysis and Design of Switching Regulators," Ph.D. Thesis, California Institute of Technology, Department of Electrical Engineering, Pasadena, California, September 13, 1979.

[8] John D. Krauss and Keith R. Carver, *Electromagnetics*, Mcgraw-Hill, 1973.

[9] W. R. Smythe , *Static and Dynamic Electricity*, Mcgraw-Hill, 1968.

[10] Robert M. Fano, Lan Jen Chu, and Richard B. Adler, *Electromagnetic Fields, Energy, and Forces,* John Wiley & Sons, 1960.

[11] Wally E. Rippel and Colonel W. T. Mclyman, "Design Techniques for Minimizing the Parasitic Capacitance and Leakage Inductance of Switched-Mode Power Transformers," Proceedings of the Ninth International Solid-State Power Electronics Conference, Powercon 9, 1982.

[12] E. C. Snelling, *Soft Ferrites*, London Iliffe Books Ltd, 1969.

[13] W. T. Duerdoth, "Equivalent Capacitances of Transformer Windings", Wireless Engineer, 23, 1946, p. 161.

[14] H. Zuhrt, "Einfache Naherungsformeln für die Eigen-kapazitat Mehrlagiger-Spullen," Elektrotech Z., 55, 1934, p. 662.

[15] R. D. Middlebrook, "Design Considerations and Noise Reduction in Switching Converters," Power Conversion International Magazine, Vol. 9, no 8, September 1983.

[16] J. K. Watson, *Applications of Magnetism,* John Wiley & Sons, 1980.

APPENDIX A

REVIEW OF THE PRINCIPLE OF DUALITY

This appendix shows how to derive the electric circuit model of a magnetic circuit from the reluctance model. The technique is a simplified version of that found in [5] and [16].

A.1 Duality and Magnetic Circuits

Given the reluctance circuit model of a magnetic structure, the electric circuit model can be obtained by use of the principle of duality.

The dual of the reluctance circuit model of a magnetic structure is an electric circuit in which the nodes are replaced by loops, the loops by nodes, the reluctances by inductances, and finally, the sources that represent the windings are replaced by ideal transformers.

A.2 Construction of Electric Circuit Model by Duality

What follows is a description of the general steps used to construct the electric circuit model, given the reluctance circuit. The reluctance circuit model for the two-winding side-by-side bobbin core arrangement discussed in Chapter 9 and illustrated in Fig. A.1 will be used as an example.

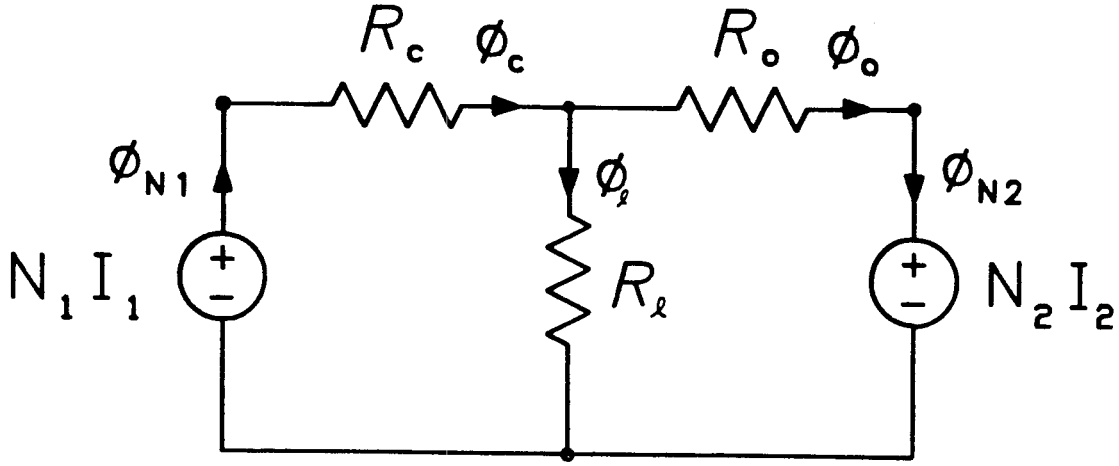

Fig. A.1 *Reluctance model for two-winding side-by-side arrangement.*

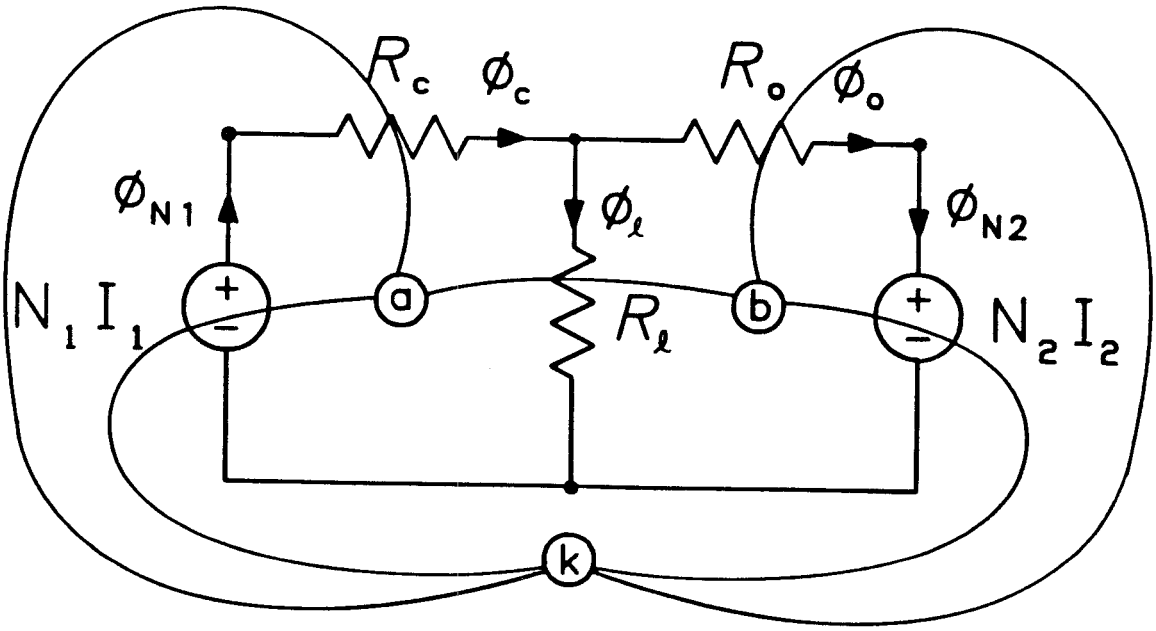

Fig. A.2 *The loops in the reluctance model are assigned reference dots, which are connected by lines passing through one and only one element.*

A.2.1 The Reference Winding

Before the dual of the reluctance model is obtained, a reference winding must be selected. This is the winding to which all the inductance elements will be reflected automatically.

The selection of the reference winding can in general be arbitrary, but a careful selection can facilitate further simplification and the interpretation of the resultant electric circuit model. For example, in the case of isolation transformers the primary N_1 is usually selected as the reference winding. In other applications such as coupled inductors and integrated magnetics, a different winding can be selected if this makes it easier to simplify or interpret the electric circuit model. Nevertheless, the input-output characteristics of the circuit are always the same no matter which winding is selected as the reference.

For the reluctance model in Fig. A.1, the primary N_1 will be used as the reference.

A.2.2 Reference Dots and Topological Transformation of Reluctance Model

A reference dot ((a), (b) in Fig. A.2) is assigned to each of the internal loops inside the reluctance model, and a reference dot (k) is assigned outside the circuit as shown in Fig. A.2. These dots will become the nodes in the electric circuit model.

A line is drawn between any two nodes passing through <u>one and only one</u> circuit element. These lines are also shown in Fig. A.2.

The dual of any reluctance R_x between two of the reference dots is an inductance connected between the two associated nodes in the electric circuit model, and of value

$$L_x = \frac{N_r^2}{R_x} \tag{A.1}$$

where N_r is the preselected reference winding.

The dual of any source $N_x I_x$ is an ideal transformer as shown in Fig. A.3, where N_r is again the preselected reference winding, and the polarity of the transformer is determined by use of the usual voltage polarity convention, which is based on how the corresponding windings (N_r and N_x in this generic case) are originally wound on the structure.

The process is repeated for all the reluctances and mmf sources in the reluctance model. The complete electric circuit model derived from the reluctance model in Fig. A.2 is shown in Fig. A.4. Notice the correspondence between the reluctances in Fig. A.2 and the inductances in the electric circuit model in Fig. A.4. Finally, the ideal transformer on the left ($N_1:N_1$) corresponds to the primary source N_1, and can be eliminated as shown in Fig. A.5. This will always be the case with the reference winding.

If the secondary winding N_2 had been selected as the reference winding, the resultant electric circuit model would be that in Fig. A.6. This is the same electric circuit model obtained by reflection of all the inductances in Fig. A.5 to the secondary N_2.

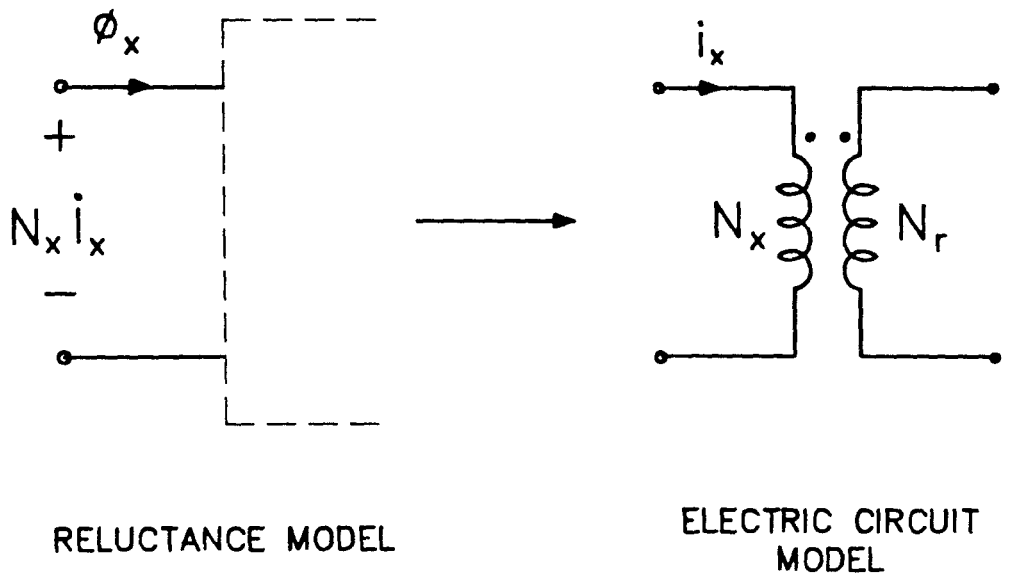

Fig. A.3 *The dual of any pair of terminals or source of mmf in the reluctance model is an ideal transformer, where N_r corresponds to the reference winding, and N_x to the corresponding winding of the mmf source.*

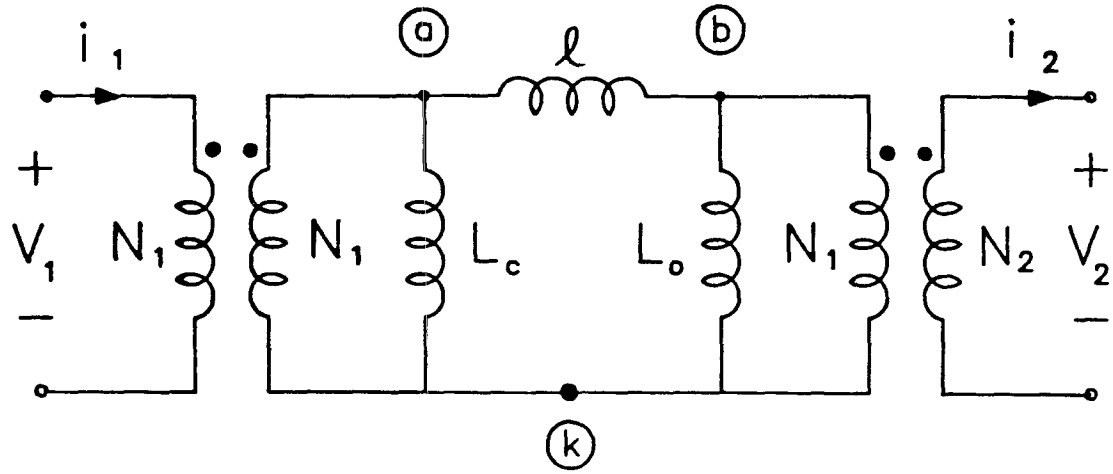

Fig. A.4 Electric circuit model derived from the reluctance model in Fig. A.2.

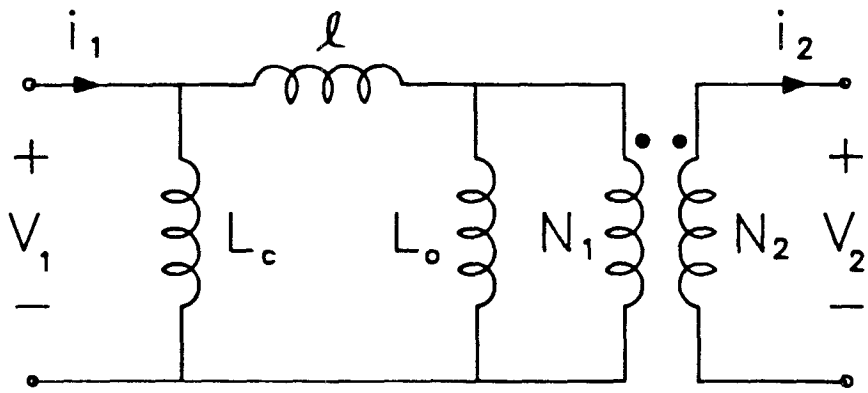

Fig. A.5 The ideal transformer (N_1:N_1) on the left in Fig. A.4 can be eliminated as shown in the figure.

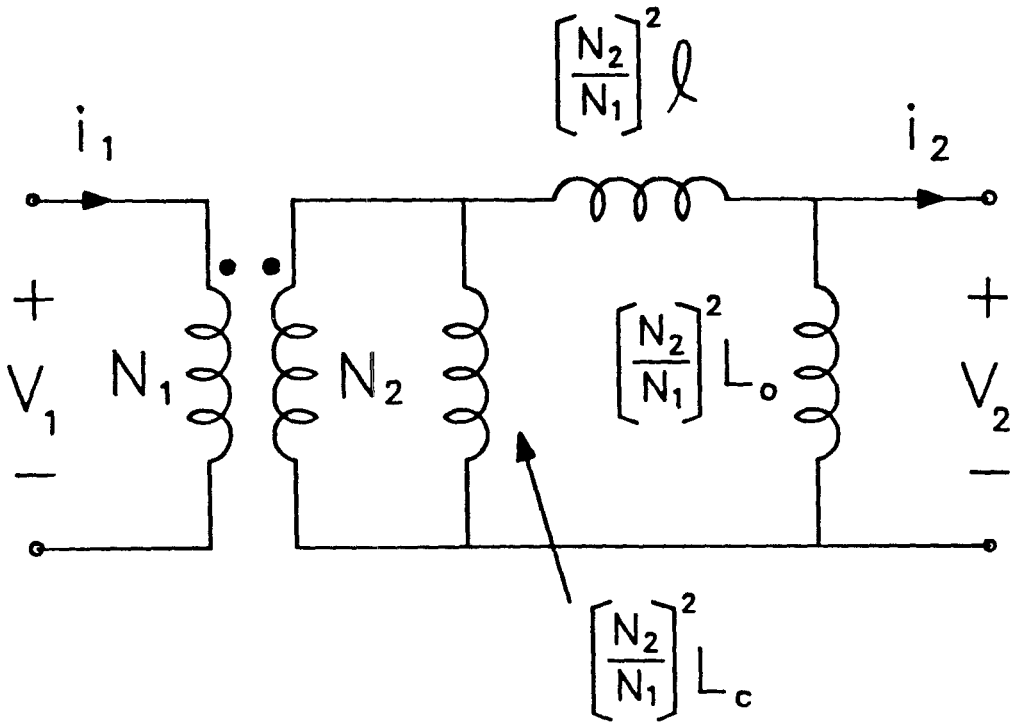

Fig. A.6 *If the secondary winding N_2 in Fig. A.2 is used as the reference winding, the resultant electric circuit model is as shown in the figure. This is the same result that is obtained if all the inductances in Fig. A.5 are reflected to the secondary N_2.*

Another example is the reluctance model for the three-winding side-by-side arrangement (Chapter 10) illustrated in Fig. A.7. Selection of the primary N_1 as the reference winding, and the dots and connecting lines as shown in Fig. A.7, the dual electric circuit model, is as shown in Fig. A.8.

If the inductances L_o and ℓ_{23} are reflected to N_3, the electric circuit model reduces to that in Fig. A.9, which reflects the "transformer quality" of the magnetic component more than does the circuit model in Fig. A.8.

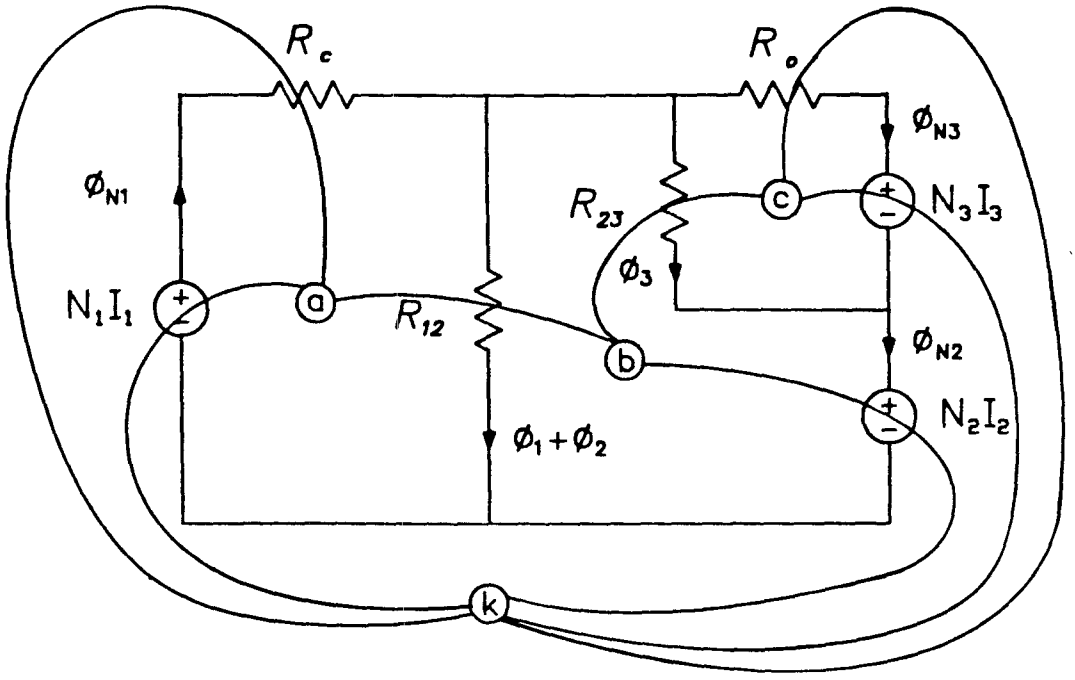

Fig. A.7 Reluctance model for three-winding side-by-side bobbin core arrangement with the reference dots and lines illustrated.

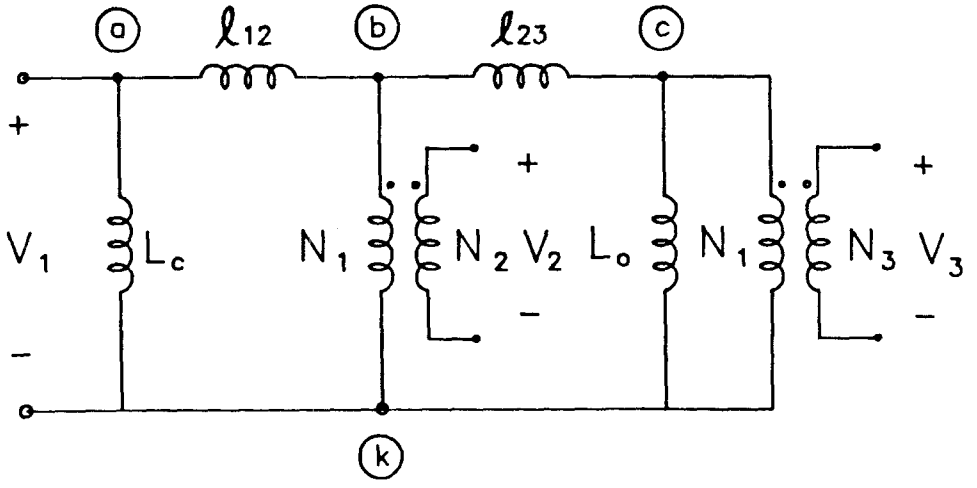

Fig. A.8 Electric circuit model for three-winding side-by-side arrangement.

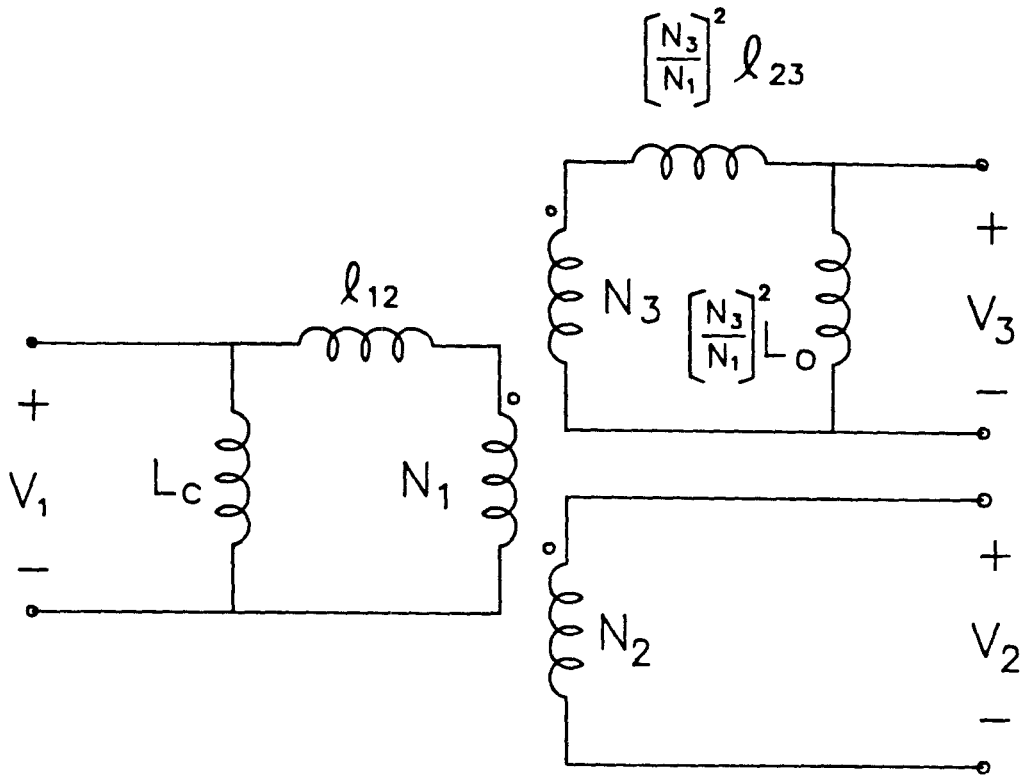

Fig. A.9 *If the inductances L_o and ℓ_{23} in Fig. A.8 are reflected to N_3, the electric circuit model in Fig. A.8 reduces to that shown in this figure, which reflects the "transformer quality" of the magnetic component more than does the circuit model in Fig. A.8.*